Vortices in the New Superconductors

Madsen, Søren Peder; Pedersen, Niels Falsig; Christiansen, Peter Leth; Tønnesen, Ole

Publication date:
2006

Document Version
Publisher's PDF, also known as Version of record

Vortices in The New Superconductors

a Ph.D. thesis by Søren Madsen
Electric Power Engineering, Ørsted·DTU

Main Supervisor:	Prof. Niels Falsig Pedersen	Ørsted·DTU
Supervisors:	Prof. Peter Leth Christiansen	Department of Physics and IMM, DTU
	Prof. Ole Tønnesen	Ørsted·DTU

Financed by the STVF framework programme
“New Superconductors: Mechanisms, processes, and products”

Abstract

This thesis deals with vortices in stacked long Josephson junctions and in two-gap superconductors. The first part is about Josephson vortices, or fluxons, in stacked long Josephson junctions. The thesis introduces the model which is related to high T_c superconductors. Some of the well-known and very important solutions to the non-linear equations are discussed. A possible relationship between the linear and non-linear modes is investigated numerically. The fluxon-solutions can be made to shuttle back and forth in the junctions and they may emit radiation near the junction edge. This radiation is typically in the THz range. The main problem is, however, that the radiated power in a single junction is too small for applications. This is usually solved by stacking more junctions and getting the fluxons in the different junctions to bunch, radiate coherently, and thus increase the emitted power. The main problem is that the vortices repel each other and therefore prefer to be far apart, preventing coherent radiation. Some different ways of obtaining bunched solutions are discussed. A microwave field is shown to be able to introduce bunching in weakly coupled systems. This may also be done using a cavity instead of a microwave field. And finally, the very important flux-flow modes are investigated numerically. It is shown, that in some cases the flux-flow modes spontaneously jump from a triangular fluxon-lattice to a square fluxon-lattice, even in stacks with a strong inductive coupling.

The second subject is vortices in two-gap superconductors, such as MgB_2. These superconductors are investigated through the two-component Ginzburg-Landau theory. The usual Abrikosov vortex is investigated in the two-component version. The equations are solved in the far-field and the effect of a Josephson-type coupling is considered. The subject of vortex-vortex interaction is briefly discussed in the case of zero Josephson coupling. Due to the added complexity of having two order parameters, new features arise. A texture vortex solution is found analytically and numerically in the two-component theory for the case of zero magnetic field. The case of non-zero magnetic field is investigated numerically. The textured vortex seems to be unstable in even a small applied magnetic field.

Dansk Resumé

Denne afhandling omhandler vortex'er i stakkede lange Josephson dioder og i to-gabs superledere. Den første del omhandler Josephson vortex'er, også kaldt fluxoner, i stakkede Josephson dioder. Afhandlingen introducerer modellen, som er relateret til høj T_c superledere. Nogle af de velkendte og meget vigtige løsninger til de ikke-linære partielle differentialligninger bliver diskuteret. En muligt sammenhæng imellem de linære og ikke-linære løsninger bliver undersøgt numerisk. Fluxon-løsningerne kan man få til at løbe frem og tilbage i dioderne og de vil udsende stråling når de rammer ind i diode-kanten. Denne stråling er typisk i THz området. Hovedproblemet er, at effekten af den udsendte stråling i en enkelt diode er for lille til anvendelser. Dette problem løses normalt ved at stakke flere dioder og få fluxonerne i de forskellige dioder til at udstråle i fase og derved øge den udsendte effekt. Problemet er, at fluxonerne frastøder hinanden og de vil derfor foretrække at være langt fra hinanden og ikke udstråle i fase. Nogle forskellige måder at få fluxonerne til at "bunche" på bliver undersøgt. Det vises, at et mikrobølgefelt er i stand til at presse de frastødende fluxoner sammen. Det samme kan man også gøre vha. en kavitet. Desuden bliver de meget vigtige flux-flow løsninger undersøgt numerisk. Det vises, at i nogle tilfælde vil disse løsninger spontant hoppe fra et triangulært gitte til et firkantsgitter, også selvom dioderne er strækt induktivt koblede.

Det andet emne er vortex'er i to-gabs superledere, såsom MgB_2. Denne type superledning undersøges vha. en to-komponent udgave af Ginzburg-Landau teorien. Det velkendte Abrikosov vortex bliver undersøgt i to-komponentsteorien. Ligningerne løses i fjern-feltet og effekten af en Josephson kobling bliver diskuteret. Vortex-vortex vekselvirkningen vil også bliver diskuteret kort, i det tilfælde hvor

der ingen Josephson kobling er. Det vil også blive vist, at der opstår nye interassante fenomener pga. de ekstra frihedsgrader. Et textureret vortex bliver fundet analytisk og numerisk for tilfældet uden magnetfelt. Tilfældet med magnetfelt bliver undersøgt numerisk. Det texturerede vortex lader til at være ustabilt, når der sættes et lille magnetfelt på kanten af superlederen.

Preface

This Ph.D. thesis is the outcome of three years of study at the Section of Electrical Power Engineering (ELTEK) at Ørsted·DTU in Lyngby. The contents is essentially two subjects; stacked long Josephson junctions and two-gap superconductivity. Originally in the planning of the three year study was the subject of Abrikosov vortex pinning in bulk superconductors. During the project it became clear, that a new compound, MgB_2, was behaving differently than other superconductors and many people found the compound interesting. It was then decided to skip Abrikosov vortex pinning and instead looked at models for this new compound, which is a so-called two-gap superconductor.

During the three years I have had the opportunity to work with a lot of people which have all been extremely nice, helpful, and cooperative. I would like to thank Yuri B. Gaididei, Niels Grønbech-Jensen, Giovanni Filatrella, Mogens Samuelsen, Milorad Milosevic, François Peeters, Lev Boulaevskii, Kim Ø. Rasmussen, and last but certainly not least all of my supervisors without whom this thesis would not exist. Thanks a lot to Niels Falsig Pedersen, Peter Leth Christiansen, and Ole Tønnesen.

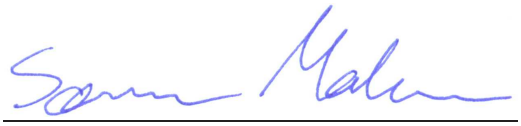

Søren Madsen, Frederiksberg, January 2006

Contents

Chapter 1

Introduction

1.1 Historical Overview

Though it is not extraordinarily cold in the Netherlands, the country hosted "the coldest place on earth" in 1908, more precisely the physics laboratory in Leiden where Kamerlingh-Onnes had successfully liquefied Helium[1], boiling at a temperature of only 4.2K at atmospheric pressure. The liquefaction of helium opened up for many new low temperature experiments. One unresolved question in the beginning of the 20th century was how resistance in metals behaves at very low temperature. It was known that resistance drops with temperature, and at room-temperature this effect is linear, yielding the possibility that resistance will go to zero when the temperature goes to zero. At the time, it was also known that the temperature-dependence of resistance in metals weakened when the temperature was lowered, which naturally lead some to suggest that the resistance reaches a finite value at 0K. A third possibility suggested at the time was, that since resistance is due to atomic motion it will decrease with decreasing temperature, but when the atomic motion is very small at very low temperature, the electrons may bind to the atoms, resulting in lack of electron mobility. From this scenario, the resistance will drop with temperature, reach a finite minimum, then increase, and go to infinity as the temperature goes to zero.

Being the only one on earth with liquefied helium at his disposal, Kamerlingh-Onnes had the best possible position for solving the question about the temperature-dependence of resistance in metals. The metal had to be extremely pure for this type of measurement in order to rule out the influence of impurities. Initial experiments had shown a purity dependent residual resistance to be present in samples of platinum and gold. Kamerlingh-Onnes decided to study mercury, as it could be made the purest of all metals at the time. Measurements on mercury showed a surprising effect. The resistance did approach zero when the temperature was lowered, but not in a continuous fashion. Near 4.2K the resistance suddenly dropped below the measuring capabilities of the experimental apparatus. Kamerlingh-Onnes' measurement can be seen in Fig. 1.1. Initially, he was cautious and reported "the resistance would,

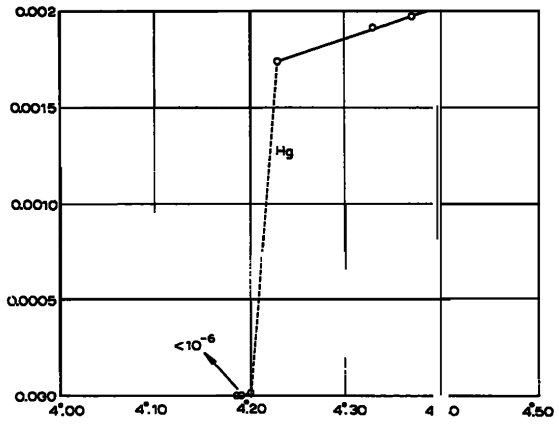

Figure 1.1: Measurement of the superconductivity of mercury by Kamerlingh-Onnes[2, 3].

within the limits of experimental accuracy, become zero.". However, after studying more mercury samples he wrote in 1911 that mercury "passed into a new state, which on account of its extraordinary electrical properties may be called the superconducting state.". Later, he discovered that also lead and tin became superconducting and in 1913 he was awarded the Nobel prize "for his investigations on the properties of matter at low temperatures which led, inter alia, to the production of liquid helium"[4].

Just as surprising as zero resistance is the Meissner effect. In 1933 Meissner and Ochsenfeld discovered that superconductors expel magnetic fields from their interior. If some material has zero resistance, then it is known from Maxwell's equations that it will not allow a magnetic field to enter through the boundaries. If, however, the magnetic field is present *before* the material becomes a perfect conductor, then it will remain inside the material. If a superconductor, which is also a perfect conductor, is placed in a magnetic field and then cooled below the transition temperature, it will expel the magnetic field from the interior of the superconductor. A superconductor is thus not merely a perfect conductor, but it also has some special magnetic properties. A, by now, classical table-top experiment of the Meissner effect is to take a superconductor, place a small magnet on top of it, and cool the superconductor below the transition temperature. The Meissner effect will then make the magnet levitate above the superconductor.

Theorists always strive to understand new and strange phenomena, but it took more that 20 years after the experimental discovery by Kamerlingh-Onnes to make the first theory of superconductivity. The phenomenological London-theory was proposed by the London brothers in 1935[5]. They proposed the relationship

$$\nabla \times \mathbf{J}_s = -\frac{n_s e^2}{mc}\mathbf{H}, \tag{1.1}$$

where $\mathbf{J}_s$ is the supercurrent density, n_s is the density of supercurrent carriers, m is the mass of a supercurrent carrier, and $\mathbf{H}$ is the magnetic field. Such a relationship together with Maxwell's and Newton's equations leads to the Meissner effect, but also superconducting vortices may be described by the theory.

Another phenomenological theory was put forth in 1950 by Landau and Ginzburg. The theory combined Landau's theory of second order phase transitions with a Schrödinger-like wave equation, and has great success in explaining many properties of superconductors. A breakthrough was made by Abrikosov who showed the existence of two types of superconductors and the vortex state, only found in Type-II superconductors. It is known that in some limit the theory reduces to the London theory. Ginzburg, Abrikosov, and Legget (superfluids) received a Nobel prize in 2003 "for pioneering contributions to the theory of superconductors and superfluids"[6].

Since both the London theory and the Ginzburg-Landau theory are phenomenological theories, they do not provide a true explanation for superconductivity. Such an explanation came in 1957 in the form of a quantum-theory for superconductivity. The theory is named the BCS theory after its inventors Bardeen, Cooper, and Schrieffer. All three were awarded the Nobel prize in 1972 "for their jointly developed theory of superconductivity, usually called the BCS-theory"[7].

In 1959 Gor'kov showed that the BCS theory reduces to the phenomenological Ginzburg-Landau theory when the temperature is close to the transition temperature[8]. This is tremendously important, since it explains the validity of the Ginzburg-Landau theory allowing in many cases for simpler calculations than the BCS theory.

The extremely important phenomenon of tunneling in superconductors was discovered around 1960. Giaever did experiments on superconducting tunneling systems and a few years later, Josephson explained tunneling in superconductors theoretically. Giaever, Josephson, and Esaki (semiconductors) received a Nobel prize in 1973 for their work. Esaki and Giaever "for their experimental discoveries regarding tunneling phenomena in semiconductors and superconductors, respectively"[9] and Josephson "for his theoretical predictions of the properties of a supercurrent through a tunnel barrier, in particular those phenomena which are generally known as the Josephson effects"[9].

Another milestone in the field of superconductivity came in 1986 when Müller and Bednorz discovered superconductivity in copper-oxide based compounds. For this discovery they were awarded the Nobel prize as soon as in 1987 "for their important break-through in the discovery of superconductivity in ceramic materials"[11]. The accomplishment of Müller and Bednorz was that they showed a measurement with a transition temperature above 30K of a compound consisting of La, Ba, Cu, and O. This measurement was at first met with skepticism since the previous record in transition temperature was around 23K. However the measurement was reproduced in Japan, and in the end of 1986 Müller and Bednorz measured $La_{1.85}Ba_{0.15}CuO_4$ to have a transition temperature of 35K. As soon as in January

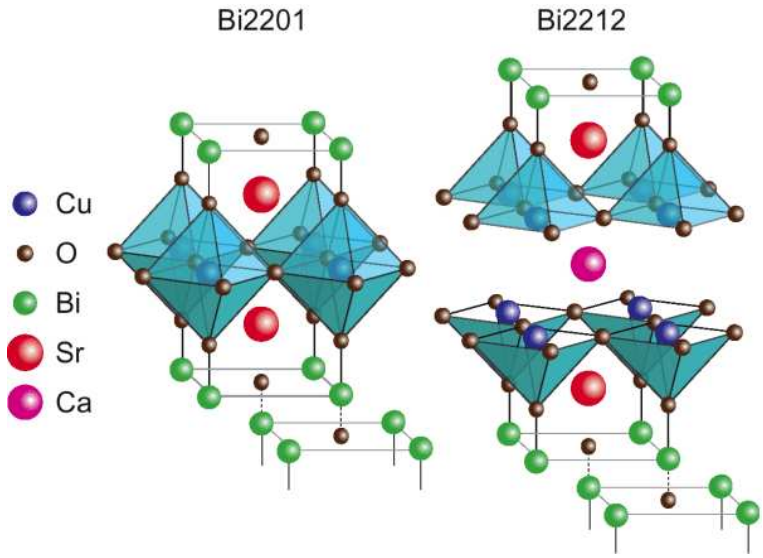

Figure 1.2: The atomic structure of the high T_c superconductors $Bi_2Sr_2CuO_6$ (T_c=36K) and $Bi_2Sr_2CaCu_2O_8$ (T_c=96K)[10].

1987, Chu and Wu discovered the, now famous, high T_c superconductor $YBa_2Cu_3O_7$ (YBCO) with $T_c = 95$K. With this discovery superconductivity entered a new era, since superconductors could then be cooled with liquid nitrogen, boiling at 77K and much cheaper than liquid helium.

The quest for even higher transition temperatures continues, and the present record is 164K for the compound $HgBa_2Ca_2Cu_3O_8$ at high pressure (30GPa). The Holy Grail would be to find a room-temperature superconductor, which has not yet happened. What has also become clear is that the BCS theory can not account for the high T_c superconductors. Nobody knows for sure how they work, if a completely new theory of superconductivity is needed, and if a modified BCS theory might is "enough".

The latest major excitement in the field of superconductivity came in 2001, when a transition temperature of 39K was detected for MgB_2[12]. While the transition temperature is quite low compared to the high T_c cuprates, it is higher than the classical low temperature superconductors. It has been found that MgB_2 behaves like a superconductor described by a modified version of the BCS theory allowing for two "types" of charge-carriers, a so-called two-gap BCS theory[13].

1.2 Outline

This thesis will try to explain the basic concepts of superconductivity with the Ginzburg-Landau theory as the foundation. Most terms are explained in the text, such that it may be read without too much prior knowledge about superconductivity. The main subject of the thesis is vortices in the new superconductors, as the title suggests. Three different kinds of vortices are considered: The Josephson vortex, the Abrikosov vortex, and the textured vortex. The three vortices are quite different from one another and each posses some unique properties. The Josephson vortex is considered mostly in the context of building a microwave oscillator in the THz range, but also some generic properties are investigated. The Abrikosov vortex in a two-component system is important for the application of the compound MgB_2, but also interesting in its own right. The textured vortex is a vortex without a magnetic field and does not have an analogue in ordinary Ginzburg-Landau theory because it is present due to the two order parameters.

Chapter One is the present chapter. It introduces superconductivity and explains the structure of and the philosophy behind this text.

Chapter Two will serve as an introduction to superconductivity with special emphasis on Ginzburg-Landau theory and the Josephson effect, since these two subjects are the cornerstones of the Ph.D. project. Some basic consequences of the Ginzburg-Landau theory of superconductivity are derived and explained, including the Meissner-effect, the phase diagram of superconductors, and the Abrikosov vortex. The chapter also contains an introduction to the Josephson junction and its basic solutions and

solution methods. All this will serve as an introduction to chapters three, four, and five which presents the main results of the project.

Chapter Three introduces the reader to the Josephson junction stack. The model is derived and explained in detail. The similarity between stacked Josephson junctions and high T_c superconductors is discussed. Many important solutions are demonstrated analytically, which serve to understand many of the phenomena in these systems. The model is highly complex and non-linear and the last section deals numerically with a possible relationship between linear solutions (plasma modes) and non-linear solutions (fluxons) in the model.

Chapter Four looks at the possibility for using a stack of Josephson junctions as an oscillator, potentially operating in the THz range. The idea is to get the junctions to radiate coherently to greatly increase the emitted power above that of a single junction. Investigated first is how much the emitted power is increasing by using more than one junction and it is shown that all the junctions does not necessarily have to be in the all-fluxon in-phase mode for the stack to radiate effectively. The next section is kind of the reverse situation, because it shows that it is possible to obtain coherent motion by applying an external microwave field to two coupled junctions containing one fluxon each. In the following section it is discussed how a stack of junctions radiating into a cavity allows for the possibility to enhance and induce coherence, because the cavity feedback to the junctions behaves much like an external microwave field. The fourth section looks at the idea of applying a large homogeneous magnetic field to the stack. This will generate Josephson vortices at one end, traveling to the other end of the junction where they are annihilated and radiation is emitted. The connection between the fluxon-lattice and features of the voltage vs. magnetic field characteristics of stacks is discussed in detail.

Chapter Five looks at an extended version of the Ginzburg-Landau theory, applicable to two-gap superconductors like MgB_2. First, the Abrikosov vortex solution is considered. The interaction between two Abrikosov vortices are derived in the extended theory and compared to the usual Ginzburg-Landau theory. Next, it is shown how a so-called textured vortex solution may be constructed analytically in the theory. This vortex shows depression of the superconducting order parameter *without* a magnetic field. The effect on the textured vortex of a Josephson type coupling between the two order parameters is considered. The last section shows numerically what happens when a magnetic field is applied to the textured vortex solution.

Chapter Six summarizes the new results for an easy overview and concludes the thesis.

1.3 Publications

The main purpose of this thesis is to tell about the research which has been conducted during the three years of Ph.D. study. The work has been done in close collaboration with Niels Falsig Pedersen, Yuri B. Gaididei, Peter Leth Christiansen, Niels Grønbech-Jensen, and Giovanni Filatrella. The contributions from all of these people have of course been invaluable. Most of the research has already been published; nine papers in international journals with referee and two in conference proceedings. The papers are listed as numbers 3-13 in Appendix A. Publications 1 and 2 are previous publications by the author.

Since most of the research have already been published, many of the figures and sections of this thesis are almost direct copies from the papers in Appendix A, though the text and figures have been edited (some more than others) to fit seamlessly into the context of the thesis. The table on page 5 shows how the sections and figures in the thesis relates to the papers in Appendix A.

In addition to the results published in the papers, Sections 4.3, 5.2, and 5.4 contains previously unpublished material. Section 4.3 deals with a cavity coupled to a long Josephson stack. The previously unpublished results are the connection with the applied external microwave field considered in Section 4.2 and the analytical analysis of the system in the weak coupling limit with fluxons modeled as δ-function pulses to the cavity. Section 5.2 looks at the Abrikosov vortex in the two-gap Ginzburg-Landau theory and the interaction between two vortices are derived for zero Josephson coupling. Section 5.4 looks numerically at what happens to the textured vortex when a magnetic field is applied to the system.

Section α contains results and/or text from paper no. β in Appendix A. Fig. γ in the thesis is the same as Fig. δ in paper no. β.			
α	β	γ	δ
3.2.2	3		
	3	3.3	2
3.2.2	5		
3.3	3		
	3	3.6	3
	3	3.9	4
	3	3.10	5
	3	3.11	6
	3	3.12	7
3.3	4		
	4	3.9	2
3.3	5		
	5	3.7	2
	5	3.8	3
	5	3.13	4
4.1	4		
	4	4.1	4
	4	4.2	5
	4	4.3	6
	4	4.4	7
4.2	10		
	10	4.6	1
	10	4.7	2
4.3	6		
	6	4.10	4
	9		
4.4	12		
	12	4.15	2
	12	4.16	3
	12	4.17	4
	12	4.19	5
	12	4.20	6
	12	4.21	7
4.4	13		
	13	4.18	2,3,...,10
5.3	11		
	11	5.3	1
	11	5.4	2
	11	5.5	3
	11	5.6	4
	11	5.7	5
	11	5.8	6
B	11		

Chapter 2

General Properties of Superconductors

This chapter gives the reader a quick introduction to superconductivity though the use of Ginzburg-Landau theory. Many important concepts will be derived and discussed. Most important are the Abrikosov vortex and the Josephson junction which are central subjects of the text. It must be noted, though, that the situation in real superconductors are sometimes more complicated than presented here where only the case of isotropic low T_c superconductors are considered. Anisotropy may be included in the calculations but it makes the calculations considerably more complicated and the introductory aspect will be lost. High T_c superconductors is considered in Chapter 3 as a stack of Josephson junctions.

2.1 The Ginzburg-Landau Theory

The Ginzburg-Landau theory was first introduced in 1950 by Ginzburg and Landau as a phenomenological theory[14]. Later it was shown by Gor'kov[8] that the theory could be derived in the limit where T is close to T_c of the microscopic theory of superconductivity, the BCS theory[15]. The theory has been very successful in explaining many aspects of superconductors and it is thus very actively studied today. The theory is non-linear in nature and it is therefore hard to work with analytically. It is also a very popular choice when simulating superconductors on a computer.

Although the Ginzburg-Landau theory can be derived from the BCS theory, it will not be done in this text. Rather, the view that it is a phenomenological theory, which has been shown to work well by experiment, will be taken. The heart of the theory is called the order parameter, denoted here by ψ. One may think of the order parameter as the wave-function of the charge-carriers, Cooper-pairs, in the superconductor and $|\psi|^2$ is then the density of Cooper-pairs. The order parameter is subject to a 4th order potential[14, 16]

$$V(|\psi|) = -\alpha|\psi|^2 + \frac{\beta}{2}|\psi|^4 \ . \tag{2.1}$$

Two "constants" are present in this potential, α and β, where α is taken to be a function of the temperature, such that a phase transition happens at $T = T_c$. This can be obtained if

$$\alpha(T) = K(1 - T/T_c) \ , \tag{2.2}$$

where $K > 0$ is some constant, to be determined by experiment, and $\beta > 0$ is independent of temperature. With this choice it is seen that $T > T_c \Rightarrow \alpha < 0$ making the sign in front of the $|\psi|^2$ term in the potential positive, while $T < T_c$ gives the $|\psi|^2$ term a negative sign. This means, that the minimum of the potential for $T > T_c$ is at $\psi = 0$ and for $T < T_c$ the minimums are at non-zero values of ψ, resulting in the generation of Cooper-pairs when T_c is crossed. Fig. 2.1 shows a plot of Eq. (2.1) for the two cases, $\alpha < 0$ ($T > T_c$) and $\alpha > 0$ ($T < T_c$).

Another important effect of superconductivity is the Meissner-effect, where magnetic fields are expelled from the interior of a superconductor. To explain such an effect, magnetism must obviously be taken into account. This is done in the standard way by introducing a vector potential and replacing

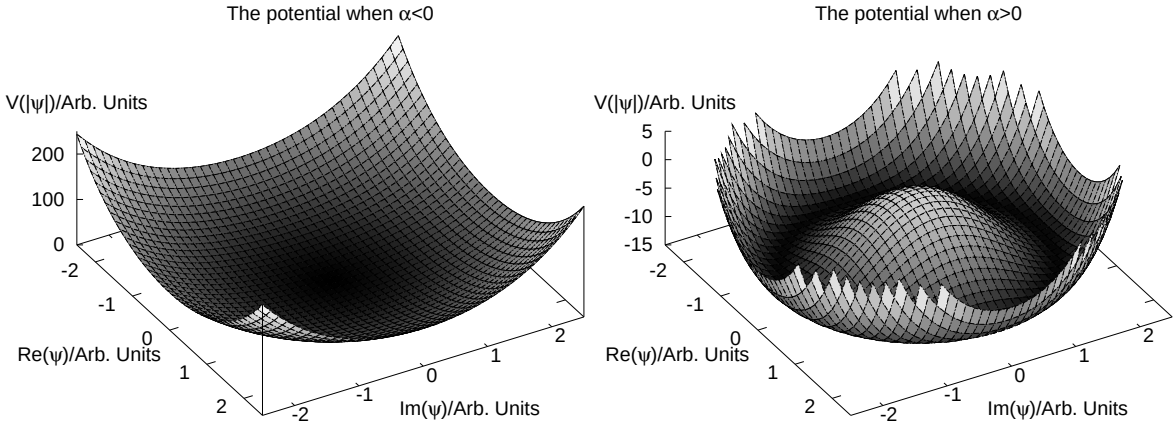

Figure 2.1: The minimum of the potential depends on the sign of the parameter α. For $\alpha < 0$ ($T > T_c$) the minimum is when $\psi = 0$, corresponding to the normal phase. $\alpha > 0$ ($T < T_c$) is the superconducting phase, where the minimum of the potential is for non-zero order parameter, corresponding to the existence of Cooper-pairs.

derivatives with covariant-derivatives[17]. A free energy functional, including the order-parameter and magnetism, thus becomes[16, 18]

$$G = \int_\Omega d^3R \left(\frac{1}{2m} \left| (i\hbar\nabla + q\mathbf{A})\psi \right|^2 - \alpha|\psi|^2 + \frac{\beta}{2}|\psi|^4 + \frac{(\mathbf{B}_a - \mathbf{B})^2}{2\mu_0} \right) , \tag{2.3}$$

where the vector $\mathbf{A}$ is the vector potential, $\mathbf{B} = \nabla \times \mathbf{A}$, $\mathbf{B}_a$ is the applied magnetic field[1], $m = 2m_e$ and $q = 2e$ are the mass and charge of a Cooper-pair, respectively. The free energy functional, G, can be interpreted as a Gibbs free energy of the system[16, 18]. Time-dependence may also be introduced into the theory, but it will not be considered explicitly here, though it is actually used when the equations are solved numerically.

Minimizing the free energy functional in Eq. (2.3) by applying standard variational calculus, the Ginzburg-Landau equations together with boundary conditions are obtained to be[16, 18]

$$\frac{1}{2m}\Big(i\hbar\nabla + q\mathbf{A}\Big)^2\psi - \alpha\psi + \beta|\psi|^2\psi = 0 \qquad in \qquad \Omega \ , \tag{2.4}$$

$$\Big(i\hbar\nabla\psi + q\mathbf{A}\psi\Big) \cdot \mathbf{n} = 0 \qquad on \qquad \partial\Omega \ , \tag{2.5}$$

$$\frac{\nabla \times \mathbf{B}}{\mu_0} = -\frac{q\hbar}{2m}\Big(i(\psi^*\nabla\psi - \psi\nabla\psi^*) + \frac{2q}{\hbar}|\psi|^2\mathbf{A}\Big) \equiv \mathbf{J} \qquad in \qquad \Omega \ , \tag{2.6}$$

$$\mathbf{B} = \mathbf{B}_a \qquad on \qquad \partial\Omega \ , \tag{2.7}$$

where Ω is the system domain, $\partial\Omega$ is the surface of Ω and $\mathbf{n}$ is a normal vector to $\partial\Omega$. Introduced in these equations is the supercurrent, $\mathbf{J}$, as can be justified by comparing Eq. (2.6) with Maxwell's equations.

2.1.1 Numerical Method

The Ginzburg-Landau Eqs. (2.4)-(2.7) are very general equations possessing a lot of interesting solutions. A good way to see some of these solutions are to solve the equations numerically. A program has been written to solve the more general Eqs. (5.4)-(5.9), which are going to be discussed in Chapter 5. The program is also able to solve the normal Ginzburg-Landau equations since Eqs. (5.4)-(5.9) reduce to Eqs. (2.4)-(2.7) when $\psi_1 \equiv \psi$ and $\psi_2 \equiv 0$. The present section contains some details on how the numerical solutions are obtained, using, for simplicity, Eqs. (2.4)-(2.7) as the example. The extension to solve Eqs. (5.4)-(5.8) is straight forward and will not be discussed.

The method used here is the link-variable approach[19, 20] combined with an Euler method[21]. The reader interested in details is advised to look in Refs. [19], [20], and [21], as only a rather short

[1]The phrase "magnetic field" will be used throughout the text for both $\mathbf{B}$ and $\mathbf{H}$ since $\mathbf{B} = \mu_0\mathbf{H}$ is usually assumed.

description is given here. The method is based on finite-differences to discretize the partial differential equations. The straight-forward discretization has, however, one problem, because the resulting discrete equations are *not* gauge-invariant. Lack of gauge-invariance does not render the straight-forward method useless[22], but maintaining gauge-invariance in the discretized equations improves convergence for high magnetic fields[19]. The equations which are solved are actually not exactly Eqs. (2.4)-(2.7), but rather the time-dependent Ginzburg-Landau equations, which may be written as[20]

$$\frac{1}{2m}\Big(i\hbar\nabla + q\mathbf{A}\Big)^2\psi - \alpha\psi + \beta|\psi|^2\psi = -\frac{\hbar^2}{2mD}\left(\frac{\partial}{\partial t} + i\frac{q}{\hbar}\phi\right)\psi \qquad in \qquad \Omega\ , \tag{2.8}$$

$$\Big(i\hbar\nabla\psi + q\mathbf{A}\psi\Big)\cdot\mathbf{n} = 0 \qquad on \qquad \partial\Omega\ , \tag{2.9}$$

$$\frac{\nabla\times\mathbf{B}}{\mu_0} + \frac{q\hbar}{2m}\Big(i(\psi^*\nabla\psi - \psi\nabla\psi^*) + \frac{2q}{\hbar}|\psi|^2\mathbf{A}\Big) = -\sigma\left(\frac{\partial\mathbf{A}}{\partial t} + \nabla\phi\right) \qquad in \qquad \Omega\ , \tag{2.10}$$

$$\left(\frac{\partial\mathbf{A}}{\partial t} + \nabla\phi\right)\cdot\mathbf{n} = 0 \qquad on \qquad \partial\Omega\ , \tag{2.11}$$

$$\mathbf{B} = \mathbf{B}_a \qquad on \qquad \partial\Omega\ . \tag{2.12}$$

D is termed the diffusion constant. Before trying to solve the equations numerically, they are of course normalized first, see Refs. [19] and [20] for the details. Normalization of the time-independent equations is discussed in Chapter 5.

The time-dependent Ginzburg-Landau equations are invariant under the gauge-transformation[2]

$$\psi \to e^{i\chi(\mathbf{r},t)}\psi \quad , \quad \mathbf{A} \to \mathbf{A} - \frac{\hbar}{q}\nabla\chi(\mathbf{r},t) \quad , \quad \phi \to \phi + \frac{\partial\chi(\mathbf{r},t)}{\partial t} \tag{2.13}$$

where $\chi(\mathbf{r},t)$ is some function depending on space and time. The transformation enables one to remove the dependence of the scalar potential, ϕ, in the equations. This is called the zero potential gauge, and it is common to use in numerical solutions of the Ginzburg-Landau equations. The equations will after such a gauge-transformation only contain the time-derivative of $\mathbf{A}$ and ψ on the right hand side. If these time-dependent equations are solved and the numerical code is stopped when the conditions

$$\frac{\partial\phi}{\partial t} = 0 \quad \text{and} \quad \frac{\partial\mathbf{A}}{\partial t} = 0 \tag{2.14}$$

are fulfilled, then a solution to Eqs. (2.4)-(2.7) have been obtained.

The link-variables, U_μ^a, enters through the vector potential as

$$U_\mu^a = e^{i\int_{\mu_0}^{a} A_\mu d\mu} \quad , \quad \mu = x,\ y,\ \text{or}\ z\ , \tag{2.15}$$

where μ_0 is some point common for all link-variables with direction μ. The actual derivation of the discretized time-dependent Ginzburg-Landau equations in terms of the link-variables is a bit tedious, so only some of the properties of the link-variables will be shown here to give the reader a feeling of what the link-variables are. Refs. [19] and [20] provide more information on the subject.

The product of a link-variable and the conjugate of a link-variable is

$$\left(U_\mu^a\right)^* U_\mu^b = e^{i\int_a^b A_\mu d\mu} \equiv U_\mu^{ab}\ . \tag{2.16}$$

Consider a square in two dimensions with corners $a = (-L/2, -L/2)$, $b = (L/2, -L/2)$, $c = (L/2, L/2)$, and $d = (-L/2, L/2)$. The magnetic field at $(x, y) = (0, 0)$ may then be calculated by

$$U_x^{ab}U_y^{bc}U_x^{cd}U_y^{da} = e^{-i\oint_{abcda}\mathbf{A}\cdot d\mathbf{r}} = e^{-\int_{Area(abcd)}B_z dS} \approx 1 - iL^2B_z(0,0)\ . \tag{2.17}$$

Using relations similar to the above and finite differences for the order parameter, one is able to express the time-dependent Ginzburg-Landau equations in terms of the link-variables and the order parameter without breaking the gauge-invariance.

The time-stepping is done using an Euler procedure and stopped when the conditions in Eq. (2.14) are satisfied within some tolerance. Due to the slow nature of the Euler-procedure, the program is only designed to solve the Ginzburg-Landau equations in two spatial dimensions. It is possible, however, to formulate other schemes for solving the discretized equations, which are much faster and allows for solutions in three dimensions[26]. The simple Euler procedure is nevertheless good enough for the small number of calculations in this text.

[2] This transformation is also called a local $U(1)$ transformation in mathematical physics. The time-dependent Ginzburg-Landau theory may thus be considered as a non-relativistic version of the Abelian Higgs model, widely used in particle physics and cosmology[23, 24, 25].

2.2 Basic Consequences of the Ginzburg-Landau Equations

The first thing to check with a theory is if it explains the very simple things. In this case, solutions corresponding to a normal phase and to a perfect Meissner phase must exist. The normal phase solution is seen to exist if ψ is set to zero (i.e. no Cooper-pairs) in Eqs. (2.4)-(2.6) which simplifies to $\nabla \times \mathbf{B} = 0$. This equation has a solution where $\mathbf{B}$ is constant. To satisfy the boundary conditions, this constant must be $\mathbf{B}_a$, resulting in $\mathbf{B} = \mathbf{B}_a$. This is precisely the solution of a normal phase with no Cooper pairs and the magnetic field is just penetrating the superconductor like if it was not there. To construct the Meissner phase solution $\mathbf{A}$ is put equal to zero in the Ginzburg-Landau equations, yielding

$$-\frac{\hbar^2}{2m}\nabla^2\psi - \alpha\psi + \beta|\psi|^2\psi = 0 \ , \tag{2.18}$$

which can be solved by $|\psi|^2 = \alpha/\beta$. This give a constant non-zero Cooper-pair density and no magnetic field in the sample, thus a perfect Meissner phase.

One may also be more ambitious and derive the $H-T$ phase diagram of a superconductor using the Ginzburg Landau theory. Looking at Eq. (2.3) and interpreting the integrand as a Gibbs free energy density, the energy of the normal phase and of the Meissner phase may be compared. Inserting the normal phase solution and the Meissner phase solution into Eq. (2.3), the energy density is obtained to be

$$g_N = 0 \tag{2.19}$$

for the normal phase and

$$g_M = -\frac{\alpha^2}{2\beta} + \frac{\mathbf{B}_a^2}{2\mu_0} \tag{2.20}$$

for the Meissner phase. It is seen, that for zero applied magnetic field, the Meissner phase has lower energy density than the normal phase. Equating the two energy densities, the point where the normal phase becomes energetically favorable over the Meissner phase may be calculated. This defines the thermodynamic maximum field, H_c, to[16]

$$H_c = \sqrt{\frac{\alpha^2}{\mu_0\beta}} \ . \tag{2.21}$$

An expression for the maximum magnetic field where superconductivity can exist, H_{c2}, will now be found. If the magnetic field is so high that the sample is in the normal state and it is lowered just enough to make the system slightly superconducting, it is fair to assume that $|\psi|^2$ is small, and the non-linear term may be neglected in the scalar Eq. (2.4), which reduces to

$$\frac{1}{2m}\left(i\hbar\nabla + q\mathbf{A}\right)^2\psi = \alpha\psi \ . \tag{2.22}$$

Since the system is close to the normal phase, the magnetic field must, to a good approximation, penetrate the superconductor. Thus, $\mathbf{A} = (0, \mu_0 x H_z, 0)$ is a good guess for the vector potential, since it corresponds to a constant magnetic field in the z-direction. This turns Eq. (2.22) into

$$\frac{1}{2m}\left(-\hbar^2\nabla^2 + 2i\mu_0 q\hbar x H_z\frac{\partial}{\partial y} + (\mu_0 q x H_z)^2\right)\psi = \alpha\psi \ . \tag{2.23}$$

This equation is formally equivalent to the Schrödinger equation for a charged particle in a magnetic field, and the solution may be looked up in most textbooks on quantum mechanics. The solution to the eigenvalue equation may be expressed as[16, 27]

$$H_z = 2\frac{m\alpha - \frac{1}{2}\hbar^2 k_z^2}{\mu_0 q\hbar(2n+1)} \tag{2.24}$$

where n is the "energy quantum number" and k_z is the "momentum quantum number" as normally defined in the Schrödinger equation[27]. The main interest is here for the highest H_z, which is found when $n = k_z = 0$. This H_z is named H_{c2} and becomes[16]

$$H_{c2} = \frac{2m\alpha}{\mu_0 q\hbar} = \sqrt{2}\kappa H_c \quad , \quad \text{where } \kappa \equiv \sqrt{\frac{2m^2\beta}{\mu_0 q^2\hbar^2}} \ . \tag{2.25}$$

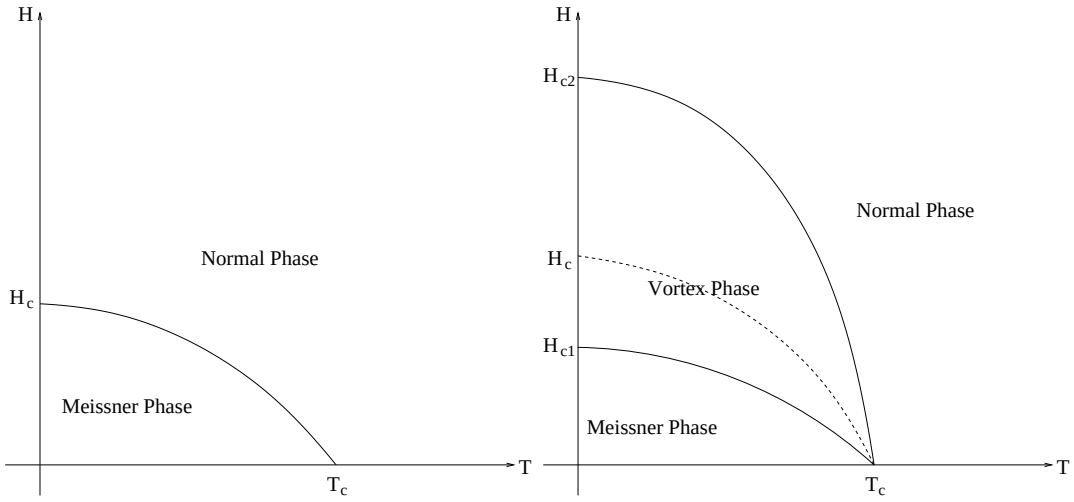

Figure 2.2: Sketch of the phase-diagrams for Type I (left) and Type II (right) superconductors as derived from Ginzburg-Landau theory.

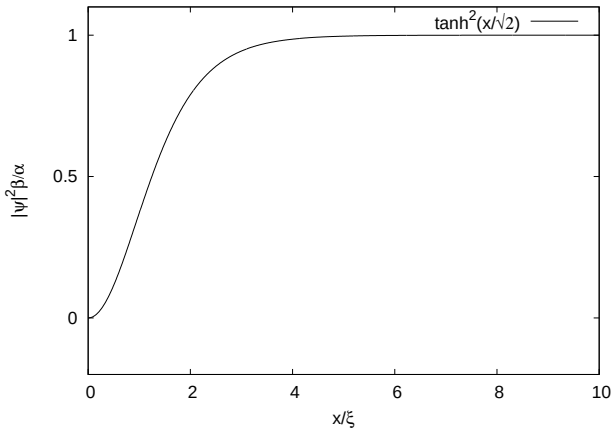

Figure 2.3: Plot of the solution in Eq. (2.30) showing how the density of Cooper pairs, $|\psi|^2$, changes in space from a normal state to a Meissner state.

The new parameter, κ, is called the Ginzburg-Landau parameter. Depending on the size of the Ginzburg-Landau parameter, superconductors are divided into two categories. If $\kappa < 1/\sqrt{2}$ then H_{c2} is lower than the thermodynamic field H_c, and superconductivity may exist in the sample up to H_c. But if $\kappa > 1/\sqrt{2}$, then H_{c2} is larger than H_c, which means superconductivity survives beyond H_c and up to H_{c2}. It is therefore custom to classify superconductors according to[16, 18]:

$$\begin{array}{ll} \text{Type I Superconductor} & \text{if} \quad \kappa < \frac{1}{\sqrt{2}} \\ \text{Type II Superconductor} & \text{if} \quad \kappa > \frac{1}{\sqrt{2}} \end{array}$$

In addition to the fields H_c and H_{c2} one may also derive a field named H_{c1} for Type-II superconductors. The fields correspond to a new phase, where the superconductor is in a sort of a mixture of the normal-phase and the Meissner-phase. This phase is named the vortex phase. The derivation of H_{c1} will not be done here due to the complexity. H_{c1} was first calculated by Abrikosov and it lead him to postulate the existence of the vortex-phase. His calculations showed that[28]

$$H_{c1} = \frac{1}{2\kappa} \left(\ln \kappa + 0.08 \right) H_c \ . \tag{2.26}$$

Using the temperature dependence of α in Eq. (2.2) the $H - T$ phase-diagram of the two types of superconductors has been sketched in Fig. 2.2.

Returning to Eq. (2.18), it is clearly seen that the normal phase solution, $\psi = 0$ and the Meissner phase solution, $|\psi|^2 = \alpha/\beta$, are not the only solution to this equation because it resembles the famous non-linear Schrödinger equation[29]. A simple solution will now be demonstrated. Looking at the one dimensional case and letting $\psi = \sqrt{\alpha/\beta}\,\tilde{\psi}$ and $x = \sqrt{\hbar^2/(2m\alpha)}\,\tilde{x}$, the normalized equation

$$\tilde{\psi}'' + \tilde{\psi} - |\tilde{\psi}|^2\tilde{\psi} = 0 \tag{2.27}$$

is obtained where primes denotes differentiation with respect to $\tilde{x}$. A simple solution can be found if the order parameter is assumed to be real. The first integral then is found to be

$$\frac{1}{2}(\tilde{\psi}')^2 + \frac{1}{2}\left(\tilde{\psi}^2 - \frac{1}{2}\tilde{\psi}^4\right) = E \ , \tag{2.28}$$

which has the form of a mechanical energy equation, thus it seem natural to assume $E > \frac{1}{2}\left(\psi^2 - \frac{1}{2}\psi^4\right)$ such that the "kinetic energy", $(\tilde{\psi}')^2/2$, is positive. Under this assumption, the variables are separated and the equation becomes

$$\int \frac{d\tilde{\psi}}{\sqrt{E - \frac{1}{2}\left(\tilde{\psi}^2 - \frac{1}{2}\tilde{\psi}^4\right)}} = \sqrt{2}\,\tilde{x} \ , \tag{2.29}$$

where a $\pm$ sign has been omitted. The integral on the left hand side can be evaluated in the general case using Jacobi elliptic functions, but when $E = 1/4$ it may be written using elementary functions. Inserting the Meissner solution into Eq. (2.28), the value of E is luckily found to be $1/4$, justifying this choice. Now, using that $f < 1$ and setting the constant of integration to zero in Eq. (2.29), the solution is found to be

$$\psi = \sqrt{\frac{\alpha}{\beta}}\tanh\left(\frac{x}{\sqrt{2}\,\xi}\right) \ , \tag{2.30}$$

where a transformation back to the original variables were used and

$$\xi \equiv \sqrt{\frac{\hbar^2}{2m\alpha}} \ , \tag{2.31}$$

is called the coherence length. A plot of the square of this solution can be seen in Fig. 2.3. It is seen, that it is zero at $x = 0$ and it goes to α/β for $x \to \infty$, thus approaching asymptotically the Meissner solution. This corresponds intuitively to an infinite superconductor in the positive half-plane. The coherence length, ξ, introduced above determines how quickly ψ changes from, here, 0 to $\sqrt{\alpha/\beta}$.

Note, that although the solution *intuitively* corresponds to a normal-superconductor interface it actually does *not* satisfy the boundary condition in Eq. (2.5) for $\mathbf{A} = 0$ since $\nabla\psi|_{x=0} \neq 0$, though $\nabla\psi^2|_{x=0} = 0$. The solution is a domain wall separating the $\psi = -\sqrt{\alpha/\beta}$ ($x \to -\infty$) domain from the $\psi = \sqrt{\alpha/\beta}$ ($x \to \infty$) domain.

The magnetic field Eq. (2.6) can be solved in a similar way, to get a more detailed look at the magnetic field in the Meissner phase. Setting $\psi = \sqrt{\alpha/\beta}$ in Eq. (2.6), it reduces to

$$\frac{\nabla \times \mathbf{B}}{\mu_0} = -\frac{q^2\alpha}{m\beta}\mathbf{A} \ . \tag{2.32}$$

Taking the curl on both sides, the 2nd London equation is recovered as

$$\nabla^2\mathbf{B} = \frac{1}{\lambda^2}\mathbf{B} \quad , \quad \frac{1}{\lambda^2} = \frac{\mu_0 q^2\alpha}{m\beta} \ . \tag{2.33}$$

Here, the new parameter, λ, is called the (London) penetration depth of the superconductor and is the "coherence length" of the magnetic field. Note, that the Ginzburg-Landau parameter, κ in Eq. (2.25), may now be written as the ratio between the penetration depth and the coherence length,

$$\kappa = \frac{\lambda}{\xi} \ , \tag{2.34}$$

which is the form usually used in the literature.

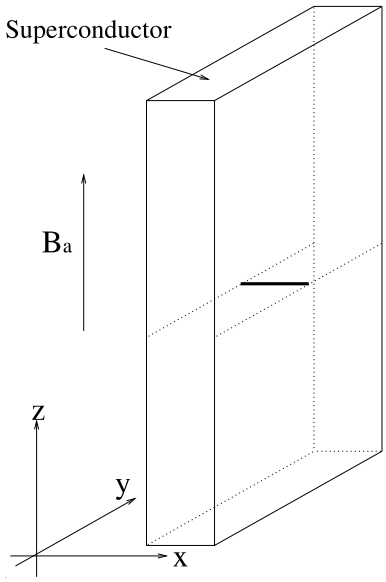

Figure 2.4: To solve the 2nd London Eq. (2.33), the simple case where $\mathbf{B}_a$ and $\mathbf{B}$ only have a z component and the variation of $\mathbf{B}$ in the y and z direction can be neglected is considered. This corresponds to looking at the magnetic field along the thick line. The origin is arbitrarily placed in the picture.

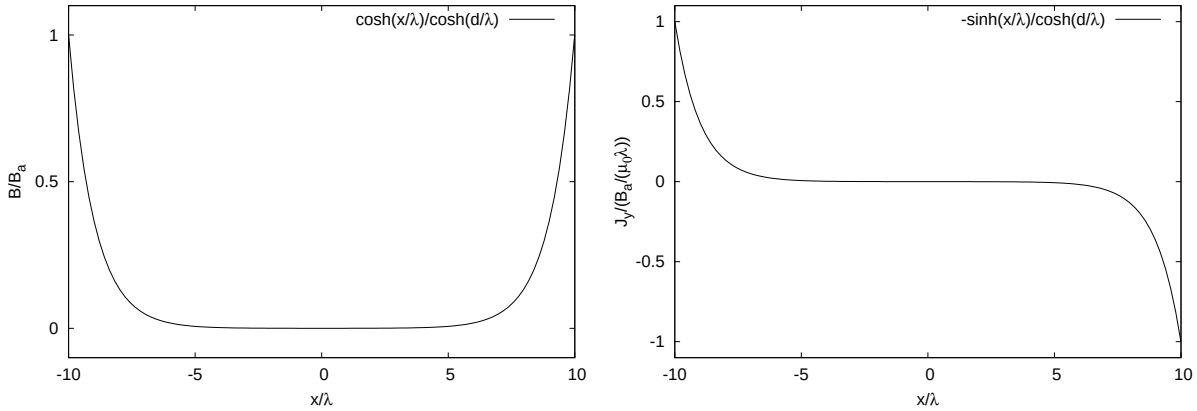

Figure 2.5: The magnetic field in Eq. (2.36) (left) and the current in Eq. (2.37) (right) for $d = 10$.

To solve the 2nd London equation (2.33), a simple one-dimensional case is considered. $\mathbf{B}_a$ and $\mathbf{B}$ are assumed to have only a component in the z direction and a place deep inside the superconductor is considered, such that $\mathbf{B}$ does not change in the y and z directions. This situation is depicted in Fig. 2.4. The 2nd London equation reduces to the simple ordinary differential equation

$$\frac{d^2 B_z}{dx^2} = \frac{1}{\lambda^2} B_z \ , \tag{2.35}$$

which can be solved, together with the boundary conditions $B_z(\pm d) = B_a$, by

$$B_z = \frac{\cosh(x/\lambda)}{\cosh(d/\lambda)} B_a \ . \tag{2.36}$$

This solution is plotted in Fig. 2.5. The magnetic field is seen to decrease exponentially into the sample and becomes zero in the interior.

According to Eq. (2.6) a spatially changing magnetic field induces a supercurrent. Using the solution for $\mathbf{B}$ in Eq. (2.36), the current density can easily be calculated by insertion, yielding

$$J_x = 0 \quad , \quad J_y = -\frac{1}{\mu_0 \lambda} \frac{\sinh(x/\lambda)}{\cosh(d/\lambda)} B_a \quad , \quad J_z = 0 \ . \tag{2.37}$$

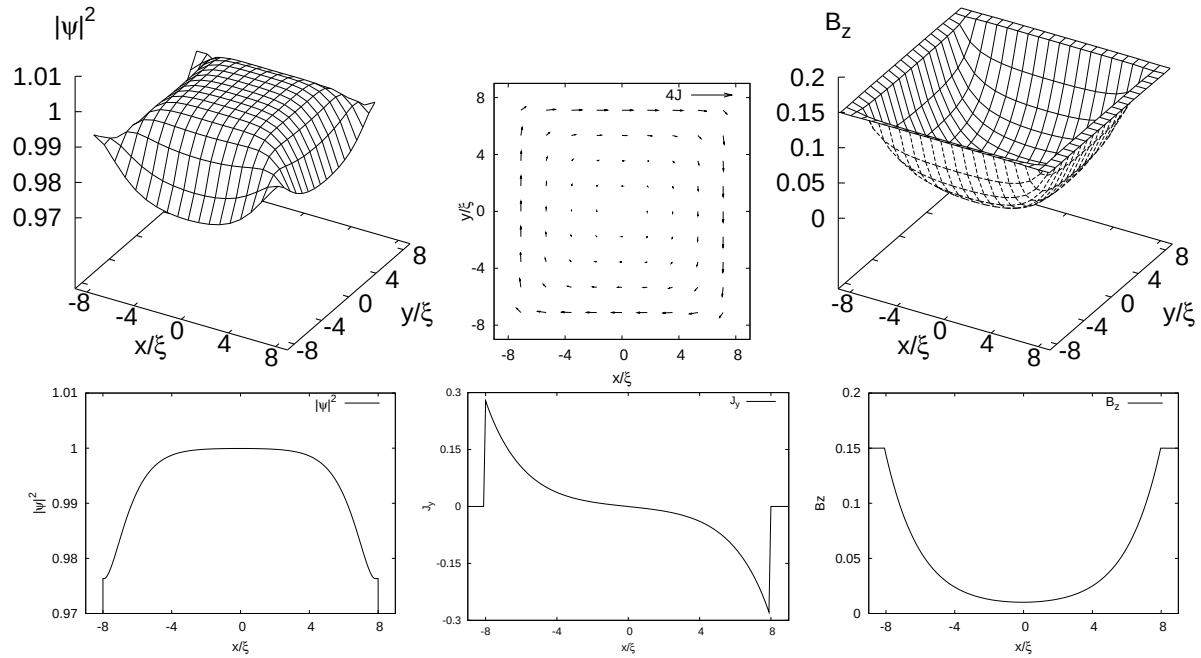

Figure 2.6: Plot of the Cooper pair density $|\psi|^2$ (left), the current (J_x, J_y) (middle), and the magnetic field B_z (right) from a full numerical solution of the Ginzburg-Landau equations with $\kappa = \sqrt{2}$ and $B_a = 0.15B_{c2}$. A detailed view of the situation far from the corners, $y = 0$, is shown in the lower row. The plots show the same overall behavior as the plots in Figs. 2.3 and 2.5. Note that space is normalized to the coherence length, ξ, in all plots.

Shown in Fig. 2.5 is the above current associated with the magnetic field. From the directions of the current in the figure, a magnetic field *opposite* to the applied field is seen to be generated. This results in a screening of the interior of the sample from the applied field, thus creating the Meissner effect.

The Ginzburg-Landau equations have been solved numerically for a square of size $8\xi \times 8\xi$ and the result is presented in Fig. 2.6. Far from the edges, behavior similar to the one derived analytically in Figs. 2.3 and 2.5 is found.

From the previous discussion it is evident, that superconductors have some unique material properties. The Ginzburg-Landau theory is only a phenomenological theory, and it does not allow for a direct calculation of the parameters for different superconductors. Many explicit formulas for the important parameters were given above, but they usually contain the phenomenological constants α and/or β. These two constants are not a priori known and the theory provides no means of calculating them. For this, a microscopic theory is needed. However, the parameters may be determined by experiment. If the coherence length and the penetration depth of some superconductor is measured at a given temperature, the Ginzburg-Landau theory enables us to calculate many more properties. A list of physical properties of some common superconductors is provided below:

Low T_c Material	T_c/K	ξ/nm		λ/nm		H_{c2}/T	
Nb[30]	9.25	40		85		0.198	
Pb[30]	7.2	90		40		0.08	
NbTi[30]	9.5	4		300		13	
PbBi[30]	8.3	20		200		0.5	
High T_c Material	T_c/K	ξ_{ab}/nm	ξ_c/nm	λ_{ab}/nm	$\lambda_c/\mu m$	$H_{c2\perp}/T$	$H_{c2\parallel}/T$
$Bi_2Sr_2CaCu_2O_{8+\delta}$[18]	94	2	0.1	200-300	15-150	>60	>250
$YBa_2Cu_3O_{7-\delta}$[18]	93	1.6	0.3	150	0.8	110	240

It is easy to spot the difference between the low T_c and high T_c superconductors in the above table. The high T_c materials in the table above are very anisotropic. It means that direction plays a role in the compound and, for example, the coherence length is different when measured in different directions. The subscript ab refers to the parameter in the CuO-plane while subscript c is perpendicular to the CuO-plane for the two high T_c superconductors BSCCO and YBCO. It should be noted, that also

some low T_c materials posses anisotropy. Nb is for example slightly anisotropic. The Ginzburg-Landau theory discussed in this text does not take anisotropy into account, but it may be modified to do so, for example by introducing the charge-carrier mass, m, as a tensor instead of a scalar[16]. The extreme anisotropic nature of $Bi_2Sr_2Ca_2Cu_3O_{10}$ (BSCCO) will be explored later by viewing it as a stack of long Josephson junctions.

2.3 The Abrikosov Vortex

As stated in the previous section, the Ginzburg-Landau equations have a great variety of solutions. One of them is the Abrikosov vortex solution[28], which will now be examined in some detail. The order parameter may be written as

$$\psi = \sqrt{\frac{\alpha}{\beta}} e^{i\phi} \ , \tag{2.38}$$

where ϕ is a general phase and may be a function of the spatial coordinates. This choice of order parameter corresponds to a Meissner solution with constant Cooper-pair density, which may be inserted into the current density in Eq. (2.6) to give

$$\mathbf{J} = \frac{q\hbar\alpha}{m\beta}\left(\nabla\phi - \frac{q}{\hbar}\mathbf{A}\right). \tag{2.39}$$

This current density is then integrated following a closed circular path to get the total current, I, along this path. Using Stokes theorem, noting that the phase, ϕ, changes by $2\pi n$ where $n \in \mathbb{N}$, the current is obtained to be

$$I \equiv \oint_C \mathbf{J}\cdot d\mathbf{r} = \frac{q\hbar\alpha}{m\beta}\left(2\pi n - \frac{q}{\hbar}\int_S \mathbf{B}\cdot d\mathbf{S}\right), \tag{2.40}$$

where C is the closed circular path and S is the area enclosed by C. Choosing C to be at a place without current, $I = 0$, and noting that the last term is the magnetic flux, Φ, through the area S, the equation

$$\Phi = n\frac{h}{q} \equiv n\Phi_0 \tag{2.41}$$

is obtained. This equation shows that the magnetic flux through an area, S, of the superconductor is quantized in terms of the *flux quantum*, $\Phi_0 \equiv h/q \approx 2.1 \times 10^{-15} Tm^2$ for $q = 2e$.

Odd as it may seem to consider the magnetic flux through a superconductor in the Meissner phase, this type of solution is extremely important for Type II superconductors and will be considered in more detail. As it was shown, the phase changes by $2\pi n$ when one revolution around the circle C is made. Using cylindrical coordinates, it thus seem natural to try with an order parameter of the form

$$\psi = \sqrt{\frac{\alpha}{\beta}}\, f(r) e^{in\theta}, \tag{2.42}$$

where r is the radius and θ is the polar coordinate. The simplest case for the magnetic field is having only a z-component. Taking

$$A_r = 0 \quad , \quad A_\theta = \frac{\hbar}{q}\frac{n - P(r)}{r} \quad , \quad A_z = 0 \ , \tag{2.43}$$

and calculating the magnetic field by $\mathbf{B} = \nabla \times \mathbf{A}$, gives

$$B_r = 0 \quad , \quad B_\theta = 0 \quad , \quad B_z = -\frac{\hbar}{q}\frac{P'}{r} \ , \tag{2.44}$$

which shows that only the z-component of $\mathbf{B}$ is non-zero with the above ansatz on $\mathbf{A}$. The ansatz is referred to as the Nielsen-Olesen ansatz after the paper in Ref. [31].

Inserting the above *ansatz* for the order parameter and vector potential, Eqs. (2.42) and (2.43), into the Ginzburg-Landau Eqs. (2.4) and (2.6) yields

$$\xi^2\left(f'' + \frac{1}{r}f' - \frac{P^2}{r^2}f\right) + (1 - f^2)f = 0 \ , \tag{2.45}$$

$$\lambda^2\left(P'' - \frac{1}{r}P'\right) - f^2 P = 0 \ . \tag{2.46}$$

Space is now normalized to the coherence-length, ξ, which turns the above Eqs. into[23]

$$f'' + \frac{1}{r}f' - \frac{P^2}{r^2}f + (1-f^2)f = 0 \ , \tag{2.47}$$

$$P'' - \frac{1}{r}P' - \frac{1}{\kappa^2}f^2 P = 0 \ . \tag{2.48}$$

Boundary conditions for f and P will now be derived. First, the flux through a circular surface, S, with radius r is calculated to be

$$\Phi(r) = \int_S \mathbf{B}\cdot d\mathbf{S} = \Phi_0\Big(n - P(r)\Big) \ . \tag{2.49}$$

The flux through a surface with zero radius should of course be zero, leading to $P(0) = n$. Since the flux through the superconductor is quantized, $\lim_{r\to\infty} P(r) = 0$ leads to the quantization from Eq. (2.41). Now, multiplying Eq. (2.47) by r^2, taking $r \to 0$, and using $P(0) = n$ gives $n^2 f(0) = 0$ yielding the boundary condition $f(0) = 0$. For the last boundary condition, it is required that the order parameter in Eq. (2.42) approaches the Meissner solution as $r \to \infty$ leading to $\lim_{r\to\infty} f(r) = 1$. To summarize, the boundary conditions on the functions f and P have been obtained to be[23]

$$f(0) = 0 \quad , \quad \lim_{r\to\infty} f(r) = 1 \ , \tag{2.50}$$

$$P(0) = n \quad , \quad \lim_{r\to\infty} P(r) = 0 \ . \tag{2.51}$$

An analytical solution to the coupled Eqs. (2.47) and (2.48) subject to the boundary conditions (2.50) and (2.51) is, to the authors knowledge, now known. One may, however, find analytical solutions in the two cases $r \to \infty$ and $r \to 0$. The trick is straight forward: To get the solutions for, say, f the boundary condition for P is inserted into Eq. (2.47) and the uncoupled equation is then solved in the limit of the boundary condition. Taking $r \to \infty$, Eq. (2.47) reduces to

$$f'' + (1-f^2)f = 0 \ , \tag{2.52}$$

which is the same as Eq. (2.27) when $\tilde{\psi}$ is real and $\tilde{\psi} = f$. One solution is therefore given in Eq. (2.30) with $\alpha/\beta = 1$ and $\xi = 1$ since the f-equation is normalized, thus

$$f_\infty = \tanh\left(\frac{r - r_0}{\sqrt{2}}\right) \tag{2.53}$$

is the solution in the far-field. Near the origin, the non-linear term in f may be neglected since f is small, and the equation

$$f'' + \frac{1}{r}f' + \left(1 - \frac{n^2}{r^2}\right) f = 0 \tag{2.54}$$

must be solved. This is an example of a Bessel equation, so the solution is easily found to be

$$f_0 = C_0 J_n(r) \ , \tag{2.55}$$

where J_n is the Bessel function of the first kind of order n and C_0 is an undetermined constant.

For $r \to \infty$, Eq. (2.48) reduces to

$$P'' - \frac{1}{r}P' - \frac{P}{\kappa^2} = 0 \ . \tag{2.56}$$

Luckily, this equation can be re-arranged to a modified Bessel equation on the form

$$\left(\frac{P}{r}\right)'' + \left(\frac{P}{r}\right)' - \left(\frac{1}{\kappa^2} - \frac{1}{r}\right)\left(\frac{P}{r}\right) = 0 \ , \tag{2.57}$$

which has the solution

$$P_\infty = B_\infty r K_1\left(r/\kappa\right) \ , \tag{2.58}$$

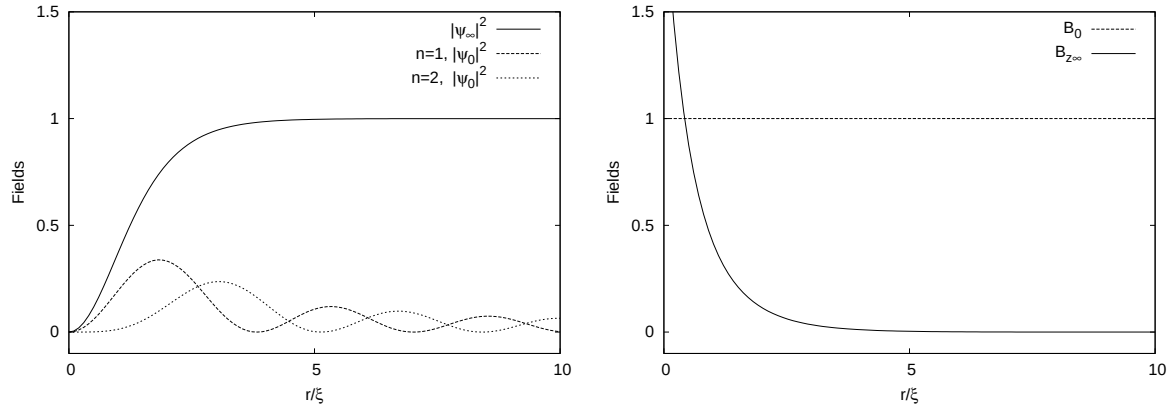

Figure 2.7: Plot of the near- and far field solutions in Eqs. (2.53), (2.55), (2.58), and (2.60) in terms of the magnetic field in Eq. (2.44) and the Cooper-pair density, $|\psi|^2 = f^2$, which are the physically relevant quantities. Unknown constants has been put equal to 1 except $r_0 = 0$. Note that B_z corresponding to Eq. (2.60) is constant and equal to B_0.

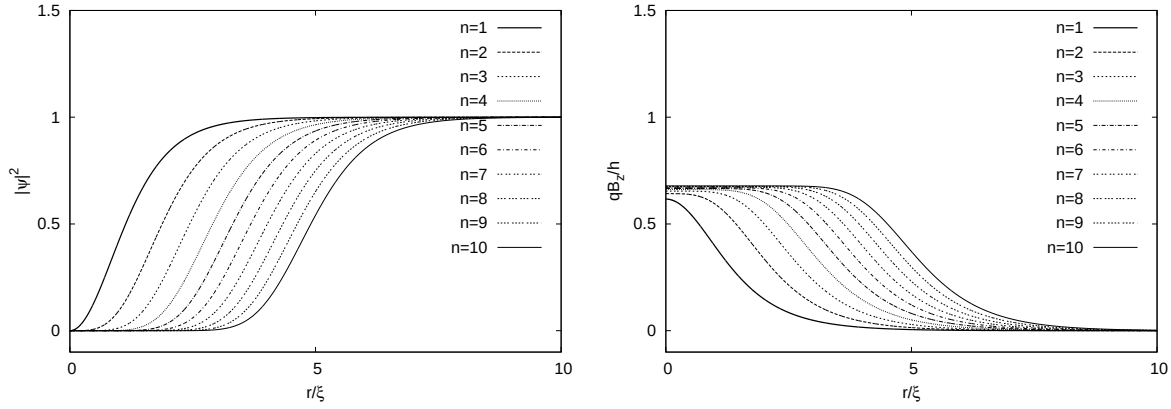

Figure 2.8: Numerical solutions to Eqs. (2.47), (2.48), (2.50), and (2.51) shown in terms of the magnetic field, B_z, and the Cooper-pair density, $|\psi|^2 = f^2$ for one flux quantum to ten flux quanta with $\kappa = 1$. At first sight the approximate solutions in Fig. 2.7 may look somewhat different from these solutions, but when one fits the unknown constants in the approximate solutions and only considers the range in which they were derived, the resemblance is quite good.

where K_1 is the modified Bessel function of the second kind of order 1 and B_∞ is an undetermined constant. Near $r = 0$, Eq. (2.48) simplifies to

$$P'' - \frac{1}{r}P' = 0 \tag{2.59}$$

which is solved by

$$P_0 = n - B_0 r^2 \ , \tag{2.60}$$

where B_0 is an undetermined constant.

In Fig. 2.7 the near- and far-field solutions in Eqs. (2.53), (2.55), (2.58), and (2.60) have been plotted in terms of the Cooper pair density and the magnetic field for the cases $n = 1$ and $n = 2$, i.e. one quantum and two quanta of magnetic flux. It is seen, that the magnetic field is constant near the center and so is the Cooper-pair density, especially if there are more than one quantum of flux in the vortex. The Cooper pair density goes to the Meissner phase and the magnetic field goes to zero as $r \to \infty$.

One way to get more accurate solutions to Eqs. (2.47) and (2.48) with boundary conditions (2.50) and (2.51) is to solve the equations numerically. There are two common methods for solving such equations where the boundary conditions are not all at the same point; Shooting and Relaxation. Shooting does

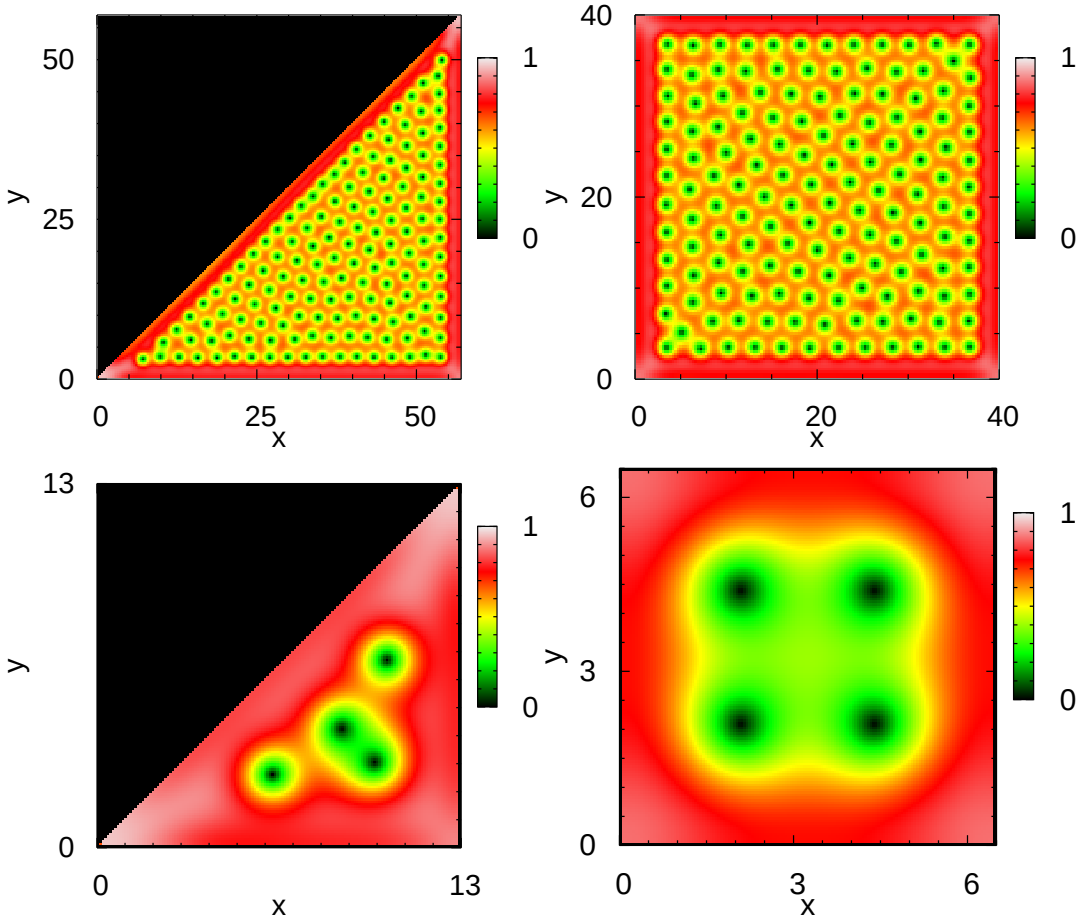

Figure 2.9: $|\psi|^2$ shown for four different superconducting samples with $\kappa = \sqrt{2}$ and $B_a = 0.8B_{c2}$. The figure shows the differences between the vortex-lattice in large and small systems. In the small systems the boundary plays a major role for the vortex-arrangement. The length-scale is normalized to the coherence-length.

not work very well for this type of equations, so a relaxation method has been used[21]. The resulting solutions can be seen in Fig. 2.8, which are seen to agree well with the analytical solutions in Fig. 2.7 in the limits where the analytical solutions were derived.

In addition to the Abrikosov vortex-solution presented here, anti-vortex solutions ($n < 0$) may also be found. The reader with too much spare time is advised to find these solutions.

It was mentioned in Section 2.2 that Abrikosov vortices start to enter the superconductor when the magnetic field is raised above H_{c1} and the superconductor enters the vortex phase. The vortex solutions considered in the above analysis were isolated, which is usually not the case in a real superconductor. The vortices enter the sample and form what is called a vortex-lattice. The formation of the lattice depends on at least two things, the vortex-vortex interaction and the interaction with the boundary. The latter plays a minor role in large samples, but recently there has been a lot of interest in mesoscopic samples where the boundary plays a major role. These mesoscopic superconductors have usually been investigated by numerically solving the Ginzburg-Landau equations[32]. Fig. 2.9 shows the vortex-lattice of such a numerical solution for four different systems with the same penetration depth, coherence length, and applied magnetic field. The system-size is large in the top plots, while smaller in the bottom plots to show the effects of the boundary in mesoscopic systems. The total superconducting area is the same for the square and the triangle geometries. One could easily push one more vortex into the large system without disturbing the remaining vortices too much, while it inevitable would completely change the lattice-structure in the small systems. The interaction with the boundary is repulsive and so is the vortex-vortex interaction, which is why the vortices will try to maximize the distance to each other and to the boundary. The vortex-anti vortex interaction is, however, attractive. The vortex-vortex interaction in a two-component Ginzburg-Landau theory will be investigated in detail in Section 5.2.

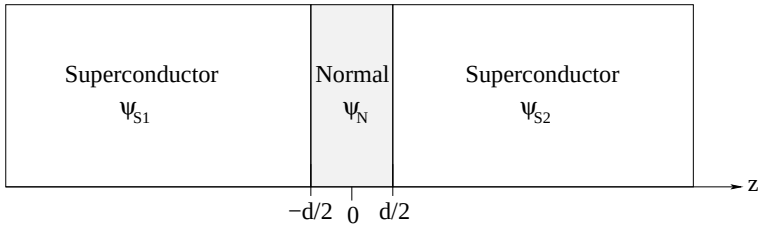

Figure 2.10: Schematic view of a one-dimensional Josephson junction.

2.4 The Long Josephson Junction

As the Ginzburg-Landau theory shows, superconductivity in a closed system can be described quite well by a single wave-function (order parameter). Due to this, superconductivity is sometimes referred to as a *macroscopic quantum phenomenon*. An important consequence of this fact, called the Josephson effect, was discovered by Brian D. Josephson in 1962[33]. Two separate superconductors are moved really close together, but still separate. Classically, they do not interact with each other, but due to the quantum mechanical nature of superconductivity the wave-functions of the superconductors are not zero outside the superconductors, but decays exponentially. If the two superconductors are really close, the wave-functions will penetrate into the other superconductor and there is thus a probability for Cooper-pairs to tunnel from one superconductor to the other. This is the Josephson effect, and two superconductors separated by a very thin layer of non-superconducting material is called a Josephson junction.

Assuming no magnetic fields, the scalar Ginzburg-Landau equation is

$$-\frac{\hbar^2}{2m}\nabla^2\psi - \alpha(T)\psi + \beta|\psi|^2\psi = 0 \ . \tag{2.61}$$

To model the one-dimensional Josephson junction shown in Fig. 2.10, $\alpha(T)$ is chosen as

$$\alpha(T) = \begin{cases} -|\alpha_S| & \text{for } z < -d/2 \\ |\alpha_N| & \text{for } -d/2 < z < d/2 \\ -|\alpha_S| & \text{for } z > d/2 \end{cases} \ , \tag{2.62}$$

corresponding to a superconducting state for $|z| > d/2$ and a normal state for $|z| < d/2$ (see Fig. 2.1). The superconducting order parameter is expected to decay exponentially outside the superconductors, so for the normal part of the system $|\psi|^2$ is small. This means, that the non-linear term, $\beta|\psi|^2\psi$, may be dropped[3]. The resulting linear equation is

$$\frac{\hbar^2}{2m}\psi''(z) + |\alpha_n|\psi(z) = 0 \ . \tag{2.63}$$

The solution to this equation may be expressed as

$$\psi_N = C_1 \cosh(z/\zeta) + C_2 \sinh(z/\zeta) \ , \tag{2.64}$$

with $\zeta = \sqrt{\hbar^2/(2m|\alpha_n|)}$, called the decay length of the *normal* material. Solutions inside the superconductors are also needed, which unfortunately require the solution of the general non-linear Ginzburg-Landau equation (2.61) for $\alpha(T) = -|\alpha_S|$. Avoiding to solve this complicated non-linear equation, the order parameters of the superconductors are chosen, without loss of generality, to

$$\psi_{S1} = \sqrt{n_1(z)}\ e^{i\phi_1(z)} \ , \tag{2.65}$$

$$\psi_{S2} = \sqrt{n_2(z)}\ e^{i\phi_2(z)} \ . \tag{2.66}$$

Demanding the order parameter to be continuous throughout the entire system, the equations $\psi_{S1}(-d/2) = \psi_N(-d/2)$ and $\psi_{S2}(d/2) = \psi_N(d/2)$ may be solved for C_1 and C_2, yielding

$$C_1 = \frac{\sqrt{n_1}e^{I\phi_1} + \sqrt{n_2}e^{I\phi_2}}{\cosh(d/(2\zeta))} \ , \tag{2.67}$$

$$C_1 = \frac{\sqrt{n_1}e^{I\phi_1} - \sqrt{n_2}e^{I\phi_2}}{\sinh(d/(2\zeta))} \ , \tag{2.68}$$

[3]See Ref. [34] for a treatment including the non-linearity of the problem.

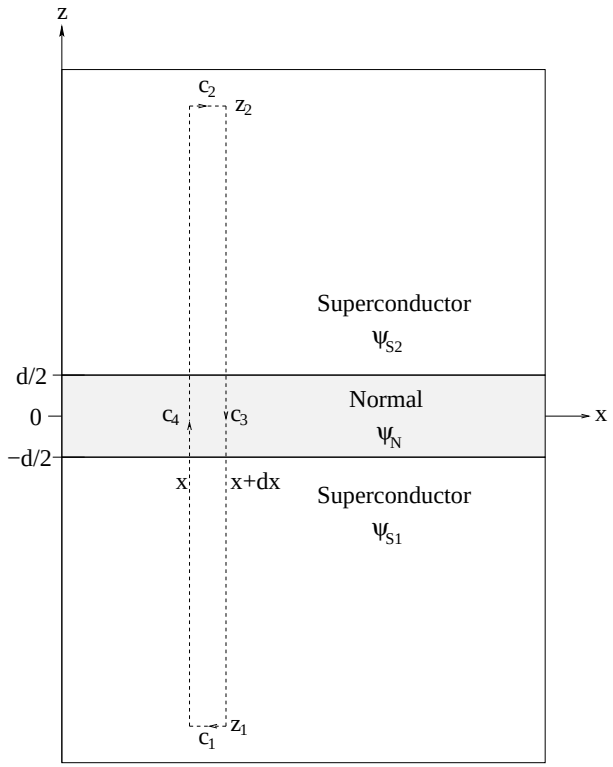

Figure 2.11: Schematic view of a long Josephson junction.

with $n_1 \equiv n_1(-d/2)$, $n_2 \equiv n_2(d/2)$, $\phi_1 \equiv \phi_1(-d/2)$, and $\phi_2 \equiv \phi_2(d/2)$. Inserting the solution of the normal area into the current, Eq. (2.6), for zero magnetic field,

$$J_z = \frac{q\hbar\sqrt{n_1 n_2}}{m\zeta \sinh(d/\zeta)} \sin(\phi_2 - \phi_1) \equiv J_J \sin(\phi_2 - \phi_1) \tag{2.69}$$

is obtained as the supercurrent across the normal area. If there is a difference in the complex phase between the two superconductors, there is a current across the normal material, which has an absolute maximum value of J_J for $\phi_2 - \phi_1 = (1/2 + n)\pi$, $n \in \mathrm{N}$. Eq. (2.69) is called the Josephson current-phase relation[30].

The Josephson current-phase relation, Eq. (2.69), was derived assuming no magnetic fields and the resulting equation is therefore not gauge-invariant. The Ginzburg-Landau equations (2.4)-(2.7) are invariant under the gauge-transformation

$$\psi \to e^{i\chi(\mathbf{r})}\psi \quad , \quad \mathbf{A} \to \mathbf{A} - \frac{\hbar}{q}\nabla\chi(\mathbf{r}) \ , \tag{2.70}$$

where $\mathbf{r}$ is short for (x, y, z). Under a gauge-transformation phases are added $\chi(\mathbf{r})$ and the phase difference in Eq. (2.69) is added $\chi(z = d/2) - \chi(z = -d/2)$. To make Eq. (2.69) gauge invariant, the extra phase must be subtracted, and

$$J_z = J_J \sin\phi \quad , \quad \phi = \theta_2 - \theta_1 - \frac{q}{\hbar}\int_{-d}^{d} A_z dz \ , \tag{2.71}$$

is obtained as a gauge-invariant version of the Josephson current-phase relation which holds in the presence of a magnetic field. ϕ is correctly termed "the gauge invariant phase difference", but often it is referred to just as "the phase".

A long Josephson junction will now be considered, where the width in the x-direction is taken into account. See Fig. 2.11 and consider the path $c_1 + c_4 + c_2 + c_3$. Assuming the superconductors are in the Meissner-phase, the relation between the current, phase and vector potential is given by Eq. (2.39).

Re-arranging terms and integrating Eq. (2.39) along segments c_1 and c_2 gives

$$\begin{aligned}\int_{c_1} \nabla\theta \cdot d\mathbf{l} + \int_{c_2} \nabla\theta \cdot d\mathbf{l} &= \theta_2(x+dx) - \theta_1(x+dx) - (\theta_2(x) - \theta_1(x)) \\ &= \frac{\lambda^2 \mu_0 q}{\hbar} \int_x^{x+dx} (J_2 - J_1)\, dx + \frac{q}{\hbar} \int_{c_1+c_2} \mathbf{A} \cdot d\mathbf{l} \ , \end{aligned} \tag{2.72}$$

where $\theta_i(x)$ is short for $\theta_i(x, z_i)$ and J_1 and J_2 are the current densities at sides 1 and 2, respectively. The integration path is chosen such that it extends far inside the superconductors where there are no currents, thus $J_1 = J_2 = 0$. The integral of $\frac{q}{\hbar}\mathbf{A}$ along segments c_3 and c_4 is now added on both sides of the above equation, and using that the magnetic field is only non-zero between z=$-d/2 - \lambda$ and $z = d/2 + \lambda$, the equation

$$\frac{\hbar}{q(d+2\lambda)} \frac{\partial \phi}{\partial x} = B_y \tag{2.73}$$

is obtained as a relationship between the magnetic field in the normal area and the gauge invariant phase difference, which has been defined as

$$\phi(x) \equiv \theta_2(x) - \theta_1(x) - \frac{q}{\hbar} \int_{z_1}^{z_2} A_z dz \ . \tag{2.74}$$

To get a relation for the electric field, consider the Maxwell equation

$$\nabla \times \mathbf{E} = -\frac{\partial B}{\partial t} \ , \tag{2.75}$$

and use Eq. (2.73) to calculate $\mathbf{E}$ to

$$E_x = 0 \quad , \quad E_y = 0 \quad , \quad E_z = \frac{\hbar}{(d+2\lambda)q} \frac{\partial \phi}{\partial t} \ . \tag{2.76}$$

From this equation, the voltage across the junction may be calculated to

$$V = \frac{\hbar}{q} \frac{\partial \phi}{\partial t} \ . \tag{2.77}$$

Now, the equation of motion for the long Josephson junction is obtained by using the Maxwell equation

$$\nabla \times \mathbf{B} = \mu_0 \mathbf{J} + \epsilon_0 \mu_0 \frac{\partial \mathbf{E}}{\partial t} \ , \tag{2.78}$$

which yields the Klein-Gordon equation

$$\frac{\hbar}{(d+2\lambda)q} \frac{\partial^2 \phi}{\partial x^2} = \mu_0 J_z + \frac{\mu_0 \epsilon_0 \hbar}{(d+2\lambda)q} \frac{\partial^2 \phi}{\partial t^2} \ . \tag{2.79}$$

J_z is the current density across the junction[4] found in Eq. (2.71), turning the equation into

$$\frac{\hbar}{(d+2\lambda)q} \phi_{xx} - \frac{\mu_0 \epsilon_0 \hbar}{(d+2\lambda)q} \phi_{tt} - \mu_0 J_J \sin\phi = 0 \ , \tag{2.80}$$

which is a special case of the Klein-Gordon equation named the sine-Gordon equation. Here, a subscript is used for the differential operators, in agreement with most literature on the sine-Gordon equation. The equation describes the electro-dynamics of the long Josephson junction in the loss-less case. From microscopic theory an additional term appears, which describes losses due to tunneling electrons[35]. In experiments a bias current is usually applied in the $+z$ direction, yielding yet an additional term. With these two extra terms, the equation is called the *perturbed* sine-Gordon equation, given by

$$\frac{\hbar}{\mu_0(d+2\lambda)q} \phi_{xx} - \frac{\epsilon_0 \hbar}{(d+2\lambda)q} \phi_{tt} - J_J \sin\phi = \frac{\hbar}{qR} \phi_t - J_B \ . \tag{2.81}$$

[4]It is often custom to include the displacement current density, $\epsilon_0 \partial \mathbf{E}/\partial t$, in a quantity called J_z

This equation is one of the classical equations of non-linear science, see for example Ref. [29] for a good review.

To simplify the perturbed sine-Gordon equation, it will be normalized according to

$$\begin{aligned} x = \sqrt{\frac{\hbar}{J_J \mu_0 d' q}}\,\tilde{x} \equiv \lambda_J \tilde{x} \quad &, \quad t = \sqrt{\frac{\hbar \epsilon_0}{J_J d' q}}\,\tilde{t} \equiv \omega_0^{-1}\tilde{t}\ , \\ B = \sqrt{\frac{J_J \mu_0 \hbar}{q d'}}\tilde{B} \quad &, \quad J_z = J_J \tilde{J}_z\ , \\ \alpha \equiv \sqrt{\frac{\hbar d'}{J_J \epsilon_0 q R^2}} \quad &, \quad \gamma \equiv \frac{J_B}{J_J}\ , \end{aligned} \tag{2.82}$$

where the tilde-variables are the normalized ones. Some new symbols were introduced here: λ_J is the Josephson penetration depth, ω_0 is the Josephson plasma frequency, α is controlling the amount of dissipation, γ is the normalized bias current, and $d' \equiv d + 2\lambda$ is the effective width of the junction. The normalization scheme yields

$$\phi_{xx} - \phi_{tt} - \sin\phi = \alpha\phi_t - \gamma\ , \tag{2.83}$$

where the tildes have been skipped.

2.5 The Josephson Vortex

A particular interesting solution to Eq. (2.83) is the Josephson vortex. Since the equation is non-linear, conventional methods such as Fourier-analysis can not readily be used to solve the equation. Looking at the unperturbed case, $\alpha = \gamma = 0$, and consider a traveling wave solution of the form

$$\phi(x,t) = \phi(x - vt)\ . \tag{2.84}$$

This yields the ordinary differential equation

$$(1 - v^2)\phi'' = \sin\phi\ , \tag{2.85}$$

where prime denotes differentiation with respect to $\zeta = x - vt$. This equation can be integrated once to

$$\frac{1}{2}(1 - v^2)(\phi')^2 = C - \cos\phi\ , \tag{2.86}$$

where C is a constant of integration. This equation has several different solutions depending on the value of C, which plays the role of energy of the system[29]. The case of $C = 1$ allows one to write the equation as

$$\frac{1}{2}(1 - v^2)(\phi')^2 = 2\sin^2\left(\frac{\phi}{2}\right) \tag{2.87}$$

which can easily be integrated to yield the solution[29]

$$\phi(x,t) = 4\tan^{-1}\exp\left(\pm\frac{x - vt - x_0}{\sqrt{1 - v^2}}\right). \tag{2.88}$$

This is the Josephson vortex (+ is a vortex, − is an anti-vortex), which is also termed a sine-Gordon soliton, a sine-Gordon kink, a 2π-kink, and a Josephson fluxon. The solution has several interesting properties, which have been plotted in Fig. 2.12 in terms of $\xi = x - vt - x_0$. Shown first is the difference between the vortex and the anti-vortex. The vortex goes from 0 to 2π while the anti-vortex goes from 2π to 0 as ξ goes from $-\infty$ to ∞. Next is the solution plotted for several different values of the speed, v. As $v \to 1$ the vortex becomes more narrow and more steep due to the Lorentz-contraction and invariant under the Lorentz-transformation[29]

$$x \to \chi = \frac{x - vt - x_0}{\sqrt{1 - v^2}} \quad , \quad t \to \tau = \frac{t - v(x - x_0)}{\sqrt{1 - v^2}}\ . \tag{2.89}$$

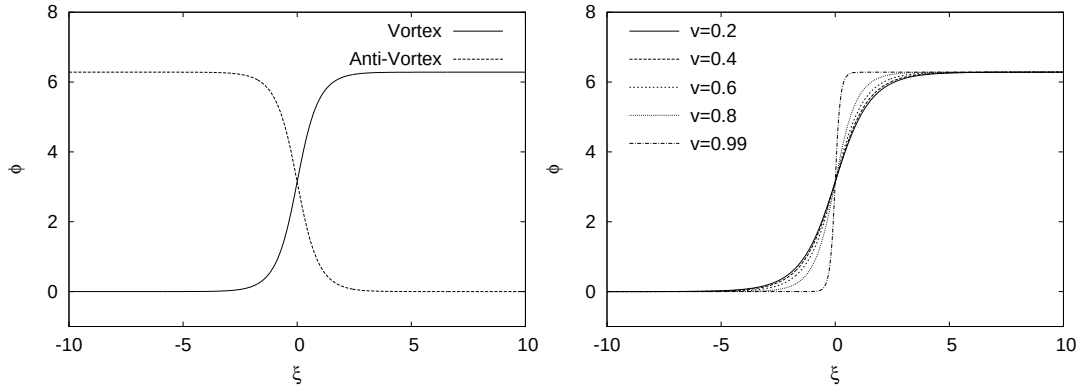

Figure 2.12: The Josephson vortex given by Eq. (2.88) with $\xi = x - vt - x_0$. Left: A vortex and an anti-vortex solution. Right: Vortex solution for $v = 0.2,\ 0.4,\ 0.6,\ 0.8$, and 0.99 demonstrating Lorentz-contraction.

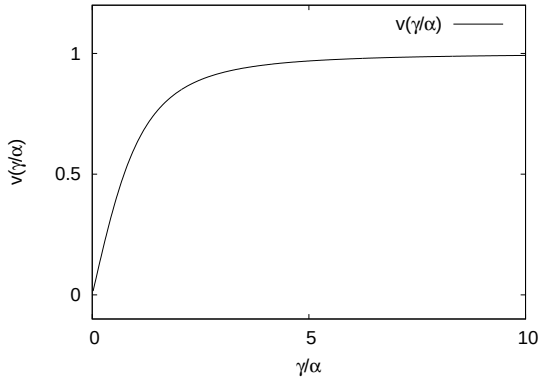

Figure 2.13: The speed of the Josephson vortex given by Eq. (2.97) plotted as a function of γ/α. As γ is increased with constant α, the vortex speed increases asymptotically towards 1.

The vortex solution thus have some similarities to a relativistic particle.

Real systems have finite size, so in order to consider these in detail, some boundary conditions should be derived for the phase, ϕ. These have, in fact, already been derived. If a system of length L in the x-direction is considered, the boundary conditions are found by evaluating the normalized version of Eq. (2.73) at $x = 0$ and $x = L$, giving

$$\frac{\partial\phi}{\partial x}\Big|_{x=0} = B_y(0) \equiv \Gamma \quad , \quad \frac{\partial\phi}{\partial x}\Big|_{x=L} = B_y(L) \equiv \Gamma \ , \tag{2.90}$$

where the *applied* magnetic field at $x = 0$ and $x = L$ was labeled Γ.

The Hamiltonian of the long Josephson junction is given by[29, 36]

$$H = \int_0^L \left(\frac{1}{2}\phi_x^2 + \frac{1}{2}\phi_t^2 + 1 - \cos\phi \right) dx \ . \tag{2.91}$$

Using the sine-Gordon Eq. (2.83), the rate of change in energy is calculated to be[29, 36]

$$\frac{dH}{dt} = -\alpha \int_0^L \phi_t^2 dx + \eta \int_0^L \phi_t dx + \left(\phi_t(L) - \phi_t(0)\right)\Gamma \ . \tag{2.92}$$

There are thus three ways to add and subtract energy to the system. The dissipative α-term always subtracts energy from the system, the bias current term, η, may add energy, and the surface terms may add energy in one end and subtract energy in the other. There is thus a wide range of way to perturb the system using these three terms.

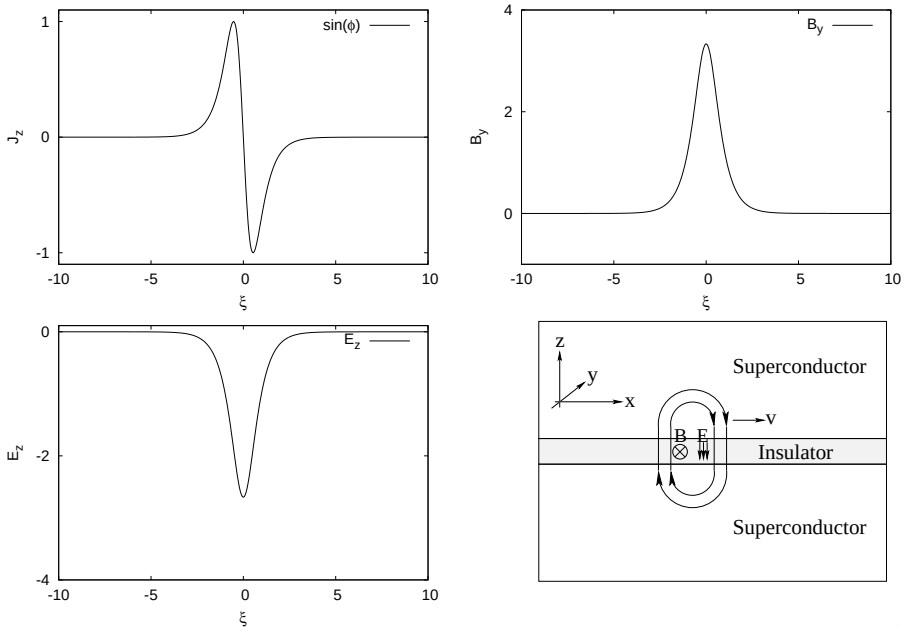

Figure 2.14: Physical properties of the Josephson vortex given by Eq. (2.88). Top Left: Josephson current density, $\sin(\phi)$. Top Right: Magnetic field, B_y. Bottom Left: Electric field, E_z. Bottom Right: Schematic drawing of the current, magnetic field, and electric field of a vortex in a Josephson junction.

Consider the case of zero applied field, $\Gamma = 0$, and the case where the system is infinite. Inserting the Josephson vortex solution, Eq. (2.88), into the Hamiltonian, the energy of the Josephson vortex is calculated to

$$H_J = \frac{8}{\sqrt{1-v^2}} \ , \tag{2.93}$$

and the rate of change of energy, given by Eq. (2.92), is

$$\frac{dH_J}{dt} = \frac{-8v^2\alpha}{\sqrt{1-v^2}} - 2\pi v\eta \ . \tag{2.94}$$

Now, consider the case where v is a function of time in Eq. (2.93), and dH/dt may be calculated to

$$\frac{dH_J}{dt} = \frac{8v(t)}{(1-v(t)^2)^{3/2}} v'(t) \ . \tag{2.95}$$

Equating the two expressions for dH_J/dt gives an approximative differential-equation for the development of the speed of the Josephson vortex as a function of time. The equation is[29, 36]

$$v'(t) = -\alpha(1-v(t)^2)v(t) - \frac{1}{4}\pi\eta(1-v(t)^2)^{3/2} \ . \tag{2.96}$$

To obtain the steady-state speed of the Josephson vortex under a constant α and γ perturbation, the equation is solved using $v'(t) = 0$, yielding

$$v = \frac{\pm 1}{\sqrt{1+\frac{16\alpha^2}{\pi^2\gamma^2}}} \ . \tag{2.97}$$

Since α is a property of the junction and cannot be change easily in an experimental setup, the bias current can be used to change the speed of which the Josephson vortex moves through the junction. Fig. 2.13 shows a plot of Eq. (2.97).

Fig. 2.14 shows some physical properties of the Josephson vortex, which allows for an easy understanding of why the fluxon speed is increasing when the bias current is increased. The top left plot in

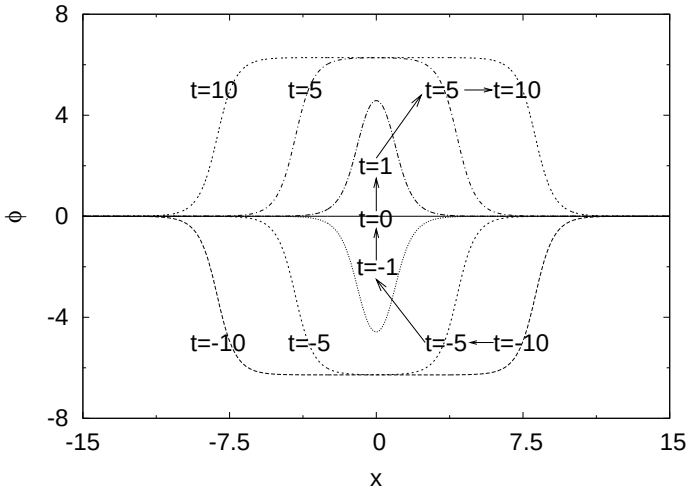

Figure 2.15: Two-fluxon solution given by Eq. (2.98), which is a collision at $t = 0$ between a vortex and an anti-vortex moving with asymptotic speed v, shown for $v = 0.8$. The solution can be used to model the boundary condition $\frac{\partial\phi}{\partial x}|_{x=0} = 0$. Follow the arrows to see what happens in such a boundary-collision.

the figure shows the Josephson current derived from Eqs. (2.71) and (2.88). It is seen to be positive on the left side of the vortex and negative on the right side, corresponding to a flow in the $+z$ and $-z$ directions respectively. The top right plot shows the magnetic field derived from Eq. (2.73), which is seen to be in the $+y$ direction. The bottom right plot shows a schematic version of how the situation in the Junction is in the vicinity of the Josephson vortex. There are circulating currents around the vortex and the vortex has a magnetic field in the $+y$ direction. When the bias current is applied, the vortex is subject to a Lorentz force between its magnetic field and the applied bias current, driving the vortex along the junction and giving rise to the relation in Eq. (2.97). Also shown as the bottom left plot in Fig. 2.14 is the electric field derived from Eq. (2.76), which is pointing in the $-z$ direction. The electric field depends on the direction of the motion of the vortex, such that if the vortex moved in the $-x$ direction instead, E_z would point in the $+z$ direction.

The Josephson vortex is not the only exact solution to the unperturbed sine-Gordon equation, Eq. (2.83) with $\alpha = \gamma = 0$. Ref. [29] contains a derivation of various solutions. Of particular interest to this text are the so-called multi-fluxon solutions, which describe collisions between vortices and (anti)vortices in the Josephson junction. They may be derived by a Bäcklund transformation[29], but this is outside the scope of this text. Instead, a particular important two-fluxon solution will be given as

$$\phi(x,t) = 4\tan^{-1}\left(\frac{\sinh(v(t-\tau)/\sqrt{1-v^2})}{v\cosh(x/\sqrt{1-v^2})}\right), \tag{2.98}$$

and the reader is advised to check by insertion that this is indeed a solution to Eq. (2.83) when $\alpha = \gamma = 0$. The above solution describes a collision between a vortex and an anti-vortex at time $t = \tau$. The solution is shown in Fig. 2.15 for different values of t when $\tau = 0$. A vortex is moving from the right towards $x = 0$ while an anti-vortex is moving from the left towards $x = 0$. At $t = 0$ they collide at $x = 0$. The motion after the collision is not change by the collision, such that they move away from each other, each with (asymptotic) speed $|v|$.

Of particular importance in Fig. 2.15 is the shape of ϕ at $x = 0$. The x-derivative of ϕ at $x = 0$ is seen to be zero at all times, thus $\phi_x(x = 0, t) = 0$ for the above two-fluxon formula. This is precisely the boundary condition in Eq. (2.90) for zero applied magnetic field. Eq. (2.98) thus models a collision of a vortex with the left boundary at $x = 0$. What happens in the collision is that the vortex is reflected by the boundary and moves in the opposite direction as an anti-vortex with (asymptotic) speed v. The boundary condition in Eq. (2.90) for zero magnetic field are therefore termed *reflective* boundary conditions.

2.6 Flux-Flow Solutions

When applying a uniform magnetic field in the y direction to a long Josephson junction it will be expelled from the superconductors due to the Meissner effect. If it is large enough, however, it may generate a fluxon at one end of the junction. This fluxon is forced to move to the other end of the junction, if the bias current is large enough to overcome losses, generating a flux-flow through the junction. Reaching the other end of the junction, the fluxon will be annihilated by the applied magnetic field. The problem is difficult to analyze when the applied magnetic field is small, because the generated fluxons are spaced far apart and appear as individual fluxons, thus the problem is non-linear. The case of a large magnetic field (or small junction length) will generate closely spaced fluxons, and the overall phase in the junction will look like a linear background with small disturbances, allowing for a linear analysis of the small disturbances.

In Ref. [37] it is argued, by comparing with numerical solutions of the sine-Gordon equation, that a good trial-function for the situation with a large applied magnetic field is

$$\phi = \phi_0 + \Gamma x + \omega t + \delta\phi(x,t) \tag{2.99}$$

which allows for small disturbances in the junction through the function $\delta\phi << 1$ which must satisfy the boundary conditions $\delta\phi_x(0,t) = \delta\phi_x(L,t) = 0$ for the above trial-function to satisfy the boundary conditions $\phi_x(0,t) = \phi_x(L,t) = \Gamma$. Inserting into the perturbed sine-Gordon equation and expanding the sin-term around $\phi_0 + \Gamma x + \omega t$ to first order in $\delta\phi$ gives

$$\delta\phi_{xx} - \delta\phi_{tt} - \sin(\phi_0 + \Gamma x + \omega t) - \cos(\phi_0 + \Gamma x + \omega t)\,\delta\phi = \alpha(\omega + \delta\phi_t) - \gamma \ , \tag{2.100}$$

as an equation for $\delta\phi$. This equation is a linear wave-equation, and the solution may be expressed as a Fourier-series[37],

$$\delta\phi = \sum_{n=0}^{\infty} (A_n \cos\omega t + B_n \sin\omega t)\cos k_n x \tag{2.101}$$

with $k_n = n\pi/L$. The series does not contain $\sin k_n x$ components, since these do not satisfy the boundary conditions for $\delta\phi$. The amplitudes A_n and B_n may be determined by inserting the Fourier series into the equation of motion, multiplying by $\cos k_m x$, and integrating over the spatial extend of the system, resulting in[38]

$$A_n = \frac{2}{1+\delta_{n,0}} \frac{(\omega^2 - k_n^2)I_s + \alpha\omega I_c}{(\omega^2 - k_n^2)^2 + \alpha^2\omega^2} \ , \tag{2.102}$$

$$B_n = \frac{2}{1+\delta_{n,0}} \frac{(\omega^2 - k_n^2)I_c - \alpha\omega I_s}{(\omega^2 - k_n^2)^2 + \alpha^2\omega^2} \ , \tag{2.103}$$

where $\delta_{n,m}$ is the Kronecker delta function and

$$I_s = \Gamma L \frac{\cos\phi_0 - (-1)^n \cos(\Gamma L + \phi_0)}{\Gamma^2 L^2 - k_n^2 L^2} \ , \tag{2.104}$$

$$I_c = \Gamma L \frac{(-1)^n \sin(\Gamma L + \phi_0) - \sin\phi_0}{\Gamma^2 L^2 - k_n^2 L^2} \ . \tag{2.105}$$

Eqs. (2.99) and (2.101) and the constants A_n and B_n determine the solution in the case of a large applied magnetic field.

Eq. (2.92) gives the rate of change of energy in the system. For a steady-state solution, the average of dH/dt over one period (or over infinite time) must be zero. The above flux-flow solution is oscillating with frequency ω, and a steady state solution must therefore satisfy the power balance equation[36]

$$\frac{\omega}{2\pi} \int_{t_0}^{t_0 + 2\pi/\omega} \frac{dH}{dt} dt = 0 \ . \tag{2.106}$$

Inserting the flux-flow solution, Eqs. (2.99) and (2.101), into the above condition yields[37]

$$\gamma = \alpha\omega + \frac{\alpha\omega}{4} \sum_{n=0}^{\infty} (1+\delta_{n,0}) \left(A_n^2 + B_n^2\right) \ , \tag{2.107}$$

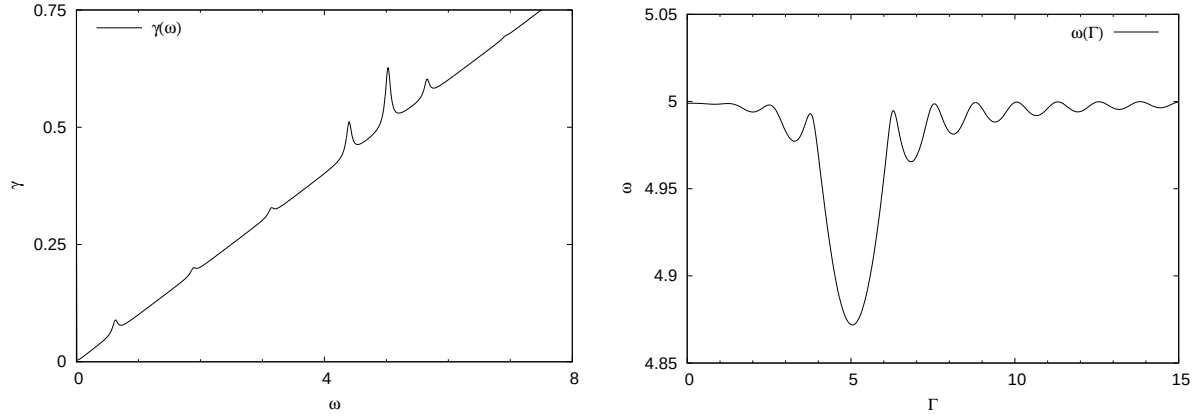

Figure 2.16: Flux-flow solution from Eq. (2.108) with $L = 5$. Left is the current as a function of the voltage, with $\Gamma = 5$, showing a linearly increasing background with resonances at $\omega = \pi n/L$. The right plot shows the voltage as a function of the applied magnetic field obtained by solving Eq. (2.108) numerically for $\gamma = 0.5$ and $\alpha = 0.1$.

as the current voltage characteristic of the flux flow mode. Insertion of A_n and B_n gives[37]

$$\gamma = \alpha\omega \left(1 + \frac{1}{2} \sum_{n=-\infty}^{\infty} \frac{\Gamma^2 L^2}{(\Gamma^2 L^2 - k_n^2 L^2)^2} \frac{\sin^2\left(\frac{\Gamma L - k_n L}{2}\right)}{(\omega^2 - k_n^2)^2 + \alpha^2\omega^2} \right) , \tag{2.108}$$

after some tedious manipulations. Note the lack of dependence of the constant phase θ_0, because it only corresponds to a translation of the time-coordinate. The first term on the r.h.s. gives the Ohmic part of the current-voltage characteristic and the second part gives an infinite number of resonances, having distance $\Delta\omega = \pi/L$ and width α. The left plot in Fig. 2.16 shows a plot of $\gamma(\omega)$ from the above solution. It is easily seen that the current increases linearly with the voltage and at some specific points there are resonances. In measurements of current-voltage characteristics of Josephson junctions such resonances are also visible and they are named Fiske steps[37, 39]. The above theory thus explains these equidistant singularities in the current-voltage characteristics as cavity-resonances.

In some measurements, the current through the junction is fixed and the voltage is measured as a function of the applied magnetic field, Γ. Eq. (2.108) is also applicable in this case, although one has to solve it numerically to obtain such a plot, which is shown in the right side of Fig. 2.16. For a large value of Γ, oscillations appear with a period of $2\pi/L$ due to the cavity resonances[40].

2.7 The McCumber Solution

The normalized version of Eq. (2.77) states that the normalized voltage across the junction is equal to ϕ_t. The Josephson vortex from the previous section generates a localized voltage-pulse, see Fig. 2.14. It can also happen that the phase generates a constant (in space) voltage-drop. Such a solution is called a McCumber solution[41], and it is found by first considering solutions to Eq. (2.83) with $\alpha = \gamma = 0$ and $\phi_{xx} = 0$, resulting in the equation

$$\phi_{tt}(t) = -\sin\phi(t) \ . \tag{2.109}$$

Multiplying by ϕ' and integrating once gives

$$\phi'^2 = 2\cos\phi + C_1 \ , \tag{2.110}$$

where C_1 is the constant of integration. This equation is easily integrated to[43]

$$\phi = 2\mathrm{am}\left(\pm\frac{t - t_0}{\sqrt{m}} \middle| m \right) , \tag{2.111}$$

where the second constant of integration is t_0 and am is the Jacobi amplitude function with modulus[42] $m = 4/(2 + C_1)$. The voltage at time t is[43]

$$V(t) = \frac{2}{\sqrt{m}}\mathrm{dn}\left(\pm\frac{t - t_0}{\sqrt{m}} \middle| m \right) , \tag{2.112}$$

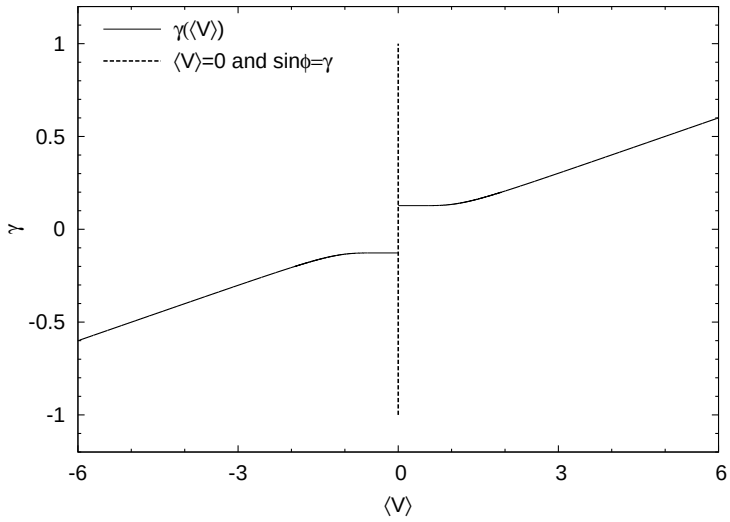

Figure 2.17: Current-voltage characteristic of a Josephson junction in the McCumber state, obtained from Eqs. (2.113) and (2.115) with $\alpha = 0.1$. When $|\gamma| \leq 1$ there is an additional solution given by $\langle V \rangle = 0$, resulting in hysteretic behavior.

which is periodic with a period of $2\sqrt{m}K(m)$, where $K(m)$ is the complete elliptic integral of the first kind. Using this periodicity, the average voltage over one period may be calculated as[43]

$$\langle V \rangle = \frac{1}{2\sqrt{m}K(m)} \int_{t_0}^{t_0+2\sqrt{m}K(m)} \phi_t dt = \pm \frac{\pi}{\sqrt{m}K(m)} \ . \tag{2.113}$$

The modulus m is still undetermined, but if it is assumed that Eq. (2.111) solves the perturbed sine-Gordon equation (with $\phi_{xx} = 0$) in the power balance approximation, the modulus may then be calculated. The power balance is determined from Eq. (2.92), yielding

$$\left\langle \frac{dH}{dt} \right\rangle = \frac{L}{2\sqrt{m}K(m)} \int_{t_0}^{t_0+2\sqrt{m}K(m)} \left(\gamma\phi_t - \alpha\phi_t^2\right) dt = 0 \ . \tag{2.114}$$

Inserting Eq. (2.111), the relation[43]

$$\gamma = \frac{4\alpha E(m)}{\pi\sqrt{m}} \tag{2.115}$$

is obtained, where $E(m)$ is the complete elliptic integral of the second kind. Together, Eqs. (2.113) and (2.115) determines the current-voltage characteristic of the junction in the McCumber state.

Fig. 2.17 shows a plot of $\gamma(\langle V \rangle)$ obtained from Eqs. (2.113) and (2.115). It is easy to see from the plot that for large $\langle V \rangle$ the relation $\langle V \rangle \approx \gamma/\alpha$ is true. This is also seen from the equations by expansion when m is small. Moving from large to small $\langle V \rangle$ on the graph, the point where $\langle V \rangle$ becomes zero and the graph touches the y-axis is determined by setting $m = 1$ in Eq. (2.115), giving $\gamma = 4\alpha/\pi$.

In the case of zero voltage, $\phi_t = \phi_{tt} = 0$, the perturbed sine-Gordon equation reduces to

$$\sin\phi = \gamma \ , \tag{2.116}$$

with solutions for real ϕ when $|\gamma| \leq 1$. Thus, in addition to the McCumber solution given by Eqs. (2.113) and (2.115) there are, at a given value of $|\gamma| \leq 1$, also the zero-voltage solution and measurements on Josephson junctions in the McCumber state therefore show hysteretic behavior. The zero-voltage solution is also shown in Fig. 2.17.

Just because a solution can be found analytically, does not make it show up in experiments. The fluxon and McCumber solutions are, however, well known from experiments, because both types of solutions are stable in some regions of parameter-space. An interesting relationship between fluxon solutions and the McCumber solution was found in Ref. [43], where the stability of the above McCumber

solution was analyzed. It was found that instabilities of the McCumber solution leads to the presence of zero-field steps, which are solutions with fluxons shuttling back and forth in the junction.

As a curiosity, it should be noted that while it is not possible to obtain an exact analytical solution to the equation considered here, $\phi_{tt} + \alpha\phi_t + \sin\phi = \gamma$, the seemingly more complicated equation, $\phi_{tt} + \alpha\phi_t^2 + \sin\phi = \gamma$, is known to have exact solutions[44].

2.8 Applications of Superconductors

The discovery of superconductivity led scientists to dream of the devices which could be made using superconductors. Since there is zero resistance, a superconducting coil would be the ideal solution for storing electrical energy produced at night when the load is low and used during the day when more energy is needed in the cities.

Similar superconducting coils can also be used to generate a large permanent magnetic field. Such coils are widely used in particle accelerators to bend the particle beam. The use of superconducting technology greatly reduces the energy consumption by the magnet, since the current is permanent and thus, essentially only energy for cooling is needed.

The Meissner effect can be utilized as a frictionless bearing in many applications. An alternative energy storage device could be made of a large fly-wheel rotating in vacuum with a superconducting bearing resulting in near zero resistance. The fly-wheel is set to rotate and energy is stored as mechanical energy in the rotation which can be harvested as needed.

One obvious possibility with superconductors is to replace *all* copper-wire by superconducting wires to reduce losses due to resistance, thus reducing the power-consumption of almost any device. Associated with such a replacement are of course some technical difficulties. For example a complete overhaul of the electrical systems would be required since the wires would have to be cooled by liquid nitrogen or a new superconductor working above room temperature would have to be found. It has, however, been tried to use superconducting wires inside power plants to transport large amount of currents. A well-prepared superconducting cable with internal cooling system can carry much more energy than an equally sized system of copper-wire, making this type of superconducting technology interesting for power applications[45].

In addition to the more obvious applications, the special properties of superconductors can also be utilized. One example is the SQUID (Superconducting Quantum Interference Device) which consists of two Josephson junction connected in parallel by superconducting wires. Such a device is able to measure magnetic fields generated by the human brain ($\approx$ 1fT), and is thus used in hospitals all over the world.

The Josephson junction can also be utilized to generate radiation in the THz range. This is the subject of Chapter 4 and an essential part of this thesis. Usual crystals used for generating oscillators can hardly be used in the THz range and Josephson junctions present a very interesting alternative. Applications for such oscillators can be found in many areas, for example in astronomical detection equipment and full-body scanners in airport security.

An obstacle to widespread applications is the fact that most high T_c superconductors are ceramic based, and consequently does not handle bending well. One current solution is to make tapes from the ceramics. A piece of silver tube is filled with some superconductor, for example BSCCO, which is then drawn into a long tape. The tape then has a superconducting core (usually several filaments) surrounded by a softer shell. Such a system is able to bend a lot more than the bare ceramic superconductor and is much better for many power applications. The relatively new superconducting compound MgB_2 is also being considered for tapes. The next generation of wires are so-called coated conductors where the high temperature superconductor, for example YBCO, is coated on a Nickel-Tungsten alloy substrate[46]. These wires are able to carry more current and sustain higher magnetic fields than the BSCCO multifilament tape.

The potential amount of applications for superconductor is immense, but a major shift to superconducting technology has yet to happen. Most predictions about when this will happen have failed. This is partly because a room-temperature superconductor has yet to be found and because superconducting technology is competing with the fast development of existent technology. Superconductors are, nevertheless, extraordinary materials possessing unique properties and it seems likely that someday superconducting technology will be part of our everyday life. When, is outside the scope of this thesis to predict.

Chapter 3

The Long Josephson Junction Stack

This Chapter takes a theoretical view of the long Josephson junction stack. First, the model is introduced and a relationship to high T_c superconductors is discussed. It has become very popular to use high T_c superconductors as Josephson stacks in experiments. Some of the analytical solutions to the coupled non-linear partial differential equations of the model are then presented. The last section looks at a possible relationship between linear plasma modes and non-linear fluxon modes.

3.1 The Model

To derive the equations for a stack of long Josephson junctions, Ref. [47] will be followed in the case of identical junctions. A similar type of derivation can be found in Ref. [48], although Kleiner and Müller only consider the static case. The model geometry is sketched in Fig. 3.1. There are $N+1$ superconductors in the stack resulting in N Josephson junctions, each characterized by a gauge-invariant phase difference $\phi^i(x,t)$. The superconductors are assumed to be in the Meissner-phase, such that Eq. (2.39) may be used inside the superconductors. Isolating the phase leads to

$$\nabla\theta = \frac{\lambda^2\mu_0 q}{\hbar}\mathbf{J} + \frac{q}{\hbar}\mathbf{A} \ . \tag{3.1}$$

Integrating this equation along C_1 and C_2 in Fig. 3.1 results in

$$\begin{aligned}\int_{C_1}\nabla\theta\cdot\mathbf{dl} + \int_{C_2}\nabla\theta\cdot\mathbf{dl} &= \theta^{i+1}(x+dx) - \theta^i(x+dx) - \left(\theta^{i+1}(x) - \theta^i(x)\right) \\ &= \frac{\lambda^2\mu_0 q}{\hbar}\int_x^{x+dx}\left(J_L^{i+1} - J_U^i\right)dx + \frac{q}{\hbar}\int_{C_1+C_2}\mathbf{A}\cdot\mathbf{dl} \ , \end{aligned} \tag{3.2}$$

where J_L^{i+1} denotes the current density at the lower edge of superconductor $i+1$ and J_U^i denotes the current density along the upper edge of superconductor i. Adding to both sides of the equality the integral of $\mathbf{A}$ along C_3 and C_4 and using $\int_x^{x+dx} J dx = J(x)dx$, the equation becomes

$$\frac{\hbar}{\mu_0 q}\frac{\partial\phi^i}{\partial x} = \lambda^2\left(J_L^{i+1} - J_U^i\right) + \frac{1}{\mu_0}B^i d \ , \tag{3.3}$$

where

$$\phi^i(x) \equiv \theta^{i+1}(x) - \theta^{i-1}(x) - \frac{q}{\hbar}\int_{z_i}^{z_i+d} A_z(x,z)dz \tag{3.4}$$

is the gauge invariant phase difference across junction number i. The screening current densities, J_L^{i+1} and J_U^i may be related to the magnetic field between the two superconductors by solving the 2nd London Eq. (2.33) to obtain the magnetic fields inside the superconductors. For the geometry in Fig. 3.1, the solution becomes

$$B^i = \frac{B^{i-1}\sinh\left(\frac{t-2z-2z_0^i}{2\lambda}\right) + B^i\sinh\left(\frac{t+2z+2z_0^i}{2\lambda}\right)}{\sinh\left(t/\lambda\right)} \tag{3.5}$$

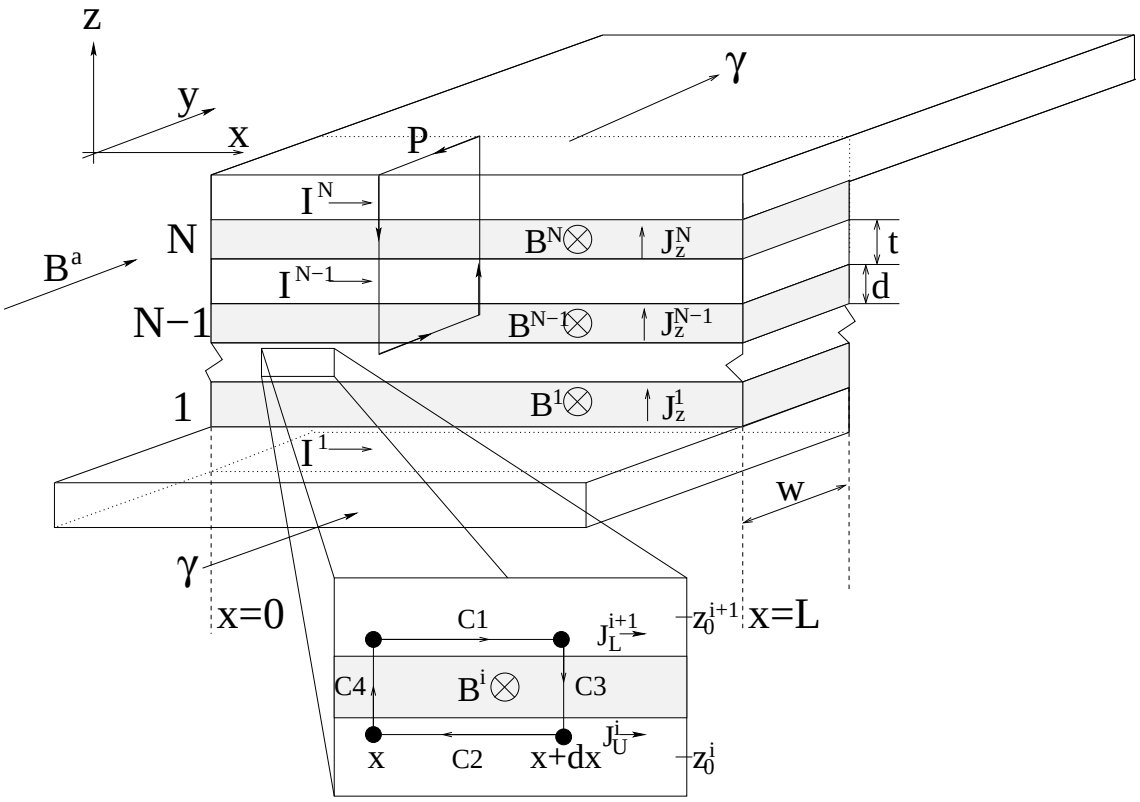

Figure 3.1: Schematic view of the stacked Josephson junctions. White layers are superconductors and gray insulators. B^a is an applied magnetic field in the y-direction and γ is an added bias current. The case where γ depends on the junction number and becomes γ^i is considered but only the case where $\gamma^i = \gamma$ seems experimentally feasible for $N > 2$.

leading to the current densities

$$J_L^{i+1} = \frac{-1}{\mu_0}\frac{\partial B^{i+1}}{\partial z}\Big|_{z=z_0^{i+1}-t/2} = \frac{B^i\cosh(t/\lambda) - B^{i+1}}{\mu_0\lambda\sinh(t/\lambda)} \tag{3.6}$$

and

$$J_U^i = \frac{-1}{\mu_0}\frac{\partial B^i}{\partial z}\Big|_{z=z_0^i+t/2} = \frac{B^{i-1} - B^i\cosh(t/\lambda)}{\mu_0\lambda\sinh(t/\lambda)} \ . \tag{3.7}$$

Eqs. (3.3) now become

$$\frac{\hbar}{q}\frac{\partial\phi^i}{\partial x} = d'B^i + s\left(B^{i-1} + B^{i+1}\right) \tag{3.8}$$

with the definitions

$$d' \equiv d + \frac{2\lambda\cosh(t/\lambda)}{\sinh(t/\lambda)} \quad \text{and} \quad s \equiv -\frac{\lambda}{\sinh(t/\lambda)} \ . \tag{3.9}$$

These equations are valid for all junctions, $i = 1, ..., N$, if $B^0 = B^{N+1} \equiv B_a$ are defined. The corresponding equation for the electric field is obtained using $\nabla \times \mathbf{E} = -\partial\mathbf{B}/\partial t$, resulting in

$$\frac{\hbar}{q}\frac{\partial\phi^i}{\partial t} = d'E^i + s\left(E^{i-1} + E^{i+1}\right) \ , \tag{3.10}$$

where E^i is the electric field in the z-direction in the i'th junction and $E^0 = E^{N+1} \equiv 0$ are defined.

Integrating the magnetic induction along the path P gives

$$\oint_P \mathbf{B}\cdot\mathbf{dl} = w\left(B^i - B^a\right) = \mu_0\sum_{n=i+1}^{N+1} I^n \tag{3.11}$$

where I^n is the current along the x-direction in the n'th superconducting layer. This current may be related to the current in the z-direction by using $\nabla \times \mathbf{B} = \mu_0 \mathbf{J}$ with $\mathbf{B} = B_y \hat{y}$, resulting in

$$\frac{\partial J_x}{\partial x} = -\frac{\partial J_z}{\partial z} \ . \tag{3.12}$$

Using $\partial J_z^i/\partial z|_{z=z_i} \approx (J_z^i - J_z^{i-1})/t$ and $I^i \approx wtJ_x^i$, the relation

$$\frac{1}{w}\sum_{n=k}^{N+1} \frac{\partial I^n}{\partial x} = J_z^{k-1} \ , \tag{3.13}$$

valid for $1 \leq k \leq N$ is obtained, with z_i being the middle of the i'th superconducting layer. By differentiating Eq. (3.8) with respect to x, the system of equations can now be written as[47]

$$\frac{\hbar}{\mu_0 q}\frac{\partial^2 \boldsymbol{\phi}}{\partial x^2} = \mathbf{S}\ \mathbf{J}_z \ , \tag{3.14}$$

where the i'th element of $\boldsymbol{\phi}$ is ϕ^i, and the $N \times N$ coupling matrix, $\mathbf{S}$, has the form[47]

$$\mathbf{S} = \begin{pmatrix} d' & s & & & & \\ s & d' & s & & & \\ & s & d' & s & & \\ & & \ddots & \ddots & \ddots & \\ & & & s & d' & s \\ & & & & s & d' \end{pmatrix} \ , \tag{3.15}$$

and the i'th element of $\mathbf{J}_z$ is the current across junction i in the z-direction, J_z^i. From the perturbed sine-Gordon equation of a single junction, Eq. (2.81), the total current density in the z direction over a single junction can be read off, thus[47]

$$J_z^i = \frac{\hbar C}{q}\frac{\partial^2 \phi^i}{\partial t^2} + \frac{\hbar}{qR}\frac{\partial \phi^i}{\partial t} + J_J \sin\phi^i - J_B^i \ , \tag{3.16}$$

where $C \approx \epsilon_0\epsilon_r/d'$ is the unit area capacitance, R is the unit area resistance, J_J is the maximum Josephson current density, and J_B^i is an added bias current density, which in the general case is taken to be dependent of the junction number, but only the case where the sign of J_B^i changes from junction to junction will be considered. However, only the case where all J_B^i are equal seem experimentally feasible for $N > 2$.

Boundary conditions are obtained by evaluating Eq. (3.8) at $x = 0$ and L, giving[47]

$$\frac{\hbar}{q}\frac{\partial \phi^i}{\partial x}\Big|_{x=0,L} = (d' + 2s)B^a \tag{3.17}$$

showing that the uniform applied magnetic field enters through the boundaries.

It is of course more convenient to work with normalized equations. The equations for the long Josephson stack can be normalized in the following way

$$x = \lambda_J \tilde{x} = \sqrt{\frac{\hbar}{q\mu_0 J_J d'}}\ \tilde{x} \quad , \quad t = \omega_0^{-1}\tilde{t} = \sqrt{\frac{\hbar C}{qJ_J}}\ \tilde{t} \ , \tag{3.18}$$

$$B = \sqrt{\frac{\hbar\mu_0 J_J}{qd'}}\ \tilde{B} \quad , \quad J_z^i = J_J \tilde{J}_z^i \ , \tag{3.19}$$

where the tilde denotes normalized variables, λ_J is the Josephson penetration depth, and ω_0 is the Josephson plasma frequency. This yields

$$\frac{\partial^2 \boldsymbol{\phi}}{\partial \tilde{x}^2} = \tilde{\mathbf{S}}\ \tilde{\mathbf{J}}_z \ , \tag{3.20}$$

$$\tilde{J}_z^i = \frac{\partial^2 \phi^i}{\partial \tilde{t}^2} + \alpha\frac{\partial \phi^i}{\partial \tilde{t}} + \sin\phi^i - \gamma^i \ , \tag{3.21}$$

$$\tilde{\mathbf{S}} = \begin{pmatrix} 1 & S & & & & \\ S & 1 & S & & & \\ & S & 1 & S & & \\ & & \ddots & \ddots & \ddots & \\ & & & S & 1 & S \\ & & & & S & 1 \end{pmatrix} , \tag{3.22}$$

with boundary conditions

$$\frac{\partial \phi^i}{\partial \tilde{x}}\Big|_{\tilde{x}=0,\tilde{L}} = (1+2S)\tilde{B}^a \equiv \Gamma \ . \tag{3.23}$$

In the above equations, the following definitions where used

$$S \equiv \frac{s}{d'} \quad , \quad \alpha \equiv \sqrt{\frac{\hbar}{qJ_J C R^2}} \quad , \quad \gamma^i \equiv \frac{J_B^i}{J_J} \ . \tag{3.24}$$

Note, $t \to \infty \Rightarrow S \to 0$ and $t \to 0 \Rightarrow S \to -1/2$.

Equations (3.20)-(3.23) are the normalized equations describing a stack of inductively coupled long Josephson junctions, which will be used in the rest of this text, except the tildes will be skipped from now on.

Finally, it must be noted, that Eqs. (3.20)-(3.23) where derived by assuming all junctions are equal. Usually when looking at a stack with, say, only two junctions, the two junctions have the outer superconductors much larger than the inner superconductor, thus the two junctions are not equal leading to slightly different expressions. The form of the equations are the same, but the definitions of the parameters are slightly different and usually the boundary conditions are changed to $\partial\phi^{1,N}/\partial x = (1+S)B^a$ for the two outer junctions. This also applies for the *usual* single junction case[35], which is only recovered if $S = 0$ (corresponding to infinitely thick superconducting layers).

3.1.1 Artificial Stacks and High T_c Superconductors

The structure of the Josephson stack can be made in the laboratory using low T_c superconducting material. The parameters such as thickness of the insulating layer and even the superconductor characteristics such as the London penetration depth can be controlled by using different types of superconductors. The stack may thus be made with just the right properties for some application. Example values of the parameters for a low T_c stack are[49]

N	S	I	λ	λ_J	c_0	J_J
2	Nb	AlO_x	90nm	25μm	7×10^6m/s*	200A/cm^2
	L	W	d	t	S	ω_0
	200μm	40μm	5nm*	30nm	-0.46*	100GHz*

The values marked with * have been estimated from the values given in Ref. [49].

The structure of a stack of Josephson junctions have some similarities to the structure of the high T_c superconductor shown in Fig. 1.2, which also consists of alternating superconducting and insulating layers. It is known that the superconduction takes place in the copper oxide planes of high T_c superconductors, and the other atoms essentially acts as insulating spacers, making both structures in Fig. 1.2 behave as a stack of Josephson junctions[48]. One disadvantage of using such naturally occurring stacks is that the parameters cannot be easily controlled as in the artificial case, i.e. one has to work with what nature provides. The major advantage is of course that they are readily available and much easier to make than the artificial counterparts. Some example parameters for a Josephson stack made out of BSCCO are[50]

N	High T_c Material	λ	λ_J	c_0	J_J
120	$Bi_2Sr_2CaCu_2O_8$	170nm	0.34μm	4×10^5m/s*	1015A/cm^2
	L	W	d	t	S	ω_0
	10μm	1.8μm	12Å	3Å	-0.5*	500GHz*

The values marked with * have been estimated from the values given in Ref. [50].

It is easily seen that the width of both the insulators, d, and the superconductors, t, are somewhat different in the two cases shown here. Also, the London penetration depth is about two times larger in the intrinsic stack than in the artificial stack. The smaller width of the insulator and the larger London penetration depth of the intrinsic stack leads to the larger absolute value of S because the magnetic field from surrounding junctions penetrates the superconductors more easily. It should be noted that the values provided above are temperature dependent and the strength of the inductive coupling in the low T_c stack may easily be made much smaller.

One important parameter in both artificial and intrinsic stacks are the number of junctions in the stack. The effect of the number of junctions plays a major role in the dynamics, as will be evident from the later parts of the text. Though it might not at first seem to be the case, the number of junctions in an intrinsic stack is also a controllable parameter. People have even succeeded in making only a few number of Josephson junction from BSCCO[51]. The process is first to start with some number of junctions and then etch down into the stack by a known rate. The etching process is then stopped when there is exactly the desired number of junctions left.

3.1.2 Numerical Method

Eqs. (3.20)-(3.23) are coupled non-linear partial differential equations and a general analytical solution seem unlikely. Numerical solutions are, however, very likely and some remarks on how these are obtained in this text are presented here. The equations are straight-forward to discretize using symmetric second order finite differences for the spatial derivative with spacing Δx. The boundary conditions, Eq. (3.23), are also discretized using second order finite differences. This gives, for example, the following

$$\frac{\phi_1^i(t) - \phi_{-1}^i(t)}{2\Delta x} = \Gamma \tag{3.25}$$

condition at $x = 0$, where the subscript referrers to the x-coordinate by $\phi^i(x_n, t) \equiv \phi_n^i(t)$ with $x_n = n\Delta x$. The above condition enables one to determine the value of ϕ at the *virtual* point x_{-1} in such a way that the desired boundary condition is satisfied. In this case it gives

$$\phi_{-1}^i(t) = \phi_1^i(t) - 2\Delta x\Gamma \ . \tag{3.26}$$

The $N\Delta x$ ODEs in t, resulting from the discretization of the spatial variable, is solved using a fifth-order Runge-Kutta method with adaptive step-size control[21]. Sometimes it is desired to have the solution at evenly spaced times, and in this case a 2nd or 4th order Runge-Kutta method is employed[21]. A 2nd order Verlet integrator is also a popular choice.

3.2 Solutions

Analytic solutions to the non-linear coupled partial differential equations describing the inductively coupled Josephson stack, Eqs. (3.20)-(3.23), are of great practical interest. Here, a few special cases will be examined, which all have tremendous importance for the understanding of Josephson stacks and the stack-like behavior of high T_c superconductors.

3.2.1 Plasma Oscillations

The Josephson plasma oscillations are small amplitude solutions to Eqs. (3.20)-(3.23). The solutions have previously been derived in Refs. [52, 53, 54, 55, 56]. It is assumed that $\alpha = 0$, i.e. there are no losses in the system. The phase is assumed to be small amplitude oscillations around the equilibrium on the form

$$\phi = a^i \cos(kx - \omega t) + \sin^{-1}\gamma^i \ , \tag{3.27}$$

where $\phi_0^i \equiv \sin^{-1}\gamma^i$ is the equilibrium of the i'th junction. Assuming $a^i << 1$ the non-linear term in Eq. (3.21) may be expanded to obtain the eigen-value equation

$$\mathbf{Sa} = \frac{k^2}{\omega^2 - \omega_p^2}\mathbf{a} \equiv \lambda_m \mathbf{a} \ , \tag{3.28}$$

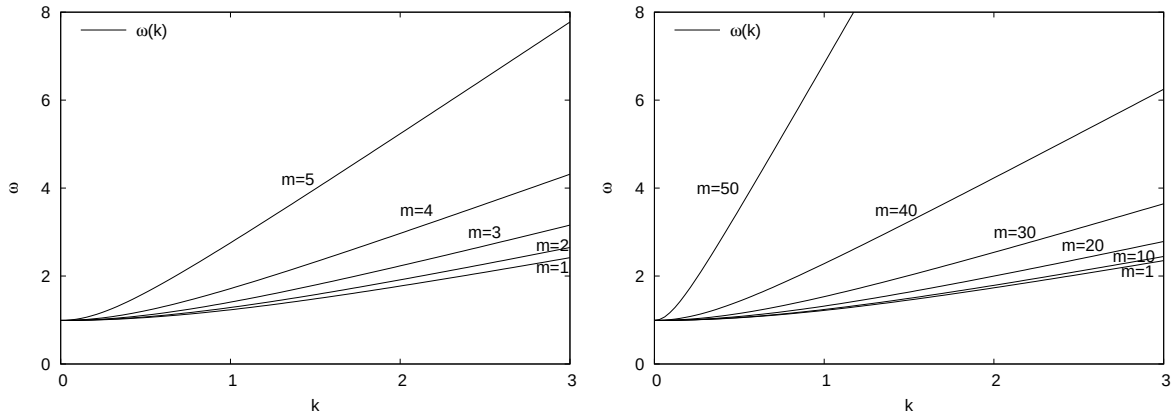

Figure 3.2: Plot of the dispersion relation, Eq. (3.30), for positive ω with $\gamma = -0.2$ and $S = -0.49$. Left plot shows $N = 5$ and right plot shows selected modes for $N = 50$.

with $\omega_p^2 \equiv \sqrt{1-\gamma^2}$ and where it was used that the bias currents are restricted to the case of a change of sign, thus $\gamma^2 \equiv (\gamma^i)^2 = (\gamma^j)^2$ for all i, j. The term ω_p^2 is called the (bias dependent) plasma frequency of the stack.

The solution to the eigen-value Eq. (3.28) can be found in Ref. [53], and may be expressed as

$$\begin{aligned} a_m^i &= \sqrt{\frac{2}{N+1}} \sin\left(\frac{i(N-m+1)\pi}{N+1}\right) , \\ \lambda_m &= 1 - 2S\cos\left(\frac{m\pi}{N+1}\right) \quad , \quad m = 1, ..., N , \end{aligned} \tag{3.29}$$

which of course are N eigen-vectors, $\mathbf{a}_m$, together with N eigen-values, λ_m. Using the definition of λ_m from Eq. (3.28) together with Eq. (3.29), m dispersion relations are found to be

$$\omega^2 = \omega_p^2 + c_m^2 k^2 , \tag{3.30}$$

where the group velocity, c_m was defined as

$$c_m^N \equiv \lim_{k\to\infty} \frac{d\omega}{dk} = \frac{1}{\sqrt{1 - 2S\cos\left(\frac{n\pi}{N+1}\right)}} . \tag{3.31}$$

These velocities, c_m^N, are also termed the characteristic velocities of the stack, and m is referred to as "the mode". The explicit form of the oscillating part of the plasma solution is denoted by A_m^i and trivially given by

$$A_m^i(x,t) = \sqrt{\frac{2}{N+1}} \sin\left(\frac{i(N-m+1)\pi}{N+1}\right) \cos(kx - \omega t) . \tag{3.32}$$

A plot of the dispersion relation, Eq. (3.30), can be seen in Fig. 3.2 for two different stack-sizes. For the large stacksize it is seen, that the low order modes are very close.

3.2.2 Fluxon Solutions

The fluxon solutions for a single junction were considered in great detail in Section 2.5 and similar kink-solutions are known to exist for the stack. Starting out in the same way as for the single junction, the case $\alpha = \gamma = 0$ is considered, such that the coupled equations become

$$\left(\mathbf{S}^{-1}\boldsymbol{\phi}_{xx}\right)^i = \phi_{tt}^i + \sin\phi^i , \tag{3.33}$$

which is easily seen to be N coupled equations, where the l.h.s contains ϕ^i_{xx} for $i = 1, ..., N$, thus coupling the different junctions. For the simplest stacked case, $N = 2$, the equations read

$$\frac{1}{1-S^2}\phi^1_{xx} - \frac{S}{1-S^2}\phi^2_{xx} = \phi^1_{tt} + \sin\phi^1 \ , \tag{3.34}$$

$$\frac{1}{1-S^2}\phi^2_{xx} - \frac{S}{1-S^2}\phi^1_{xx} = \phi^2_{tt} + \sin\phi^2 \ . \tag{3.35}$$

It is easily seen that they are symmetric with respect to exchanging ϕ^1 and ϕ^2 (as they should be), and it thus seem natural to try with a solution of the form $\phi^1 = \pm\phi^2 \equiv \phi$, resulting in the single equation,

$$\frac{1}{1 \pm S}\phi_{xx} = \phi_{tt} + \sin\phi \ , \tag{3.36}$$

for the phase. This is just the sine-Gordon equation with a re-scaled length coordinate, and the fluxon-solutions are easily found to be[57]

$$\phi(x,t) = 4\tan^{-1}\exp\left(\sigma\sqrt{1 \pm S}\frac{x - vt - x_0}{\sqrt{1-(1 \pm S)v^2}}\right) \ , \tag{3.37}$$

where $\sigma = \pm 1$ is the polarity of the solution. Since ϕ is real, the condition

$$v^2 < \frac{1}{1 \pm S} \tag{3.38}$$

is obtained. The two solutions thus have different maximum velocities for the fluxon. The solution $\phi^1 = -\phi^2$ has a maximum fluxon velocity of $1/\sqrt{1-S}$ and the solution $\phi^1 = \phi^2$ has a maximum fluxon velocity of $1/\sqrt{1+S}$. These two velocities are exactly the two characteristic velocities obtained in Eq. (3.31) when $N = 2$, i.e. $c_1^2 = 1/\sqrt{1-S}$ and $c_2^2 = 1/\sqrt{1+S}$. It is common to rename c_1^2 to c_- and c_2^2 to c_+ and write the bunched fluxon solutions as

$$\phi(x,t) = 4\tan^{-1}\exp\left(\sigma\frac{1}{c_\pm}\frac{x - vt - x_0}{\sqrt{1 - v^2/c_\pm^2}}\right) \ . \tag{3.39}$$

In-Phase Mode of a Three Junction Stack

For stacks with more than two junctions, the situation becomes more complicated. Notice that the outer junctions only couple directly to one junction, while an inner junctions couple directly to the junctions on both sides. This means, that the simple solutions in the two-junction case can not be trivially generalized to more junctions. One possibility is to devise a more advanced method to study the fluxon-solutions, which was done by Gorria et. al. in Refs. [58, 59] by piece-wise linearizing the sin-term in the equations for $N = 3$, resulting in linear equations which are fitted together to make the solution continuous. Here, however, a more simple approach will be taken for the $N = 3$ case, where only the in-phase solution is studied. The in-phase solution in three stacked junctions should have $\phi^1 = \phi^3$ due to symmetry and it seems fair to assume that ϕ^2 only deviates slightly from the other two phases. The following ansatz is therefore adopted

$$\begin{aligned} \phi^1 &= \phi + \delta\phi = \phi^3 \ , \\ \phi^2 &= \phi - \kappa\delta\phi \ , \end{aligned} \tag{3.40}$$

where κ is some, yet, unknown constant, and $\delta\phi$ represents a small difference between the solutions, such that $\kappa\delta\phi << 1$. Introducing the ansatz into Eqs. (3.20) yields

$$\begin{aligned} J^1 &= \frac{1}{1-2S^2}\Big((1-S)\phi_{xx} + (1+\kappa S)\delta\phi_{xx}\Big) \ , \\ J^2 &= \frac{1}{1-2S^2}\Big((1-2S)\phi_{xx} - (\kappa+2S)\delta\phi_{xx}\Big) \ . \end{aligned} \tag{3.41}$$

Using $\kappa\delta\phi << 1$, the difference $J^1 - J^2$ becomes

$$\begin{aligned} \delta\phi_{tt} + \alpha\delta\phi_t + \cos(\phi)\,\delta\phi = \\ \frac{1}{(1+\kappa)(1-2S^2)}\Big(S\phi_{xx} + \big(1 + 2S + (1+S)\kappa\big)\delta\phi_{xx}\Big) \ . \end{aligned} \tag{3.42}$$

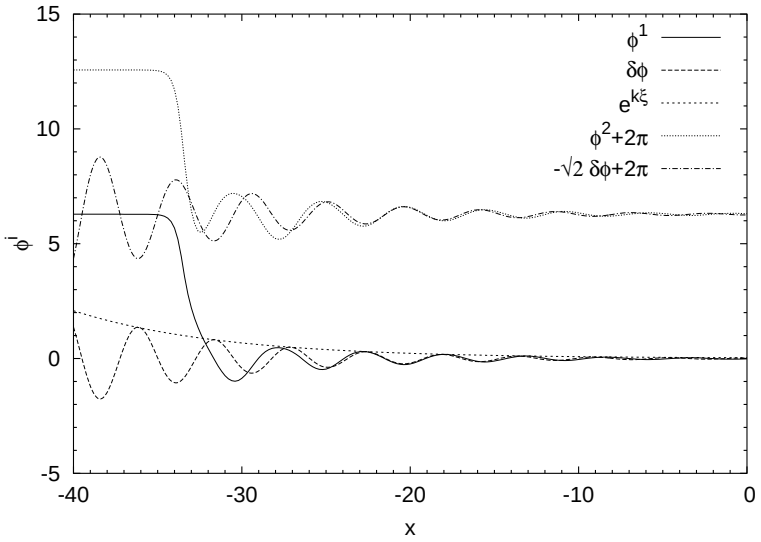

Figure 3.3: Plot showing a numerical solution of the bunched mode of the 3 junction stack which clearly shows the oscillating tail. Also plotted is the analytical expression in Eq. (3.45) and the exponential decay curve is shown separately. The constants A_1 and A_2 have been fitted numerically. Parameters in the numerical solution are $\alpha = 0.1$, $\gamma = -0.48$, $v = 1.13$ and $S = -0.2$. ϕ^3 is not shown, because it is indistinguishable from ϕ^1. The analytical expression fits well away from the fluxon center, which is expected from the assumptions made in the derivation of Eq. (3.45).

This equation is coupled to an equation for ϕ (obtained by calculating $J^1 + J^2$), and a general solution of these two coupled equations will probably be quite complicated. Consider the case $\sin\phi = \phi_{xx} = 0$ for a 2π-kink, corresponding to looking at solutions to $\delta\phi$ away from the fluxon-center, located at $x = vt + x_0$. Doing this, the equation

$$\delta\phi_{\xi\xi} - \frac{1}{v^2 - \frac{1+2S+(1+S)\kappa}{(1+\kappa)(1-2S^2)}}\Big(\alpha v\ \delta\phi_\xi - \delta\phi\Big) = 0 \tag{3.43}$$

is obtained, where the self-coordinate, $\xi \equiv x - vt - x_0$, has been introduced. If only the interval $\xi < 0$ is considered, the solution of this type of equation has an exponential decaying term and an exponential growing term. The exponential growing term contradicts the assumption that $\kappa\delta\phi$ is small and is discarded. The nature of the remaining term depends on the magnitude of v^2. Thus, if

$$v^2 > \frac{1 + 2S + (1+S)\kappa}{(1+\kappa)(1-2S^2)} \tag{3.44}$$

an oscillating solution (discarding terms of second order and higher in α) is obtained. Oscillations, termed Cherenkov radiation, are found when the in-phase solution is moving with a velocity above c_-[60]. By equating the l.h.s. and the r.h.s. in Eq. (3.44) and inserting $v = c_-$, the value $\kappa = \sqrt{2}$ is obtained. The amplitude in junction 2 is therefore about $\sqrt{2}$ times bigger than the amplitude in junctions 1 and 3. The oscillations in the junctions $1 + 3$ and 2 are in anti-phase and exponentially decaying (due to dissipation) with a decay constant, k, given by $k = \alpha v/(2(v^2 - c_-^2))$. The angular frequency, ω, of the oscillations is $\omega = 1/\sqrt{v^2 - c_-^2}$ and the solution becomes

$$\delta\phi = e^{k\xi}\Big(A_1\cos(\omega\xi) + A_2\sin(\omega\xi)\Big), \tag{3.45}$$

valid for $\xi << 0$ and $v > c_-$, where A_1 and A_2 are unknown constants. Fig. 3.3 shows the solution $\delta\phi$ and compares it to a numerical solution of the partial differential equations. The constants A_1 and A_2 has been determined by fitting to the numerical solution. The oscillating tail is seen to fit quite well with the numerical solution.

Cherenkov radiation for different fluxon modes was considered by Goldobin et. al in Ref. [61] and it was found in Refs. [62, 63] to be very important for the formation of stable bunched fluxon modes.

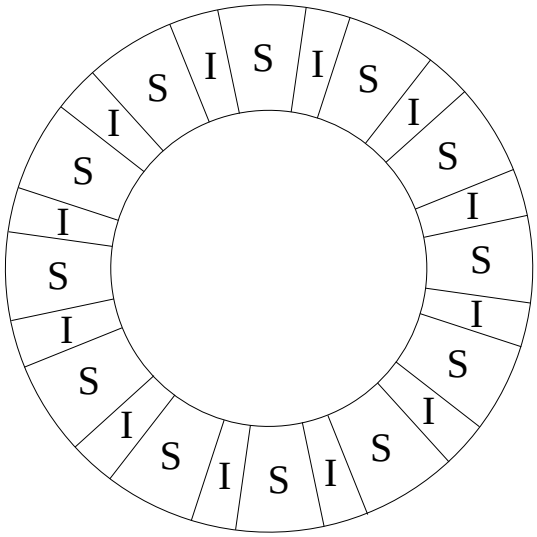

Figure 3.4: Schematic view of a circular Josephson stack. "S" is short for Superconductor and "I" for Insulator. In this configuration, all junctions are on an equal footing.

Circular Stack

A simple way to get some idea on how a large stack may behave is to restore the symmetry broken by the outer junctions and consider a circular stack, see Fig. 3.4, where one neglect the curvature of the stack[64]. This is equivalent to the case $N \to \infty$[64]. In both cases, every junction is an "inner" junction and the stack is describes by Eqs. (3.20) and (3.21) with $\mathbf{S}$ given as

$$\mathbf{S} = \begin{pmatrix} 1 & S & & & & S \\ S & 1 & S & & & \\ & S & 1 & S & & \\ & & \ddots & \ddots & \ddots & \\ & & & S & 1 & S \\ S & & & & S & 1 \end{pmatrix} , \tag{3.46}$$

where blank elements are zero. It then seem likely to find the symmetric solution where $\phi^i = \phi^{i+1}$ for all $i \in [1; N]$, defining $\phi^{N+1} \equiv \phi^1$. The anti-symmetric case, $\phi^i = -\phi^{i+1}$, is only possible for an even number of junctions. For this reason the case $\phi^i = \pm\phi^{i+1} \equiv \phi$ with an even number of junctions is considered, and the equation

$$\frac{1}{1 \pm 2S}\phi_{xx} = \phi_{tt} + \sin\phi \tag{3.47}$$

is obtained in the unperturbed case ($\alpha = \gamma = 0$). It is easily seen, that the maximum fluxon velocities of the two solutions are $1/\sqrt{1-2S}$ and $1/\sqrt{1+2S}$ for the anti-phase and in-phase solutions respectively. The characteristic velocities of the modes 1 and N in Eq. (3.31) when $N \to \infty$ gives exactly these two velocities. The fluxon solutions to the above sine-Gordon equation are easily found to be Eq. (3.39) with $c_- = 1/\sqrt{1-2S}$ and $c_+ = 1/\sqrt{1+2S}$.

Empty-Junction Solutions

Continuing with simple ways to get fluxon-solutions to the stacked Eqs. (3.20)-(3.22), one of the inner junctions is considered to be empty (does not contain a fluxon). The inner junctions are described by

$$\phi^i_{xx} = J^i_z + S\left(J^{i-1}_z + J^{i+1}_z\right) . \tag{3.48}$$

If ϕ^i, for some i, is the constant $\sin^{-1}\gamma^i$, the above equation states that $J^{i-1}_z = -J^{i+1}_z$. This condition is satisfied if

$$\phi^{i-1} = -\phi^{i+1} \quad \text{and} \quad \gamma^{i-1} = -\gamma^{i+1} . \tag{3.49}$$

Thus, if there is an "empty" junction in the stack, the stack may be divided into two substacks which are related by the relations (3.49).

The simplest case where this can be used is in the case of 3 junctions, where $J_z^2 = 0$ is considered. The top and bottom junctions are then related through Eq. (3.49), meaning that if junction 1 contains a fluxon, then junction 3 must contain an anti-fluxon, resulting in the solution

i	1	2	3
	$\uparrow$	0	$\downarrow$

for the stack of 3 junctions. Here $\uparrow$ means a fluxon, 0 means no fluxon (ϕ^i is constant), $\downarrow$ means an antifluxon, and i referrers to the junction number. A single junction has the maximum fluxon velocity $c_1^1 = 1$ which is the same as c_2^3 (c_2^3 is sometimes denoted by c_0), thus c_2^3 is a maximum fluxon speed for the above solution. For the single junction an exact analytical solution is known when $\alpha = \gamma = 0$ which thus leads to an exact solution for $N = 3$.

A little more complicated example is to take a stack of 7 junctions and consider $J_z^4 = 0$. Two substacks of size 3, which are related through Eq. (3.49) is then found. The in-phase mode was previously considered in the case of three junctions, and the following solution

i	1	2	3	4	5	6	7
	$\uparrow$	$\uparrow$	$\uparrow$	0	$\downarrow$	$\downarrow$	$\downarrow$

is then found for the stack of 7 junctions. The solution of the 3 junction substack has the characteristic velocity $c_3^3 = 1/\sqrt{1+\sqrt{2}S}$ so the above solution of the 7 junction stack must also have this characteristic velocity. Inspecting the plasma modes for the 7 junction stack, Eq. (3.31) with $N = 7$, it is found that the above solution corresponds to mode 6 ($m = 6$), having a characteristic velocity of $c_6^7 = 1/\sqrt{1+\sqrt{2}S}$.

Consider again the case $N = 7$ with $J_z^4 = 0$. The above solutions for the 3 junction stack with the empty middle junction may be used as a solution for the 3 junction substack of the $N = 7$ case, resulting in the solution

i	1	2	3	4	5	6	7
	$\uparrow$	0	$\downarrow$	0	$\uparrow$	0	$\downarrow$

consisting essentially of single junctions having a maximum fluxon speed of 1. The 7 junction stack characteristic velocity $c_4^7 = 1$.

One could continue this way to build different fluxon solutions using Eq. (3.31) from the known solutions in the case of 1, 2 and 3 stacked junctions, however, only the first condition in Eq. (3.31) were really used. The second condition states that the bias current should have opposite sign for the different sides of the empty junction. This seem hard to realize in an experimental setup, especially for intrinsic BSCCO stacks where one would have to attach electrodes to the individual atomic sized layers. The bias current interacts with the magnetic field of the fluxons through the Lorentz force and since a fluxon and an anti-fluxon have different directions of the magnetic field, they will be pushed in the same direction only if the bias currents are opposite. With the much more realistic unidirectional bias current (referred to as "natural" biasing) the fluxons and anti-fluxons would move in opposite directions and break the first (and second) condition in Eq. (3.31). In Section 3.3, these types of solutions will, among other things, be considered numerically with both types of bias currents. Numerical solutions showing the empty-junction solutions can be found in that Section: The empty-junction solution for the 3 junction stack is shown as the middle plots of Fig. 3.7 while the case with natural biasing is shown as the middle plots of Fig. 3.10. The solutions for the 7 junction stack are shown as the middle and right plots of Fig. 3.8.

3.2.3 Flux-Flow Solutions

Like in the case of a single Josephson junction, the external magnetic field may generate vortices at one edge of the long Josephson junction stack, which move to the other end by means of the bias current and gets annihilated by the external magnetic field. A similar analysis as the one in Section 2.6 may be done for the case of coupled junctions. Here, however, only the case of two coupled junctions will be considered due to the simplicity. The analysis is due to Ref. [65], which will be followed closely.

The equations of motion for a stack of two junctions may be expressed in the variables

$$u = \frac{1}{2}\left(\phi^1 + \phi^2\right) \quad , \quad v = \frac{1}{2}\left(\phi^1 - \phi^2\right) \ , \tag{3.50}$$

turning the equations of motion, Eq. (3.20), into

$$c_+^2 u_{xx} = u_{tt} + \alpha u_t + \sin u \cos v - \gamma^+ \ , \tag{3.51}$$
$$c_-^2 v_{xx} = v_{tt} + \alpha v_t + \sin v \cos u - \gamma^- \ , \tag{3.52}$$

with $c_+ \equiv c_2^2$, $c_- \equiv c_2^1$, $\gamma^+ = (\gamma^1 + \gamma^2)/2$, and $\gamma^- = (\gamma^1 - \gamma^2)/2$. Eq. (3.23) are the boundary conditions which become

$$u_x(0) = u_x(L) = \Gamma \quad , \quad v_x(0) = v_x(L) = 0 \ . \tag{3.53}$$

If Γ is large, the direct generalization of Eq. (2.99) is[65]

$$\phi^1 = \phi_0^1 + \Gamma x + \omega t + \delta\phi^1(x,t) \ , \tag{3.54}$$
$$\phi^2 = \phi_0^2 + \Gamma x + \omega t + \delta\phi^2(x,t) \ , \tag{3.55}$$

where $\delta\phi^i << 1$ are small perturbations in each of the junctions. The above form describes ϕ^i as having a constant phase of ϕ_0^i and a spatial slope of Γ across the junctions, each having a voltage drop of ω. To satisfy the boundary conditions, it must be required that $\delta\phi_x^i(0,t) = \delta\phi_x^i(L,t) = 0$. The ansatz, Eqs. (3.54) and (3.55), translates into

$$u = u_0 + \Gamma x + \omega t + \delta u \ , \tag{3.56}$$
$$v = v_0 + \delta v, \tag{3.57}$$

when expressed in terms of u and v, where $u_0 = (\phi_0^1 + \phi_0^2)/2$, $v_0 = (\phi_0^1 - \phi_0^2)/2$, $\delta u = (\delta\phi^1 + \delta\phi^2)/2$, and $\delta u = (\delta\phi^1 - \delta\phi^2)/2$. This ansatz is inserted into Eqs. (3.51) and (3.52) and expanded to first order in δu and δv, resulting in two coupled linear equations for δu and δv (not shown). The variables δu and δv may then be expressed as Fourier series

$$\delta u = \sum_{n=0}^{\infty} \left(U_n^1 \cos\omega t + U_n^2 \sin\omega t \right) \cos k_n x \ , \tag{3.58}$$
$$\delta v = \sum_{n=0}^{\infty} \left(V_n^1 \cos\omega t + V_n^2 \sin\omega t \right) \cos k_n x \ , \tag{3.59}$$

with $k_n = \pi n/L$. Inserting into the coupled linear equations for δu and δv (not shown), multiplying by $\cos k_n x$, and integrating over the spatial dimension, equations to determine U_n^1, U_n^2, V_n^1, and V_n^2 are obtained as[65]

$$\left(\omega^2 - c_+^2 k_n^2\right)\left(U_n^1 \cos\omega t + U_n^2 \sin\omega t\right) + \alpha\omega\left(U_n^1 \sin\omega t - U_n^2 \cos\omega t\right) = \cos v_0 \left(Z_n \cos\left(u_0 + \omega t\right) - Y_n \sin\left(u_0 + \omega t\right)\right) \ , \tag{3.60}$$
$$\left(\omega^2 - c_-^2 k_n^2\right)\left(V_n^1 \cos\omega t + V_n^2 \sin\omega t\right) + \alpha\omega\left(V_n^1 \sin\omega t - V_n^2 \cos\omega t\right) = \sin v_0 \left(Y_n \cos\left(u_0 + \omega t\right) - Z_n \sin\left(u_0 + \omega t\right)\right) \ , \tag{3.61}$$

where

$$Y_n = -\frac{2\Gamma L}{1+\delta_{n,0}} \frac{(-1)^n \sin\Gamma L}{k_n^2 L^2 - \Gamma^2 L^2} \ , \tag{3.62}$$
$$Z_n = -\frac{2\Gamma L}{1+\delta_{n,0}} \frac{1 - (-1)^n \cos\Gamma L}{k_n^2 L^2 - \Gamma^2 L^2} \ . \tag{3.63}$$

In the coupled case, there are two constant phases, v_0 and u_0. It is clear from Eqs. (3.54) and (3.55) that these phases can be changed by choosing a different zero-point for the time-coordinate. This is done such that u_0 becomes zero, and the constants U_n^1, U_n^2, V_n^1, and V_n^2 are determined to[65]

$$U_n^1 = \frac{Z_n\left(\omega^2 - c_+^2 k_n^2\right) + Y_n \alpha\omega}{(\omega^2 - c_+^2 k_n^2)^2 + \alpha^2\omega^2} \cos v_0 \ , \tag{3.64}$$
$$U_n^2 = \frac{Y_n\left(\omega^2 - c_+^2 k_n^2\right) - Z_n \alpha\omega}{(\omega^2 - c_+^2 k_n^2)^2 + \alpha^2\omega^2} \cos v_0 \ , \tag{3.65}$$
$$V_n^1 = \frac{Y_n\left(\omega^2 - c_-^2 k_n^2\right) - Z_n \alpha\omega}{(\omega^2 - c_-^2 k_n^2)^2 + \alpha^2\omega^2} \sin v_0 \ , \quad \text{and} \tag{3.66}$$
$$V_n^2 = \frac{-Z_n\left(\omega^2 - c_-^2 k_n^2\right) - Y_n \alpha\omega}{(\omega^2 - c_-^2 k_n^2)^2 + \alpha^2\omega^2} \sin v_0 \ . \tag{3.67}$$

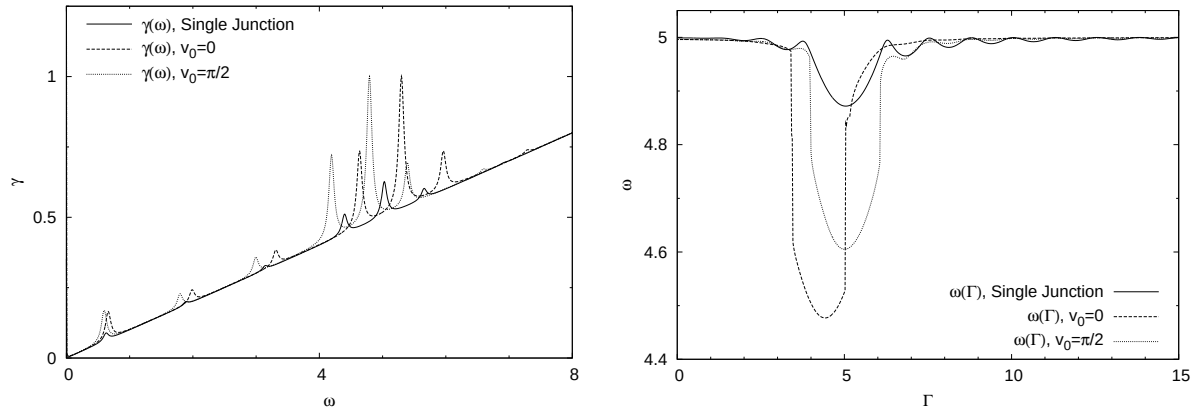

Figure 3.5: Flux-flow solution from Eq. (3.69) with $L = 5$, $S = -0.1$, $v_0 = 0$, and $v_0 = \pi/2$. Also shown are the corresponding curves from the single junction case, Eq. (2.108). Left is the current as a function of the voltage, with $\Gamma = 5$, showing a linearly increasing background with resonances at $\omega = c_\pm \pi n/L$. The right plot shows the voltage as a function of the applied magnetic field obtained by solving Eq. (3.69) numerically for $\gamma = 0.5$.

The flux-flow solution in the case of two coupled junctions with a large applied magnetic field is now complete. The solution is seen to depend on v_0, which expresses the phase-difference between the two junctions. The case $v_0 = 0$ makes the constants V_n^1 and V_n^2 zero, such that only terms with c_+^2 survive. In the same way, in the case $v_0 = \pi/2$ only terms with c_-^2 are left. These two extreme cases of the phase-difference contains the same two characteristic velocities as the in-phase (c_+) fluxon mode and the anti-phase (c_-) fluxon mode. But unlike the case of fluxon modes, the flux-flow solutions are know in the cases corresponding to mixtures of the in-phase and anti-phase modes, i.e. $0 < v_0 < \pi/2$. Both the in-phase, $v_0 = 0$, and anti-phase, $v_0 = \pi/2$, modes have been observed experimentally in Ref. [66].

Exactly like the case of the single junction, the current-voltage curve may be derived in the power-balance approximation. The rate of change of energy in the two junction perturbed coupled case is[65]

$$\frac{dH}{dt} = \frac{\Gamma}{1-S^2}\left[(1-S)\phi_t^1 + (1-S)\phi_t^2\right]_0^L - \alpha\int_0^L \left((\phi_t^1)^2 + (\phi_t^2)^2\right) dx + \gamma\int_0^L \left(\phi_t^1 + \phi_t^2\right) dx \ . \tag{3.68}$$

Requiring power-balance (the total change of energy in one period is zero), the current-voltage characteristic is obtained as[65]

$$\begin{aligned} \gamma &= \alpha\omega + \frac{\alpha\omega}{4}\sum_{n=0}^{\infty}(1+\delta_{n,0})\left((U_n^1)^2 + (U_n^2)^2 + (V_n^1)^2 + (V_n^2)^2\right) \\ &= \alpha\omega + 2\alpha\omega\sum_{n=-\infty}^{\infty}\frac{\Gamma^2L^2\sin^2\left((\Gamma L - n\pi)/2\right)}{(\Gamma^2L^2 - n^2\pi^2)^2}\left(\frac{\cos^2 v_0}{\left(\omega^2 - c_+^2 n^2\pi^2/L^2\right)^2 + \alpha^2\omega^2}\right. \\ &\qquad \left. \frac{\sin^2 v_0}{\left(\omega^2 - c_-^2 n^2\pi^2/L^2\right)^2 + \alpha^2\omega^2}\right) . \end{aligned} \tag{3.69}$$

Note here the mixing of the two terms involving the characteristic velocities, c_+ and c_-, controlled by the phase-difference v_0. Plots of the current voltage characteristic can be seen in Fig. 3.5 which compares the coupled case for $v_0 = 0$ and $\pi/2$ to the single junction case. The resonances are located at $\omega = c_\pm n\pi/L$ in the coupled case and at $\omega = n\pi/L$ in the single junction case, such that the inductive coupling has the effect of shifting the resonances on the ω axis. For the $\omega(\Gamma)$ plots, the phase of the oscillations is unchanged from the single junction case, since no $c_\pm$ is present in the terms containing $\Gamma L - n\pi$. These terms are responsible for the oscillations in the voltage as a function of applied magnetic field curve and the oscillations thus have a period of $2\pi/L$ in both the coupled and single junction cases.

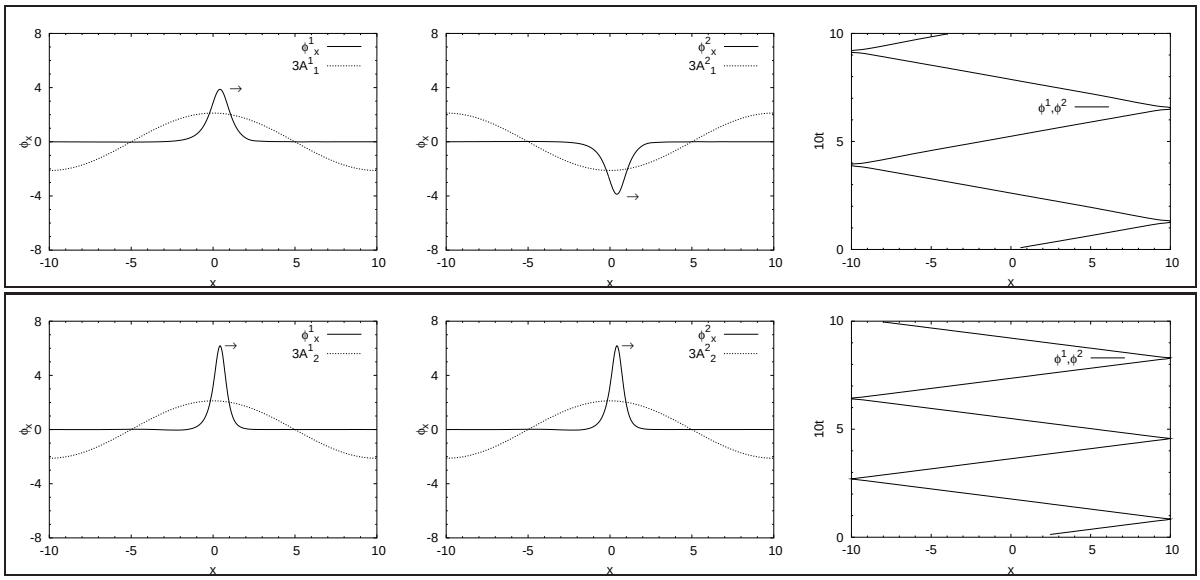

Figure 3.6: Illustration of the could-be relationship between the plasma oscillations and the fluxon modes of the 2 junction stack with unnatural biasing. The top plots are mode 1 ($\gamma^1 = -\gamma^2$) and the bottom plots are mode 2 ($\gamma^1 = \gamma^2$). The right-most figures are the trajectories of the fluxons. Parameters are $\alpha = 0.1$, $S = -0.2$, $\gamma = -0.2$ (top), -0.44 (bottom) and $v = 0.75$ (top), 1.07 (bottom).

3.3 Fluxons and Plasmons - Any Relation?

In this section, a proposed relationship between the plasma modes and the fluxon modes will be investigated numerically. First, the case where γ^i can be $\pm\gamma^j$ will be considered, and referred to as "unnatural" biasing, because it is hard, if not impossible, to realize this in an experimental set-up for $N > 2$. For $N = 2$ it has been done experimentally, see Ref. [67]. After this, the focus will be on "natural biasing" ($\gamma^i = \gamma^j$) which is of greater practical interest. The results presented in this section should be regarded as "experimental" numerical observations and not as exact results. Only the case without an applied magnetic field, $\Gamma = 0$, is considered.

For the 2 junction stack, there are two plasma modes: The anti-phase oscillations and the in-phase oscillations. Following Ref. [67], there are, however, more fluxon modes than two. With one fluxon in each junction and the bias current having the same direction in both junctions there are

(i) an in-phase moving fluxon-fluxon mode with characteristic velocity c_+ and
(ii) an anti-phase moving fluxon-antifluxon mode with characteristic velocity c_-.

If the bias current has opposite directions in the two junctions (see Refs. [67] and [56]) there are in addition

(iii) an in-phase moving fluxon-antifluxon mode with characteristic velocity c_- and
(iv) an anti-phase moving fluxon-fluxon mode.

The latter is not discussed, but (i)-(iii) are shown in Figs. 3.6 and 3.9. The phase-plots are supplemented by trajectories of the fluxons, which are found numerically by determining the position of a fluxon in junction i by finding the lowest value of ϕ^i_t. In order to get the value as good as possible, without too large a number of x-mesh points, the shape of ϕ_t around the minimum was approximated by a second order polynomial. Doing this at several times and plotting the positions as a function of time, the trajectory-plots are obtained. It is easy to see the fluxon motion of the three modes in this type of plot.

3.3.1 "Unnatural" Biasing

For the 2 junction stack, the two plasma modes may be mapped into two in-phase moving fluxon modes. It is proposed, that the anti-phase plasma oscillations maps into the in-phase moving fluxon-antifluxon mode (iii) and the in-phase plasma oscillations maps into the in-phase moving fluxon-fluxon mode (i). This requires the bias current to be chosen in different ways for the two modes, i.e. in opposite directions for (iii) and in same directions for (i). The velocities of the two modes are expected to be smaller than

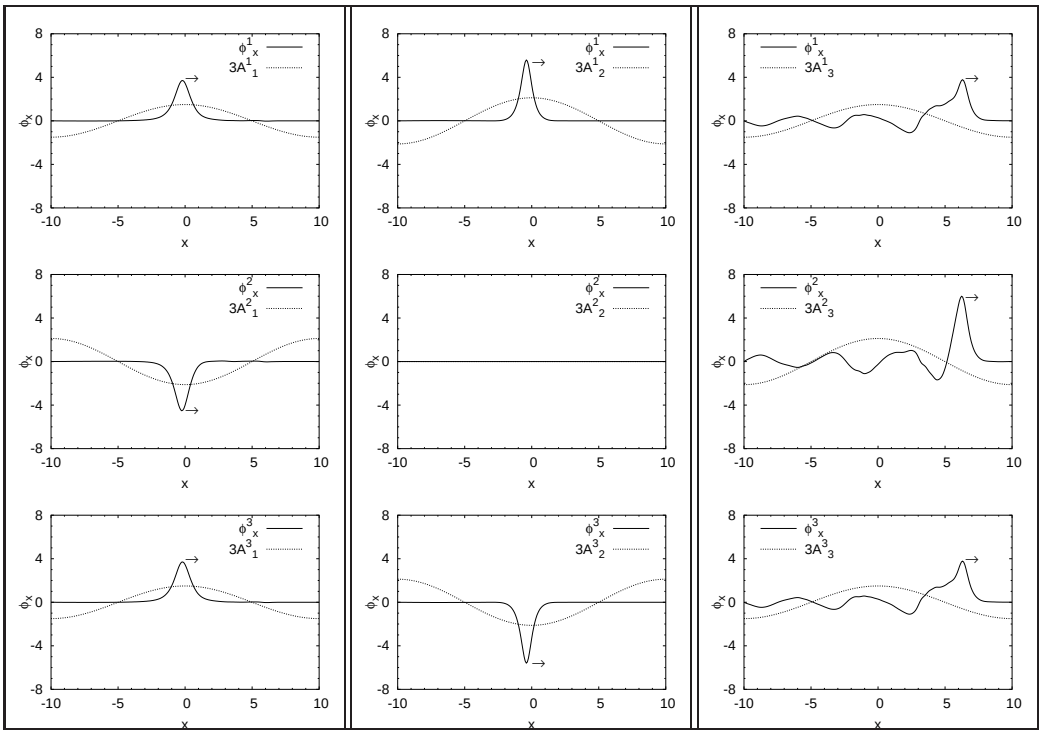

Figure 3.7: Numerical solutions of mode 1 (left), 2 (middle) and 3 (right) of the 3 junction stack. The empty junction solution in the middle plots and the oscillating tail of the right plots were considered analytically in Section 3.2.2. The bias current is chosen such that fluxons and antifluxons are driven in the same direction. Parameters are $\alpha = 0.1$, $S = -0.2$ and $\gamma = -0.2$ (left), -0.35 (middle), -0.45 (right). The relative signs of γ^i can be deduced from A^i_m which are also shown in the plots.

the characteristic velocity for each mode[67]. The mapping is illustrated in Fig. 3.6. Note that the plasma-oscillations in this and all other plots in this section have been multiplied by 3 in order to show them more clearly. The two fluxon modes were found analytically in Section 3.2.2, and their maximum velocities are exactly the characteristic velocities of the plasma modes in the unperturbed case ($\alpha = \gamma = 0$).

The above illustrates the mapping for the 2 junction stack, which will be generalized, such that a mode consists of at most one fluxon (or antifluxon) in each junction and the polarity of the fluxons are determined by the relative phases of the plasma oscillations. To be more precise, the following scheme is used to generate the fluxon/antifluxon configuration in mode m[1]:

a. $a^i_m > 0$: Junction i contains a fluxon and $\gamma^i = \gamma$.
b. $a^i_m < 0$: Junction i contains an antifluxon and $\gamma^i = -\gamma$.
c. $a^i_m = 0$: Junction i has no 2π phase shift and $\gamma^i = \gamma$.

a^i_m is given by Eq. (3.29). The velocity of the fluxons of mode m should be in the interval $[0, c^N_m]$, because c^N_m is the maximum velocity of the mode. It is not expected that the upper bound should be exactly valid, because it is known that, when examined carefully, it does not hold in the perturbed case[64].

The bias current is chosen such that it drives all the fluxons and antifluxons in the same direction. The careful reader will here notice, that for the highest mode ($m = N$, where all fluxons have the same polarity) this "unnatural" way of choosing the bias current actually becomes the "natural" way. Nevertheless, this will be referred to as the "unnatural" way of choosing the bias current, although it is only "unnatural" in $N - 1$ modes out of a total of N modes.

As have already been shown, the above proposed mapping holds for the 2 junction stack. In the following it will be shown how it generalizes for up to 7 junctions.

[1]The terms fluxon and anti-fluxons are of course arbitrary, because reflective boundary conditions are used. What is meant, which should be clear from the context, is that the relative polarities of the fluxons are determined by the signs of a^i_m.

In order to find the modes, an initial fluxon configuration using the above scheme is generated and some values of α, γ, L, and S are chosen. It is then observed how the configuration evolved in time. If a satisfactory steady-state solution is not found, the value of the bias-current, γ, is changed while holding α, L and S fixed. The lowest order mode is usually found first. From IV-curves of small stacks it is known that the different modes will probably only exist for some finite range of γ, and that the lowest value of $|\gamma|$ where a modes is stable is increasing with the mode number[68]. This is why the searching is started at the lowest mode, to get a lower bound on the value of γ which can be used to find the modes.

The above procedure generates three fluxon modes for a 3 junction stack. Mode 1 is the anti-phase mode which contains a fluxon, an anti-fluxon, and a fluxon in junctions 1, 2, and 3 respectively. Mode 2 has an empty middle junction and junctions 1 and 3 contain a fluxon and an anti-fluxon respectively. Mode 3 is the highly desirably in-phase mode with fluxons in all junctions. These three modes have been found numerically and they can be seen in Fig. 3.7.

The remaining modes, for $N \leq 7$, generated by the above procedure have also been found numerically, but with some minor discrepancies, which will now be pointed out. For stack sizes of more than 3 junctions, it was observed that the modes with the highest mode number, $m = N$, the outer junctions are switching to the McCumber curve (see Section 2.7), but everything else is as expected. More comments on these modes can be found in the next section about natural biasing. In addition to this, 4 other modes have been found, which only showed the expected behavior if some of the junctions had switched to finite voltage. In addition to the switched $m = N$-modes, the following discrepancies were observed:

N	m	Expected	Found
4	3	$\uparrow\uparrow\downarrow\downarrow$	$\uparrow MM\downarrow$
6	4	$\uparrow\uparrow\downarrow\downarrow\uparrow\uparrow$	$\uparrow M\downarrow\downarrow M\uparrow$
6	5	$\uparrow\uparrow\uparrow\downarrow\downarrow\downarrow$	$\uparrow\uparrow MM\downarrow\downarrow$
7	5	$\uparrow\uparrow\downarrow\downarrow\downarrow\uparrow\uparrow$	$\uparrow\uparrow M\downarrow M\uparrow\uparrow$

Here, $\uparrow$ means $a_m^i > 0$, $\downarrow$ means $a_m^i < 0$ and M means that the junction has switched to the McCumber curve. Junction number 1 is the leftmost arrow in each row, and the junction number is increasing to the right. The results were calculated with $S = -0.2$ and $\alpha = 0.1$, but other values were tried and the results seem to be valid for a wide range of parameters. The scheme thus predicts, rather reliably, a number of different fluxon configurations. Some of these configurations have a junction without a fluxon ($a_m^i = 0$) and were considered analytically in Section 3.2.2. The 2nd mode of the 3 junction stack can be mentioned as an example. This modes has $a_2^1 > 0$, $a_2^2 = 0$, and $a_2^3 < 0$ and maps into a fluxon mode with a fluxon in junction 1, nothing in junction 2, and an anti-fluxon in junction 3, see the middle plots of Fig. 3.7. This was precisely the fluxon solution shown analytically to exists in Section 3.2.2. For $N \leq 7$, the empty-junction configurations obtained from the mapping of the plasma-modes are

N	m	Configuration
3	2	$\uparrow 0\downarrow$
5	2	$\uparrow\downarrow 0\uparrow\downarrow$
5	3	$\uparrow 0\downarrow 0\uparrow$
5	4	$\uparrow\uparrow 0\downarrow\downarrow$
7	2	$\uparrow\downarrow\uparrow 0\downarrow\uparrow\downarrow$
7	4	$\uparrow 0\downarrow 0\uparrow 0\downarrow$
7	6	$\uparrow\uparrow\uparrow 0\downarrow\downarrow\downarrow$

which are all seen to be derivable from Eq. (3.49) and the solutions found in Section 3.2.2, assuming the solution $\uparrow\downarrow\uparrow$ exists in the 3 junction stack (this solution can easily be found numerically, see Fig. 3.7 left). The proposed plasma mode to fluxon solution map also has the bias-current chosen in accordance with Eq. (3.49), and the maximum fluxon velocity found from the exact solutions is also in accordance with the proposed plasma-fluxon relationship. Modes 2, 4, and 6 of the 7 junction stack can be seen in Fig. 3.8.

3.3.2 "Natural" Biasing

For the case of natural biasing, it was proposed in Ref. [69] that there also in this case could exist a relationship between the linear modes and the fluxon modes of a Josephson stack. For a 2 junction stack

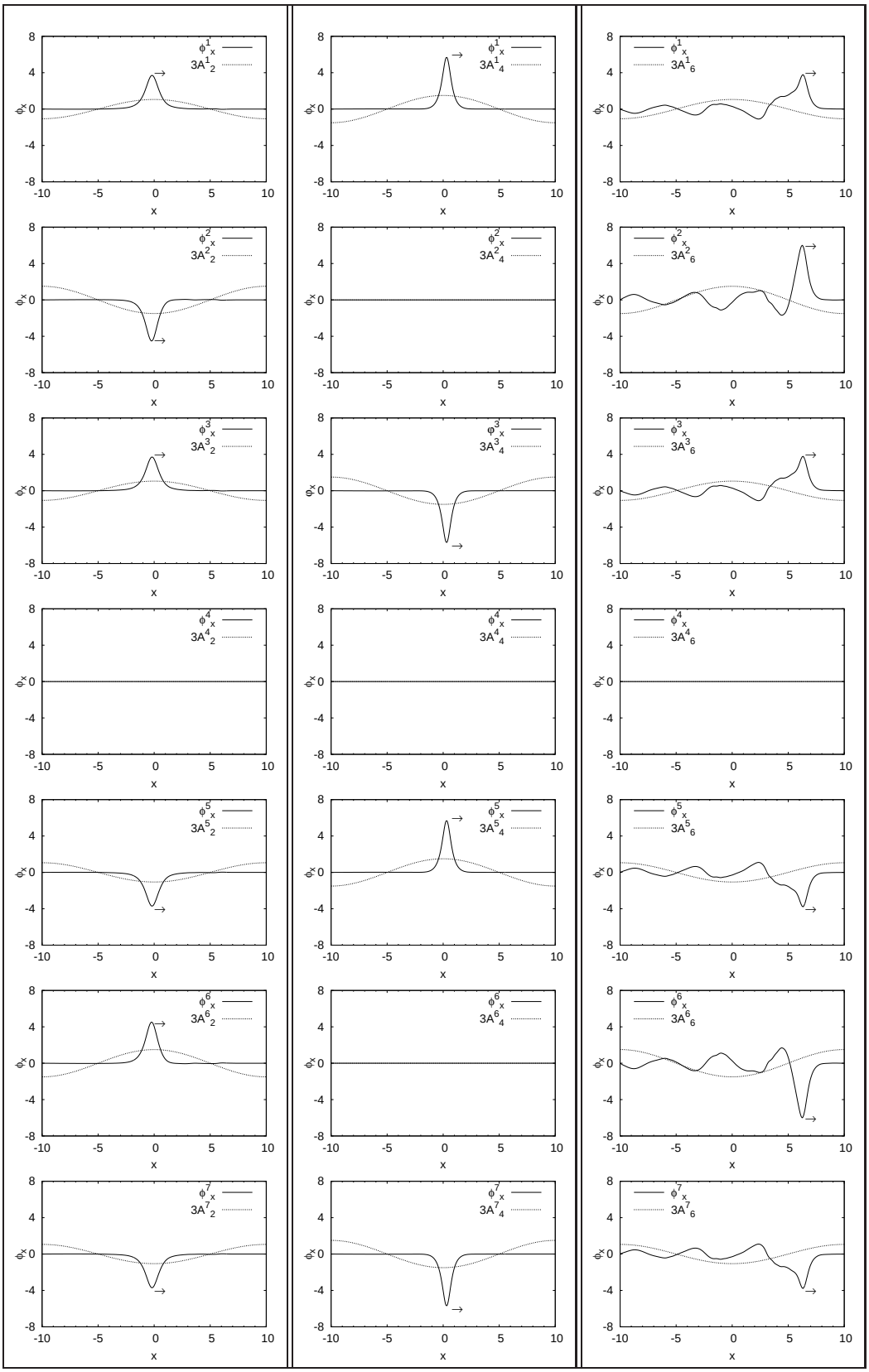

Figure 3.8: Numerical solutions of mode 2 (left), mode 4 (middle), and 6 (right) of the 7 junction stack. These solutions are cases of the empty junction solutions considered in Section 3.2.2. Compare with mode 1, 2, and 3 of the 3 junction stack from Fig. 3.7. Parameters used: $\alpha = 0.1$, $S = -0.2$, and $|\gamma^i| = 0.2$ (left), 0.35 (middle), 0.45 (right). The relative signs of γ^i can be deduced from A^i_m, which are also shown in the plots.

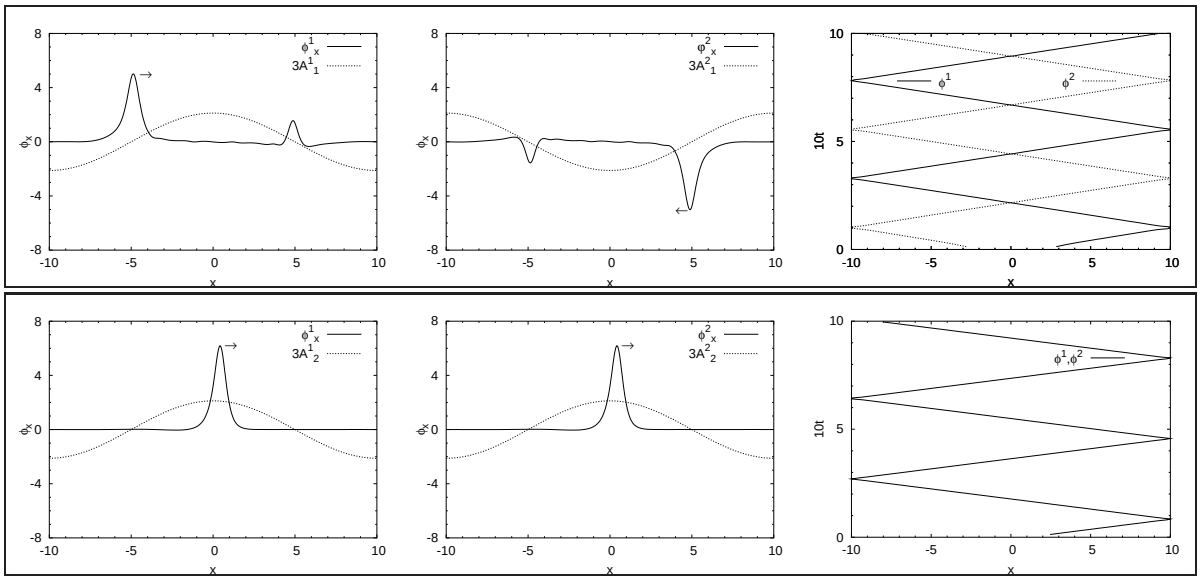

Figure 3.9: Illustration of the could-be relationship between the plasma oscillations and the fluxon modes of the 2 junction stack with natural biasing. The top plots are mode 1 and the bottom plots are mode 2. The right-most figures are the trajectories of the fluxons. Parameters are $\alpha = 0.1$, $S = -0.2$, $\gamma = -0.3$ (top), -0.44 (bottom) and $v = 0.87$ (top), 1.07 (bottom).

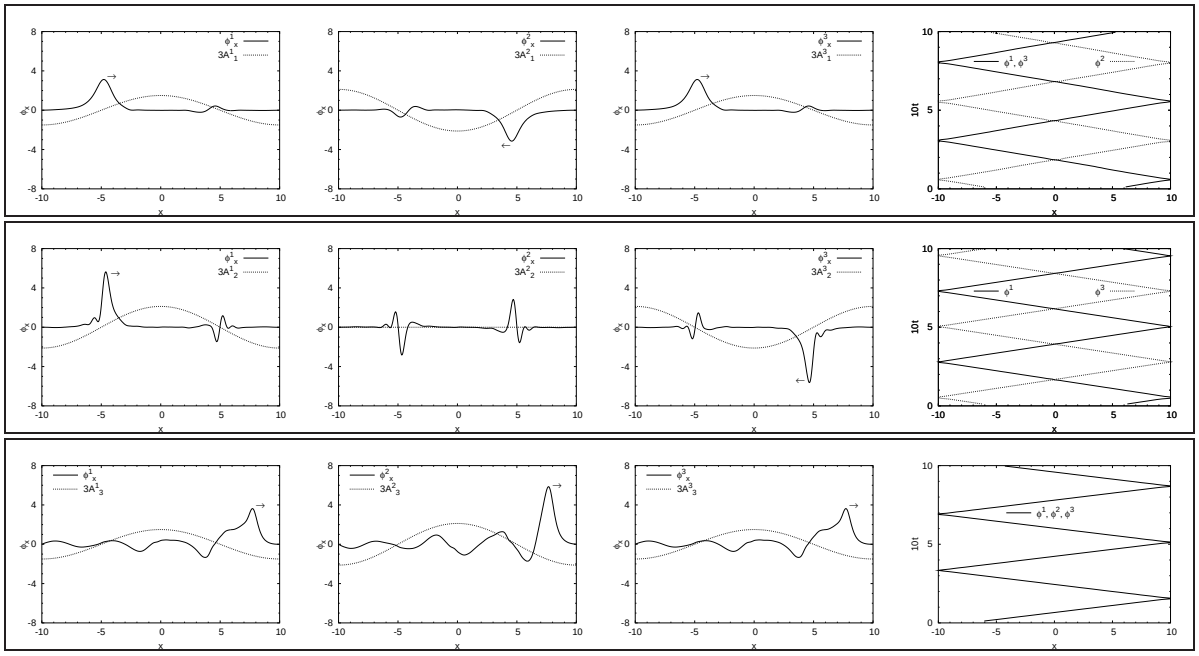

Figure 3.10: The plasma oscillations and the fluxon modes of the 3 junction stack with natural biasing. The middle figures has no fluxon in the middle junction, thus only the first and third junction are present in the trajectories plot. Parameters for the simulations are $\alpha = 0.1$, $S = -0.2$, $\gamma = -0.2$ (top), -0.375 (middle), -0.44 (bottom) and $v = 0.79$ (top), 0.89 (middle), 1.12 (bottom).

it was noted, that the anti-phase plasma oscillations with characteristic velocity c_- could correspond to the mode (ii) which has an anti-phase fluxon motion, and the in-phase plasma oscillations with characteristic velocity c_+ could correspond to the mode with in-phase fluxon motion (i). The similarity of the plasma oscillations and the fluxon mode is illustrated in Fig. 3.9 for the 2 junction stack. For the anti-phase mode in Fig. 3.9, the smaller peak is not a fluxon but the trace of the fluxon in the other junctions. This was also observed in Ref. [47].

The above behavior is expected if the map from plasma modes to fluxon modes proposed in Section

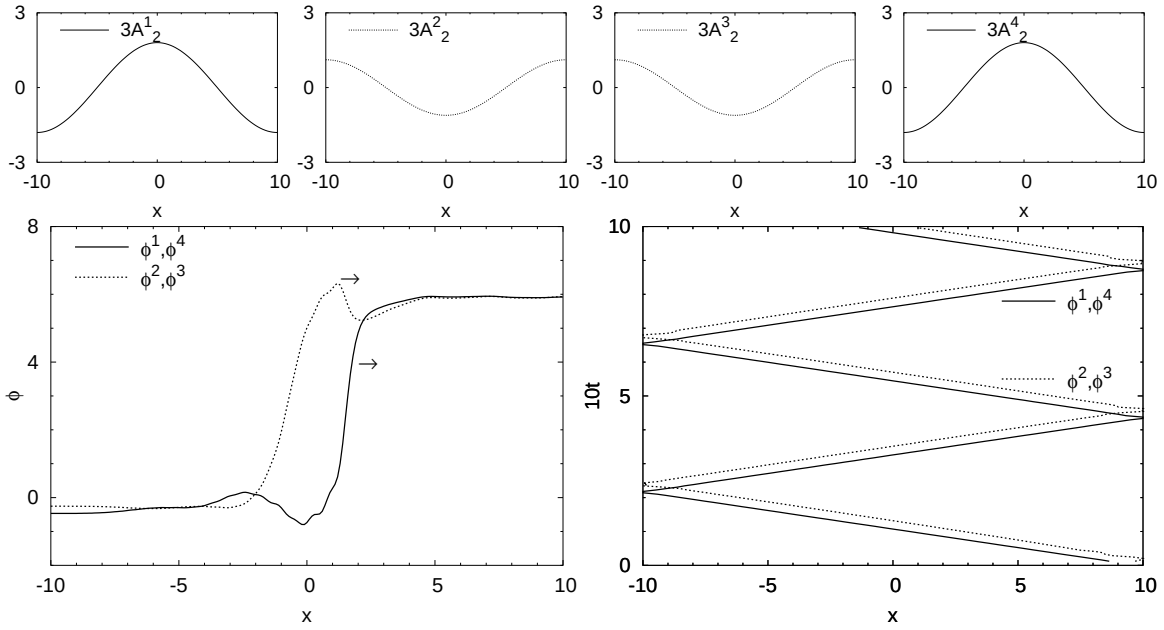

Figure 3.11: Top plots are the plasma-oscillations of the 2nd mode of the 4 junction stack with natural biasing. The bottom-left plot is the phases, ϕ^i, of this mode, and the bottom-right is the trajectories of the fluxons. Parameters for the plots are $\alpha = 0.1$, $\gamma = -0.35$, $S = -0.2$ and the velocity is $v = 0.92$.

3.3.1 is assumed. The relative polarities of the fluxons are the same as in Section 3.3.1, so the only difference is the bias current. If the bias current is chosen to be the same in all junctions, then fluxons and antifluxons will be driven in different directions. It is therefore expected, that mode $m = 1$ with unnatural biasing for a 2 junction stack will translate into fluxons moving in an anti-phase pattern, i.e. that the situation (ii) discussed in the beginning of this section is obtained.

In this section, the proposal from Ref. [69] will be investigated, by searching for similar modes in stacks with more than two junctions. The procedure is simply to see if there is a fluxon mode which corresponds to a given plasma mode. The idea is to generalize the observation in Ref. [69] of the 2 junction stack. To be more precise, there should exists a steady-state fluxon configuration in mode m, where the relative fluxon polarities are chosen according to the scheme in Section 3.3.1. Fluxons should move in an anti-phase manner with anti-fluxons, since the bias current drives them in opposite directions. And finally, the velocity, v, of the fluxons should approximately belong to the interval $[0, c_m^N]$.

In Fig. 3.9 it was already seen that the 2 junction stack behaves like proposed. After being encouraged by the 2 junction stack, the 3 junction stack is analyzed. The 3 junction stack has been investigated by several groups[49, 58, 59, 63], since it represents a manageable non-trivial system.

The results from the 3 junction stack are presented in Fig. 3.10. This figure shows, that the lowest mode (top) has the plasma-oscillations of junctions 1 and 3 in-phase and junction 2 anti-phase with junctions 1 and 3. A fluxon mode where the fluxons in junctions 1 and 3 are moving together and the fluxon in junction 2 is moving in an anti-phase manner with the fluxons in junctions 1 and 3 has been found. The magnitude of the velocity of all the fluxons is the same, namely $v = 0.79$ for the parameters used in the figure, i.e. in the range $[0, c_1^3]$ where, from Eq. (3.31), $c_1^3 \approx 0.88$ when $S = -0.2$.

Although the present section is meant as an empirical observation of a plasma mode-fluxon mode relationship, it is noted that a careful calculation of the trajectory in the top right of Fig. 3.10 shows that the ϕ^2 velocity is slightly different from the ϕ^1 and ϕ^3 velocity, and may even exceed the c_1^3-velocity. Such subtleties (mostly not visible to the naked eye) are sometimes observed, but beyond the empirical scope of the present section.

The second mode of the 3 junction stack is seen as the middle plots of Fig. 3.10. Here, the plasma-oscillations shows, that a fluxon mode where fluxons in junctions 1 and 3 are moving in anti-phase and junction 2 contains no fluxon should exist. This is indeed found, and the magnitude of the velocities of the fluxons in junctions 1 and 3 are calculated to be $v = 0.89$, which is well below c_2^3 when $S = -0.2$, and therefore in the desired range.

The third mode predicted by the proposal was also found, and it is the well-known and very desirable in-phase mode of the 3 junction stack, which was also discussed in Section 3.2.2. It is shown in the

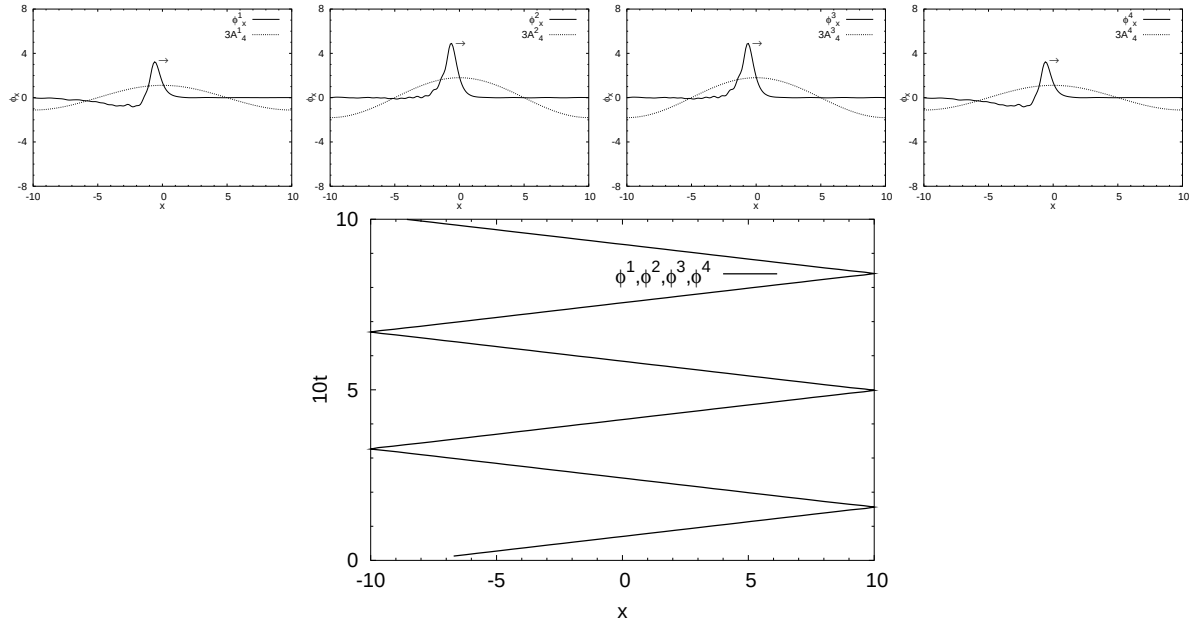

Figure 3.12: The top 4 plots are ϕ_x of the 4th mode of the 4 junction stack with natural biasing together with the plasma-oscillations of this mode. It is hard to tell from ϕ_x, that no fluxon is present in the 1st and 4th junctions. The bottom plot is the trajectories of the "fluxons". Parameters for the plots are $\alpha = 0.1$, $\gamma = -0.54$, $S = -0.2$ and the velocity is $v = 1.17$.

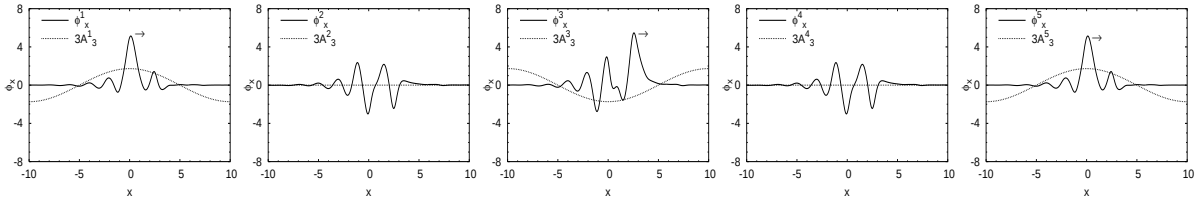

Figure 3.13: In mode 3 of the 5 junction stack with natural biasing, the center fluxon is found to move slower than the outer fluxons when started in the expected anti-phase movement configuration. This results in the configuration depicted here, where all fluxons move with the same velocity. This configuration was not expected from the plasma oscillations. Note that the arrow marks the place of the fluxon, and junctions 2 and 4 do not contain a fluxon, but they only contain the image from the fluxons in junctions 1, 3 and 5. Parameters used are $\alpha = 0.1$, $\gamma = -0.53$, $L = 20$, and $S = -0.2$.

bottom plots of Fig. 3.10. Again, it is found that the mode conforms to the proposal, and that the velocity is in the desired range.

A very interesting question is now how well the proposal predicts the fluxon modes when there are more than 3 junctions. The numerical calculations show, that it can predict many fluxon modes, but with some discrepancies. Here, some of the modes which deviate from the proposed behavior will be explained in detail. It must be noted, though, that in the non-predicted modes the basic symmetries of the plasma modes still seem to be preserved.

For the 4 junction stack, the second mode deviates from what is expected. From the plasma-oscillations, fluxons in junctions 1 and 4 should bunch and so should fluxons in junctions 2 and 3. This is also found, but the fluxons in junctions 1 and 4 should move anti-phase with respect fluxons in junctions 2 and 3, which is not observed. Instead, a configuration where all fluxons are almost bunched is found. Fluxons in junctions 1 and 4 are moving together, lightly in front of the fluxons in junctions 2 and 3. All fluxons are moving with the same velocity, which is in the desired interval $[0, c_2^4]$. The mode can be seen in Fig. 3.11.

The 4th mode of the 4 junction stack deviates from the expected behavior, which was also noted in Section 3.3.1. This is the mode which should be totally bunched, but it has been found that the fluxons in the two outer junctions have disappeared, and instead the junctions have switched to the McCumber-curve. Although there is no fluxon in the outer junctions, an image in the outer junctions

from the fluxons in the middle junctions is still seen. This means, that ϕ_x^i looks more or less like there *is* a fluxon in all the junctions, as can be seen in Fig. 3.12.

Mode 3 of the 5 junction stack should have fluxons in the two outer junctions moving in-phase and in anti-phase with an anti-fluxon in the center junction. When the numerical simulation is started out in this configuration, the center fluxon moves with a somewhat different velocity than the outer junctions, and they thus do not move in an anti-phase manner. The outer fluxons move faster than the middle fluxon, and they then, after some time, end up in the configuration depicted in Fig. 3.13, where they move with the same velocity with a small distance between the outer-fluxons and the fluxon in the middle junction.

In order not to go through every discrepancy in detail, the results have been summarized in Table 3.1. For up to a 7 junction stack, Table 3.1 shows the validity of the initial proposal: That it is possible to predict a family of fluxon modes by just looking at the analytical expression of the plasma modes. Note, that a different short-hand notation than in the previous section us used in the table to emphasize the fluxon motion and not the fluxon polarity.

In Table 3.1 the horizontal direction gives the number of junctions in the stack, N, and the vertical direction gives the order of the mode, with mode 1 always being the clean anti-phase mode and mode N being the in-phase mode (at least for the plasma excitations). In each square, the right hands side shows the plasma-mode prediction, and the left part shows the fluxon-mode obtained from numerical simulations. The trivial case $N = 1$, that has both a plasma mode and a fluxon mode in agreement with the prediction, has been omitted in Table 3.1.

Moving horizontally, the first set of squares shows the predicted anti-phase moving fluxon modes with every fluxon moving in opposite direction to that in the neighboring junction. If the squares are followed in the direction of the diagonal, the plasma mode prediction method suggests in-phase fluxon modes. This is also found, except for $N \geq 4$. Here the two outer junction fluxons are replaced by a similar looking pulse (in-phase with the other fluxons) but on top of the voltage corresponding to the McCumber curve. A different value of the inductive layer-to-layer coupling strength, S, could presumably convert the outer pulses back to clean fluxon pulses. However, the predicted pulse geometry is preserved, and the change is not essential to the total power output from the in-phase pulses, as will be shown in Section 4.1. Even the squares with crosses, which indicate discrepancies, show that the numerically obtained fluxon mode has some of the features in common with the prediction from the linear plasma modes.

3.4 Conclusion

In this section the equations of motion for a stack of Josephson junctions were derived. The equations were coupled non-linear sine-Gordon equations, and thus difficult to handle analytically. It was, however, shown that some simple solutions could be found which provided insight into the dynamics of the stack. Some of the solutions were later found numerically in a connection with a numerical experiment to see if there exists a simple relationship between fluxon modes and plasma modes. The proposed relationship first required the bias current to be chosen (potentially) differently for each junction in the stack. In this case of unnatural biasing, the proposed relationship was seen to hold up quite well. The proposal was then modified to account for a natural, or unidirectional, bias current and it was checked numerically to see if it still could predict non-linear fluxon modes from the linear plasma oscillations. The number of discrepancies increased and the predictive capabilities were thus diminished. However, in all cases the fluxon modes seemed to exhibit some of the symmetries of the plasma modes. Since the investigation was based on numerical experiments it does not provide or suggest a deep mathematical relationship between linear and non-linear solutions of non-linear differential equations. Such a deep relationship in the simple form presented here would seem to be a kind of a Holy Grail for non-linear science and probably too much to ask for. The investigation does, however, suggest that one can obtain some kind of information about non-linear solutions from the linear limit, which is likely since some of the symmetries present in the linear equations are also present in the non-linear ones, for example $\phi \rightarrow -\phi$ since $\sin\phi$ is an odd function.

m \ N	2	3	4	5	6	7
1						
2						
3						
4						
5						
6						
7						

Table 3.1: Summary of what have been found with natural biasing. An arrow means a fluxon, a line means no fluxon, a dashed line means the junction is on the McCumber-curve, a dashed arrow means McCumber with a clear image of a fluxon, $\times$ means that something is *not* according to the proposal, M means that some junctions have switched to the McCumber-curve but otherwise OK and $\surd$ means that everything is according to the proposal. The arrows to the left of the symbols, $\surd$, M and $\times$, show the mode found numerically, and the ones to the right show the mode expected from the proposal. A small horizontal shift between arrows implies that the fluxon distance (away from the boundaries) in x-space is greater than λ_J, and no spacing means that the distance is much smaller than λ_J.

Chapter 4

The Long Josephson Junction as an Oscillator

The previous chapter introduced the long Josephson junction stack and looked at different types of solutions to the equations of motion. This chapter is devoted to the use of some of these solutions to make an oscillator in the THz regime, which is hard to make by conventional oscillator technology. The chapter will discuss two methods for making such an oscillator. One method is trying to utilize a fluxon shuttling back and forth in a stack, previously discussed in Section 3.2.2. The trick is then to obtain a solution where all fluxons in the stack are moving in phase to increase the radiated power. The other method applies a large magnetic field to the edges of the stack such that fluxons are created at one end, traveling under the bias current to the other end where they are annihilated and radiation is emitted, i.e. the flux-flow solution discussed in Section 3.2.3 is utilized. Due to the practical nature of this chapter, only the case of an uniform bias current will be considered, i.e. $\gamma^i \equiv \gamma$ for $i = 1, ..., N$.

4.1 Microwave Output

In the loss-less case with zero applied magnetic field, the fluxons are totally reflected when they arrive at the edge of the junction, see Fig. 2.15. In reality, this does not happen. Due to the loss-term, $\alpha\phi_t$, the fluxons may be annihilated even at zero field if the bias current is too small[70]. In addition, some fraction of the fluxons energy is emitted out of the junction as radiation, and only if the radiated fraction is small enough is the fluxon is reflected back into the junction, even with an applied bias current.

A greatly simplified model of this scenario is depicted in Fig. 4.1. Total voltage, $V(t)$, over all of the oscillators (junctions) and the power dissipated in the load resistor R_L may be related for $R_L >> R_G$ as

$$P(t) \approx \frac{1}{2}\frac{V(t)^2}{R_L} \ . \tag{4.1}$$

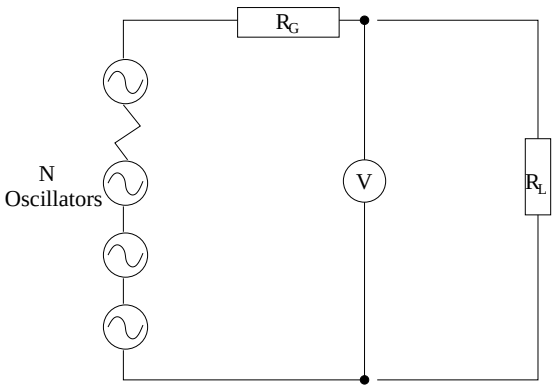

Figure 4.1: Simplified model of the stacked Josephson junction being used as an oscillator.

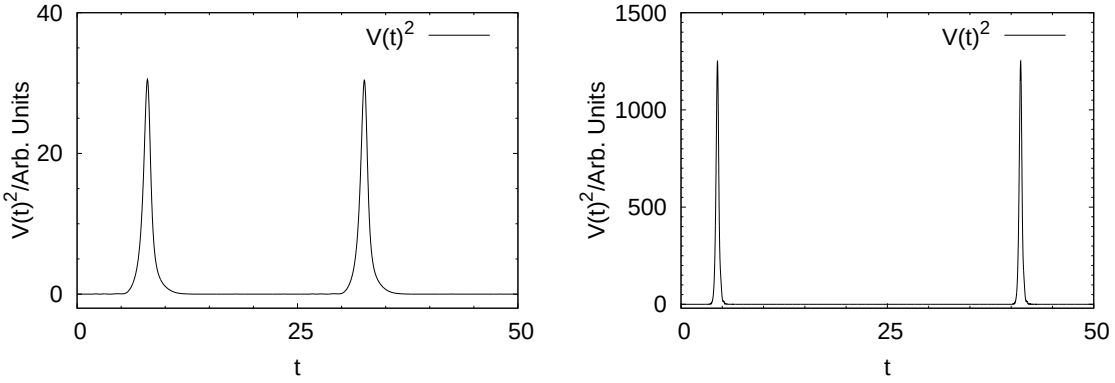

Figure 4.2: Voltage squared across a 2 junction stack measured at one end as a function of time for both the anti-phase mode (left) and the in-phase mode (right). Parameters are $\alpha = 0.1$, $L = 20$, $S = -0.2$, $\gamma = -0.2$(left), and $\gamma = -0.55$(right).

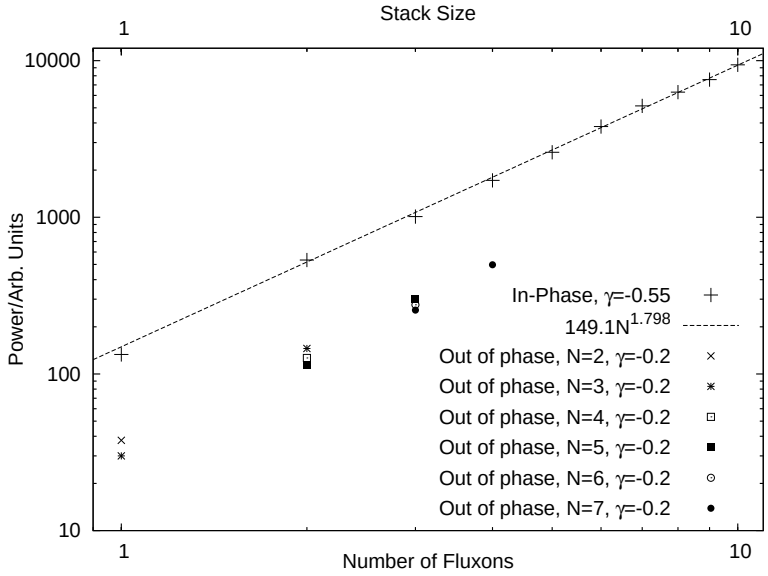

Figure 4.3: Plot showing the integrated output of a pulse as a function of the number of junctions. The in-phase output is approximated well by the power-law $P(N) = 149N^{1.8}$. The top x-axis is the stack size used in the in-phase mode and the bottom x-axis is the number of fluxons arriving at the boundary at the same time in the anti-phase mode. Parameters used: $\alpha = 0.1$, $L = 20$, and $S = -0.2$.

Using Eq. (3.10), the approximate expression

$$P(t) \propto \left(\sum_{i=1}^{N} \phi_t^i(L,t) \right)^2 \tag{4.2}$$

is obtained. This is a measure of the potential maximum output one can hope for in a stack of N junctions. The real output is expected to be a lot smaller, but the potential maximum output may always be maximized in order to maximize the real output.

The usual way to maximize the output is to make all the fluxons in all the junctions arrive at the end of the stack at the same time. This is exactly what they do in the in-phase mode. It is therefore expected that the maximum output is larger in the in-phase modes than in the anti-phase modes. Fig. 4.2 shows the total voltage squared calculated at one of the end of a stack with two junctions as a function of time for both the anti-phase mode and the in-phase mode. It is easy to see that V^2 is much larger for the in-phase mode. Also, note that the time between the pulses for the anti-phase mode is about half that of the in-phase mode, in agreement with the fluxons moving in anti-phase.

In Section 3.3.2 it was shown that it is hard, if not impossible, to find the in-phase mode with N fluxons in a stack with more than three junctions. Instead a mode where the outer junctions had

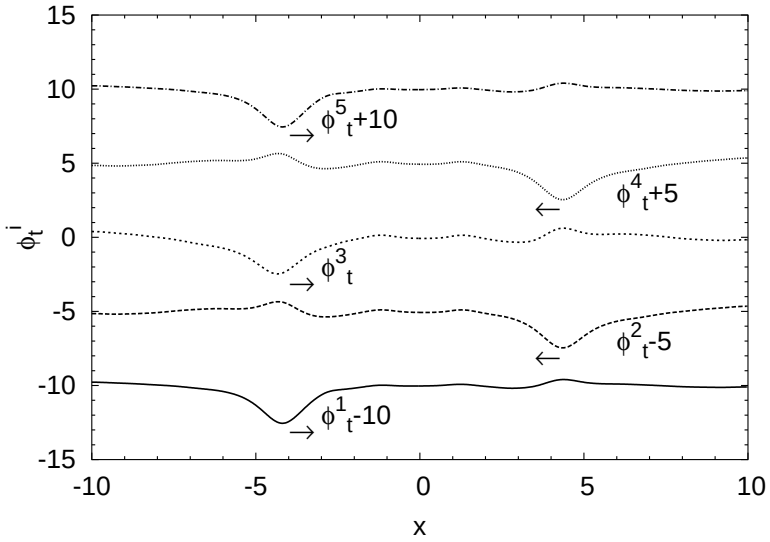

Figure 4.4: The anti-phase mode of the 5 junction stack. For clarity, the curves have been displaced by 5 units, as indicated. Parameters are $N = 5$, $L = 20$, $\alpha = 0.1$, $\gamma = -0.2$, and $S = -0.2$.

switched to finite voltage was found. However, the image from the inner junctions in the outer junctions showed a pulse in ϕ_t^i which looked much like a fluxon, although it is important to stress, that there is no fluxon and only a voltage pulse in the outer junctions. One can now ask, if it matters to the output of the stack, if the top and bottom junctions have switched to the McCumber-curve, when the image of the inner fluxons in the top and bottom junctions looks like a fluxon-pulse.

In Fig. 4.3 the total voltage of the junction at $x = L$ have been integrated over one fluxon collision with the boundary and the square of this have been plotted for different stack sizes. Both the in-phase modes and the anti-phase modes from Section 3.3.2 are considered. For the in-phase modes with switched junctions, the DC-voltage due to the switched junctions has been subtracted in order to get only the pulse. The main thing seen in the plot is, that it does not seem to matter much that the outer junctions have switched in the in-phase modes. For ideal in-phase fluxon motion, it is expected that the power is increasing with the square of the number of junctions. With the switched modes, it is proportional to $N^{1.8}$ for the parameters used, showing that the switched junctions only deteriorate the output power slightly. The system with outer junctions switched to the McCumber curve is still very useful for microwave generation in terms of available power.

One can ask what to expect if the inductive layer-to-layer coupling strength, S, is changed. For a single junction, this coupling is not present, so the output is independent of S. It is also expected, independently of S, that the output is growing as N^2. Thus, ideally the output is expected to be largely independent on the inductive layer-to-layer coupling strength. This being said, it is expected that it will be slightly different though, because the number of switched junctions may depend on S. Also the (slight) separation of the in-phase fluxons may depend on S. Altogether, the output is expected to be relatively insensitive to S. A plot similar to Fig. 4.3 but for $S = -0.4$ shows very similar looking curves, signaling the insensitivity to S. The plot is not shown.

Holding the number of fluxons arriving at the boundary fixed and looking at the anti-phase modes, the output gets smaller when the stack size increases (going vertically at constant N in Fig. 4.3). In the anti-phase mode, the neighboring junction of a fluxon is in some sense empty. When the stack size is increased, more of these "empty" junctions will appear. It turns out, that the image of the fluxons in the "empty" junctions is having a negative effect on the maximum output for the anti-phase mode. This is easily seen in Fig. 4.4, where the images in the neighboring junction has the opposite sign of the fluxon, thus giving rise to a decrease in the maximum output. Then, when the two fluxons in junctions 2 and 4 are hitting the boundary, they will give rise to less voltage than two fluxons of the anti-phase mode of a 4 junction stack, because the 5 junction stack has three junctions with negative images and the 4 junction stack only has two. This is quite the opposite of what is happening in the in-phase mode, where the image in the switched junctions was giving more output.

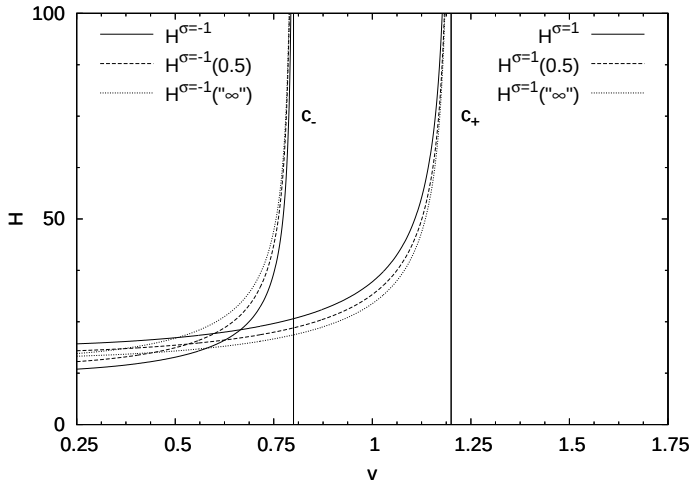

Figure 4.5: Energies given by Eqs. (4.5) and (4.8) for $S = -0.2$. The anti-phase bunched state is energetically stable while the in-phase bunched state is energetically unstable.

4.2 Bunching using an External Microwave Source

As shown in the previous section, to make an oscillator is just a matter of starting a stack of many coupled Josephson junctions out in the in-phase mode and harvest the emitted radiation. It sound very easy, but there is at least one obstacle for doing this. When fluxons are somehow induced in the junctions in an experimental setup, the fluxons are likely to be induced at different times in different junction such that they do not initially move in an in-phase configuration. Thus, some way to bring them into in-phase motion is needed.

In this section, the case of two coupled junction will be considered to show how one may bring the shuttling fluxons from an anti-phase configuration into an in-phase configuration. To help a bit on the analytical calculations, it is a good idea to re-normalize space in Eqs. (3.34) and (3.35) by letting $x \to (1-S^2)^{-1/2}x$ giving

$$\phi_{xx} - \phi_{tt} - \sin\phi - S\psi_{xx} = \alpha\phi_t - \gamma \ , \tag{4.3}$$

$$\psi_{xx} - \psi_{tt} - \sin\psi - S\phi_{xx} = \alpha\psi_t - \gamma \ , \tag{4.4}$$

where $\phi \equiv \phi^1$ and $\psi \equiv \phi^2$. These equations are simpler to work with analytically, and since they only corresponds to a change of the length-scale they are completely equivalent to Eqs. (3.34) and (3.35). Also, notice that the old and the new length-scales are equal up to first order in S.

The energy of the in-phase and anti-phase bunched fluxon solutions may be calculated from the Hamiltonian,

$$H = \int_0^L dx \left(\frac{1}{2}(\phi_x)^2 + \frac{1}{2}(\phi_t)^2 + 1 - \cos\phi + \frac{1}{2}(\psi_x)^2 + \frac{1}{2}(\psi_t)^2 + 1 - \cos\psi - S\phi_x\psi_x \right) ,$$

for the two junction stack. Straight forward insertion of Eq. (3.39) gives[62]

$$H^\sigma = \frac{16c_\sigma}{\sqrt{1-v^2/c_\sigma^2}} \ , \tag{4.5}$$

if the integration is extended to go from $-\infty$ to ∞ and $\sigma = \pm 1$. H^+ is the energy of the bunched in-phase solution and H^- is the energy of the bunched anti-phase solution. Note, with the new normalization of space the characteristic velocities are given by $c_\sigma = c_\pm = c_{\pm 1} = \sqrt{1 \mp S}$. It is worth considering how these two energies compares to the energy of a solution with one fluxon (or anti-fluxon) in each junction separated by some distance, r, each traveling with a velocity v. This situation may be approximated well by the phases

$$\phi = 4\sigma_\phi \tan^{-1} \exp\left(\frac{1}{c_\sigma} \frac{x - vt - r/2}{\sqrt{1-v^2/c_\sigma^2}} \right) \ , \tag{4.6}$$

$$\psi \quad = \quad 4\sigma_\psi \tan^{-1} \exp\left(\frac{1}{c_\sigma}\frac{x - vt + r/2}{\sqrt{1 - v^2/c_\sigma^2}}\right) \ , \tag{4.7}$$

if the coupling S is small, $\sigma_\phi = \pm 1$, $\sigma_\psi = \pm 1$, and $\sigma = \sigma_\phi \sigma_\psi$. Insertion into Eq. (4.5) gives[57]

$$H^\sigma(r) = \frac{8(1 + c_\sigma^2)}{\sqrt{c_\sigma^2 - v^2}} - \frac{8S\sigma_\phi\sigma_\psi r}{(c_\sigma^2 - v^2)\sinh\left(r/\sqrt{c_\sigma^2 - v^2}\right)} \ . \tag{4.8}$$

A plot of the different energies can be seen in Fig. 4.5 for $S = -0.2$. For the anti-phase solution ($\sigma = -\sigma_\phi = \sigma_\psi = -1$) the energy for the bunched state, Eq. (4.5), is seen to be lowest and the energy is rising if r is increased in Eq. (4.8) for $\sigma = -1$. For the in-phase solution, the opposite is true. The bunched state ($\sigma = \sigma_\phi = \sigma_\psi = 1$) has the highest energy, and the energy is decreasing if the distance is increased in Eq. (4.8) for $\sigma = 1$. This means that the bunched in-phase state is energetically unfavorable while the bunched anti-phase is energetically favorable over an unbunched state with equal polarity[62] and that the interaction between two fluxons of equal polarity is repulsive[57]. Due to this, it might seem strange that the bunched in-phase state was observed numerically in Fig. 3.6, but Grønbech-Jensen et. al. have found, by linear stability analysis, the bunched in-phase state to be stable if $|v| > c_-$ and unstable otherwise[62]. The stability of the energetically unfavorable mode is due to Cherenkov radiation from the incommensurate characteristic velocities, $c_\pm$.

Despite the existence and stability of the energetically unfavorable bunched in-phase fluxon mode it is not clear how to experimentally obtain such state, due to the repulsive nature of the interaction between equal polarity fluxons. It is thus highly unlikely that an experimental situation, which is usually initiated at low fluxon velocity, will spontaneously result in formation of a bunched fluxon state. In fact, while several other types of excitations have been shown to exhibit both branches of in-phase and out-of-phase modes[63, 71], direct observations of the bunched, repulsive fluxon mode are not easily made.

In the following it is investigated how the energetically unfavorable in-phase bunched fluxon mode can be obtained by experimentally controllable parameters. A recipe is demonstrated by which the bunched fluxon state is produced starting from an initial energetically favorable unbunched mode of two mutually repulsive fluxons, and explicit expressions for experimental parameters are developed, such that this may happen in weakly coupled systems. The method is to apply an oscillating magnetic field through the edges of two coupled junctions. Such a microwave field can phase-lock a shuttling fluxon[72, 73], and may therefore provide an effective force between the fluxons and the microwave phase that can overcome the repulsive force between the fluxons of the different junctions.

To model an external microwave field, the boundary conditions

$$\phi_x(0) = \psi_x(0) = \phi_x(L) = \psi_x(L) = \Gamma \sin(\Omega t) \ , \tag{4.9}$$

are used together with Eqs. (4.3) and (4.4) for the junctions. The boundary conditions model a microwave field with amplitude Γ and frequency Ω, both in normalized units.

Since the interest is in single fluxon modes and their interaction with an external magnetic field acting through the junction boundaries, solutions generalizing Eq. (2.98) to two coupled junctions are considered. The solutions[74]

$$\phi_\sigma \quad = \quad 4\sigma_\phi \tan^{-1}\left(\frac{c_\sigma}{v}\frac{\sinh\left(\frac{t-\tau_1}{\sqrt{1-\sigma S}}v\gamma(v/c_\sigma)\right)}{\cosh\left(\frac{x}{\sqrt{1-\sigma S}}\gamma(v/c_\sigma)\right)}\right) \ , \tag{4.10}$$

$$\psi_\sigma \quad = \quad 4\sigma_\psi \tan^{-1}\left(\frac{c_\sigma}{v}\frac{\sinh\left(\frac{t-\tau_2}{\sqrt{1-\sigma S}}v\gamma(v/c_\sigma)\right)}{\cosh\left(\frac{x}{\sqrt{1-\sigma S}}\gamma(v/c_\sigma)\right)}\right) \ , \tag{4.11}$$

to the semi-infinite ($L \to \infty$) system describe two single fluxons moving with the asymptotic velocity v and distance $r = v\,(\tau_2 - \tau_1)$, where τ_1 and τ_2 are the collision times for the fluxons of ϕ and ψ system, respectively. The Lorentz factor is

$$\gamma(v) \quad = \quad \frac{1}{\sqrt{1 - v^2}} \ . \tag{4.12}$$

These functions, Eqs. (4.10) and (4.11), are exact solutions to the l.h.s. of Eqs. (4.3) and (4.4) for $L \to \infty$, $\tau_1 = \tau_2$, and $\Gamma = 0$ when $\phi = \sigma\psi$ and $\sigma = \sigma_\phi\sigma_\psi$. Inserting the above ansatz into the expression for the total energy clearly reveals that the $\sigma = \sigma_\phi\sigma_\psi = 1$ solution is energetically unstable and that $\sigma = \sigma_\phi\sigma_\psi = -1$ provides a stable state for $\tau_1 = \tau_2$, like it was shown above for the case of the single-fluxon solutions in Eqs. (4.6) and (4.7).

The ansatz for the perturbed problem will be adopted, such that the solutions for $\sigma = -1$ is used for all cases where $\phi \neq \psi$; thus, $\sigma_\phi\sigma_\psi = 1$ will generally be assumed regardless of σ. Since the objective of the present section is to investigate if phase-locking to an external magnetic field can force $\tau_1 = \tau_2$, the phase-locking properties of the system will first be explored by adapting the wave profiles of Eqs. (4.10) and (4.11) to the phase-locking analysis found in Ref. [73].

Phase-locking requires two conditions to be fulfilled. The first is that a fluxon must travel one half period through the junction in the time it takes for the external ac magnetic field to complete a quarter period (or any integer, N, multiples thereof). Defining the fluxon positions to be at $\phi = \pi$ and $\psi = \pi$, the condition becomes[73]

$$\frac{c_\sigma}{v}\sinh\left(\frac{\pi N v\gamma(v/c_\sigma)}{2\Omega\sqrt{1-\sigma S}}\right) = \cosh\left(\frac{L\gamma(v/c_\sigma)}{2\sqrt{1-\sigma S}}\right) \ , \tag{4.13}$$

from which the asymptotic velocity, v, can be determined for a given set of parameters. The other condition is that the net flux of energy into the system must be zero when averaged over one period of steady state motion; i.e.

$$\Delta H = \int_{t_0-\frac{\pi N}{2\Omega}}^{t_0+\frac{\pi N}{2\Omega}} \dot{H}dt = 0 \ , \tag{4.14}$$

where the rate of change in energy, $\dot{H}$, is given by Eq. (3.68), yielding

$$\frac{dH}{dt} \quad = \quad -\alpha\int\left(\phi_t^2+\psi_t^2\right)dx + \gamma\int\left(\phi_t+\psi_t\right)dx + (1-S)\Big[\phi_t+\psi_t\Big]_0^L\Gamma\sin(\Omega t) \ , \tag{4.15}$$

for the new spatial normalization. The spatial integration is understood to be over the system size. However, because the ansatz (4.10) and (4.11) are used, which is a solution to the semi-infinite system ($L \to \infty$), the spatial integrations will for mathematical convenience be completed for the semi-infinite system when developing analytical results. The consequence of this slight inconsistency is minor since the fluxon position is considered to be located only in the interval $[0, L/2]$.

Inserting the ansatz (4.10) and (4.11) into Eq. (4.14) gives

$$\Delta H = -\alpha\int\int_{t_0-\frac{\pi N}{2\Omega}}^{t_0+\frac{\pi N}{2\Omega}}\left(\phi_t^2+\psi_t^2\right)dtdx + \gamma I - \Delta H_b \ , \tag{4.16}$$

where the first term on the right hand side represents energy losses due to normal electron tunneling, the second term represents the energy absorption from the bias current, I being given implicit by

$$\sinh\left(\frac{I\gamma(v/c_\sigma)}{8\pi\sqrt{1-\sigma S}}\right) = \frac{c_\sigma}{v}\sinh\left(\frac{\pi N v\gamma(v/c_\sigma)}{2\Omega\sqrt{1-\sigma S}}\right) \ , \tag{4.17}$$

and the third term is the energy exchange with the external magnetic field,

$$\Delta H_B \quad = \quad 2\kappa\Gamma\sin(\Omega\tau_0)\cos(\Omega\frac{\delta\tau}{2}) \ , \tag{4.18}$$

where $\tau_0 = \frac{1}{2}(\tau_1+\tau_2)$, $\delta\tau = \tau_2 - \tau_1$, and

$$\kappa \quad = \quad 4\pi(1-S)\frac{\cosh\left(\frac{\Omega\sqrt{1-\sigma S}}{2v\gamma(v/c_\sigma)}\cos^{-1}\left(2\frac{v^2}{c_\sigma^2}-1\right)\right)}{\cosh\left(\frac{\pi\Omega\sqrt{1-\sigma S}}{2v\gamma(v/c_\sigma)}\right)} \ . \tag{4.19}$$

For a given asymptotic distance, $r = v\delta\tau$, between the fluxons, the condition for phase-locking is therefore represented by

$$\gamma - \gamma_0 = 2\Gamma\frac{\kappa}{I}\sin(\Omega\tau_0)\cos(\Omega\frac{\delta\tau}{2}) \ , \tag{4.20}$$

with $\gamma = \gamma_0$ for $\Gamma = 0$ and the fluxons can be phase-locked if the bias γ is in the current range

$$\gamma_0 - \frac{1}{2}\Delta\gamma \;\leq\; \gamma \;\leq\; \gamma_0 + \frac{1}{2}\Delta\gamma \;, \tag{4.21}$$

$$\Delta\gamma \;=\; 4\Gamma\frac{\kappa\cos(\Omega\frac{\delta\tau}{2})}{I} \;, \tag{4.22}$$

$$\gamma_0 \;=\; \frac{\alpha}{I}\int\int_0^{\pi N/\Omega}\left(\phi_t^2+\psi_t^2\right)dtdx \;. \tag{4.23}$$

In order to investigate if the phase-locked state will collapse into a bunched, $r = \delta\tau = 0$, state, the force

$$\begin{aligned} F &= -\frac{\Omega}{N\pi}\int_0^{N\pi/\Omega}\frac{\partial H}{\partial r}dt \\ &= -\frac{\Omega}{N\pi}\left(\Omega\kappa\Gamma\sin(\Omega\tau_0)\sin(\frac{\Omega r}{2v})+\int_0^{N\pi/\Omega}\frac{\partial H_I}{\partial r}dt\right) \end{aligned} \tag{4.24}$$

must be evaluated for $\sigma = -1$ and with $H_I \equiv -S\int\phi_x\psi_x dx$. F is an expression of the effective force between the two fluxons, the first term representing the synchronizing force from the ac magnetic field and the second term representing the inductive coupling induced fluxon-fluxon force. Steady state dynamics must imply that $F = 0$ for a given steady state distance, r, between the fluxons. While $H_I(r,t)$ can be evaluated analytically with the ansatz (4.10) and (4.11) for $L \to \infty$, the expression (not shown) is rather cumbersome and not suitable for explicit temporal integration. However, the simple traveling wave solution in Eqs. (4.6) and (4.7), which is valid when the fluxons are far from the boundaries, yields the last term in Eq. (4.8) as the interaction energy. This is a constant of motion and easily differentiated with respect to r. Notice that this expression is used as a repulsive interaction ($\sigma_\phi\sigma_\psi = 1$) regardless of the value of $\sigma = \pm 1$. Assuming that the boundary effect is small, i.e., that the time during which both fluxons interact with the boundary is small compared to the total time of a half-period of motion, $\int H_I dt \approx \int H_I^\infty dt$ will be used with H_I^∞ being the interaction energy given by the second term in Eq. (4.8). The transition, $F = 0$, is then given by

$$\kappa\Gamma\cos(\Omega\tau_0)\sin\left(\Omega\frac{r}{2v}\right) = \frac{8S\sigma_\phi\sigma_\psi\pi v\gamma^2(v/c_\sigma)}{\Omega(\sqrt{1-\sigma S})\sinh\left(\frac{\gamma(v/c_\sigma)r}{\sqrt{1-\sigma S}}\right)}\left(1-\frac{\gamma(v/c_\sigma)\,r\cosh(\frac{\gamma(v/c_\sigma)r}{\sqrt{1-\sigma S}})}{\sqrt{1-\sigma S}\sinh(\frac{\gamma(v/c_\sigma)r}{\sqrt{1-\sigma S}})}\right) \;. \tag{4.25}$$

The maximum value of $\Gamma\cos(\tau_0\Omega)$, necessary to ensure $r \to 0$, is found for $r = 0$ (for $\sigma = -1$). Notice, however, that the largest force between two traveling fluxons is not at $r = 0$, but at[57]

$$r_0 \;\approx\; 1.606\frac{\sqrt{1-\sigma S}}{\gamma(v/c_\sigma)} \;. \tag{4.26}$$

For $|r| \ll 1$ Eq. (4.25) gives

$$\frac{1}{6}\frac{\gamma^2(v/c_\sigma)\,r^2}{1-\sigma S} = \frac{-S\sigma_\phi\sigma_\psi 16\pi\gamma^3(v/c_\sigma)\,v^2}{3(1-\sigma S)\Gamma\cos(\tau_0\Omega)\kappa\Omega^2} - 1 \;, \tag{4.27}$$

and for $r = 0$ the critical value, Γ_c, of the amplitude of the ac magnetic field beyond which two phase-locked, mutually repulsive fluxons will collapse into a bunched state is obtained as

$$\Gamma_c = -\frac{16S\sigma_\phi\sigma_\psi\pi v^2\gamma^3(v/c_\sigma)}{3\kappa(1-\sigma S)\Omega^2\cos(\Omega\tau_0)} \;. \tag{4.28}$$

This result shows that the ac magnetic field induced bunching of fluxons is most effective at the center of a phase-locked step in the current-voltage characteristics, i.e. for $\gamma \approx \gamma_0$ since $\tau_0 = 0$. The focus will therefore be on this case when conducting numerical simulations.

One more condition must be satisfied for inducing bunching through phase-locking; namely that the resulting bunched state fulfills the phase-locking conditions for $\sigma = 1$ with the parameters used to phase-lock and collapse the $\sigma = -1$ fluxons. This can be investigated directly by inserting $\sigma = 1$ and

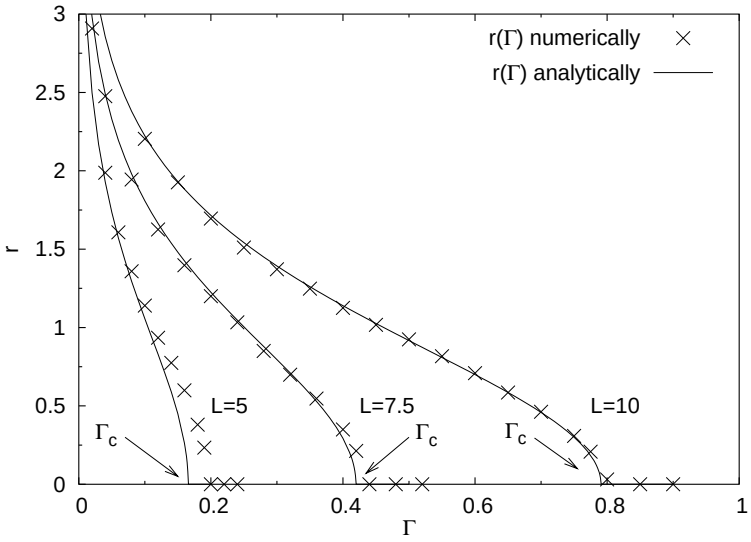

Figure 4.6: Distance, r, between two phase-locked fluxons as a function of magnetic field amplitude, Γ. Continuous curves are obtained from Eq. (4.25) and markers represent the corresponding results of numerical simulations. Parameters are: $\alpha = 0.1$, $\gamma \approx \gamma_0^{(\sigma=-1)}$, $\Omega = 2.5/L$, and $S = -0.015$.

$\delta\tau = 0$ into Eqs. (4.21)-(4.23) and determine the threshold value Γ_b of the magnetic field for which the applied bias current γ is in the phase locking range given by

$$\gamma_0^{(\sigma=1)} - \frac{1}{2}\Delta\gamma^{(\sigma=1)} \;\leq\; \gamma \;\leq\; \gamma_0^{(\sigma=1)} + \frac{1}{2}\Delta\gamma^{(\sigma=1)} \; . \tag{4.29}$$

Thus, magnetic field induced bunching requires that $\Gamma \geq \Gamma_c$ *and* $\Gamma \geq \Gamma_b$. It has been found that for most relevant cases $\Gamma \geq \Gamma_c$ results in $\Gamma \geq \Gamma_b$. Only for relatively high values of the damping parameter, α, have the condition in Eq. (4.29) been observed to be unfulfilled.

4.2.1 Numerical Simulations

In order to verify the perturbation results above, direct numerical simulations of the coupled partial differential equations (4.3) and (4.4) have been conducted. All simulations have been conducted with initial conditions describing fluxons of the two different systems moving in anti-phase. Transient evolution of > 100 periods of motion is conducted before the relative position between the fluxons is determined. The study have been limited to $\gamma \approx \gamma_0^{(\sigma=-1)}$, since the anticipated effect is most profound in the center of the phase-locked step.

Fig. 4.6 shows the steady state distance between two fluxons of different junctions, both phase-locked to a magnetic field with frequency $\Omega = 2.5/L$, as a function of the magnetic field amplitude Γ. Other parameters are: $\alpha = 0.1$, $\gamma \approx \gamma_0^{(\sigma=-1)}$, and $S = -0.015$. Solid curves represent the perturbation result Eq. (4.25) ($\sigma = -1$), where κ is given by Eq. (4.19), $\tau_0 \approx 0$, and v is given by Eq. (4.13). Markers are the results of numerical simulations, where $r = v\delta\tau$ is determined from numerically measuring $\delta\tau$ and evaluating the asymptotic velocity from Eq. (4.13). The figure clearly shows how the steady-state distance between the fluxons decreases monotonically with increasing magnetic field amplitude until a bunched state ($r = 0$) is obtained at $\Gamma = \Gamma_c$, where after the state remains bunched. It is clear from the figure that the agreement between the simple perturbation treatment and the simulations results is very good for all three system lengths. It is also noticeable that the agreement is best for the longer junction. This is in agreement with the assumptions made in the analytical treatment. One assumption is that the ansatz Eqs. (4.10) and (4.11) represent a half period of motion during a reflection at a boundary. Another is that the mutual repulsion between the fluxons due to the inductive coupling can be well described without the boundary effects. Both these assumptions are poor for a very short system (small L). Nevertheless, very convincing agreement between perturbation results and direct numerical simulations are shown in this figure.

The value of the magnetic field amplitude Γ_c, for which the mutual fluxon distance r becomes zero, was studied in detail and the results shown in Fig. 4.7. Here, the two upper continuous curves show

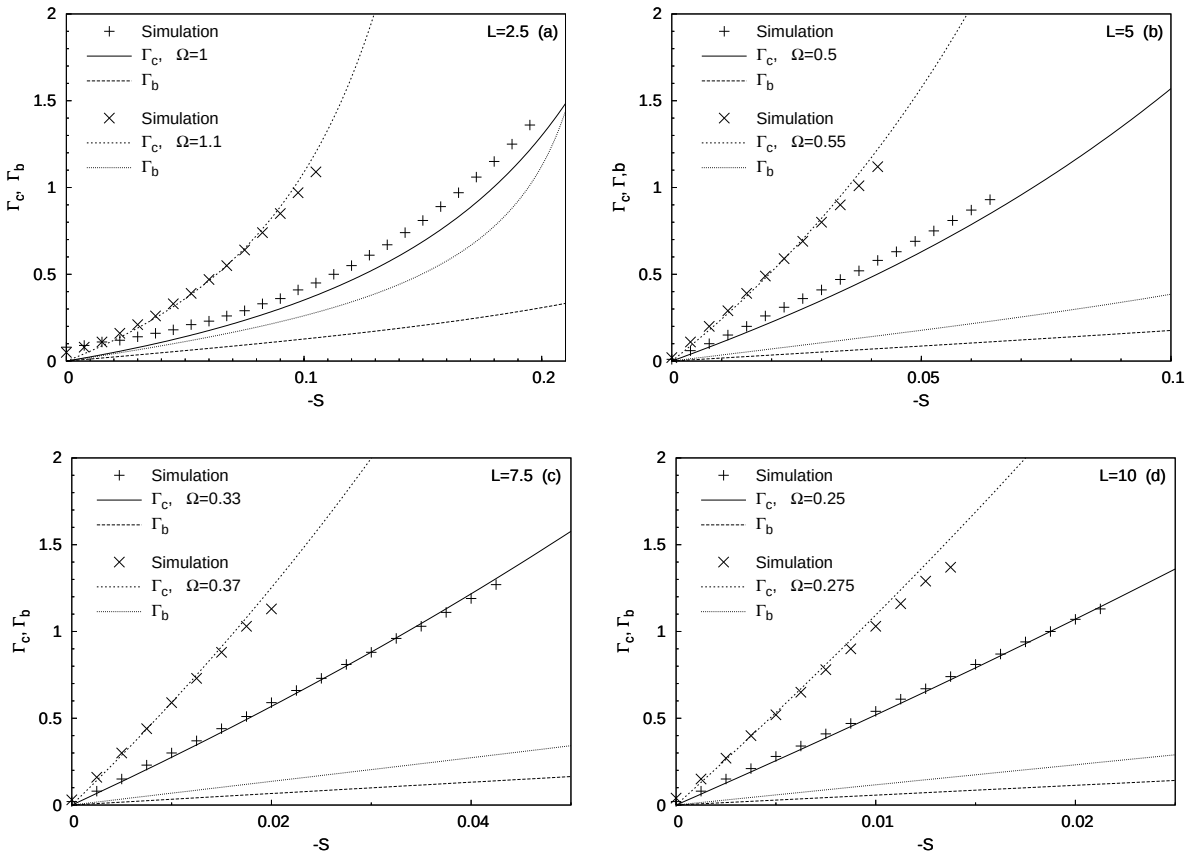

Figure 4.7: Critical magnetic field amplitude, Γ_c, for which phase-locked, mutually repulsive fluxons are forced to bunch. Continuous curves represent the perturbation result Eq. (4.28) for two different applied microwave frequencies (upper curves), and two lower curves represent the magnetic field amplitude Γ_b, necessary for phase-locking the resulting bunched $\sigma = 1$ state (see Eq. (4.29)). Markers represent the results of corresponding numerical simulations. Parameters are: $\alpha = 0.1$ and $\gamma \approx \gamma_0^{(\sigma=-1)}$.

the critical field amplitude Γ_c as given by Eq. (4.28), for two different values of applied frequency, as a function of the inductive coupling constant S. The two lower continuous curves represent the critical value Γ_b necessary for sustaining phase-locking of the bunched state ($\sigma = 1$). All results are obtained for $\alpha = 0.1$, and the four plots show four different system lengths, $L = 2.5$, 5, 7.5, and 10. Markers indicate the results of numerical simulations. As in Fig. 4.6, very consistent and good agreement between the analytical results of the perturbation method and the direct numerical simulations over a wide range of parameters are found. And again, the shorter systems are generally showing less good agreement than the longer systems. It is also seen that the lower frequencies (lower velocities) seem to produce larger discrepancies than higher driving frequencies do. This feature is again linked to the approximation regarding the repulsive inductive coupling, since a slow fluxon will experience a relatively longer contact time with the boundary during reflection than a fast fluxon will. This contact time is completely neglected in the expressions leading to the continuous curves displayed in Figs. 4.6 and 4.7. However, the consistent discrepancies observed in Fig. 4.7, for $L = 2.5$ and $L = 5$ (slow modes), are more likely due to a poor determination of $\gamma_0^{(\sigma=-1)}$. If the anticipated center of the phase-locked step is not well determined, then $\tau_0 \neq 0$ and all critical magnetic field amplitudes should be multiplied with $(\cos \Omega\tau_0)^{-1}$. Such a correction is consistent with the observed discrepancies in Figs. 4.7a and 4.7b. Notice, that in spite of these observed discrepancies, the observed agreement is consistently good, and the perturbation results seem to have predictive capabilities. Also, since the two lower continuous curves on each of the four plots of Fig. 4.7 are well below the corresponding upper two curves, a bunched and phase-locked $\sigma = 1$ states have indeed been produced since $\Gamma_c > \Gamma_b$ for all displayed cases.

The method presented here should be readily applicable in an experimental setup, but one would, of course, like to have the fluxons bunched after the microwave-signal has been turned off. The repulsive force is increasing with the velocity of the fluxons, which is why the velocity (and, thus, frequency) must

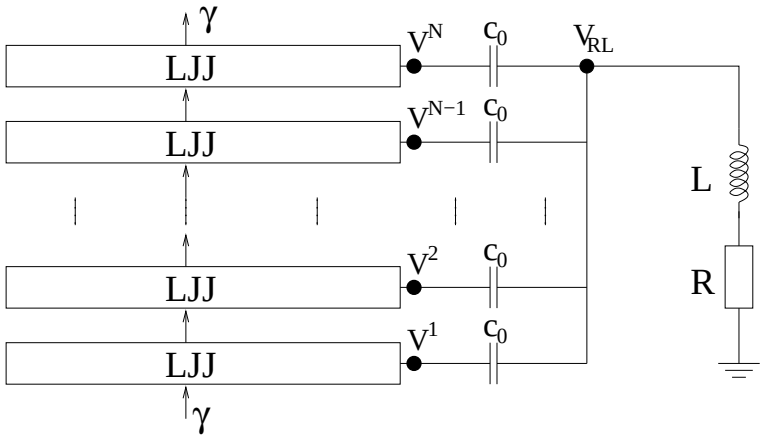

Figure 4.8: Model-system of a long Josephson junction coupled to a cavity. The cavity is modeled by a RLC circuit, R being a resistor, L an inductor, and c_0 a capacitor. The current in the cavity enters the long Josephson junctions through the boundaries.

be kept relatively small in order to overcome the repulsion for not too large Γ and realistic junction coupling, S. From Fig. 4.7 it is seen that for $\Gamma \gtrapprox 1$, the numerical data stops, because the fluxons are destroyed by the microwaves. Unfortunately, without microwaves the bunched state is only stable above c_{-1}[62], so all the solutions seen numerically may decay to the non-bunched state when the microwaves are turned off; or they will accelerate to their $c_{-1} < v < c_{+1}$ bunched steady state. Thus, to ensure a stable bunched state after microwaves are turned off (after the "slow" bunched state has been obtained with microwaves) one may increase the frequency of the microwaves slowly while keeping the system in the locking range given by Eq. (4.29) until the velocity is above c_{-1}. Then, the bunched mode will be stable and the microwaves can be turned off. Numerically, the same effect can be accomplished by simultaneously turning off the microwaves and increasing the bias current.

4.3 Coupling to a Cavity

The method of applying microwaves to the edge of the Josephson junction stack in the previous section is a little artificial. The main goal is to use the junctions to generate microwaves, so it is not of practical interest to apply microwaves to the stack to obtain the bunched fluxon state. The interest in the method is theoretical but it would also be interesting to observe the bunched state in the laboratory and the method provides a way of doing this. There is, however, the possibility to make a self-contained system which itself generates the microwaves needed to obtain the bunched state. Such a system would be of major interest to applications. If one edge of the long Josephson junction stack is inserted into a cavity, it will radiate into the cavity which then reflects the radiation back to the stack, acting as the external microwave source. The other end of the stack can then radiate into free space.

To really understand the Josephson junction-cavity system, one should solve Maxwell's equations in some dielectric outside the junctions and solve the Josephson-equations inside the junction. The electric and magnetic fields should then be matched at the boundaries. Calculations of this sort (but not with the same physics in mind) have been done by Tachiki et. al. in Ref. [75] and involves huge numerical computations on the Earth Simulator in Japan, having 5120 processors and ranked as the 7th fastest computer in the world as of November 2005[76]. Here, a simpler model will be used[1], which should show many of the essential features of the system. The model is shown in Fig. 4.8. The junctions in the stack are coupled to a RLC circuit through one of the stack-boundaries. R is a resistance, L is an inductance, and c_0 is a capacitance. Similar models have been studied in Ref. [77], but also short Josephson junction arrays coupled to a cavity have been studied in Ref. [78].

A Josephson junction stack with an in-line geometry has different boundary conditions than the overlap geometry considered in this thesis. The in-line geometry as well as the overlap geometry was considered in Ref. [47]. The boundary conditions for the in-line case are change by the current fed through the boundaries, such that $\phi^i_x(0,t) = -\eta$ and $\phi^i_x(L,t) = \eta$ where η is the normalized current

[1]The calculations for this thesis were made primarily on a dual 2.8GHz Xeon system, thus a much simpler model *must* be used.

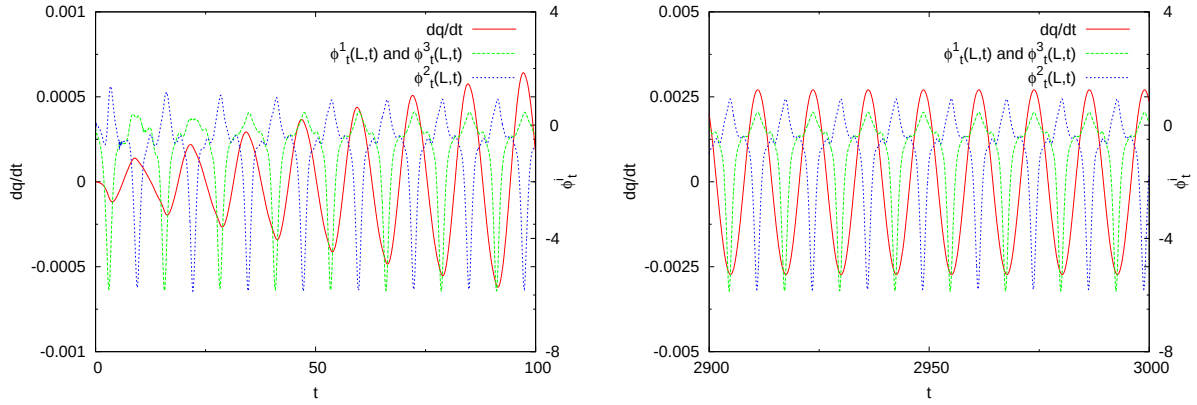

Figure 4.9: Numerical solution to Eqs. (3.20)-(3.22), (4.34), and (4.35) for $L = 5$, $\alpha = 0.1$, $\gamma = -0.208$, $Q = 100$, $c = 0.0001$, and $\Omega = 0.5$ for a three junction stack operated in the anti-phase mode. Left plot shows the beginning of the simulation where the fluxon pulses pumps up the cavity current and the right plot is at later times when the cavity current has stabilized because losses in the cavity has become equal to the gain due to fluxon pulses.

injected through the boundary at $x = 0$ and taken out at $x = L$. To connect the system to the cavity, the current from the cavity-circuit into the junction is therefore modeled by the boundary conditions

$$\phi^i_x(0,t) = 0 \quad \text{and} \quad \phi^i_x(L,t) = \eta^i \ , \tag{4.30}$$

where η^i is the current from junction number i to the cavity through the capacitor c_0. In the model, the voltage over junction i is approximated to $\hbar\phi^i_t/q$. The boundary current can then be calculated from the RLC circuit to

$$\eta^i = -c_0 \left(L\frac{d^3q}{dt^3} + R\frac{d^2q}{dt^2} - \frac{\hbar}{q}\phi^i_{tt}(L) \right) \ , \tag{4.31}$$

where q is the charge in the cavity. By calculating the current through the inductance and the resistor (the cavity current), the cavity equation is obtained to

$$L\frac{d^2q}{dt^2} + R\frac{dq}{dt} + \frac{1}{Nc_0}q = \frac{\hbar}{qN}\sum_{i=i}^{N}\phi^i_t(L,t) \ . \tag{4.32}$$

The equations are normalized by

$$t \to \omega_0^{-1}t \quad , \quad q \to \frac{J^c}{\omega_0}q \quad , \quad \Omega \equiv \frac{\omega_c}{\omega_0} \quad , \quad Q \equiv \frac{\omega_c L}{R} \quad , \quad c \equiv \frac{Nc_0}{c_J} \ , \tag{4.33}$$

where $\omega_c^2 = 1/(NLc_0)$ is the cavity frequency. The normalized equations are then calculated to

$$\phi^i_x(0,t) = 0 \quad , \quad \phi^i_x(L,t) = \frac{\dot{q}}{N} - \frac{c}{N^2}\sum_{k=1}^{N}\left(\phi^k_{tt}(L,t) - \phi^i_{tt}(L,t)\right) \equiv \eta^i \quad , \quad \text{and} \tag{4.34}$$

$$\frac{d^2q}{dt^2} + \frac{\Omega}{Q}\frac{dq}{dt} + \Omega^2 q = \Omega^2\frac{c}{N}\sum_{i=1}^{N}\phi^i_t(L,t) \ , \tag{4.35}$$

which must be solved together with Eqs. (3.20)-(3.22).

Fig. 4.9 shows a numerical solution to Eqs. (3.20)-(3.22), (4.34), and (4.35) for $L = 5$, $\alpha = 0.1$, $\gamma = -0.208$, $Q = 100$, $c = 0.0001$, and $\Omega = 0.5$ for a three junction stack operated in the anti-phase mode. The left plot shows the initial "pumping" of the cavity current, which is changed each time a fluxon hits the boundary. The right plot shows the situation after some time, when the cavity current has stabilized, because the losses due to the resistance have become equal to the gain from the fluxon pulses.

Fig. 4.10 shows a numerical solution for $L = 5$, $N = 3$, $\alpha = 0.05$, $S = -0.1$, $c = 0.0001$, $Q = 100$, and $\Omega = 0.67$ for a three junction stack operated in the in-phase mode after the cavity current has stabilized.

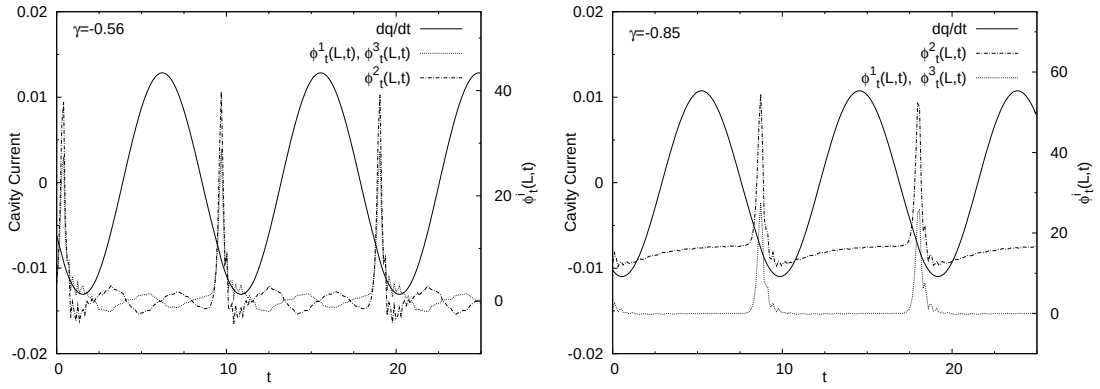

Figure 4.10: Numerical solution with $L = 5$, $N = 3$, $\alpha = 0.05$, $S = -0.1$, $c = 0.0001$, $Q = 100$, and $\Omega = 0.67$ at two values of γ when the stack if operated in the in-phase mode.

The figure shows two different values of the bias γ. The left plot shows the three-fluxon in-phase mode and the right-plot shows a mode where the middle junction has switched to the McCumber curve but contains an in-phase trace from the outer junctions. The amplitude of the cavity current is almost equal in the two cases, which signals that the switched in-phase modes discussed in Section 3.3.2 may also be quite effective in the cavity system.

The cavity system will now be analyzed analytically. A general solution to the linear cavity Eq. (4.35) is easily obtained to

$$\begin{aligned} q = c_1 e^{m_1 t} + c_2 e^{m_2 t} \quad &+ \quad \frac{e^{m_1 t}}{m_1 - m_2} \int e^{-m_1 t} \frac{\Omega^2 c}{N} \sum_{i=1}^{N} \phi_t^i(L,t) dt \\ &- \quad \frac{e^{m_2 t}}{m_1 - m_2} \int e^{-m_2 t} \frac{\Omega^2 c}{N} \sum_{i=1}^{N} \phi_t^i(L,t) dt \ , \end{aligned} \tag{4.36}$$

with $m_1 \equiv -\Omega \left(1 - i\sqrt{4Q^2 - 1}\right)/(2Q)$ and $m_2 \equiv -\Omega \left(1 + i\sqrt{4Q^2 - 1}\right)/(2Q)$. c_1 and c_2 are constants determined by the initial conditions. It will be assumed that $q(0) = \dot{q}(0) = 0$ resulting in $c_1 = c_2 = 0$, corresponding to the situation where the cavity charge is generated only by the Josephson stack.

As seen in the previous section, an oscillating boundary condition may phase-lock the junctions. To, for example, see when this happens, the cavity current must be determined. The general non-linear approach would be to use a kink-antikink collision solution for the Josephson phase in order to model the collision with the boundary. This would make the integrals on the right hand side of Eq. (4.36) a sum of kink-antikink collision profiles. Using this solution, the boundary current, η^i, can be calculated and used as a boundary condition for the coupled sine-Gordon system. The phase-locking and bunching conditions may then, for example, be calculated as in the previous section. This would, however, involve huge analytical computations and one would most likely not be able to evaluate the resulting equations and integrals. The situation is therefore approximated in the following way: The cavity sees the fluxons in the stacked junctions as delta-function profiles and the Josephson stack sees the cavity as a boundary current which is evenly divided by the junctions. The boundary current is thus approximated by

$$\eta^i \quad \approx \quad \frac{1}{N} \frac{dq}{dt} \ , \tag{4.37}$$

and the solution profiles which must be used in Eq. (4.35) are approximated by "periodic" delta functions

$$\phi_t^i(L,t) \approx \sum_{n=0}^{\infty} A^i \delta \left(t - \tau^i - \frac{2\pi n}{\omega^i} \right) \ , \tag{4.38}$$

such that the cavity equation becomes

$$\frac{d^2 q}{dt^2} + \frac{\Omega}{Q} \frac{dq}{dt} + \Omega^2 q = \Omega^2 \frac{c}{N} \sum_{i=1}^{N} \sum_{n=0}^{\infty} A^i \delta \left(t - \tau^i - \frac{2\pi n}{\omega^i} \right) \ , \tag{4.39}$$

instead of Eq. (4.35). This approximates fluxon pulses with frequencies ω^i and times of first collision τ^i arriving at times $\tau^i + 2\pi n/\omega^i$. The amplitudes A^i must be chosen such that the delta-function approximation corresponds to a sine-Gordon fluxon.

The right hand side of Eq. (4.39) is inserted into the solution in Eq. (4.36) and the integration is carried out, giving

$$q = \frac{\Omega^2 c}{N(m_1 - m_1)} \sum_{i=1}^{N} \sum_{n=0}^{\infty} A^i H(t - \tau^i - \frac{2\pi n}{\omega^i}) \left(e^{m_1(t-\tau^i - \frac{2\pi n}{\omega^i})} - e^{m_2(t-\tau^i - \frac{2\pi n}{\omega^i})} \right) \tag{4.40}$$

for $c_1 = c_2 = 0$ with $H(t)$ being the Heaviside step function. Inserting $m_1 = -\Omega \left(1 - i\sqrt{4Q^2 - 1}\right)/(2Q)$ and $m_2 = -\Omega \left(1 + i\sqrt{4Q^2 - 1}\right)/(2Q)$ the cavity current, $\dot{q}$, is then

$$\frac{dq}{dt} = \frac{\Omega^2 c}{N} \sum_{i=1}^{N} \sum_{n=0}^{\infty} A^i H(\tilde{t}^i) e^{-\frac{\Omega}{2Q}\tilde{t}^i} \left(\cos\left(\frac{\Omega}{2Q} \sqrt{4Q^2 - 1}\ \tilde{t}^i \right) - \frac{1}{\sqrt{4Q^2 - 1}} \sin\left(\frac{\Omega}{2Q} \sqrt{4Q^2 - 1}\ \tilde{t}^i \right) \right) , \tag{4.41}$$

where $\tilde{t}^i \equiv t - \tau^i - 2\pi n/\omega^i$ is defined to shorten the expression. A large Q results in $\sqrt{4Q^2 - 1} \approx 2Q$ and $1/\sqrt{4Q^2 - 1} \approx 0$, thus the sin-term in the above equation can be neglected. The result becomes

$$\frac{dq}{dt} = \frac{\Omega^2 c}{N} \sum_{i=1}^{N} A^i \sum_{n=0}^{\infty} H(\tilde{t}^i) e^{-\frac{\Omega}{2Q}\tilde{t}^i} \cos\left(\Omega \tilde{t}^i\right) . \tag{4.42}$$

At a given time, t, the Heaviside functions takes care that only pulses in the past are contributing to the sum. In the limit $t \to \infty$, the Heaviside functions may thus be neglected because all terms contribute to the sum. The sum over n may now be carried out, giving

$$\frac{dq}{dt} = \frac{\Omega^2 c}{N} \sum_{i=1}^{N} A^i \frac{e^{-\frac{\Omega}{2Q}(t-\tau^i)} \left(\cos[(t - \tau^i)\Omega] - e^{\frac{\pi\Omega}{Q\omega^i}} \cos[(t - \tau^i + \frac{2\pi}{\omega^i})\Omega] \right)}{1 + e^{\frac{2\pi\Omega}{Q\omega^i}} - 2e^{\frac{\pi\Omega}{Q\omega^i}} \cos[\frac{2\pi\Omega}{\omega^i}]} , \tag{4.43}$$

valid at large t. An interesting case is when the fluxon pulses are phase-locked to the cavity-frequency, i.e. $\omega^i = \Omega$ for all i. This reduces the above equation to

$$\frac{dq}{dt} = \frac{\Omega^2 c}{N} \sum_{i=1}^{N} A^i \frac{e^{-\frac{\Omega}{2Q}(t-\tau^i)} \cos[(t - \tau^i)\Omega]}{1 - e^{\pi/Q}} . \tag{4.44}$$

Provided that the delta-function approximation of the fluxon pulses is valid, the pulse frequency matches the cavity-frequency and $Q >> 1$, the cavity current is a simple sum of exponentially damped cosine functions, whose initial amplitude in junction number i is $N\epsilon^i$ with

$$\epsilon^i = \frac{\Omega^2 c}{N^2} \frac{A^i}{1 - e^{\pi/Q}} . \tag{4.45}$$

ϵ^i is the amplitude of the boundary current, η^i, for the in-phase mode ($\tau^i = \tau^j$ for $i, j = 1, ..., N$). The amplitude of the boundary current in the anti-phase mode ($\tau^i = \tau^{i+1} - (i \bmod 2)\pi/\Omega$ for $i = 1, ..., N$) is ϵ^i/N if N is odd and ~ 0 if N is even.

The amplitude of the delta-pulses, A^i, must be determined. A^i is here chosen such that a "collision" with the boundary exchanges the same amount of energy as a fluxon would have. The energy-exchange of a fluxon-pulse and an external microwave source was calculated in Section 4.2 for the case of two coupled junctions. Following that calculation, the energy-exchange will be calculated for the case of N weakly coupled junctions. The Hamiltonian of the long Josephson stack is

$$H = \int_0^L \left(\frac{1}{2}(\boldsymbol{\phi}_t)^T \boldsymbol{\phi}_t + N - \left(\sqrt{\cos\boldsymbol{\phi}} \right)^T \sqrt{\cos\boldsymbol{\phi}} + \frac{1}{2}(\boldsymbol{\phi}_x)^T \mathbf{S}^{-1} \boldsymbol{\phi}_x \right) dx , \tag{4.46}$$

where $\boldsymbol{\phi}$ is the vector of size N with the components ϕ^i and $\boldsymbol{\phi}^T$ is the transpose of this vector. $\sqrt{\cos\boldsymbol{\phi}}$ is short for the vector whose N components are $\sqrt{\cos\phi^i}$. The rate of change in energy is then

$$\frac{dH}{dt} = \int_0^L (\boldsymbol{\phi}_t)^T \Big(-\alpha\boldsymbol{\phi}_t + \boldsymbol{\gamma} \Big) dx + \Big[(\boldsymbol{\phi}_t)^T \mathbf{S}^{-1} \boldsymbol{\phi}_x \Big]_0^L , \tag{4.47}$$

where the components of the vector $\boldsymbol{\gamma}$ are all equal to the bias current, γ. The last term gives the energy exchange with the boundary. Integrating this term from $t = -\infty$ to $t = \infty$ (note: $\phi_x(0,t) = 0$) gives

$$\Delta H_b = \int_{-\infty}^{\infty} (\boldsymbol{\phi}_t(L,t))^T \mathbf{S}^{-1} \boldsymbol{\phi}_x(L,t) dt \ . \tag{4.48}$$

For small layer-to-layer coupling strength, S, the inverse of the coupling matrix may be expanded to first order in S, resulting in

$$\mathbf{S}^{-1} \approx \begin{pmatrix} 1 & -S & & & \\ -S & 1 & -S & & \\ & \ddots & \ddots & \ddots & \\ & & -S & 1 & -S \\ & & & -S & 1 \end{pmatrix} , \tag{4.49}$$

and the energy exchange becomes

$$\Delta H_b = \sum_{i=1}^{N} \int_{-\infty}^{\infty} \phi_x^i(L,t) \Big(\phi_t^i(L,t) - S\phi_t^{i-1}(L,t) - S\phi_t^{i+1}(L,t) \Big) dt \ , \tag{4.50}$$

where two dummy-functions has been defined as $\phi^0(x,t) \equiv \phi^{N+1}(x,t) \equiv 0$.

From the simplified boundary condition in Eq. (4.37) and the cavity current, Eq. (4.44), $\phi_x^i(L,t)$ becomes a sum of damped cosines. The case of a high Q cavity is considered, so the exponential damping of the cosines is negligible during the collision with the boundary, yielding

$$\phi_x^i(L,t) \approx \epsilon^i \cos[\Omega(t - \tau^i)] \ . \tag{4.51}$$

For the δ-function approximation, a single collision at time τ^i gives

$$\phi_t^i(L,t) = A^i \delta\left(t - \tau^i\right) \tag{4.52}$$

Inserting this and $\phi_x(L,t)$ from Eq. (4.51) into Eq. (4.50), the energy change for a collision becomes

$$\begin{aligned} \Delta H_b^\delta &= \sum_{i=1}^{N} \int_{-\infty}^{\infty} \epsilon^i \Big(A^i \delta(t - \tau^i) - SA^{i-1}\delta(t - \tau^{i-1}) - SA^{i+1}\delta(t - \tau^{i+1}) \Big) \cos[\Omega(t - \tau^i)] dt \\ &= \sum_{i=1}^{N} \epsilon^i \Big(A^i - SA^{i-1} \cos[\Omega(\tau^i - \tau^{i-1})] - SA^{i+1} \cos[\Omega(\tau^i - \tau^{i+1})] \Big) \ , \end{aligned} \tag{4.53}$$

with $A^0 = A^{N+1} \equiv 0$.

The case of a fluxon colliding with the boundary is now calculated. Such a collision is modeled by a fluxon-antifluxon collision at times τ^i, thus

$$\phi^i(x,t) = 4\sigma^i \tan^{-1} \left(\frac{c_-}{v} \frac{\sinh\left(\frac{v\gamma(v/c_-)}{c_-} \left(t - \tau^i\right) \right)}{\cosh\left(\frac{\gamma(v/c_-)}{c_-} (x - L) \right)} \right) \ , \tag{4.54}$$

where $\gamma(v)$ is given by Eq. (4.12), $\sigma^i = \pm 1$, and c_- is the lowest characteristic velocity, given by $(c_-)^2 \approx 1 + 2S\cos(\pi/(N+1))$ to first order in S. The collision profiles are exact solutions to Eqs. (3.20)-(3.22) with $\alpha = \gamma = 0$ in the cases $N = 1$, $N = 2$, and "$N = \infty$" when $\sigma^i = -\sigma^{i+1}$ for $i = 1, ..., N$. Between these values of N they provide good approximations for small S. They will in the following be used for $\sigma^i = 1$ for all i. Inserting the fluxon profiles into Eq. (4.50) gives

$$\Delta H_b^{Fluxon} = \sum_{i=1}^{N} \int_{-\infty}^{\infty} \epsilon^i \left(f^i(t) - Sf^{i-1}(t) - Sf^{i+1}(t) \right) \cos[\Omega(t - \tau^i)] dt \qquad \text{where} \tag{4.55}$$

$$f^i(t) = \frac{4v^2\gamma(v/c_-)}{(c_-)^2} \frac{\cosh\left(\frac{v\gamma(v/c_-)}{c_-} (t - \tau^i) \right)}{\frac{v^2}{(c_-)^2} + \sinh^2\left(\frac{v\gamma(v/c_-)}{c_-} (t - \tau^i) \right)} \qquad \text{for } i = 1, ..., N \tag{4.56}$$

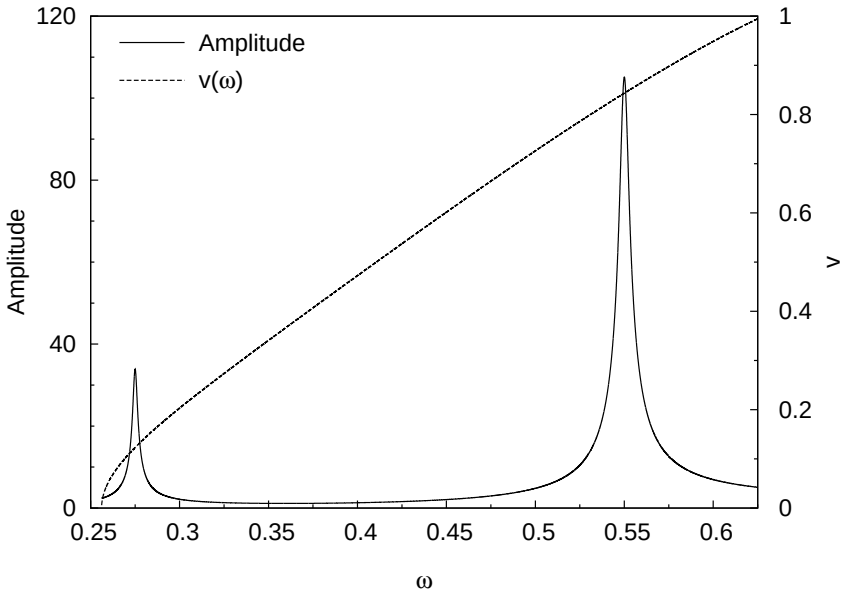

Figure 4.11: Amplitude of the cavity current in Eq. (4.43) with amplitude, A^1, given by Eq. (4.59) for $L = 5$, $\Omega = 0.55$, $Q = 100$, $c = 1$, $\alpha = 0.1$, and $N = 1$. Shown is also the asymptotic velocity from Eq. (4.13) (with $\Omega = \omega$).

and $f^0 = f^{N+1} \equiv 0$. Carrying out the integration, the result becomes

$$\Delta H_b^{Fluxon} = \sum_{i=1}^{N} \zeta \epsilon^i \left(1 - S\cos[\Omega(\tau^i - \tau^{i-1})] - S\cos[\Omega(\tau^i - \tau^{i+1})]\right) \qquad \text{where} \qquad (4.57)$$

$$\zeta = 4\pi \frac{\cosh\left(\frac{c_-}{2v\gamma(v/c_-)}\Omega\cos^{-1}\left(2\frac{v^2}{(c_-)^2} - 1\right)\right)}{\cosh\left(\frac{c_-}{2v\gamma(v/c_-)}\Omega\pi\right)} \,. \qquad (4.58)$$

Equating ΔH_b^{δ} with ΔH_b^{Fluxon}, the amplitudes which give the correct energy-exchange of the δ-function approximation may be found. Unfortunately, there is only one equation for the N unknown amplitudes A^i. However, since the junctions are weakly coupled, it may be assumed that all A^i are equal, $A \equiv A^i$. The single amplitude is then determined to

$$A = \zeta = 4\pi \frac{\cosh\left(\frac{c_-}{2v\gamma(v/c_-)}\Omega\cos^{-1}\left(2\frac{v^2}{(c_-)^2} - 1\right)\right)}{\cosh\left(\frac{c_-}{2v\gamma(v/c_-)}\Omega\pi\right)} \,. \qquad (4.59)$$

The asymptotic velocities of all the fluxons, $v = v^i$, can be determined from Eq. (4.13) with $c_\sigma = c_-$ and $\sigma = 1$.

Fig. 4.11 shows a plot of Eq. (4.43) for a single junction with $t = \tau^1$, amplitude, A^1, given by Eq. (4.59) and v given by Eq. (4.13) with $c_\sigma = c_-$, $\sigma = 1$, and $\omega^1 \equiv \omega$. Two resonances are seen in this plot. One when $\Omega = \omega$ and one when $\Omega = 2\omega$. It is easy to see from Eq. (4.43) that resonances exist when $\Omega = m\omega$ where $m \in \mathbb{N}^+$. Only $m = 1$ and 2 are visible in the figure, since at very low fluxon-frequencies the asymptotic velocity goes to zero and the fluxon can therefore not phase-lock to the cavity frequency. The numerical calculations presented in the following are only for $m = 1$.

Shown in Fig. 4.12 is a comparison of Eq. (4.43) with a full numerical simulation of the system in Eqs. (3.20)-(3.22) with boundary conditions given by Eqs. (4.34) and (4.35) for $N = 1$, $\alpha = 0.1$, $c = 0.0001$, $Q = 100$, and $\Omega = 0.5,\ 0.55$, and 0.6. The numerical data is generated by scanning a range of the bias current, resulting in different fluxon frequencies, $\omega^1 \equiv \omega$. The simulation is allowed to run for a fixed time, large enough to potentially stabilizing the cavity current. The power spectrum of the voltage at $x = L$, $\phi_t^i(L,t)$, is then calculated and the dominant frequency is used as the fluxon frequency ω. The maximum value of the cavity current obtained near the end of the simulation is then plotted as a function of ω. To find the theoretical curve, Eq. (4.43) is solved numerically for to find its maximum

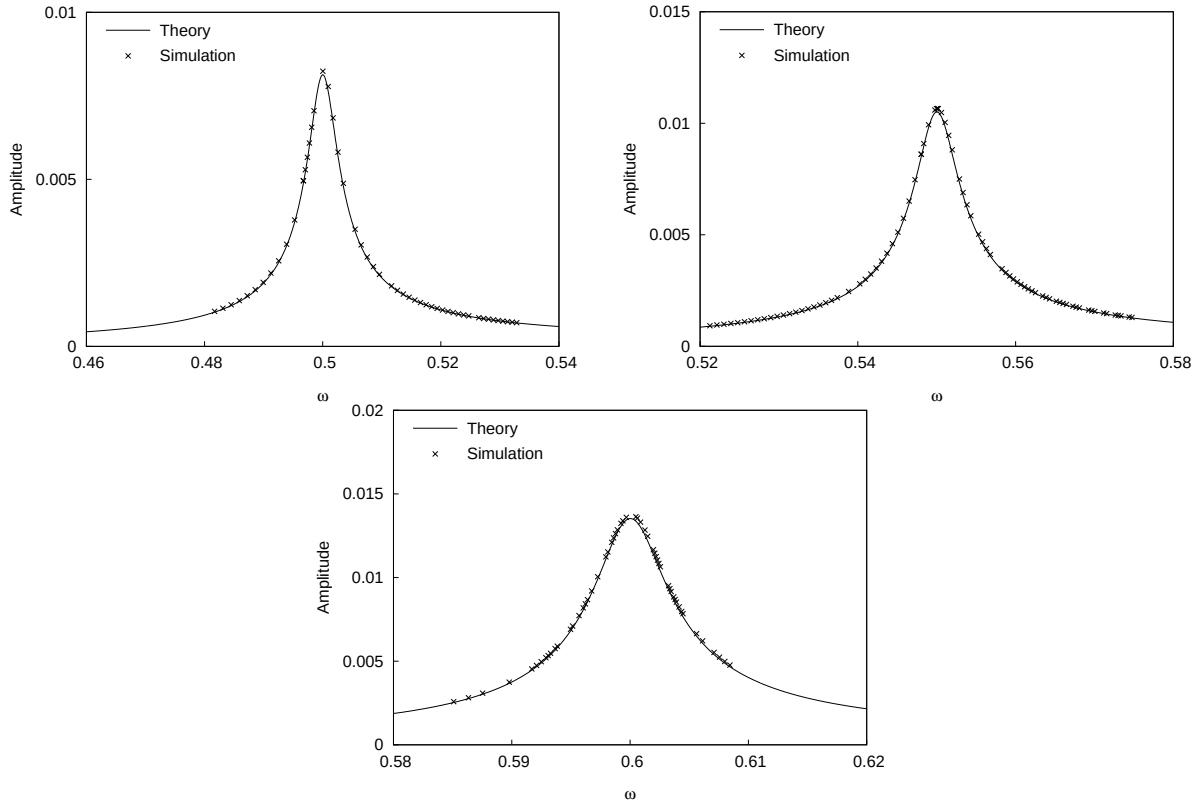

Figure 4.12: Comparison of Eq. (4.43) (line) with a full numerical simulation (markers) of the system in Eqs. (3.20)-(3.22) with boundary conditions given by Eqs. (4.34) and (4.35) for $L = 5$, $N = 1$, $\alpha = 0.1$, $c = 0.0001$, $Q = 100$, and $\Omega = 0.5$ (top left), 0.55 (top right), and 0.6 (bottom).

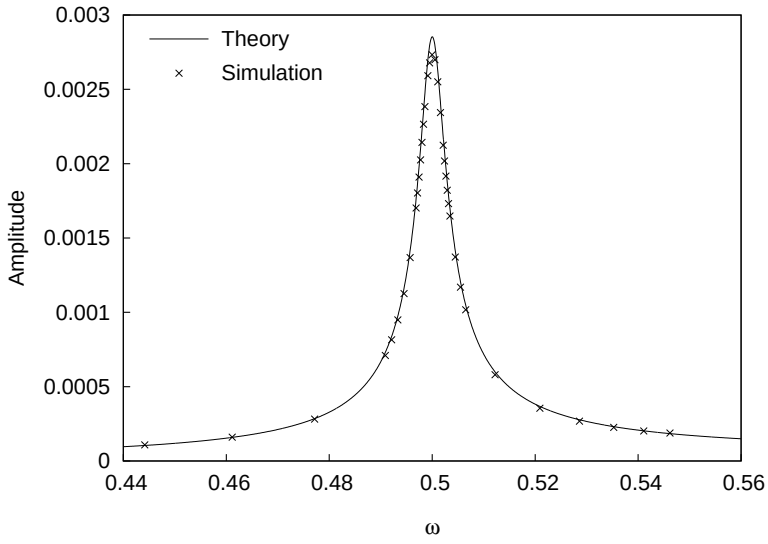

Figure 4.13: Comparison of Eq. (4.43) (line) with a full numerical simulation (markers) of the system in Eqs. (3.20)-(3.22) with boundary conditions given by Eqs. (4.34) and (4.35) for $L = 5$, $N = 3$, $\alpha = 0.1$, $S = -0.1$, $c = 0.0001$, $Q = 100$, and $\Omega = 0.5$ when the fluxons are moving in the anti-phase mode.

value, which is plotted as a function of ω. The agreement is seen to be extremely good. The amount of coupling to the cavity, c, has been chosen to be small such that the fluxons does not phase-lock to the cavity current, allowing for an easier change of fluxon frequency, ω.

For three junctions Fig. 4.13 shows another comparison between Eq. (4.43) and a numerical simulation. The three fluxons are moving in the anti-phase configuration shown in the top of Fig. 3.10.

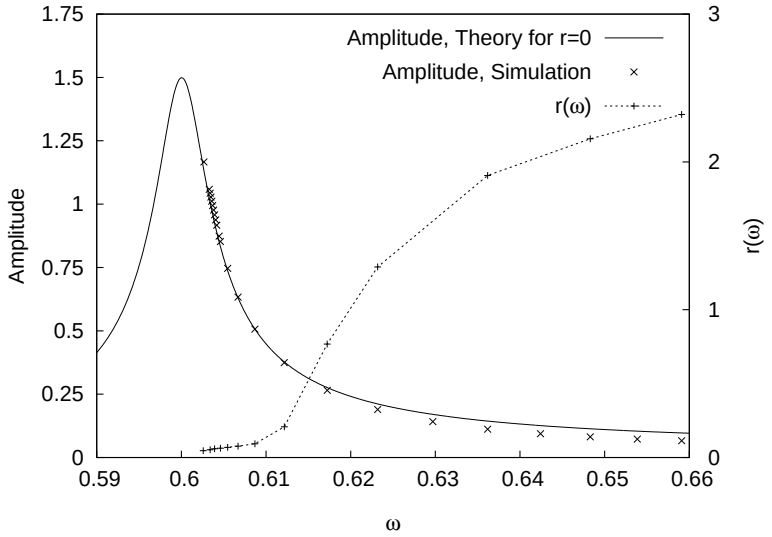

Figure 4.14: Numerical solution with $L = 4$, $N = 3$, $\alpha = 0.1$, $S = -0.005$, $c = 0.015$, $Q = 100$, and $\Omega = 0.6$. The cavity current becomes large enough to overcome the fluxon-fluxon repulsion. The theoretical curve is made by assuming $r = 0$, resulting in the discrepancies for $\omega > 0.62$. The calculation did not succeed in obtaining $\omega = 0.6$.

Parameters for the numerical simulation are $L = 5$, $N = 3$, $\alpha = 0.1$, $S = -0.1$, $c = 0.0001$, $Q = 100$, and $\Omega = 0.5$. To model the anti-phase motion, $\tau^1 = \tau^3 = 0$ and $\tau^2 = \pi/\Omega$ were chosen in Eq. (4.43). This makes the maximum height of the resonance 1/3 of the amplitude it would have been for the in-phase mode ($\tau^1 = \tau^2 = \tau^3$). The agreement between the analytical and numerical results is again very good. The maximum value of the resonance is a little too high. This must be because of the inductive coupling and the assumptions that $|S|$ is small made in the derivation of Eq. (4.43). Another assumptions was, that the amplitudes, A^i, in Eq. (4.53) were all equal which is probably not true, as, for example, the amplitudes of the plasma oscillations are a factor of $\sqrt{2}$ different from the center to the outer junctions, see Fig. 3.3.

The real interest in the cavity system was to make a self-contained fluxon-bunching mechanism. To illustrate that this can be done, Fig. 4.14 shows a calculation with $L = 4$, $N = 3$, $\alpha = 0.1$, $S = -0.005$, $c = 0.015$, $Q = 100$, and $\Omega = 0.6$. Note the large value of c in order to overcome the fluxon-fluxon repulsion. The fluxons are initiated in an anti-phase motion and the bias current is scanned to alter the fluxon frequency. For high fluxon frequency, ω, the cavity current is small and the distance between the center fluxon and the outer fluxons, $r(\omega)$, is large. As the frequency approaches the cavity frequency, $\Omega = 0.6$, the cavity current increases and the fluxon distance decreases. Near $\omega = 0.6$ the fluxons are only separated by a distance of ~ 0.1 from the center fluxon to the outer fluxons and the state can thus be considered to be bunched. The calculation did not succeed in obtaining the center of the resonance, $\omega = 0.6$. The analytical curve in Fig. 4.14 is made after the assumption that the fluxons are in the bunched state, which holds up when $r \approx 0$. This gives the minor discrepancies when $\omega > 0.62$ and r is large.

4.4 Flux-Flow Oscillator

When a magnetic field is applied along the layer direction it may generate Josephson vortices in the junctions, resulting in a Josephson vortex lattice. Recently, the dynamic properties of this lattice in BSCCO have been the subject of extensive experimental research[79, 80, 81]. Quite typically magnetic field oscillations of the flux flow voltage or the flux flow resistance with either a Φ_0 or a $\Phi_0/2$ periodicity (in applied field times layer area) has been observed. A straight forward explanation of such periodicities can be obtained by looking at the lattice structure. The vortex lattice is driven along the layers by the Lorentz force from an applied bias current. Since this vortex flow gives rise to a voltage, a periodic oscillation (in magnetic field) of the flux flow voltage can be expected. If fluxons in each junction leave simultaneously (Φ_0 periodicity) it may be an indication of a square vortex lattice (in-phase vortex configuration). If, on the other hand, a $\Phi_0/2$ period is observed it may be an indication of a triangular

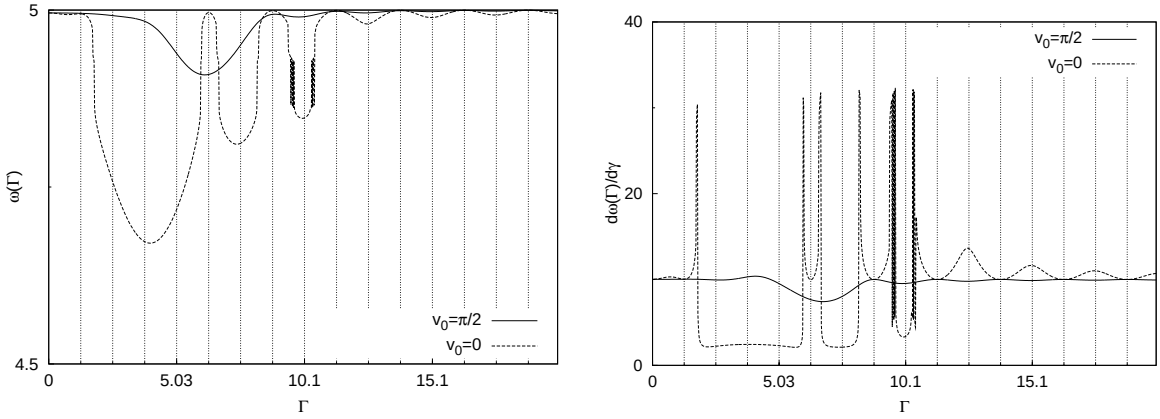

Figure 4.15: Curves obtained by solving Eq. (3.69) numerically with $v_0 = 0$ and $v_0 = \pi/2$ to obtain the voltage, $\omega(\Gamma)$ (left), and the dynamic resistance, $d\omega(\Gamma)/d\gamma$ (right). Vertical lines at $\Gamma = n\pi/L$, $n = 0, 1, ...$ Parameters used: $L = 2.5$, $\alpha = 0.1$, $\gamma = -0.5$, $S = -0.4$.

vortex lattice[79] (anti-phase vortex configuration). The crucial test for this explanation is of course a direct measurement of the frequency and power of the electromagnetic radiation emitted by the vortices leaving the sample. As shown in Fig. 4.3 for the fluxon modes, the emitted power of in-phase oscillations is much greater than that of anti-phase oscillations.

Attempts to fabricate a microwave oscillator based on the in-phase motion (square lattice) of vortices in single crystals of the $Bi_2Sr_2CaCu_2O_x$ type has been reported[81]. The frequency range is typically in the THz range which makes the ideas potentially very interesting but, at the same time, experimentally difficult to verify. So far, no direct measurement of emitted THz radiation has been reported.

In Ref. [82] a numerical simulation was done for a single long Josephson junction. Both periodicities, Φ_0 and $\Phi_0/2$, were observed, very similar to experiments and numerical simulations on stacks. Since the concepts of square and triangular vortex lattice have no meaning in a single junction, it was concluded that there is no direct connection between the periodicity and the vortex lattice ordering. This was also confirmed by numerical simulations on 3 and 10 layer stacks[83]. In Ref. [82], the origin of both the Φ_0 and the $\Phi_0/2$ oscillations was identified as being due to the Fiske modes[37, 84] discussed in Sections 2.6 and 3.2.3. See also right plot of Fig. 2.16 for a similar calculation, but showing only one of the periods (at high Γ).

In this section, numerical calculations trying to illuminate the conditions for the formation of a square vortex lattice in Josephson junction stacks are presented. By looking directly at the phases of the individual junctions, it is possible to unambiguously identify the lattice structure in the voltage vs. applied magnetic field characteristics.

The simplest case having both in-phase and anti-phase flux flow modes is the case of two coupled junctions. Flux-flow modes in this system were considered analytically in Section 3.2.3. The main result was the current-voltage characteristic given by Eq. (3.69), originally derived by Grønbech-Jensen et. al in Ref. [65]. Following Ref. [82] for the case of a single junction, Eq. (3.69) may be solved numerically to yield the $\omega - \Gamma$ characteristic at constant bias current, which is often measured in experiments. Unlike the case of a single junction, an undetermined phase difference, v_0, enters the calculations in the case of two coupled junctions. Since fluxons in different junctions repel each other (see Section 4.2 and Ref. [85]), the intuitively most stable configuration of a fluxon lattice is when the fluxon-fluxon distance is largest, i.e. the anti-phase vortex configuration corresponding to $v_0 = \pi/2$. Nevertheless, the in-phase vortex configuration, corresponding to $v_0 = 0$, has even in zero magnetic field been shown to be dynamically stable[86], and it is also the most interesting configuration for applications. In Fig. 4.15, the $\omega(\Gamma)$ curve have been plotted for both cases, by solving Eq. (3.69) iteratively. Starting at $\Gamma = 50$ and then solving Eq. (3.69) numerically to obtain ω, using $\omega = \gamma/\alpha$ as an initial value (as $\omega(\Gamma) \to \gamma/\alpha$ for $\Gamma \to \infty$). Then Γ is slightly decreased and the previously found value of ω is used as an initial value for the numerical solution of Eq. (3.69) with the new and smaller value of Γ. This is repeated until $\Gamma = 0$ is reached. In the plots, $\Gamma = n\pi/L$ ($n = 0, 1, ...$), are marked by vertical lines, corresponding to the different Fiske steps. For large Γ, a periodic behavior with a period of $2\pi/L$ is seen. At low values of Γ some complex behavior, especially for $v_0 = 0$, is evident. Oscillations with period π/L are not seen in these plots. This is probably due to the small length. It is important to note, that the $2\pi/L$ oscillations

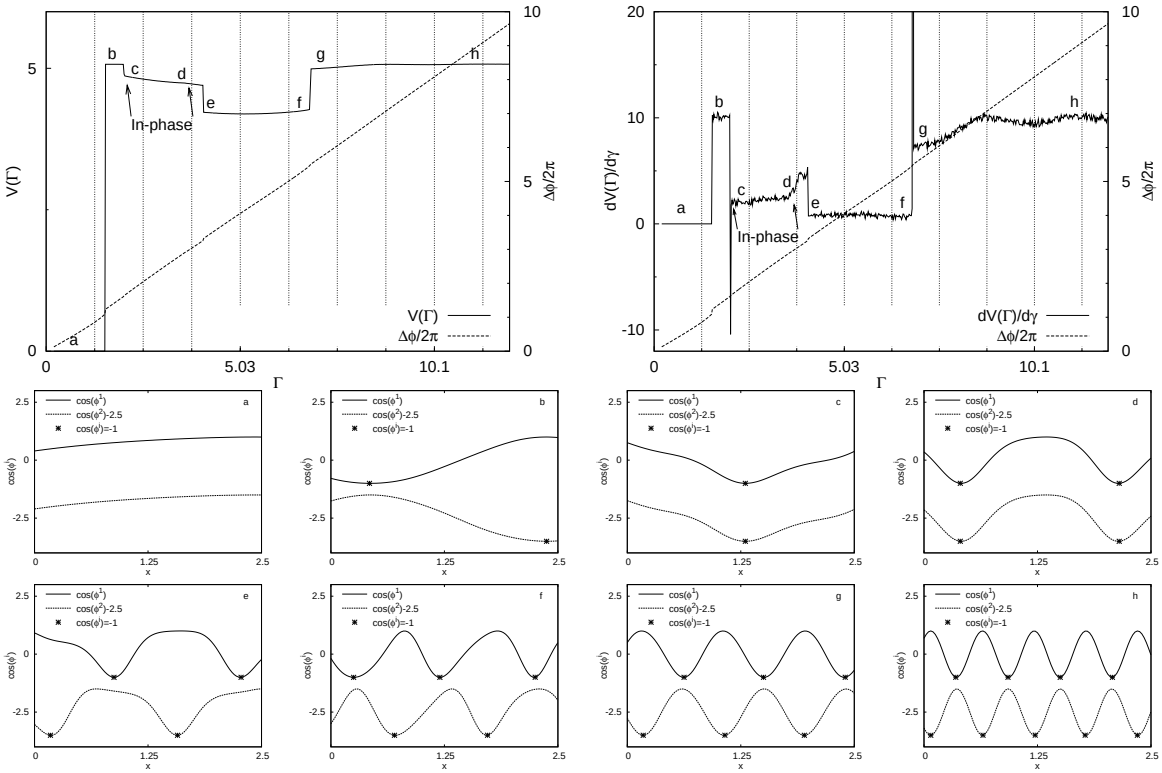

Figure 4.16: 2 junctions, $L = 2.5$, and $\gamma = -0.5$. Average voltage, $V(\Gamma)$ (top left), and dynamic resistance, $dV(\Gamma)/d\gamma$ (top right) obtained by a numerical simulation of Eqs. (3.20)-(3.23). Lower plots, (a)-(h), show $\cos(\phi^i)$ at selected values of Γ. Vertical lines at $\Gamma = n\pi/L$, $n = 0, 1, ...$ Other parameters: $\alpha = 0.1$ and $S = -0.4$. The in-phase fluxon configuration is observed in the range of magnetic field between (c) and (d).

is seen for both the in-phase ($v_0 = 0$) solution and the anti-phase ($v_0 = \pi/2$) solution.

Starting with $\phi^i = 0$ ($i = 1, ..., N$) and $\Gamma = 0$, Eqs. (3.20)-(3.23) have been solved numerically from $t = 0$ to t_m. Γ is then increased slightly, keeping all other parameters fixed. With the previous solution as initial conditions, a new solution is generated, again from $t = 0$ to t_m. This is repeated until a maximum value of Γ is reached. Taking care that t_m is large enough for the system to reach a possible steady state at each value of Γ, the voltage vs. applied magnetic field characteristic of the system is obtained. Since the individual voltages,

$$\omega^i \quad = \quad \lim_{t\to\infty} \frac{1}{L(t-t_0)} \int_{t_0}^{t} \int_{0}^{L} \phi_t^i(x,t')dxdt' \ , \tag{4.60}$$

can not be assumed to be identical for all junctions, the average voltage

$$V \quad \equiv \quad \frac{1}{N} \sum_{i=1}^{N} \omega^i \ , \tag{4.61}$$

has been computed. To get a feeling of the total number of fluxons in the system, the phase difference,

$$\Delta\phi \equiv \sum_{i=1}^{N} \left(\varphi^i(L) - \varphi^i(0)\right) \ , \tag{4.62}$$

is also calculated using

$$\varphi^i(x) \equiv \lim_{t\to\infty} \frac{1}{t-t_0} \int_{t_0}^{t} dt' \phi^i(x,t') \ . \tag{4.63}$$

$\Delta\phi$ is approximately 2π times the number of fluxons in the system.

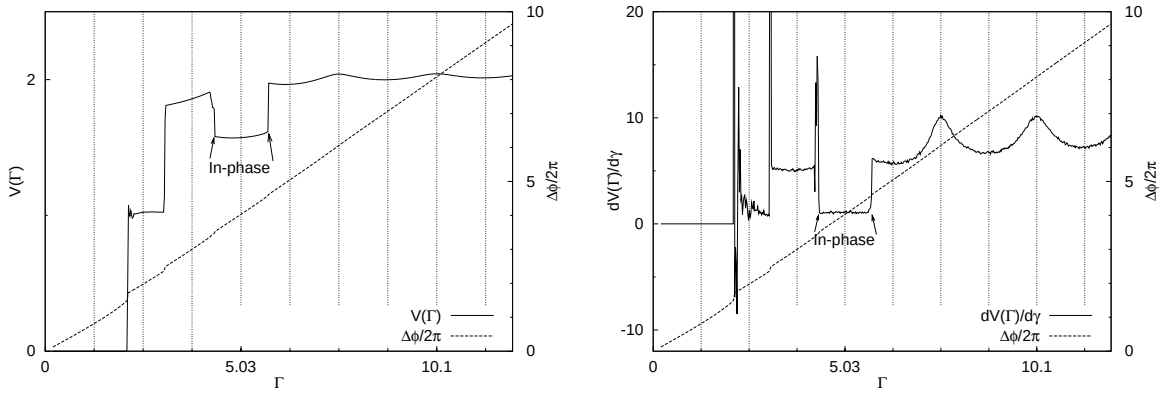

Figure 4.17: 2 junctions, $L = 2.5$, and $\gamma = -0.2$. Average voltage, $V(\Gamma)$ (left), and dynamic resistance, $dV(\Gamma)/d\gamma$ (right) obtained by a numerical simulation of Eqs. (3.20)-(3.23). Vertical lines at $\Gamma = n\pi/L$, $n = 0, 1, ...$ Other parameters: $\alpha = 0.1$ and $S = -0.4$. In-phase vortex configuration is observed, but at higher values of Γ than for the higher bias current case shown in Fig. 4.16.

Fig. 4.16 presents the results of the above method used on two stacked junctions. To investigate in detail what happens in the characteristics, $\cos(\phi^i)$ is plotted for each junction at selected values of Γ and at a selected value of t close to t_m. Marked on these figures are the points $\cos(\phi^i) = -1$, which approximates the position of a fluxon. Thus, the fluxon configuration can directly be seen at different places in the $V - \Gamma$ characteristic. For very low magnetic field (a), there are no fluxons in the junctions. At some small field (b), $\Gamma \sim 2$, fluxons start to enter the junctions and a large increase in the average voltage is observed. The fluxons are in an anti-phase configuration. Increasing the field a little more to point (c), the voltage drops a little and the two fluxons in the junctions have re-arranged themselves from the anti-phase configuration to the in-phase configuration. Increasing the field to (d), more fluxons enter the junctions, until another drop in the voltage is observed at point (e), where the fluxons have jumped from the in-phase configuration to the anti-phase configuration. As the field is increased to point (e), the voltage remains essentially constant but more and more fluxons enter the system in an anti-phase configuration. At point (g), the voltage jumps up to about γ/α and from here-on, the $2\pi/L$ oscillations appears and the fluxon always seem to be in an anti-phase configuration (h). Note that the $2\pi/L$-oscillations appears when the phases seem approximately linear as a function of x. Judging from these calculations, this happens when $\Delta\phi/(2\pi LN) \approx 1$, i.e. when the length pr. fluxon pr. junction is about unity.

Fig. 4.17 presents the $V - \Gamma$ characteristic for a system with identical parameters as the one in Fig. 4.16, but with a smaller bias current, $\gamma = 0.2$. For large magnetic field the $2\pi/L$-oscillations are seen, and they start at a value of Γ which is a little smaller than it was for the case with $\gamma = -0.5$. Again, the in-phase configuration of the vortices is observed, but for a different region of Γ, though still for Γ below the $2\pi/L$ oscillation regime.

A calculation similar to the one in Fig. 4.16 but with $L = 5$ is shown in Fig. 4.18. First, no fluxons are induced by the magnetic field and as the magnetic field is increased, the fluxons start to enter in a triangular lattice. For a little higher value of Γ the fluxon lattice shifts to a square lattice. The values of Γ where the square lattice is observed has moved up as compared to the $L = 2.5$ case, but the size of the Γ-range is almost identical. Increasing the magnetic field, the lattice shifts back to the triangular lattice and for even higher values of Γ the periodic oscillations are observed.

The phase difference, $\Delta\phi$, in Figs. 4.16 and 4.18 shows an almost linear dependence on Γ, though small jumps on the curve can be observed. This fits well with Eqs. (3.54) and (3.55), which gives $\Delta\phi \approx NL\Gamma$, neglecting $\delta\phi^i$. Since $\Delta\phi$ increases almost linearly, the fluxon entry happens almost continuously. The plot of $dVd\Gamma$ in the top right of Fig. 4.18 shows the difference $\Delta\phi - 2L\Gamma$ which is due to the $\delta\phi^i$'s in Eqs. (3.54) and (3.55). The seemingly most interesting region is the region of in-phase fluxon motion. Here, the measure $\Delta\phi - 2L\Gamma$ is large for some values of Γ and non-linear effects may therefore be important for the formation of the square lattice.

In Fig. 4.19, the length of the system has been increased to $L = 10$. This gives room for more fluxons in each junction. A large magnetic field shows again the $2\pi/L$-oscillations. In contrast to the short systems in Figs. 4.16 and 4.17 the in-phase mode is only observed for a high value of the bias current, and even here the range of magnetic field where the in-phase mode is observed is severely

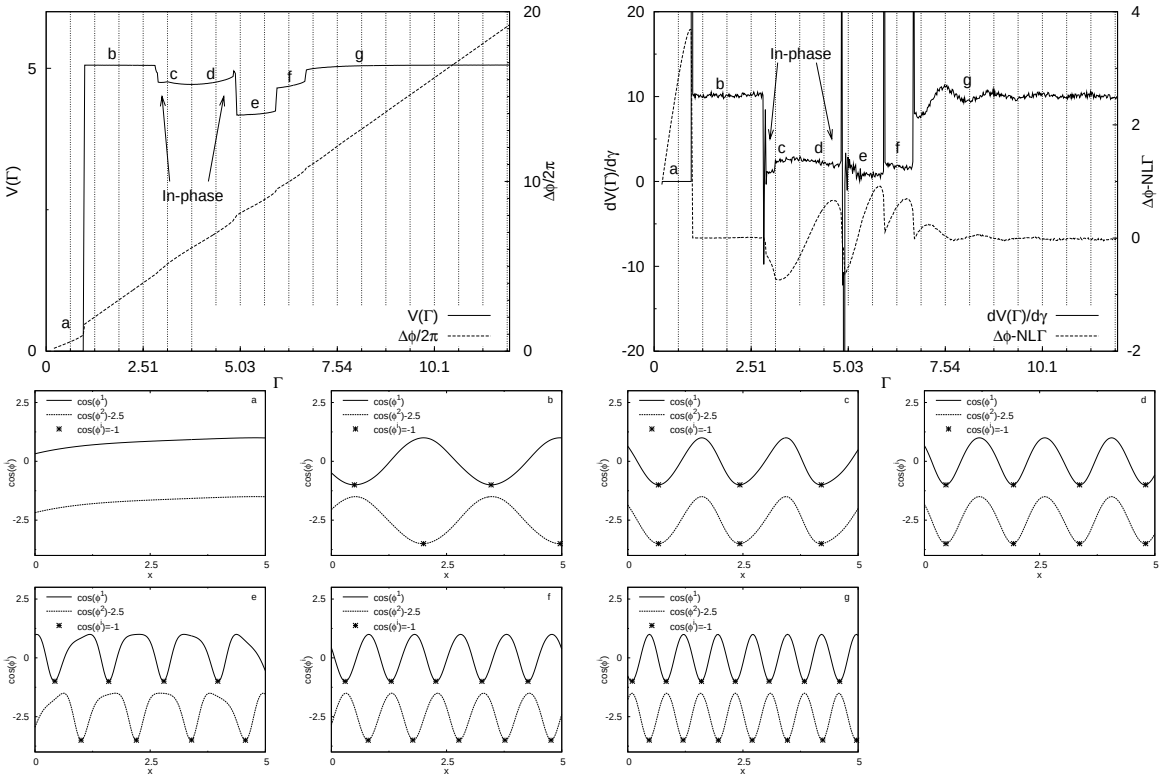

Figure 4.18: 2 junctions, $L = 5$, and $\gamma = -0.5$. Average voltage, $V(\Gamma)$ (top left), and dynamic resistance, $dV(\Gamma)/d\gamma$ (top right) obtained by a numerical simulation of Eqs. (3.20)-(3.23). Lower plots, (a)-(g), show $\cos(\phi^i)$ at selected values of Γ. Vertical lines at $\Gamma = n\pi/L$, $n = 0, 1, ...$ Other parameters: $\alpha = 0.1$ and $S = -0.4$.

shortened as compared to the $L = 2.5$ and $L = 5$ systems. The in-phase mode starts at $\Gamma \approx 3$ and ends at $\Gamma \approx 3.7$. For slightly higher values of Γ, the in-phase mode starts to become erratic. The square lattice is not observed for some Γ-values in this range, but a slight increase in Γ may change the structure of the lattice completely. This is also evident from the dynamic resistance plot, where the region labeled "Partial in-phase" shows large peaks, signaling instability.

4.4.1 More Junctions

In order to use stacked Josephson junctions for oscillators in applications, the power of the emitted radiation must be high. One way to obtain this is by increasing the number of junctions in the stack and operating the stack in the in-phase mode. As it was shown in the previous section, the square lattice is most easily obtained for a short system and a high bias current. Shown in Fig. 4.20 are calculations on systems with 5, 7, and 10 junctions. The overall picture is the same as two junctions, but some added complexity arising from the extra degrees of freedom is found. Fluxons enter around $\Gamma = 2$ and at high values of Γ the $2\pi/L$ oscillations are found, with the fluxons always arranged in a triangular lattice. Between these two values, complicated behavior is observed. Here the vortex-lattice is not very rigid due to the low fluxon density and it may be distorted considerably by the perturbations arising from the boundaries. In this "intermediate" region the lattice is quite erratic, but usually arranged in a triangular fashion due to the repulsiveness of the fluxons. But typically, a small region of Γ-values shows the interesting square lattice. Unfortunately, this region seems to become smaller when the number of junctions is increased, at least for the finite number of calculations that have been done here. Also, looking at the plots in Fig. 4.20 it is seen, that for the cases of 7 and 10 junctions, the fluxon density in the range of the in-phase configuration is seemingly below one fluxon per junction, while for the cases of 2 (Fig. 4.16) and 5 junction it may be higher. The plots of the individual phases do, however, show one fluxon in each junction arranged in the in-phase configuration for 7 (bottom of Fig. 4.21) and 10 (not shown) junctions. Unlike the case of $N = 2$ where the fluxons are exactly identical in the in-phase configuration, the fluxons for $N > 2$ in the in-phase configuration shows some dissimilarities and they

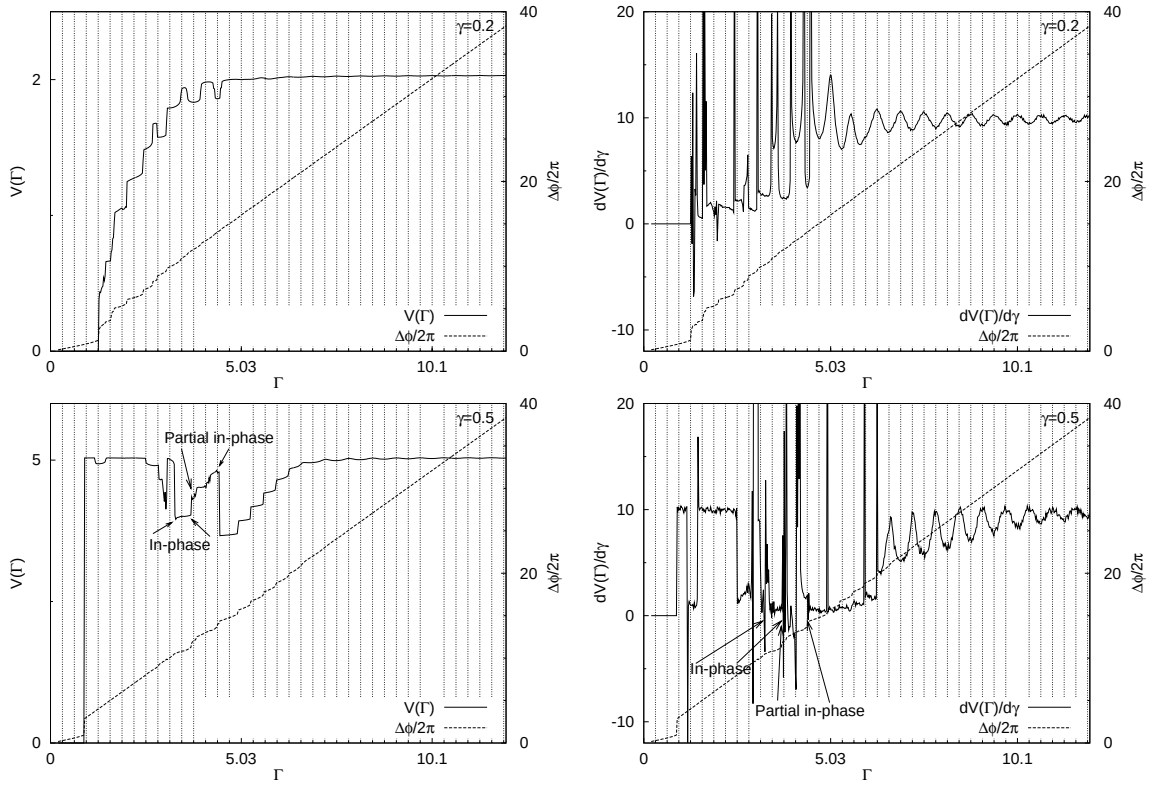

Figure 4.19: 2 junctions, $L = 10$. Average voltage, $V(\Gamma)$ (left), and dynamic resistance, $dV(\Gamma)/d\gamma$ (right) obtained by a numerical simulation of Eqs. (3.20)-(3.23). Vertical lines at $\Gamma = n\pi/L$, $n = 0, 1, ...$ Parameters used: $L = 10$, $\alpha = 0.1$, $\gamma = -0.2$ (top) and -0.5 (bottom), $S = -0.4$. Only for the high value of the bias current is the in-phase configuration observed.

may be positioned very slightly out of phase, see right plot of Fig. 4.21. Also, since the fluxon density per junction, where the in-phase configuration is observed, decreases with an increase in the number of junctions, it is concluded that the system is having trouble phase-locking a large number of fluxons.

In the plots for $N = 7$ and $N = 10$ in Fig. 4.20, the in-phase configuration is observed close to the first fluxon entry. Since the numerical code is started with $\phi^i = 0$ for $i = 1, .., N$ at $\Gamma = 0$, one might suspect that the in-phase configuration is, in these cases, only obtained due to the symmetry of the initial conditions. Shown in Fig. 4.21 is $\cos(\phi^i)$ for $\Gamma = 1.6$ and $\Gamma = 1.8$ taken from the calculations with $N = 7$ in Fig. 4.20. Before the in-phase configuration is obtained at $\Gamma = 1.8$, there is a transition from zero fluxons to a state, at $\Gamma = 1.6$, where only some of the junctions contains fluxons, thus the "in-phase symmetry" of the initial conditions has been broken.

Calculations on longer junctions and different values of the bias current have been made but not shown. The larger length allows for more "freedom" in the region of low fluxon density, giving rise to even more complicated characteristics. For high values of the magnetic field the system always seem to exhibit $2\pi/L$ oscillations with the fluxons always arranged in a triangular lattice, and the longer junctions seem to be less likely to exhibit in-phase configuration, like in the case of two junctions considered in the previous section.

4.5 Conclusion

This chapter has looked at the long Josephson junction stack as an oscillator and different techniques was discussed. First, the available power for output was calculated using the different fluxon modes found in Section 3.3.2. Not surprisingly, the in-phase fluxon modes showed by far the largest available power. It was also shown, that it does not matter much whether the outer junctions have switched to finite voltage. This could be important for applications, since the in-phase mode with one fluxon in each junction is hard to obtain, even in numerical simulations. The result in Section 4.1 shows that other possibilities may be just as good.

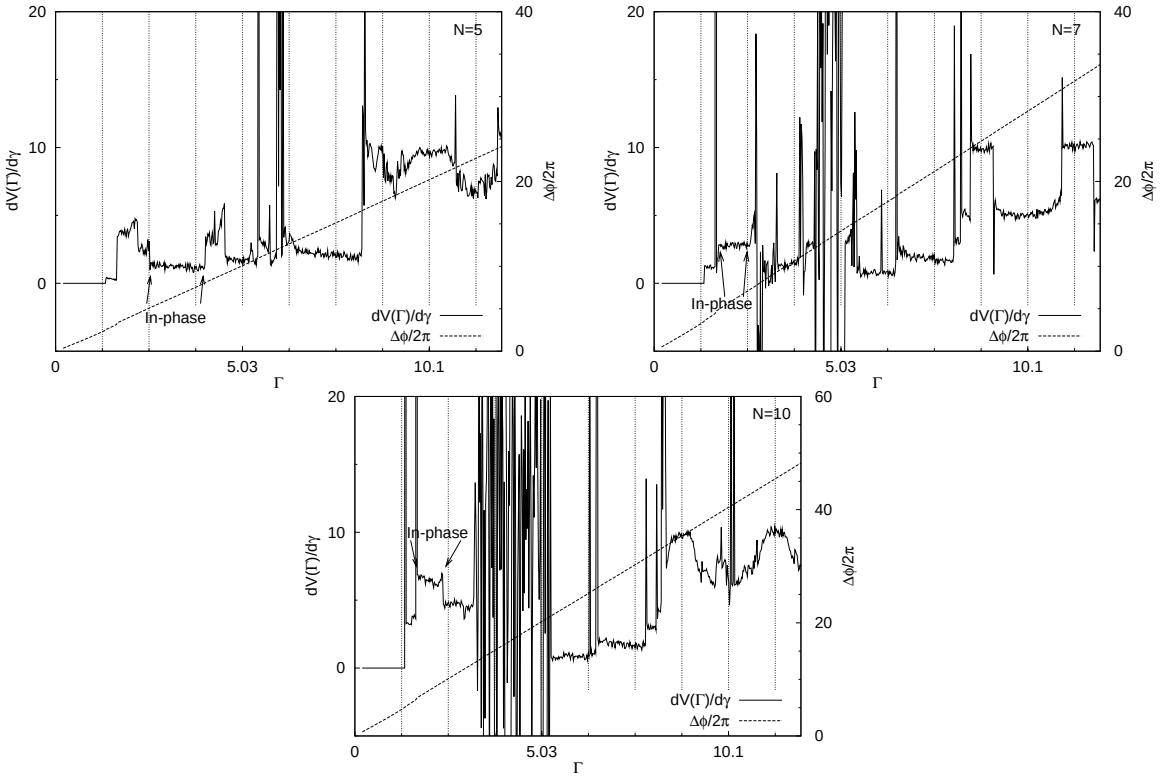

Figure 4.20: $N = 5$ (top left), $N = 7$ (top right), and $N = 10$ (bottom). Dynamic resistance, $dV(\Gamma)/d\gamma$ obtained by a numerical simulation of Eqs. (3.20)-(3.23) is shown. Vertical lines at $\Gamma = n\pi/L$, $n = 0, 1, ...$ Parameters used: $L = 2.5$, $\alpha = 0.1$, $\gamma = -0.5$, $S = -0.4$. The maximum number of fluxons pr. junction pr. length in the in-phase configuration is observed to decrease with an increase in the number of junctions.

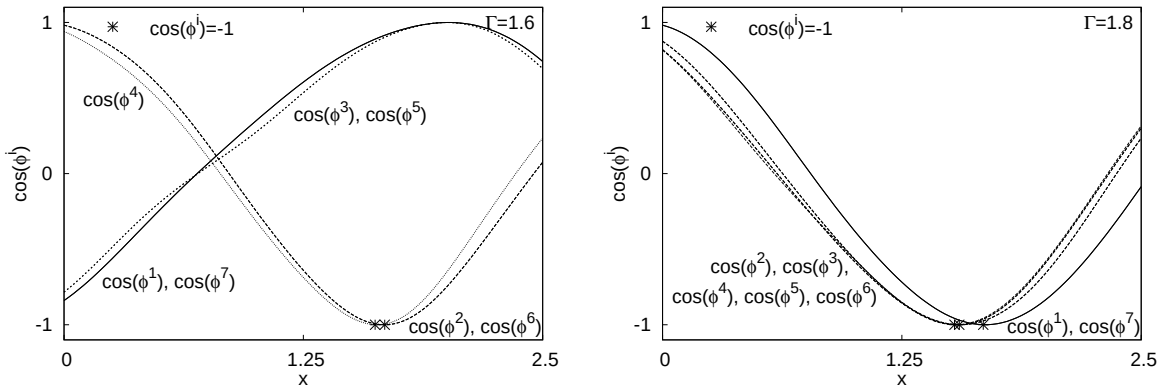

Figure 4.21: 7 junctions showing $\cos(\phi^i)$ for the two values of Γ in Fig. 4.20: $\Gamma = 1.6$ (left) and $\Gamma = 1.8$ (right). For $\Gamma = 1.6$ there are only fluxons in junctions 2, 4, and 6. Although $\Delta\phi/N < 2\pi$ for $\Gamma = 1.8$, there is a fluxon in each junction arranged in an in-phase configuration. The fluxons in the outer junctions are displaced a little away from the other fluxons, but still phase-locked.

The problem of obtaining a bunched fluxon state was discussed in Section 4.2. The desirable bunched fluxon-fluxon mode is energetically unfavorable, but may be stable once formed. It was shown, that by applying microwaves to a pair of weakly coupled junctions, the bunched in-phase solution may be obtained. The method had, however, some flaws. The trick was to apply microwaves to get the bunched state, but generally one would like to use the bunched state to obtain microwaves. The fluxons had to move quite slowly for the repulsive interaction to be small enough to be canceled by the force due to the applied microwaves. This resulted in a bunched state which was only stable when phase-locked to the microwaves. Turning the microwaves off, the fluxons would drift apart. In addition to these problems,

the method only worked for weakly coupled junctions, and it is not applicable to intrinsic stacks such as BSCCO which has a large coupling parameter, S.

The problems connected with the use of microwaves to obtain the bunched state was solved in Section 4.3 by coupling the stack to a cavity. In the weak coupling limit, the current in the cavity was calculated. The analytical solution showed generally good agreement with numerical simulations. It was also shown that the cavity may induce fluxon bunching in a weakly coupled stack of long Josephson junctions. Since the method only works for weakly coupled junctions, it still can not induce fluxon bunching in intrinsic stacks.

The last section looked at the flux-flow solutions. These solutions arise when a large magnetic field is applied to the edges of a long Josephson stack. The voltage and dynamic resistance as a function of an applied magnetic field for Josephson junction stacks with different parameters were calculated numerically. By looking at the individual phases of the junctions, it was possible to clearly distinguish between in-phase (square lattice) and anti-phase (triangular lattice) vortex configurations. The system was mostly found to have a triangular vortex lattice, or a similar non-coherent vortex configuration. The square lattice was observed in some systems. Small length, high bias current, and a low number of junctions seemed to enhance the conditions for a square lattice, which was observed only for some values of the magnetic field. The structure of the vortex lattice was found not to be connected to oscillations in the voltage vs. magnetic field curves.

Chapter 5

Two-Gap Superconductivity

The discovery of two-gap superconductivity in MgB_2[12, 87] has created a lot of interest in this subject, both experimentally[88] and theoretically[89, 90, 91, 92]. This chapter deals with the theoretical side of the problem. One may attack this problem from different angles, using either two-gap BCS theory or a simpler approximate theory. There has been different proposals for approximate theories describing two-gap superconductivity which can all be derived from the microscopic theory. One proposal is a generalization of the Ginzburg-Landau theory to contain two order parameters[89]. In other works it is stated that the generalized Ginzburg-Landau theory does not work for MgB_2, because of the specific nature of the two energy gaps present in this compound. Thus a more general approximate theory has been derived[90, 91].

Here, the generalized Ginzburg-Landau theory will be used to investigate topological defects in two-gap superconductivity. Using this approach, one may immediately identify some of the differences between one- and two-component superconductivity. Also, one may be guided by some of the many results already found in the one-component theory and similar field-theories. Although anisotropy plays an important role in MgB_2, the effects of anisotropy will not be considered in this thesis.

The long list of physical systems where topological defects plays an important role includes such seemingly different fields as superconductivity[28], cosmology[24], and singular optics[93], to name a few. The most famous topological defect in superconductivity is without doubt the Abrikosov vortex. In cosmology, topological defects in the form of vortices have been considered as the seed of galaxy formation by their gravitational field in various different gravitational theories[25]. In singular optics, optical vortices[95] has been considered in connection with pattern formation in lasers[94]. The study of topological defects in field theoretic models are thus of broad physical interest, and the present chapter should also be interesting to people outside the field of superconductivity.

5.1 The Two-Component Ginzburg-Landau Theory

A two-gap superconductor has two different charge carriers (Cooper-pairs) due to the presence of two different energy gaps. Since the Ginzburg-Landau theory describes one charge carrier by a charged complex scalar field (order parameter) it seems natural that the two-gap version should have two such order parameters, ψ_1 and ψ_2. Since the Cooper-pairs come from two different energy bands, it is likely that there should be a coupling between these two order parameters, describing the tunneling of Cooper-pairs from one order parameter to the other. This is precisely what is found in Ref. [89], which derives the two-component Ginzburg-Landau theory from the two-gap BCS theory. The free energy functional may be written as[89]

$$\begin{aligned} G = \int_\Omega d^3R \quad \Bigg(& \quad \frac{1}{2m_1}\left|(i\hbar\nabla + q\mathbf{A})\psi_1\right|^2 - \alpha_1|\psi_1|^2 + \frac{\beta_1}{2}|\psi_1|^4 \\ & + \quad \frac{1}{2m_2}\left|(i\hbar\nabla + q\mathbf{A})\psi_2\right|^2 - \alpha_2|\psi_2|^2 + \frac{\beta_2}{2}|\psi_2|^4 \\ & - \quad \eta\left(\psi_1^*\psi_2 + \psi_1\psi_2^*\right) + \frac{\left(\mathbf{B}^a - \mathbf{B}\right)^2}{2\mu_0}\Bigg), \end{aligned} \tag{5.1}$$

where η is strength of the direct tunneling between the order parameters, also called the Josephson

coupling. There are four parameters, α_i and β_i, where the α_i's are dependent on temperature, like in Eq. (2.2), such that each of the two fourth order potentials behave like in Fig. 2.1. Note, that since the two types of charge carriers are both Cooper-pairs, the charge of both order parameters is $q = 2e$.

To work analytically with the two-component Ginzburg-Landau theory, it is a good idea to normalize it first. This will be done using the transformations

$$\psi_i \to \frac{\sqrt{m_i}}{\hbar}\sqrt{\frac{a_1}{b_1}}\psi_i \quad , \quad \alpha_i \to \frac{\hbar^2}{m_i}a_i \quad , \quad \beta_i \to \frac{\hbar^4}{m_i^2}b_i \quad , \quad x \to \xi_1 x \quad , \quad \mathbf{A} \to \frac{\hbar}{q\xi_1}\mathbf{A} \quad , \quad \eta \to \frac{2\hbar^2 a_1}{\sqrt{m_1 m_2}}\eta \ , \tag{5.2}$$

where $i = 1, 2$ and $\xi_i \equiv \sqrt{\hbar^2/(2m_i\alpha_i)} = 1/\sqrt{2a_i}$ is the coherence length of the i'th order parameter. The free energy functional then becomes

$$\begin{aligned} G \propto \int_\Omega d^3R \quad \Bigg(\quad & \frac{1}{2}\left|(i\nabla + \mathbf{A})\psi_1\right|^2 - \frac{1}{2}|\psi_1|^2 + \frac{1}{4}|\psi_1|^4 \\ + \quad & \frac{1}{2}\left|(i\nabla + \mathbf{A})\psi_2\right|^2 - \frac{a}{2}|\psi_2|^2 + \frac{b}{4}|\psi_2|^4 \\ - \quad & \eta\left(\psi_1^*\psi_2 + \psi_1\psi_2^*\right) + \frac{\kappa_1^2}{2}\left(\mathbf{B}^a - \mathbf{B}\right)^2 \Bigg) \ , \end{aligned} \tag{5.3}$$

where $a \equiv a_2/a_1$, $b \equiv b_2/b_1$, and $\kappa_i \equiv \lambda_i/\xi_i$ is the Ginzburg-Landau parameter for the i'th order parameter, using $\lambda_i \equiv \sqrt{m_i\beta_i/(\mu_0 q^2\alpha_i)} = \sqrt{\hbar^2 b_i/(\mu_0 q^2 a_i)}$ as the London penetration depth of the i'th order parameter. Note that the new parameters, a and b, are also given by $a = \xi_1^2/\xi_2^2$ and $b = \kappa_2^2/\kappa_1^2$ and hence $a/b = \lambda_1^2/\lambda_2^2$. From the normalized free energy functional, the partial differential equations for the order parameters and the magnetic field may be obtained by variational calculus to

$$\left(i\nabla + \mathbf{A}\right)^2\psi_1 - \psi_1 + |\psi_1|^2\psi_1 - 2\eta\psi_2 = 0 \qquad in \qquad \Omega \ , \tag{5.4}$$

$$\left(i\nabla\psi_1 + \mathbf{A}\psi_1\right)\cdot\mathbf{n} = 0 \qquad on \qquad \partial\Omega \ , \tag{5.5}$$

$$\left(i\nabla + \mathbf{A}\right)^2\psi_2 - a\psi_2 + b|\psi_2|^2\psi_2 - 2\eta\psi_1 = 0 \qquad in \qquad \Omega \ , \tag{5.6}$$

$$\left(i\nabla\psi_2 + \mathbf{A}\psi_2\right)\cdot\mathbf{n} = 0 \qquad on \qquad \partial\Omega \ , \tag{5.7}$$

$$\kappa_1^2\nabla\times\mathbf{B} = \frac{i}{2}\left(\psi_1\nabla\psi_1^* - \psi_1^*\nabla\psi_1 + \psi_2\nabla\psi_2^* - \psi_2^*\nabla\psi_2\right) - \left(|\psi_1|^2 + |\psi_2|^2\right)\mathbf{A} \equiv \mathbf{J} \qquad in \qquad \Omega \ , \tag{5.8}$$

$$\mathbf{B} = \mathbf{B}^a \qquad on \qquad \partial\Omega \ . \tag{5.9}$$

The equations of course look very similar to Eqs. (2.4)-(2.7) of the ordinary Ginzburg-Landau theory. But there are interactions between the two order parameters, both directly through the Josephson tunneling term and indirectly through the magnetic field. Even without *any* of these two interactions, new effects arise because of the extra degrees of freedom in the system. The theory is thus not a trivial generalization of the Ginzburg-Landau theory and deserves some interest.

To find an analogue of the Meissner-solution for the two-component theory, it is assumed that ψ_1 and ψ_2 are real constants and there is no magnetic field, $\mathbf{A} = 0$. This gives the two coupled algebraic equations

$$\left(1 - \psi_1^2\right)\psi_1 + 2\eta\psi_2 = 0 \ , \tag{5.10}$$

$$\left(a - b\psi_2^2\right)\psi_2 + 2\eta\psi_1 = 0 \ , \tag{5.11}$$

which may be solved to obtain the constant values of ψ_1 and ψ_2 when the two-component superconductor is in the Meissner-phase. The general solution is quite cumbersome and will now be shown. Instead, Fig. 5.1 shows the "potential"

$$V_M(\psi_1, \psi_2) = -\frac{1}{2}\psi_1^2 + \frac{1}{4}\psi_1^4 - \frac{a}{2}\psi_2^2 + \frac{b}{4}\psi_2^4 - 2\eta\psi_1\psi_2 \ , \tag{5.12}$$

to which the solutions of Eqs. (5.10) and (5.11) are the extrema. It is evident that for $\eta = 0$, the minima are at $\psi_1 = \pm 1$ and $\psi_2 = \pm\sqrt{a/b}$, which gives $V_M = -\frac{1}{4}(1 + a^2/b)$ at these 4 minima. The "potential" is thus four times degenerate when $\eta = 0$.

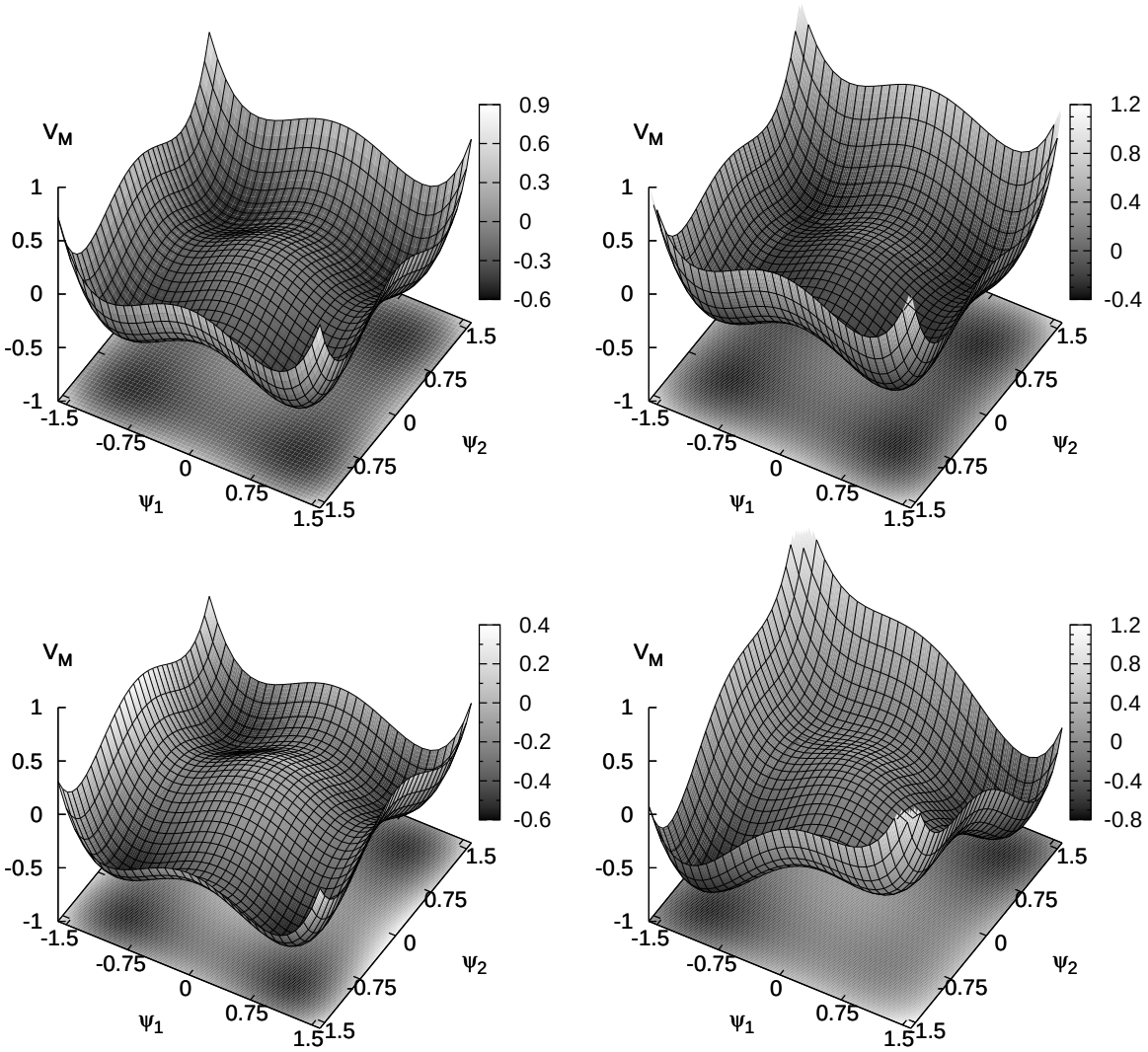

Figure 5.1: The Meissner solution corresponds to the minima of the potential V_M in Eq. (5.12). Top Left: $a = b = 1$ and $\eta = 0$. Top Right: $4a/3 = b = 1$ and $\eta = 1/2$. Bottom Left: $a = 4b/3 = 1$ and $\eta = 0$. Bottom Right: $a = b = 1$ and $\eta = 1/8$

For the case with $a = b = 1$ and non-zero η the four minima of V_M are easily found to

$$\psi_1 = \pm\sqrt{1+2\eta} = \psi_2 \quad \text{with} \quad V_M = -\frac{1}{2}(1+2\eta)^2 \ , \tag{5.13}$$

$$\psi_1 = \pm\sqrt{1-2\eta} = -\psi_2 \quad \text{with} \quad V_M = -\frac{1}{2}(1-2\eta)^2 \ . \tag{5.14}$$

Note, that V_M no longer contains four equivalent minima since the value of V_M for $\psi_1 = \psi_2$ is different than for $\psi_1 = -\psi_2$. The four fold degeneracy present in the $\eta = 0$ case is thus broken into a two fold degeneracy by the η term and when $|\eta| > 1/2$ two of the minima disappear completely. V_M for $\eta = 1/8$ and $a = b = 1$ is shown in Fig. 5.1 as the bottom right plot.

The two- and four-fold degeneracy shown in Fig. 5.1 is only a simplified version of the true situation in the two-component Ginzburg-Landau theory, because in the general case the order parameters are complex numbers. This makes plots equivalent to Fig. 5.1 five dimensional. The extension from 3d to 5d is not as complex as it may seem, because the free energy functional in Eq. (5.3) is invariant under the gauge transformation

$$\psi_1 \to e^{i\alpha(x,y,z)}\psi_1 \quad , \quad \psi_2 \to e^{i\alpha(x,y,z)}\psi_2 \quad , \quad \mathbf{A} \to \mathbf{A} + \nabla\alpha(x,y,z) \ , \tag{5.15}$$

where $\alpha(x, y, z)$ is some real function depending on the spatial variables. For zero magnetic field, $\mathbf{A} = 0$, the above transformation corresponds to a rotation of the order parameters in the complex plane. Each

minimum in Fig. 5.1 thus becomes a circle of degenerate minima in the five dimensional complex analogue of the plots. In reality, the theory is not two or four times degenerate but has an infinite number of degenerate minima.

The situation with flux-quantization is somewhat different from the one-component model[96]. Consider the case of a Meissner-phase where $\psi_1 = v_1 e^{i\phi_1}$ and $\psi_2 = v_1 e^{i\phi_2}$, where ϕ_1 and ϕ_2 are real functions depending on space and the v_i's are the value of $|\psi_i|$ corresponding to a Meissner solution of Eqs. (5.10) and (5.11). The current density in Eq. (5.8) is then

$$J = v_1^2 \left(\nabla\phi_1 - \mathbf{A}\right) + v_2^2 \left(\nabla\phi_2 - \mathbf{A}\right) \ , \tag{5.16}$$

which may be integrated along the closed curve C located at a place without current, i.e. the condition for flux-quantization

$$v_1^2 \left(2\pi n_1 - \Phi\right) + v_2^2 \left(2\pi n_2 - \Phi\right) = 0 \tag{5.17}$$

is found with Φ being the magnetic flux through the surface S, having the boundary C and where ϕ_i changes by $2\pi n_i$ $(i = 1, 2)$ when C is traversed once. The flux through S is now trivially given by

$$\Phi = 2\pi \frac{n_1 v_1^2 + n_2 v_2^2}{v_1^2 + v_2^2} \ . \tag{5.18}$$

The case known from ordinary Ginzburg-Landau theory is $n \equiv n_1 = n_2$ giving $\Phi = 2\pi n$ where the flux is quantized in terms of Φ_0 $(= 2\pi$ in normalized units). Another possibility is that ϕ_2 is constant, $n_2 = 0$, which makes the flux depend on v_1 and v_2 and it is thus *not* quantized in terms of Φ_0. The problem of flux quantization in the two-component Ginzburg-Landau theory is discussed in detail in Ref. [96]. The case $n \equiv n_1 = n_2$ is discussed in the next section.

5.2 The Abrikosov Vortex in a Two-Component System

Since the theory simplifies to the Ginzburg-Landau theory in the case $\psi_2 = 0$, it should be possible to find Abrikosov-type vortex solutions. The method used here is the same as in Section 2.3 but using the generalized ansatz

$$\psi_1 = f_1(r) e^{in\theta} \quad , \quad \psi_2 = f_2(r) e^{in\theta} \quad , \quad A_r = 0 \quad , \quad A_\theta = \frac{n - P(r)}{r} \quad , \quad A_z = 0 \ , \tag{5.19}$$

in a cylindrical coordinate system, (r, θ, z). Inserting the ansatz into Eqs. (5.4), (5.6), and (5.8) gives

$$f_1'' + \frac{1}{r} f_1' - \frac{1}{r^2} f_1 P^2 + \left(1 - f_1^2\right) f_1 + 2\eta f_2 = 0 \ , \tag{5.20}$$

$$f_2'' + \frac{1}{r} f_2' - \frac{1}{r^2} f_2 P^2 + \left(a - b f_2^2\right) f_1 + 2\eta f_1 = 0 \ , \tag{5.21}$$

$$P'' - \frac{1}{r} P' - \frac{1}{\kappa_1^2} \left(f_1^2 + f_2^2\right) P = 0 \ , \tag{5.22}$$

where prime denotes differentiation with respect to r.

It is evident that the flux through a surface S with radius r is still given by Eq. (2.49) and the boundary conditions for the magnetic field may still be expressed as $P(0) = n$ and $P(\infty) = 0$. The boundary conditions for the order parameters at $r = 0$ are found by multiplying Eqs (5.20) and (5.21) by r^2. $r = 0$ then implies $f_1(0) = f_2(0) = 0$. For the order parameters at infinity, the situation is a little different than in Section 2.3. The order parameters should approach one of the minima of the potential, which are given as the solutions to Eqs. (5.10) and (5.11) (with $\psi_1 \to f_1$ and $\psi_2 \to f_2$) which corresponds to global minima of the potential in Eq. (5.12). Since the general solution of these equations is not very nice, but easily obtainable, the solutions are written as $f_1 = v_1$ and $f_2 = v_2$, such that all the boundary conditions become

$$f_1(0) = 0 \quad , \quad \lim_{r\to\infty} f(r) = v_1 \ , \tag{5.23}$$

$$f_2(0) = 0 \quad , \quad \lim_{r\to\infty} f(r) = v_2 \ , \tag{5.24}$$

$$P(0) = n \quad , \quad \lim_{r\to\infty} P(r) = 0 \ . \tag{5.25}$$

The Abrikosov vortex in the two-component Ginzburg-Landau theory is then described by Eqs. (5.20)-(5.22) with Boundary conditions (5.23)-(5.25). The equations may be solved generally by numerical methods or analytically for near-zero or large r behavior as in Section 2.3. Here, however, only the case of large r will be considered.

The asymptotic solution to Eq. (5.22) is easily obtained by following Section 2.3 to get

$$P_\infty = BrK_1(r\sqrt{v_1^2+v_2^2}/\kappa_1)\ , \tag{5.26}$$

where B is a constant and $K_1(r)$ is the modified Bessel function of the second kind of order one.

To solve the order parameter Eqs. (5.20) and (5.21) for large r, $P=0$ is inserted, $f_i = v_i - \alpha_i(r)$ is introduced, and the equations are expanded to first order in α_i, giving

$$\alpha_1'' + \frac{1}{r}\alpha_1' - q_1^2\alpha_1 + 2\eta\alpha_2 = 0\ , \tag{5.27}$$

$$\alpha_2'' + \frac{1}{r}\alpha_2' - q_2^2\alpha_2 + 2\eta\alpha_1 = 0\ , \tag{5.28}$$

where $(1-v_1^2)v_1 + 2\eta v_2 = (a - bv_2^2)v_2 + 2\eta v_1 \equiv 0$ was used and the constants

$$q_1^2 = 3v_1^2 - 1 \quad \text{and} \quad q_2^2 = 3bv_2^2 - a \tag{5.29}$$

were defined. The boundary conditions for α_1 and α_2 are

$$\lim_{r\to\infty}\alpha_1(r) = 0 \quad , \quad \lim_{r\to\infty}\alpha_2(r) = 0\ . \tag{5.30}$$

These equations are two coupled modified Bessel equations which may be solved analytically by power series, but the solution cannot, to the authors knowledge, be written in terms of known functions. In the following, the two cases $\eta = 0$ and $q_1 >> q_2$ will be considered. $q_1 >> q_2$ corresponds, for example, to one of the coherence lengths being much larger than the other, i.e. $\xi_1 >> \xi_2$.

The case $\eta = 0$ is almost trivial, since the two equations de-couple and the solutions become

$$f_1 = v_1 - C_1K_0(q_1r) \quad , \quad f_2 = v_2 - C_2K_0(q_2r)\,, \tag{5.31}$$

where K_0 is the modified Bessel function of the second kind of order zero and C_i are undetermined constants $(i = 1, 2)$.

The case $q_1 >> q_2$ is somewhat more complicated. Assuming that α_2 is known, the solution to the homogeneous equation for α_1 is then

$$\alpha_1^H = D_1I_0(q_1r) + D_2K_0(q_2r)\,, \tag{5.32}$$

where I_0 is the modified Bessel function of the first kind of order zero.

A particular solution to the inhomogeneous equation may be expressed as

$$\alpha_1^P = 2\eta I_0(q_1r)\int_{r_1}^{r}\alpha_2(x)xK_0(q_1x)\,dx - 2\eta K_0(q_1r)\int_{r_2}^{r}\alpha_2(x)xI_0(q_1x)\,dx\ , \tag{5.33}$$

where r_1 and r_2 are to be determined by the boundary conditions. To evaluate the integrals, the asymptotic form of the modified Bessel functions are used, $K_n(r) \approx e^{-r}/\sqrt{2\pi r}$ and $I_n(r) \approx e^r/\sqrt{2\pi r}$, valid for large r. The first integral is then

$$I_1(r, r_1) \equiv \int_{r_1}^{r}\alpha_2(x)xK_0(q_1x)\,dx \approx \int_{r_1}^{r}\alpha_2(x)x\frac{e^{-q_1x}}{\sqrt{2\pi q_1x}}dx\ , \tag{5.34}$$

which may be evaluated to an infinite sum by partial integration. Assuming

$$\lim_{x\to\infty}\left|\frac{(\sqrt{x}\alpha_2(x))^{(i)}}{q_1^i\sqrt{x}\alpha_2(x)}\right| << 1 \tag{5.35}$$

for $i = 1, 2, ...$, the integral may conveniently be written as

$$I_1(r, r_1) \approx \left[\frac{x\alpha_2(x)}{q_1}K_1(q_1x)\right]_a^b\ . \tag{5.36}$$

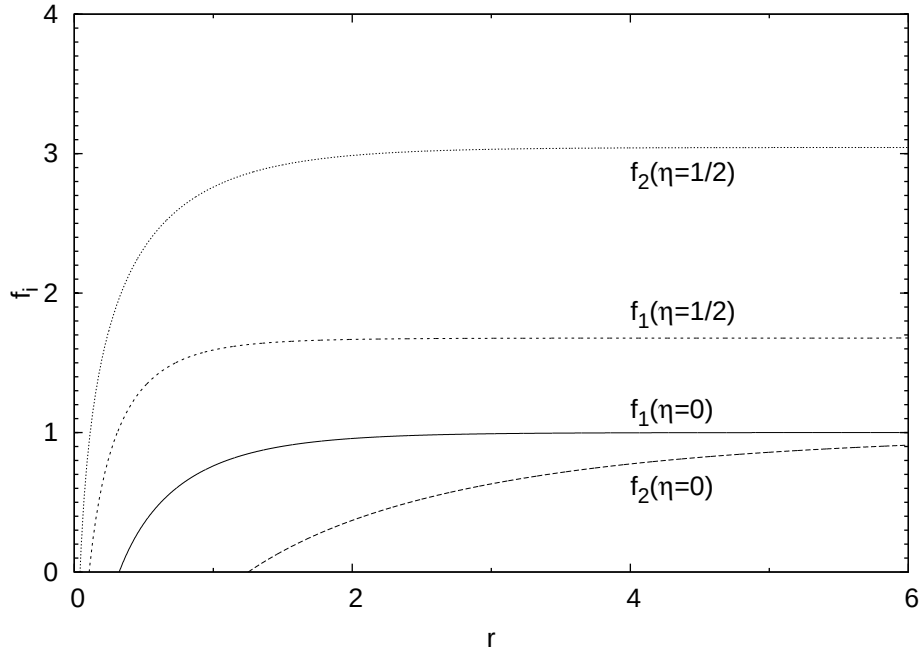

Figure 5.2: The solution in Eqs. (5.42) and (5.43) when $C = D = 1$ and $a = b = 1/15$ for $\eta = 0$ and $\eta = 1/2$. The choice of a and b corresponds to equal penetration depths, $\lambda_1 = \lambda_2$, and a $\sqrt{15}$ fold difference in coherence-lengths, $15\xi_1^2 = \xi_2^2$. The Josephson coupling seemingly has the effect of washing out the differences arising from different coherence-lengths.

Here, $f^{(i)}(x)$ means i differentiations with respect to x. Along similar lines, the second integral is calculated approximately to

$$I_2(r, r_2) \equiv \int_{r_2}^{r} \alpha_2(x) x I_0(q_1 x)\, dx \approx \left[\frac{x\alpha_2(x)}{q_1} I_1(q_1 x) \right]_a^b . \tag{5.37}$$

Using $K_{n+1}(x)I_n(x) + K_n(x)I_{n+1}(x) = -1/x$ and inserting the approximations of the integrals into Eq. (5.33),

$$\alpha_1^P \approx \frac{2\eta\alpha_2(r)}{q_1^2} + D_3 K_0(q_1 r) + D_4 I_0(q_1 r) \tag{5.38}$$

is obtained where D_3 and D_4 are unknown constants.

The complete approximate solution to Eq. (5.27) is obtained by adding up the homogeneous and the particular solutions. Since $I_0(x)$ diverges as $x \to \infty$, the constants D_1 and D_4 must be zero, giving

$$\alpha_1(r) \approx D K_0(q_1 r) + \frac{2\eta\alpha_2(r)}{q_1^2} \tag{5.39}$$

with $D \equiv D_2 + D_4$. This may be inserted into Eq. (5.28) which yields

$$\alpha_2'' + \frac{1}{r}\alpha_2' - \left(q_2^2 - \frac{4\eta^2}{q_1^2} \right) \alpha_2 + 2D\eta K_0(q_1 r) = 0 . \tag{5.40}$$

Since $q_1 << q_2$ it is expected that α_2 is a much slower function than $K(q_1 r)$ and the last term in the above equation may thus be neglected, and the solution is then

$$\alpha_2(r) \approx C K_0 \left(r\sqrt{q_2^2 - \frac{4\eta^2}{q_1^2}} \right) , \tag{5.41}$$

where it was used that $\alpha_2(r)$ must be finite for $r \to \infty$. The solution in terms of f_1 and f_2 is then trivially given by

$$f_1 \approx v_1 - D K_0(q_1 r) - 2\eta \frac{C}{q_1^2} K_0 \left(r\sqrt{q_2^2 - \frac{4\eta^2}{q_1^2}} \right) , \tag{5.42}$$

$$f_2 \approx v_2 - \alpha_2(r) \approx v_2 - CK_0\left(r\sqrt{q_2^2 - \frac{4\eta^2}{q_1^2}}\right) , \tag{5.43}$$

valid when $q_1 >> q_2$. The constants B, C, and D can not be determined by the asymptotic analysis, but must be determined from, say, a numerical solution like in Refs. [98] and [99]. Another possibility is to derive an approximate solution near $r = 0$ and then match the near- and far-field solutions at some intermediate point to determine the constants.

The rather strange condition in Eq. (5.35) may be interpreted by inserting the solution in Eq. (5.41) for α_2, resulting in

$$q_1 >> \sqrt{q_2^2 - \frac{4\eta^2}{q_1^2}} \tag{5.44}$$

for $i = 1$, which is approximately the same as $q_1 >> q_2$ and $(3v_1^2 - 1) >> (3bv_2^2 - a)$.

A plot of the solutions in Eqs. (5.42) and (5.43) is shown in Fig. 5.2 with $C = D = 1$ and $a = b = 1/15$ for $\eta = 0$ and $\eta = 1/2$. $a = b = 1/15$ corresponds to equal penetration depths, $\lambda_1 = \lambda_2$, and a $\sqrt{15}$ fold difference in coherence-lengths, $15\xi_1^2 = \xi_2^2$. This difference in coherence lengths correspond approximately to the situation in MgB_2, where the coherence lengths have been measured to $\xi_1 = 13$nm and $\xi_2 = 51$nm[97]. Without Josephson coupling, the order parameter f_2 have not yet reached its asymptotic value of $v_2 = 1$ at $r = 6$ while f_1 reaches $v_1 = 1$ at about $r = 3$. With Josephson coupling, f_1 reaches $v_1 \approx 1.68$ quickly and while f_2 is a little slower to reach $v_2 \approx 3.04$ it is still much quicker than the case without Josephson coupling. The Josephson coupling seemingly has the effect of washing out the differences arising from different coherence-lengths.

5.2.1 Abrikosov Vortex Interaction

The purpose of this section is to briefly discuss Abrikosov vortex interaction in the two-component theory. The derivation will follow Ref. [98] closely in the simple case of $\eta = 0$, but as long as it is feasible, expressions for non-zero η will be used to illustrate what needs to be done in order to consider the case of non-zero Josephson coupling.

A gauge is chosen such that the order parameters are real and they may therefore be written as

$$\psi_1 = v_1 - g_1(x, y, z) \quad \text{and} \quad \psi_2 = v_2 - g_2(x, y, z) , \tag{5.45}$$

where v_1 and v_2 are the "vacuum values" of the order parameters, given as the minima of the potential in Eq. (5.12), i.e. v_1 and v_2 satisfy Eqs. (5.10) and (5.11) with $\psi_1 = v_1$ and $\psi_2 = v_2$. The free energy functional in Eq. (5.3) is then linearized by expanding all terms and keeping only terms up to second order in the fields g_1, g_2 and $\mathbf{A}$. This gives

$$\begin{aligned} G_L = G_0 + \int_\Omega d^3R \quad \Bigg(& \frac{1}{2}(\nabla g_1)^2 + \frac{1}{2}(\nabla g_2)^2 + \frac{v_1 + v_2}{2}\mathbf{A}^2 \\ & + \frac{1}{2}\left(3v_1^2 - 1\right)g_1^2 + \frac{1}{2}\left(3bv_1^2 - a\right)g_2^2 - 2\eta g_1 g_2 + \frac{\kappa_1^2}{2}\left(\mathbf{B}_a - \mathbf{B}\right)^2 \Bigg) , \end{aligned} \tag{5.46}$$

where G_0 is a constant and hence does not contribute to the physics. Ref. [98] continues by adding point-sources to the linearized theory, such that the solutions of the field equations in the linear theory become the asymptotic solutions to the non-linear theory. The justification for doing this is, that far away from the vortex center, the vortex will look like a point. And the motivation is, that it is easy to calculate the interaction between two vortices, when one of them is considered to be a point-vortex. Adding the point-sources, the total free energy functional becomes[98]

$$G_T = G_L + \int_\Omega d^3R\left(\rho_1 g_1 + \rho_2 g_2 + \mathbf{A}\cdot\boldsymbol{\sigma}\right) , \tag{5.47}$$

where ρ_1, ρ_2, and $\boldsymbol{\sigma}$ are the point sources. Note, $\boldsymbol{\sigma}$ is a vector with three components. The field equations of the linearized theory with added point sources are

$$\nabla^2 g_1 - q_1^2 g_1 + 2\eta g_2 = \rho_1 , \tag{5.48}$$

$$\nabla^2 g_2 - q_2^2 g_2 + 2\eta g_1 = \rho_2 , \tag{5.49}$$

$$\left(\nabla^2\mathbf{A} - q_3^2\right)\mathbf{A} = -\boldsymbol{\sigma} , \tag{5.50}$$

where it was used that the divergence of $\mathbf{A}$ is zero, i.e. $\nabla \cdot \mathbf{A} = 0$ and where

$$q_3^2 \equiv \frac{v_1^2 + v_2^2}{\kappa_1^2} \tag{5.51}$$

was defined.

The task is now to determine the sources, such that the solutions to Eqs. (5.48)-(5.50) becomes the asymptotic solutions to the non-linear theory. The asymptotic solutions are given by Eqs. (5.26), (5.42), and (5.43) together with Eq. (5.19). These asymptotic solutions are however *not* in the correct gauge, so a transformation to a gauge where ψ_1 and ψ_2 are real must first be done. This is easily done using Eq. (5.15) with $\alpha(r, \theta, z) = -n\theta$, and the asymptotic solutions in the real gauge becomes

$$\psi_1 = v_1 - DK_0(q_1 r) - 2\eta \frac{C}{q_1^2} K_0\left(r\sqrt{q_2^2 - 4\eta^2/q_1^2}\right) , \tag{5.52}$$

$$\psi_2 = v_2 - CK_0\left(r\sqrt{q_2^2 - 4\eta^2/q_1^2}\right) , \tag{5.53}$$

$$A_\theta = -BK_1(q_3 r) \quad , \quad A_r = A_z = 0 . \tag{5.54}$$

For $\eta = 0$, Eqs. (5.45), (5.48), and (5.49) then provides two equations to determine ρ_1 and ρ_2

$$\left(\nabla^2 - q_1^2\right) K_0(q_1 r) = \rho_1 , \tag{5.55}$$

$$\left(\nabla^2 - q_2^2\right) K_0(q_2 r) = \rho_2 , \tag{5.56}$$

which are easily solved to find

$$\rho_1 = D\delta(r) \quad \text{and} \quad \rho_2 = C\delta(r) , \tag{5.57}$$

using[98] $(\nabla^2 - q^2)K_0(qr) = \delta(r)$. To obtain $\boldsymbol{\sigma}$ from Eq. (5.50) with $\mathbf{A}$ given by Eq. (5.54), notice that

$$\mathbf{A} = B\kappa_1 \mathbf{k} \times (\nabla K_0(q_3 r)) , \tag{5.58}$$

when $\mathbf{k}$ is a unit-vector in the direction of the vortex. Using this in Eq. (5.50) determines the last source to

$$\boldsymbol{\sigma} = -B\kappa_1 \mathbf{k} \times (\nabla \delta(r)) , \tag{5.59}$$

such that Eqs. (5.48)-(5.50) have the asymptotic solutions

$$g_1 = DK_0(q_1 r) , \tag{5.60}$$

$$g_2 = CK_0(q_2 r) , \tag{5.61}$$

$$A_\theta = -BK_1(q_3 r) \quad , \quad A_r = A_z = 0 , \tag{5.62}$$

when the sources are given by Eqs. (5.57) and (5.59). This means that the vortex is described by two scalar monopoles and one magnetic monopole of charge D, C, and $-B$ for the monopoles ρ_1, ρ_2, and $\boldsymbol{\sigma}$ respectively.

The interaction energy of two vortices (a and b) in the point source approximation is[98]

$$G_I = -\int_\Omega d^3R \left(\rho_1^{(a)} g_1^{(b)} + \rho_2^{(a)} g_2^{(b)} + \boldsymbol{\sigma}^{(a)} \mathbf{A}^{(b)}\right) . \tag{5.63}$$

This energy may be calculated explicitly by inserting Eqs. (5.57) and (5.59)-(5.62) to give

$$G_I = B^{(a)}B^{(b)}K_0(q_3|r_a - r_b|) - D^{(a)}D^{(b)}K_0(q_1|r_a - r_b|) - C^{(a)}C^{(b)}K_0(q_2|r_a - r_b|) , \tag{5.64}$$

when the vortices, a and b, are located at r_a and r_b, respectively.

The interaction energy in Eq. (5.64) is a straight forward generalization of the interaction energy between Abrikosov vortices in one-component Ginzburg-Landau theory[98]. Far from the vortex the system must be in one of the minima of the potential, which are given by $\psi_1 = \pm 1$ and $\psi_2 = \pm\sqrt{a/b}$. Since both vortex (a) and vortex (b) asymptotically approach the same minimum and the order parameters goes from zero at the vortex center to the value at the minimum, the products $D^{(a)}D^{(b)}$ and $C^{(a)}C^{(b)}$ are always positive. The result is that when $q_{1,2} >> q_3$, the vortex-vortex interaction is always attractive.

The product $B^{(a)}B^{(b)}$, however, must depend on the vorticity, n, due to the boundary conditions. This means that $B^{(a)}B^{(b)} < 0$ when (a) and (b) have different polarity and $B^{(a)}B^{(b)} > 0$ when the polarity is the same. The result is that when $q_3 >> q_{1,2}$, the vortex-interaction depends on the polarity of the vortices and it is attractive for different polarities and repulsive for equal polarities.

In the case of ordinary Ginzburg-Landau theory, the vortex-vortex interaction vanishes when $\kappa = 1/\sqrt{2}$, which separates Type-I superconductors from Type-II superconductors[100]. The possibility for this scenario is easily seen from the interaction energy in Eq. (5.64), when the case of one-component superconductivity is considered, corresponding to $C^a = C^b = v_2 = 0$ and $v_1 = 1$ resulting in $q_1^2 = 2$ and $q_3^2 = 1/\kappa_1^2$. If the interaction due to the magnetic field should cancel with the interaction due to the order parameters it must, as a minimum, be required that $q_1 = q_3$ resulting in $\kappa_1 = 1/\sqrt{2}$, which is the value separating Type-I and Type-II superconductors in ordinary Ginzburg-Landau theory. Note, for the forces to cancel the factors in front of the modified Bessel functions should be equal, but the present analysis is not able to determine these factors. If the forces should have *a chance* of canceling in the two-component case, it must be required that $q_1 = q_2 = q_3$. For the case of zero Josephson coupling, $v_1^2 = 1$ and $v_2^2 = a/b$ which together with $q_1 = q_2 = q_3$ results in the condition

$$\kappa_1^2\kappa_2^2 = \frac{1}{2}\left(\kappa_1^2 + \kappa_2^2\right) \tag{5.65}$$

for the possibility of zero net vortex-vortex interaction. The other condition reads $B^{(a)}B^{(b)} - D^{(a)}D^{(b)} - C^{(a)}C^{(b)} = 0$, but as stated before there is no way of evaluating this condition from the present analysis. It is worth noting, though, that trivially extending the result from one-gap superconductors to $\kappa_1 = \kappa_2 = 1/\sqrt{2}$ does not work in Eq. (5.65). The reason is, that both order-parameters contribute to the effective London penetration-depth, $1/q_3$. In the case where the two order parameters are interchangeable, $\kappa_1 = \kappa_2$, one of the conditions for zero net vortex-vortex interaction is $\kappa_1 = \kappa_2 = 1$.

5.3 A Vortex Without a Magnetic Field

In the present section the simplified case of equal coherence lengths ($a = b = 1$), real order parameters, and no magnetic fields, $\mathbf{A} = 0$, are considered. Even in this simple case, interesting features in the form of topological defects are found. Both domain-walls and vortex type solutions are found even without magnetic fields which were an integral part of the Abrikosov vortex considered in the previous section.

5.3.1 Domain Walls

A domain wall linking two phases is considered first. Assuming $\psi_1 = \pm\psi_2$, the equations

$$\nabla^2\psi_1 + (1 \pm 2\eta)\psi_1 - \psi_1^3 = 0 \tag{5.66}$$

is obtained from Eqs. (5.4) and (5.6). Considering the case where ψ_1 is independent of the y-coordinate, a solution to the above equation becomes

$$\psi_1 = \sqrt{1 \pm 2\eta}\tanh\left(\sqrt{\frac{(1 \pm 2\eta)}{2}}\, x\right), \tag{5.67}$$

describing a domain wall located along the y axis. The solution is very similar to Eq. (2.30). The domain wall links two minima of the potential in Eq. (5.12). For $x \to -\infty$ the system is in one minimum and as $x \to \infty$ and the system then moves along the line $\psi_1 = \pm\psi_2$ to the minimum located opposite in the top left and bottom right plots of Fig. 5.1. Note, for $\eta > 0$ ($\eta < 0$) the solution with $\psi_1 = \psi_2$ ($\psi_1 = -\psi_2$) has a lower energy than the solution with $\psi_1 = -\psi_2$ ($\psi_1 = \psi_2$), see Eqs. (5.13) and (5.14).

Notice, that since the domain wall goes through $\psi_1 = \psi_2 = 0$ (the origin of the plots in Fig. 5.1), it has a normal region and is thus somewhat similar to what is called a SNS Josephson π-junction[101]. This is a Josephson junction where the order parameters of the two superconducting sides differs (at zero applied bias current) by π radians in the complex plane, i.e. $\psi(x \to -\infty) = -\psi(x \to \infty)$[102].

5.3.2 Textured Vortices

The domain wall shown in the previous section linked two minima of the potential in Eq. (5.12). The present section looks for so-called textured vortex solutions, which divides the superconductor into two

or four areas, each corresponding to a minimum of the potential. Two areas comes out if the potential only contains two equivalent minima and four if the potential contains four equivalent minima. Thus, the number of areas the superconductor is divided into depends on the presence of the Josephson coupling term, see Fig. 5.1.

The two real order parameters may be written as

$$\psi_1 = F(x,y)\cos\phi(x,y) \quad , \quad \psi_2 = F(x,y)\sin\phi(x,y) \ , \tag{5.68}$$

where F and ϕ denote amplitude and phase, respectively. The field equations

$$\nabla\cdot\left(F^2\nabla\phi\right) + 2\eta F^2\cos 2\phi + \frac{F^4}{4}\sin 4\phi = 0 \tag{5.69}$$

and

$$\nabla^2 F - F(\nabla\phi)^2 = \frac{F^3}{4}\left(3+\cos 4\phi\right) - F\left(1+2\eta\sin 2\phi\right) \tag{5.70}$$

are then obtained from Eqs. (5.4) and (5.6) with $\mathbf{A}=0$ and $a=b=1$.

An approximate analytical solution to Eqs. (5.69) and (5.70) in the far-field (near one of the minima of the potential) is obtained by assuming vanishing derivatives of F in Eq. (5.70), leading to $F=0$ or

$$F^2 = \frac{4\left(1+2\eta\sin 2\phi - (\nabla\phi)^2\right)}{3+\cos 4\phi} \ . \tag{5.71}$$

Inserting the latter expression into Eq. (5.69) and neglecting ∇F, the approximate equation

$$\nabla^2\phi + 4\eta\cos 2\phi + \frac{1}{2}\sin 4\phi = 0 \tag{5.72}$$

is obtained. The equation is valid for $\phi \approx \pi/4 + n\pi/2$ with $n = 1, 2, ...$, (i.e. $\cos 4\phi \approx -1$).

Requiring two-fold rotational symmetry, the boundary conditions become

$$|\psi_i(r,\chi)| = |\psi_i(r,\chi+n\pi)| \quad , \quad i=1,2 \tag{5.73}$$

where $n = 1, 2, ...$, thus

$$\phi(r,\chi) = \phi(r,\chi+n\pi) + n\pi \ , \tag{5.74}$$

where (r,χ) are polar coordinates in the (x,y) plane.

Appendix B shows that an approximate solution to Eqs. (5.72) and (5.74) may be written as

$$\phi = \frac{\pi}{4} \pm \tan^{-1}\left(\beta\ \mathrm{sc}\left(\frac{2K(m)}{\pi}\chi\middle|m\right)\right) \ , \tag{5.75}$$

where $\mathrm{sc}(s|m)$ is the Jacobi elliptic function $\mathrm{sc} = \mathrm{sn}/\mathrm{cn}$ with modulus m[42], which is determined by solving

$$\frac{2K(m)}{\pi} = r\sqrt{\frac{4c}{2-m}} \ , \tag{5.76}$$

$K(m)$ being the complete elliptic integral of the first kind[42]. β and c are given by

$$\beta = \sqrt{\frac{4c}{2c+4\eta-1}\ \frac{1-m}{2-m}} \tag{5.77}$$

and

$$c = \frac{2-m}{2m}\left(\frac{2-m}{m} + \sqrt{\left(\frac{2-m}{m}\right)^2 - 1 + 16\eta^2}\right) \ . \tag{5.78}$$

Thus, m depends on r as well as η.

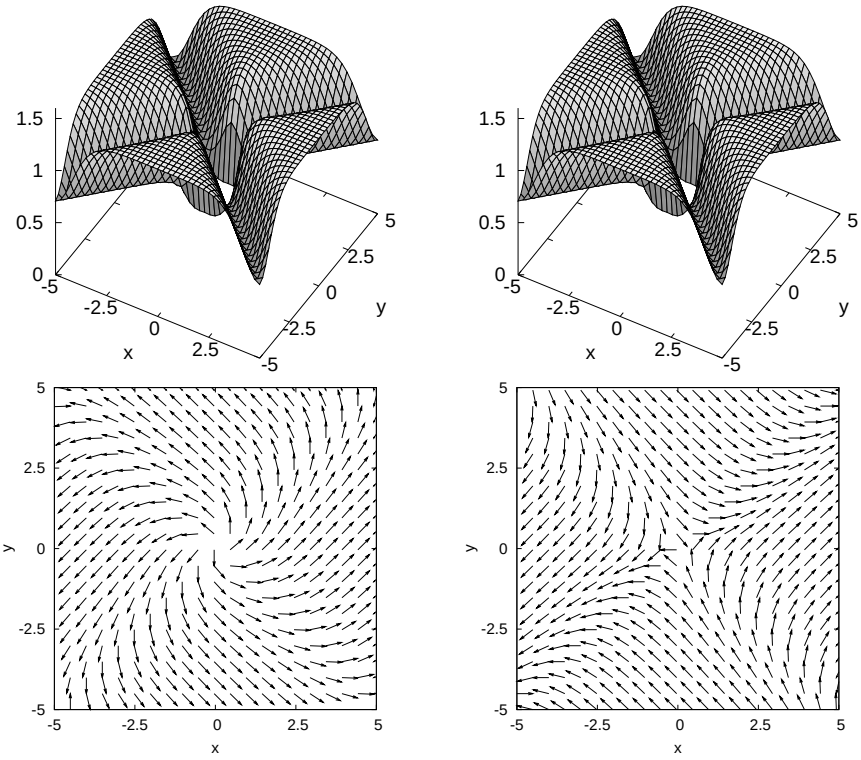

Figure 5.3: Far-field solution. Top row: F given by Eq. (5.71). Bottom row: Vector $(\cos\phi, \sin\phi)$ (not to scale). ϕ given by Eq. (5.75). $\eta = 0$. Left: Vortex (+ in Eq. (5.75)). Right: Anti-vortex (- in Eq. (5.75)). F^2 in Eq. (5.71) becomes negative near the origin, signaling the breakdown of the far-field assumption.

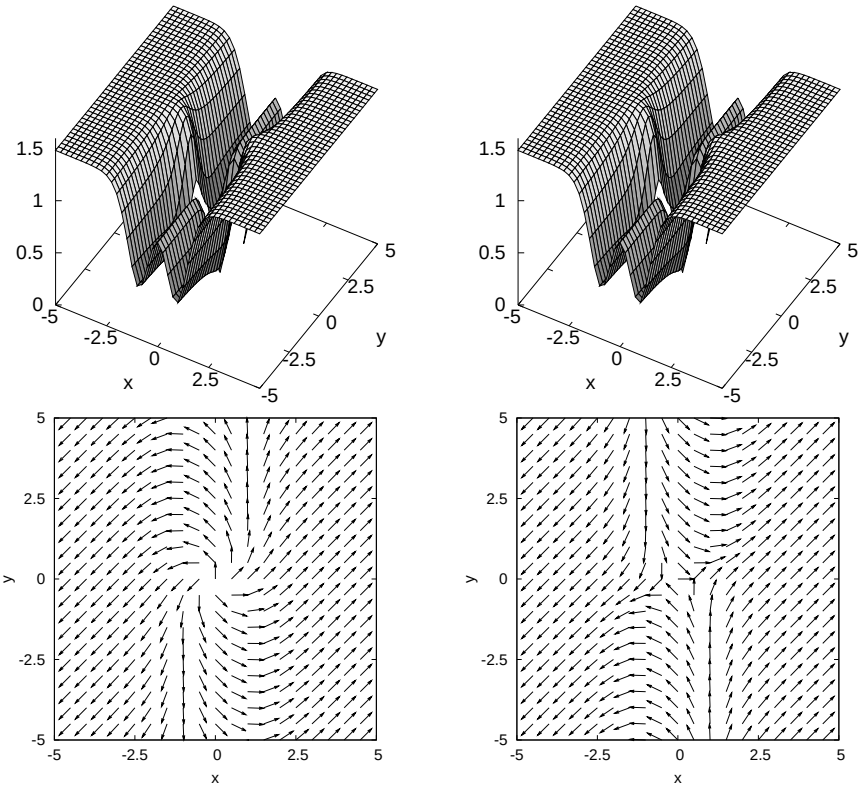

Figure 5.4: Far-field solution. Top row: F given by Eq. (5.71). Bottom row: Vector $(\cos\phi, \sin\phi)$ (not to scale). ϕ given by Eq. (5.75). $\eta = 0.05$. Left: Vortex (+ in Eq. (5.75)). Right: Anti-vortex (- in Eq. (5.75)). F^2 in Eq. (5.71) becomes negative near the origin, signaling the breakdown of the far-field assumption.

For $\eta = 0$, the two-fold symmetric boundary conditions, Eq. (5.73), become four-fold symmetric, Eqs. (5.73) and (5.74) hold when n is half-integer, and

$$\phi = \tan^{-1}\left(\frac{\sinh(y/\sqrt{2})}{\sinh(x/\sqrt{2})}\right) \ . \tag{5.79}$$

becomes an *exact* solution to Eq. (5.72)[103].

Figs. 5.3 and 5.4 show the analytical solution F, given by Eq. (5.71), and the vector $(\cos\phi, \sin\phi)$, ϕ given by Eq. (5.75), for zero and non-zero value of the Josephson type coupling strength, η. Comparing Figs. 5.3 and 5.4, it is clearly seen that the presence of the Josephson coupling term breaks the 4-fold symmetry since the system only contains two equivalent minima.

5.3.3 Numerical Solutions

First, the textured vortex solutions for $\eta = 0$, described by Eqs. (5.71) and (5.79), are considered. Using this analytical far-field solution as initial conditions for the numerical procedure discussed in Section 2.1.1, the plots in the left column of Figs. 5.5 and 5.6 have been obtained. Note, the initial conditions in the square geometry have been rotated to fit the symmetry of the geometry. The overall agreement between these plots and the plots in Fig. 5.3 is quite good, except near the origin where the numerical solution has $F = 0$ which is far from the assumptions made in the derivation of Eqs. (5.71), (5.75) and (5.79).

Next, the solutions for $\eta \neq 0$ are obtained as function of "time" by using the numerical solutions for $\eta = 0$ (just obtained) as initial conditions for the numerical procedure. The result is shown in Figs. 5.5 and 5.6. The left column is the initial conditions, the middle column is the solution at a selected time, and the right column is the numerical solution after convergence of the numerical procedure. The four-fold symmetric solution for $\eta = 0$ develops towards a two-fold symmetric solution for $\eta \neq 0$. The presence of the η-term changes the energy densities of the four phases, such that two of them has lower energy density than the other two, leading to a motion of the domain walls to minimize the area of the high-energy domains. This development occurs faster in the circular case (Fig. 5.6 shows only two domains at $t = 70$) than in the square case (Fig. 5.5 still has all four domains at $t = 327$). The difference between the "dynamics" in the square and circular geometries is caused by the Neumann boundary conditions in Eqs. (5.5) and (5.7) with $\mathbf{A} = 0$, which require that the domain walls are perpendicular to the boundary of the system. They counter-act the minimization of the high-energy domains in the square geometry. Thus, a complete elimination of the high energy domains occur for the circular case, while all four domains remain in the square case. From this it is evident that by changing η in the square geometry, the domain sizes may be changed.

To study the difference between the numerical solutions in Figs. 5.5 and 5.6, the winding number, n, is calculated using[103]

$$2\pi n \equiv \oint_C \left(\partial_x \phi(x,y)dx + \partial_y \phi(x,y)dy\right), \tag{5.80}$$

where C is an arbitrary contour around the vortex and ϕ is defined in Eq. (5.68). For vortex and anti-vortex solutions n is an integer different from zero, n positive (negative) corresponds to a vortex (anti-vortex). In Fig. 5.7, n is plotted as a function of "time" for the two cases corresponding to Figs. 5.5 and 5.6. The curve C have been chosen as a circle, centered at the origin. Two different radii have been used in each case, $r = 7$ and $r = 11$. The figure shows, that in the square case the vortex remains (i.e. $n \approx 1$ as t increases) but for the circular case the vortex moves out of the system (i.e. $n \to 0$, after reaching a maximum value, as t increases). Note that n differs from unity earlier for $r = 7$ than for $r = 11$ in agreement with the outwards vortex motion.

The Neumann boundary conditions used in the numerical simulations causes the difference between the dynamics of the square and circular geometries. For the circular system with a vortex at the exact center, the Neumann boundary conditions correspond to an image anti-vortex located at infinity. When the vortex is not located exactly at the center, the image anti-vortex lies at a finite distance. The attraction between the vortex and the image anti-vortex results in a motion of the vortex along the domain wall. For the square case, the boundary conditions lead to to multiple image anti-vortices located outside the system, thus creating a more stable state than in the circular geometry. Note, that for coarser discretization of the equations, vortex motion is also observed in the square system. Thus,

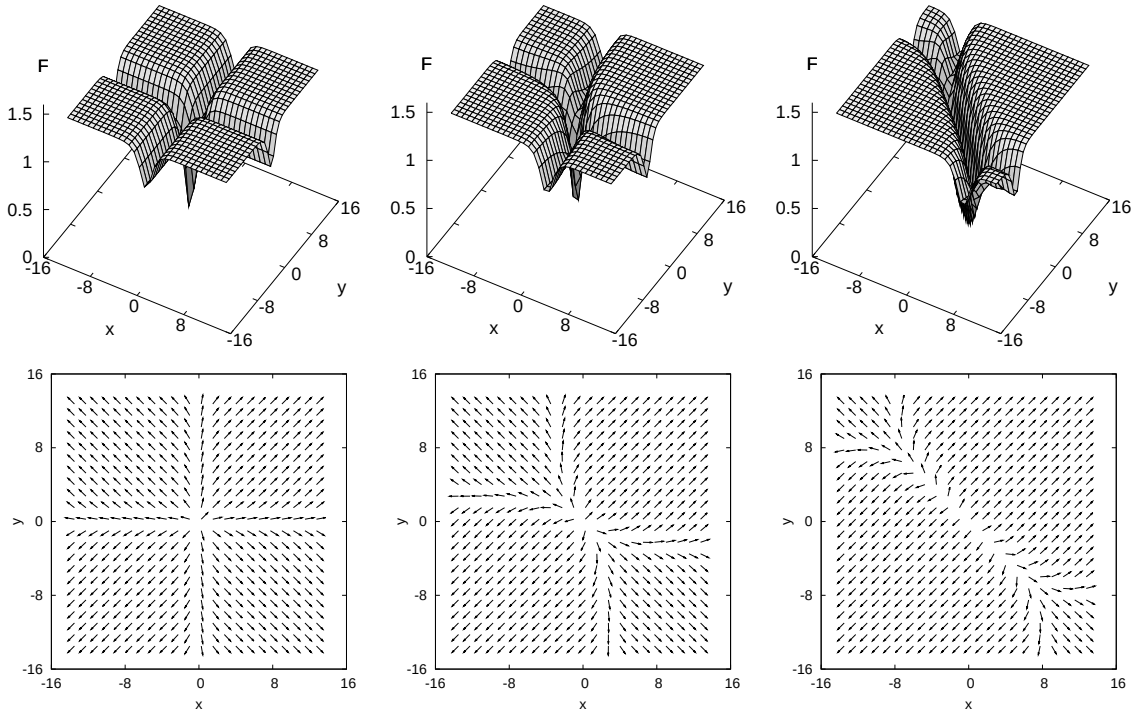

Figure 5.5: Square geometry: "Time"-evolution of F (upper) and the vector $(\cos\phi, \sin\phi)$ (lower) for $\eta = 0.02$. Initial conditions: Numerical solution for $\eta = 0$. Snapshots at: $t = 0$ (left, initial conditions), $t = 35$ (middle), and $t = 327$ (right, final stage).

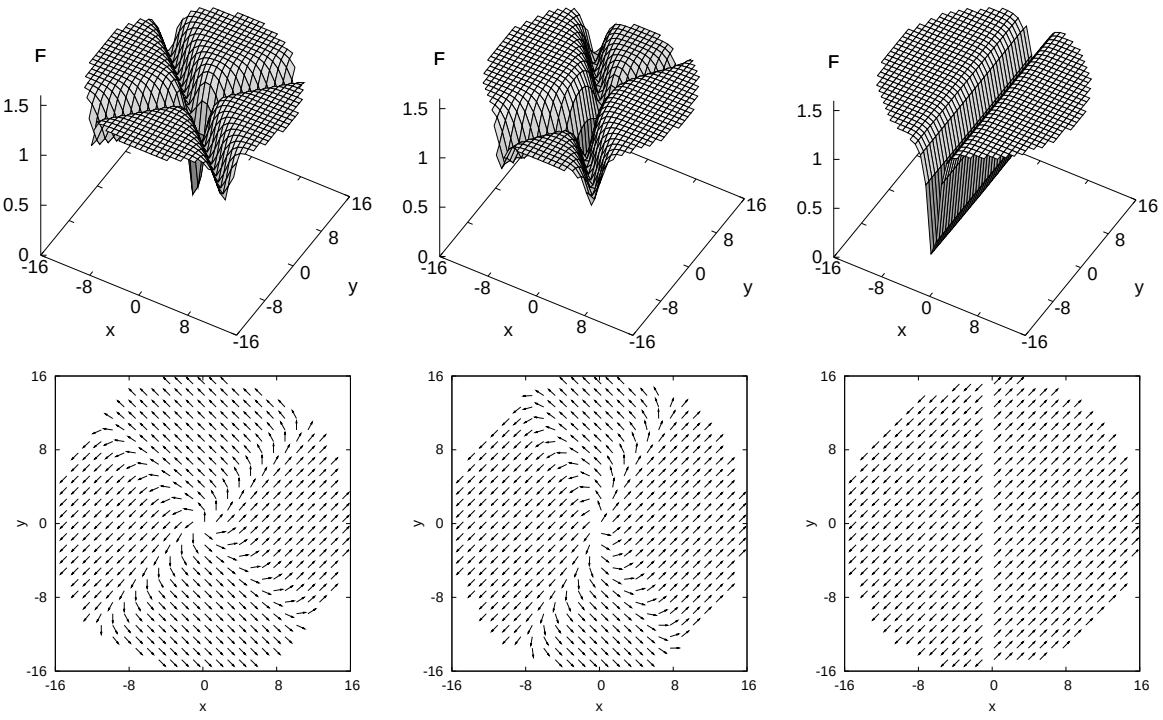

Figure 5.6: Circular geometry: "Time"-evolution of F (upper) and the vector $(\cos\phi, \sin\phi)$ (lower) for $\eta = 0.05$. Initial conditions: Numerical solution for $\eta = 0$. Snapshots at: $t = 0$ (left, initial conditions), $t = 14$ (middle), and $t = 70$ (right, final stage).

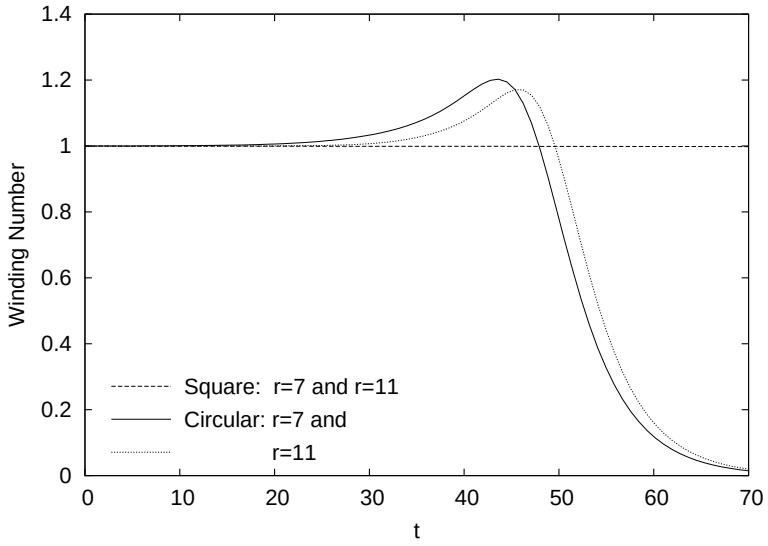

Figure 5.7: Winding number, n, given by Eq. (5.80) for square (Fig. 5.5) and circular (Fig. 5.6) geometry. In the square geometry, the vortex present at $t = 0$ remains in the system, i.e. $n \approx 1$ also for $t > 70$ (not shown). In the circular geometry the vortex disappears after approximately 70 time units.

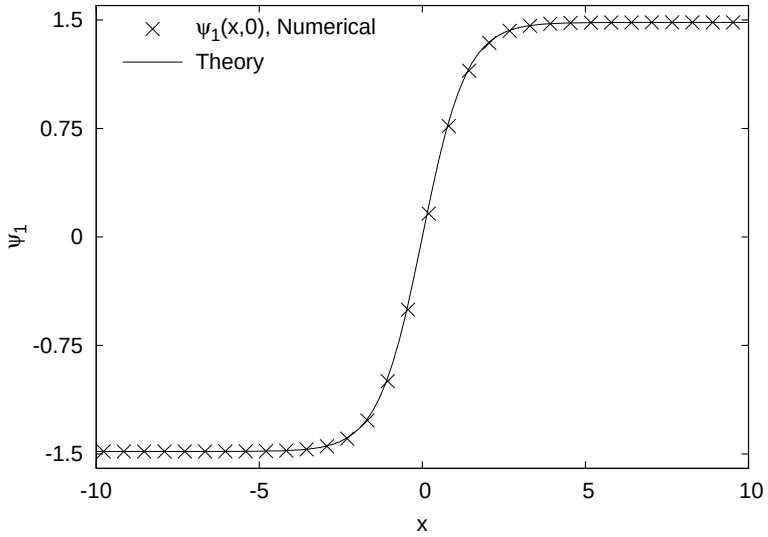

Figure 5.8: $\psi_1(x, 0)$ (crosses) from numerical solution in circular geometry (Fig. 5.6, $t = 70$, $\eta = 0.05$). The analytical domain wall solution in Eq. (5.67) (line) fits the numerical data. Since $\eta > 0$ $\psi_1 = \psi_2$.

the difference between the dynamics in the square and circular geometry is due to finite size effects which seem to play a major role.

For the circular geometry with $\eta = 0.05$ a system with only two phases linked by a domain wall is obtained numerically. This is precisely the domain wall solution found in Eq. (5.67). To check this, Fig. 5.8 shows the expression given by Eq. (5.67) as well as $\psi_1(x, 0)$ from the data in the right column of Fig. 5.6. The agreement is seen to be excellent.

The solution for $\eta \neq 0$ plotted in Fig. 5.4 is not observed as a stationary state in the numerical simulations. However, the solution in the middle column of Figs. 5.5 and 5.6 and in the outer part of the 2nd and 4th quadrant of the square in the right column of Fig. 5.5 possess some resemblance to the analytical solution plotted in Fig. 5.4. The corresponding expression in Eq. (5.75) was derived for the static case near $F^2 = 2(1 \pm 2\eta)$. Thus, such a resemblance may not be expected to hold near the origin and along the domain wall (shown in Fig. 5.6) which separates the two low-energy phases, since F^2 is here very different from $2(1 \pm 2\eta)$.

The average energy densities of the initial state (for $\eta = 0$) and final state (for $\eta \neq 0$) solutions considered in Figs. 5.5 and 5.6 are roughly $10\% - 20\%$ higher than the energy density of the homogenious

Meissner state $\psi_1 = \pm\psi_2 = \sqrt{1 \pm 2\eta}$, thus the domain wall and textured vortex solutions are excited states.

5.4 Textured Vortex in a Magnetic Field

The previous section dealt with the textured vortex solution which can be found in the two-component Ginzburg-Landau theory. The two-component Ginzburg-Landau equations were solved analytically and numerically with zero magnetic field and real order parameters, but generally the order parameters are complex and couple to the magnetic field. To get some insight into the behavior of the textured vortex in a magnetic field, this section will look at some numerical calculations where a magnetic field is applied to the edge of a superconductor containing a textured vortex. These calculations are instructive for formulating an analytical analysis of the problem, which will, however, not be done in this thesis. Only the case of a square geometry will be considered, since the vortex disappeared in the circular case with non-zero Josephson coupling shown in Fig. 5.6.

The first calculation shows how the textured vortex for $\eta = 0$ (shown in the left plots of Fig. 5.5) evolve in time when a very small magnetic field is applied to the system. Fig. 5.9 shows the magnetic field and the total Cooper-pair density, $|\psi|^2 = |\psi_1|^2 + |\psi_2|^2$ (not normalized to 1), at selected times when the system is started out in the textured vortex state and then applied a magnetic field of only $B_z^a = 0.01$ with $\kappa_1 = \sqrt{2}$, $a = b = 1$, and $\eta = 0$. The dashed square marks the edges of the superconductor and outside this dashed square $\psi_1 = \psi_2 \equiv 0$. Note that the color-axis is different among the plots. The change of the system is quite dramatic even with such a small applied field. The magnetic field penetrates the superconductor through all four domain walls of the vortex which seem to act like channels for magnetic pulses, traveling to the vortex center. In this process, the domain walls are washed out and a circulating current is generated around the vortex core (not shown). In the final plots, the vortex looks much like an Abrikosov vortex with a maximum magnetic field of $B_z \approx 0.4$ at the center, much larger than the applied field. Convergence is reached at $t = 93.6$, but indistinguishable to the naked eye from the plots at $t = 17.1$. The complex phases of the two order parameters from the converged solution are shown in Fig. 5.10. The phase does not change continuously around the vortex, as assumed in Eq. (5.19), but rather the change is localized to small areas where the domain walls of the textured vortex used to be and the complex phases have some resemblance to the phase ϕ in Eq. (5.79). Note that the two phases are rotated by $\pi/2$ relative to each other meaning that $\psi_1 \neq \psi_2$, which is not surprising since the initial textured vortex state also had $\psi_1 \neq \psi_2$.

Fig. 5.11 shows a calculation similar to the one in Fig. 5.9 but with $\eta = 0.02$. In the initial state the domain-sizes are changed by the Josephson coupling as compared to the textured vortex with $\eta = 0$ resulting in the state in the right plot of Fig. 5.5. Again the magnetic field penetrates the superconductor through the domain walls and travels to the vortex center, creating an Abrikosov vortex. Convergence is reached at $t = 63.1$, but to the naked eye the state is no different than the one at $t = 13.2$ in Fig. 5.11. In terms of $|\psi_1|^2 + |\psi_2|^2$ and B_z, the vortex looks no different from the final state in Fig. 5.9, but the complex phases shown in Fig. 5.12 does not look like Fig. 5.10. Again the complex phases change in localized places, similar to the phase in Eq. (5.75) for $\eta = 0.02$ but unlike Fig. 5.10, the phases for $\eta = 0.02$ seems to be equal. This may be the effect of the Josephson coupling, in agreement with Fig. 5.2 where it was found that the presence of the Josephson coupling neutralizes the difference between the two order parameters.

Applying a large magnetic field to the superconducting sample creates Abrikosov vortices, which enter through the boundaries. Fig. 5.13 shows a calculation where a magnetic field of $B_z^a = 0.7$ has instantaneously been applied to the textured vortex solution for $\eta = 0$, $\kappa_1 = \sqrt{2}$, and $a = b = 1$. Abrikosov vortices start to enter through the boundaries, but the first four vortices which enter do this in an unconventional way. At $t = 17.6$ it is easy to see that there are vortices in the $|\psi_1|^2$ and $|\psi_2|^2$ plots which are not located at the same positions. These four vortices shows up in the $|\psi_1|^2 + |\psi_2|^2$ plot as elliptical dots which does not have a normal core. These vortices are characterized by having a phase change in only one of the order parameters and the flux is thus given by Eq. (5.18) with either $n_1 = 0$ or $n_2 = 0$ which is not quantized in terms of Φ_0. Looking at the plots at $t = 68.6$, the separate vortices in each order parameter have, however, merged and created the usual Abrikosov vortex (they are now located closest to the vortex at the center). This suggests that vortices with only a phase-change in one of the order parameters (i.e. n_1 or n_2 in Eq. (5.18) is zero) is energetically unfavorable over the usual Abrikosov vortex ($n_1 = n_2$), which is also stated in Ref. [96].

A calculation similar to the one in Fig. 5.13 has been made using the textured vortex for $\eta = 0.02$ as

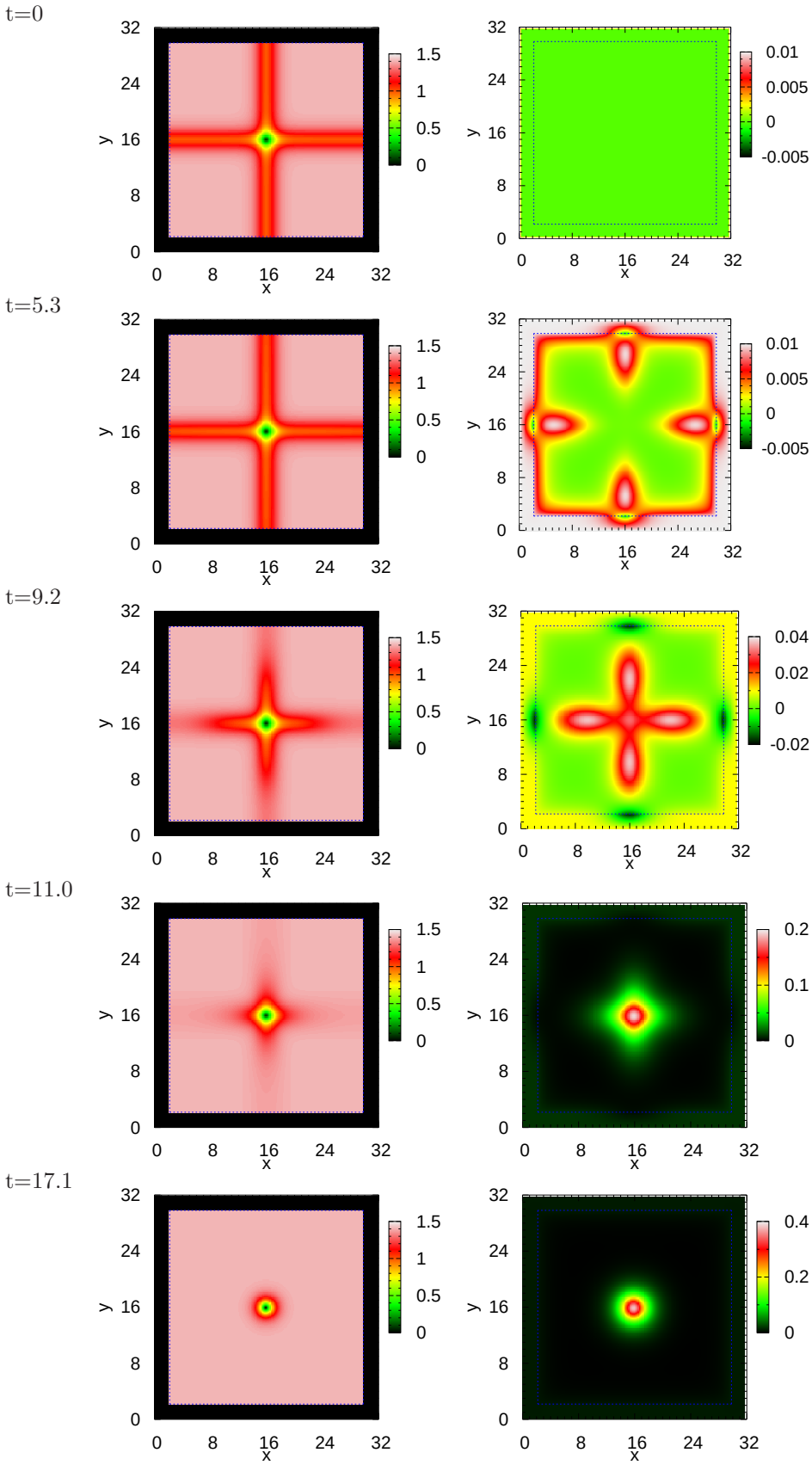

Figure 5.9: Applying a small magnetic field, $B_z^a = 0.01$, to the textured vortex for $\eta = 0$ has dramatic effects. Shown at selected times are $|\psi_1|^2 + |\psi_2|^2$ (left) and B_z (right) for $\kappa_1 = \sqrt{2}$, $a = b = 1$, and $\eta = 0$. Note the color-axis changes among the plots. The textured vortex disappears and an Abrikosov vortex is created. The dashed line marks the edges of the superconductor.

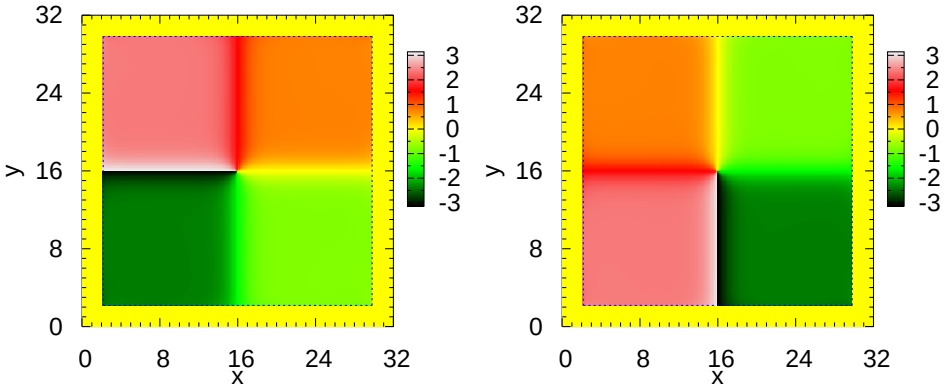

Figure 5.10: The complex phases of the order parameters after applying a small magnetic field, $B_z^a = 0.01$, to the textured vortex for $\eta = 0$. Left is $\phi_1(x, y)$ and right is $\phi_2(x, y)$ with $\psi_i = n_i(x, y)e^{i\phi_i(x,y)}$. The change in complex phase around the Abrikosov vortex at the center of the superconducting sample is localized to the places where the domain walls of the textured vortex used to be. The dashed line marks the edges of the superconductor.

initial conditions. The calculation is not shown but looks very similar to the one for $\eta = 0$, except that the vortices with $n_1 \neq n_2$ enters in different places, because the domain walls attach to the boundaries in different places.

5.5 Conclusion

The two-component Ginzburg-Landau theory was discussed in connection with two-gap superconductivity. A small energy analysis was performed, which is instructive in order to discuss topological defects in the theory. The Abrikosov vortex was discussed first and generalized from the one-component Ginzburg-Landau theory in the case where one of the coherence lengths was much longer than the other, which is the case in MgB_2. The Josephson tunneling of Cooper-pairs from one order parameter to the other was seen to wash out the differences arising from the two very different coherence-lengths. The interaction between Abrikosov vortices was then discussed briefly and the subject of Type-I vs. Type-II behavior was discussed. This division is not as clear-cut in the two-component theory as in the one-component theory.

The subject of domain walls and textured vortices in the two-component Ginzburg-Landau theory was investigated analytically and numerically. The effect of the Josephson coupling on the textured vortex was considered in detail. Without Josephson coupling a textured vortex solution is found and for non-zero Josephson coupling this textured vortex develops into a domain wall. As a consequence, the vortex is lost in the system. By changing the geometry of the system, boundary effects may prevent escape of the vortex.

Subjecting the textured vortex solution to an applied magnetic field proved to be disastrous for the solution. Even a very small magnetic resulted in the vanishing of the vortex and the creation of an Abrikosov vortex with an unusual change in complex phase. A high magnetic field created Abrikosov vortices in the system, entering through the boundaries. It was seen that vortices with a phase-change of 2π in only one of the order parameters were created initially at the boundaries, but later they developed into the usual Abrikosov vortex.

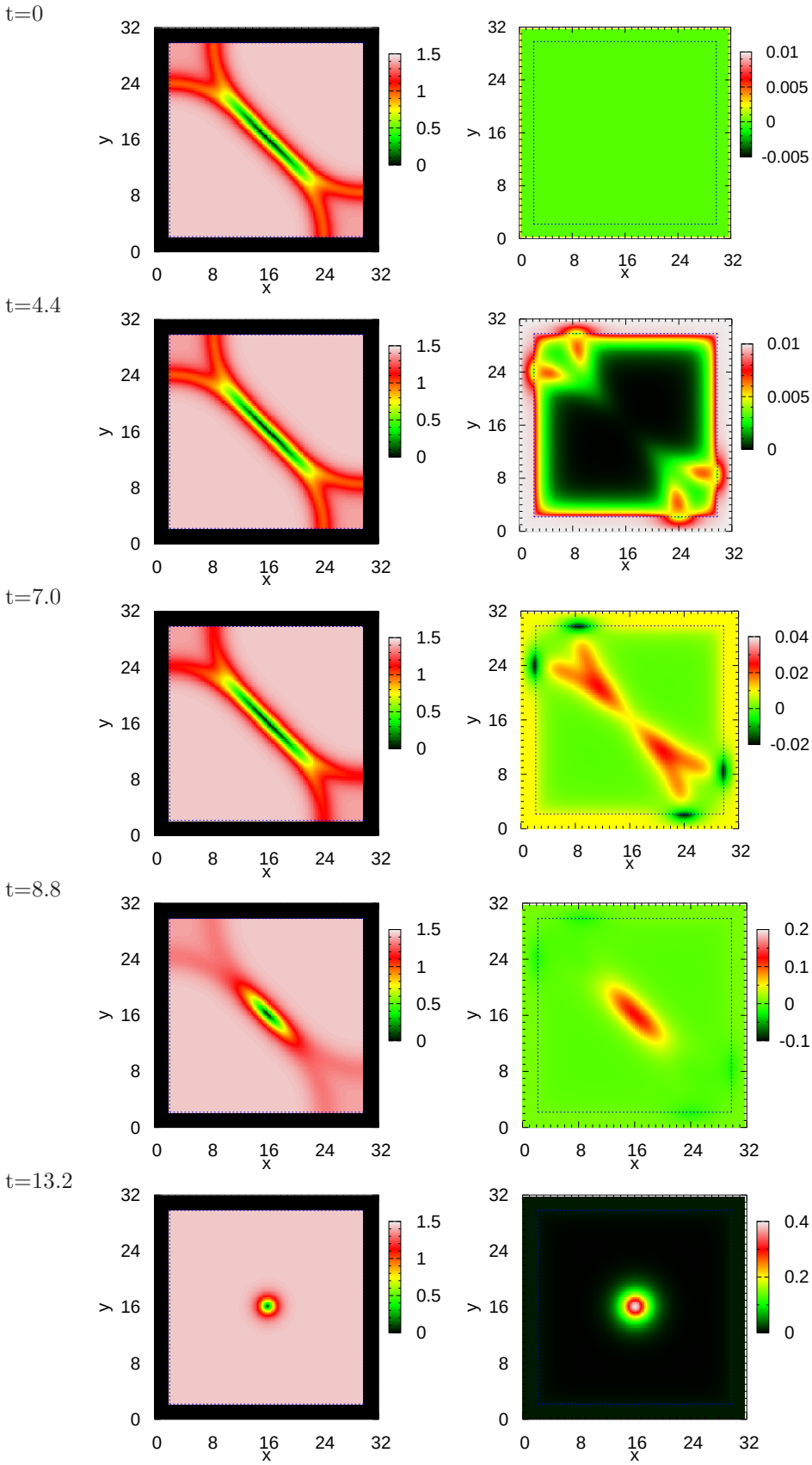

Figure 5.11: Applying a small magnetic field, $B_z^a = 0.01$, to the textured vortex for $\eta = 0.02$ has dramatic effects. Shown at selected times are $|\psi_1|^2 + |\psi_2|^2$ (left) and B_z (right) for $\kappa_1 = \sqrt{2}$, $a = b = 1$, and $\eta = 0.02$. Note the color-axis changes among the plots. The textured vortex disappears and an Abrikosov vortex is created. The dashed line marks the edges of the superconductor.

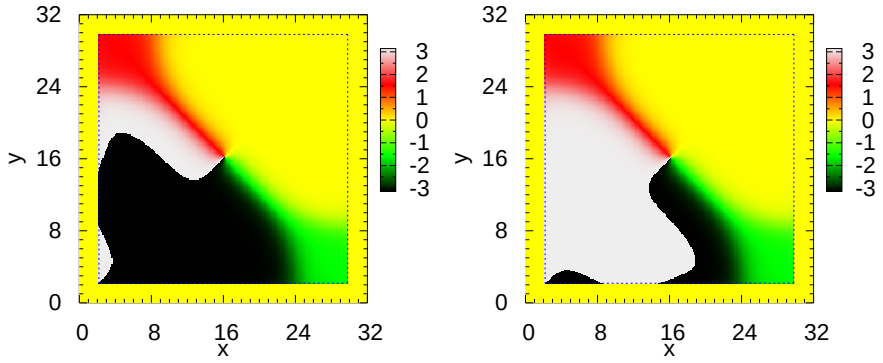

Figure 5.12: Complex phases of the order parameters after applying a small magnetic field, $B_z^a = 0.01$, to the textured vortex for $\eta = 0$. Left is $\phi_1(x, y)$ and right is $\phi_2(x, y)$ with $\psi_i = n_i(x, y)e^{i\phi_i(x,y)}$. The change in complex phase around the Abrikosov vortex at the center of the superconducting sample is localized to the places where the domain walls of the textured vortex used to be. The abrupt jump from black to white is a phase-jump from $-\pi$ to π. The dashed line marks the edges of the superconductor.

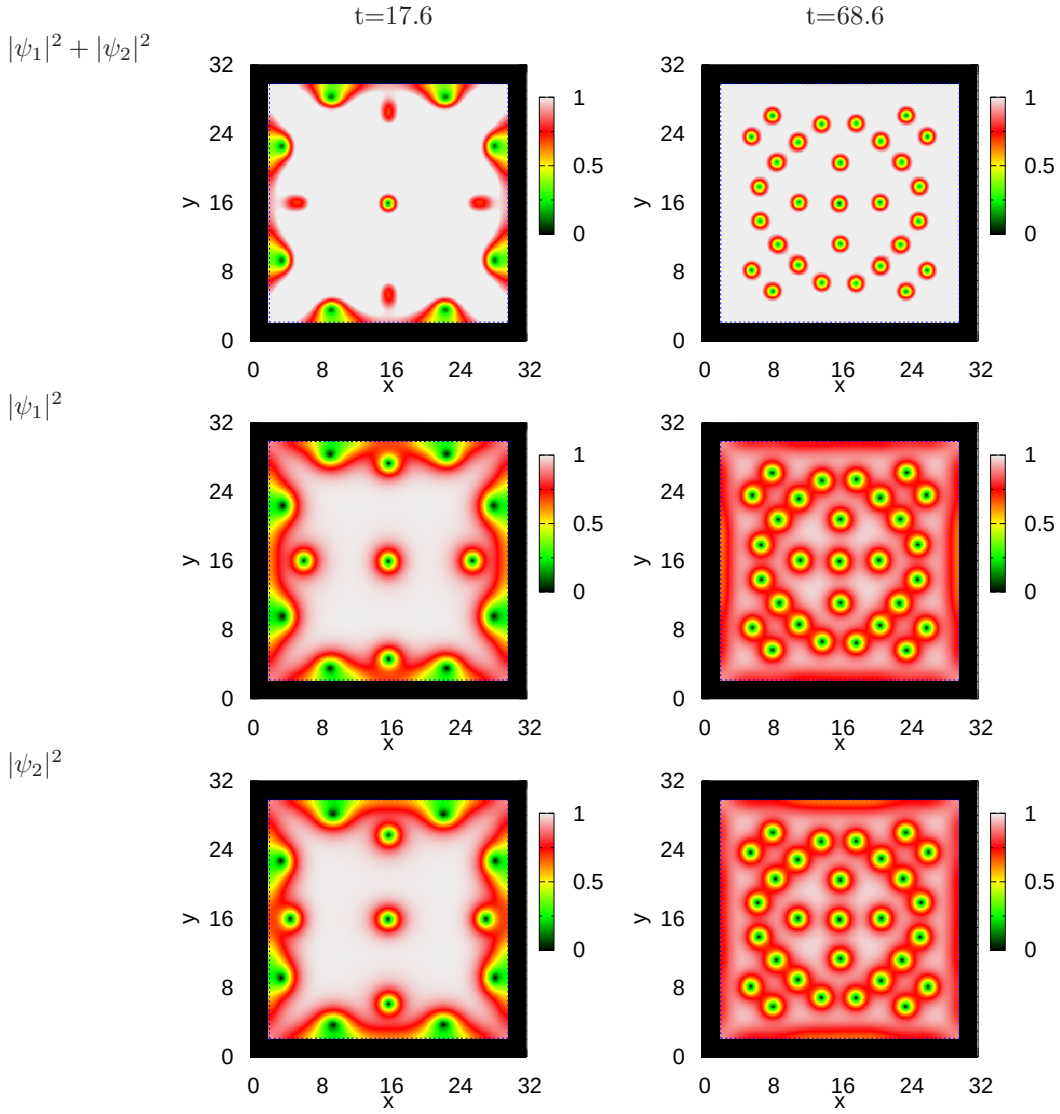

Figure 5.13: Applying a large magnetic field, $B_z^a = 0.7$, to the textured vortex for $\eta = 0$. Shown at selected times are $|\psi_1|^2 + |\psi_2|^2$ (top), $|\psi_1|^2$ (middle), and $|\psi_2|^2$ (bottom) for $\kappa_1 = \sqrt{2}$, $a = b = 1$, and $\eta = 0$. The textured vortex disappears as in Fig. 5.10 and Abrikosov vortices enters through the boundaries. Note, four vortices do not have a normal core at $t = 17.6$, but the normal core is obtained at $t = 68.6$. The dashed line marks the edges of the superconductor.

Chapter 6

Conclusion

The subject of this thesis is to investigate vortices in different superconducting systems, with special emphasis on the new materials such as BSCCO and MgB_2. The two systems are very different, but both posses some unique properties and interesting vortex solutions.

In Chapter 3 the model of a stack of long Josephson junctions was introduced and some solutions were discussed. The easily obtainable plasma-solutions was investigated in connection with the non-linear fluxon solutions. Some solutions had an empty junction and was shown to exists as both plasma and fluxon solutions. A possible relationship between linear and non-linear modes was investigated through numerics. Plasma solutions and fluxon solutions having similar features were found, but not every plasma solution had a corresponding fluxon solution. Since the method was purely empirical, no deeper relationship between linear and non-linear solutions can be made from this study.

In Chapter 4, Josephson stacks were considered as an oscillator. The power available for radiation was calculated for different fluxon solutions. The in-phase fluxon solutions had by far the most available power and it did not matter too much that the outer junctions had in some cases switched to finite voltage. With weakly coupled junctions in mind, bunching of the shuttling fluxon solutions were investigated. The conditions for bunching using an external microwave field were derived analytically and numerically. It was shown, that an external microwave field is able to induce bunching, but only in the weakly coupled system, thus the method will not work for high T_c superconductors. A stack of junction was considered to be coupled to a cavity. The cavity equation was solved, and resonances were shown analytically and numerically to exist in the cavity current. It was also shown, that the cavity essentially acts as a microwave source and it will thus be able to induce bunching, but again only for weakly coupled stacks. For strongly coupled stacks, the flux-flow modes seem to be the best solution to obtain bunched states and thereby increase the power of the emitted radiation. The current-voltage characteristics were calculated for different stacks operated in the flux-flow mode. By looking directly at the phases for the individual junctions, the formation of a square lattice was found. The flux-flow modes was typically forming a triangular lattice, but sometimes, the square lattice would spontaneously form even for strongly coupled junctions.

The possibilities to extend the present studies of the Josephson stack are many. The stack-cavity system was proven to provide a method of bunching in weakly coupled junctions, but a detailed study of the parameters needed for phase-locking and bunching in the system is still missing. BSCCO crystals are receiving a lot of interest in the research community and the flux-flow modes seemingly provide a way of obtaining coherent radiation from BSCCO crystals. These systems are very hard to study analytically, since the inductive coupling is extremely strong and perturbation methods do not work well. Furthermore, the numerical calculations on flux-flow modes in this thesis showed that the square lattice formed at low fluxon-density where non-linear effects are very strong. This adds to the complexity of the problem of finding the conditions for the formation of a square lattice, since the linear cavity modes may not be good enough in this region. And to make things even more complicated, Koshelev and Aranson found in Ref. [104] that in-plane dissipation is important for BSCCO. This dissipation can not be accounted for by the α-term in the equations used in this thesis, and more complex equations results. Josephson stacks will undoubtedly be actively studied for years to come.

The concept of two-gap superconductivity was considered in Chapter 5 by the use of a two-component Ginzburg-Landau model. The Abrikosov vortex in this model was investigated analytically and the effect of a Josephson type coupling was considered. This coupling describes tunneling of Cooper-pairs from one order parameter to the other, and it was shown to diminish the differences between the two order

parameters. The vortex-vortex interaction was also discussed, though only in the case of zero Josephson coupling. It was shown, that Type-I and Type-II superconductivity is not trivially defined for a two-component system. Since new degrees of freedom arise due to the extra order parameter, a textured vortex could be found in the theory for zero magnetic field. The vortex showed depression of the order parameters without the need for a magnetic field as in the case of an Abrikosov vortex. The effects of applying a magnetic field to a textured vortex solution were discussed and it was found that the vortex is unstable even in a tiny magnetic field.

MgB_2 is very actively studied at the moment. The preliminary analysis of a two-component system presented in this thesis, shows that two-component superconductors has some interesting properties and can be quite different from ordinary superconductors. The effect of the Josephson coupling on the vortex-vortex interaction would be a good starting-point for extending the analysis of this thesis. This could also lead to a classification of two-component superconductors into different types. The effects of anisotropy and more advanced theories than the two-component Ginzburg-Landau theory used here would also be interesting research subjects for future studies. Of particular interest could be numerical calculations of vortices in mesoscopic system using the extension of the two-component Ginzburg-Landau model presented in Ref. [90].

The possibility for exotic vortex solutions in the two-component Ginzburg-Landau model was also considered in this thesis. It would be interesting if some new topological defects could be found experimentally. This would of cause have importance for two-gap superconductivity, but also more exotic physics could benefit from such a discovery[105]. Unfortunately, many studies have been conducted on MgB_2 and no evidence for such structures have, to the authors knowledge, been found yet.

Appendix A

Publications by S. Madsen

Previous Publications

1. Classification of string-like solutions in dilaton gravity
Y. Verbin, S. Madsen, A. L. Larsen, and M. Christensen
Phys. Rev. D **65**, 063503 (2002)

2. Self-dual cosmic strings and gravitating vortices in gauged sigma models
Y. Verbin, S. Madsen, and A. L. Larsen
Phys. Rev. D **67**, 085019 (2003)

Publications in connection with the present Ph.D. project

3. Fluxon Modes in Stacked Josephson Junctions - The Role of Linear Modes
S. Madsen and N. F. Pedersen
Phys. Rev. B **69**, 064507 (2004)
Also published in: Virtual Journal of Applications of Superconductivity **6**, Issue 5, March 1 (2004)

4. Fluxon Modes and Microwave Emission in BSCCO Type Josephson Stacks
N. F. Pedersen and S. Madsen
Supercond. Sci. Technol. **17**, S117-S121 (2004)
Also published in: IOP Conf. Series **181**, 253-259, IOP Publishing Ltd., Bristol and Philadelphia (2004)

5. Fluxon modes in stacked Josephson junctions
N. F. Pedersen and S. Madsen
Physica C **404**, 273-280 (2004)

6. Interaction between a BSCCO-type intrinsic Josephson junction and a microwave cavity
S. Madsen, G. Filatrella and N.F. Pedersen
Eur. Phys. J. B **40**, No. 2, 209-215 (2004)

7. Microwave oscillator based on an intrinsic BSCCO-type Josephson junction
N.F. Pedersen and S. Madsen
IEEE Trans. Appl. Supercond. **15**, No. 2, 948 (2005)

8. Vortices in Two-Component Ginzburg-Landau Theory
S. Madsen, Yu. B. Gaididei, P. L. Christiansen, and N. F. Pedersen
Proceedings for the Plasma 2004 Conference in Tsukuba, Japan, II-128 (2004)

9. Numerical Simulations on intrinsic Josephson junctions: Building a microwave oscillator
N. F. Pedersen and S. Madsen
Proceedings for the Plasma 2004 Conference in Tsukuba, Japan, II-48 (2004)

10. Microwave induced fluxon bunching in weakly coupled Josephson junctions
S. Madsen and N. Grønbech-Jensen
Phys. Rev. B. **71**, 132506 (2005)
Also published in: Virtual Journal of Applications of Superconductivity **8**, Issue 9, May 1, 2005

11. Domain walls and textured vortices in a two-component Ginzburg-Landau model
S. Madsen, Yu. B. Gaididei, P. L. Christiansen, and N. F. Pedersen
Phys. Lett. A **344**, Issue 6, 432 (2005)

12. Numerical Simulations of Flux Flow in Stacked Josephson Junctions
S. Madsen and N. F. Pedersen
Phys. Rev. B **72**, 134523 (2005)
Also published in: Virtual Journal of Applications of Superconductivity **9**, Issue 9, November 1 (2005)

13. Search for the In-phase Flux Flow Mode in Stacked Josephson Junctions
N. F. Pedersen and S. Madsen
Accepted for publication in Physica C (2005)

Appendix B

Approximate Solution of Eq. (5.72)

The partial differential equation

$$\nabla^2\phi + a\cos 2\phi + b\sin 4\phi = 0 \ , \tag{B.1}$$

is considered, which for $a = 4\eta$ and $b = 1/2$ becomes Eq. (5.72). Following Ref. [103] the approximation $\nabla^2\phi \approx \phi''/r^2$ is made where primes denotes differentiation with respect to the angular coordinate, χ. Equation (B.1) then reduces to

$$\frac{1}{r^2}\phi'' + a\cos 2\phi + b\sin 4\phi = 0 \ , \tag{B.2}$$

which shall be solved subjected to the boundary conditions in Eq. (5.74). Introducing the auxiliary variable $\varphi \equiv \phi - \pi/4$ and integrating,

$$\frac{1}{2r^2}(\varphi')^2 + \frac{a}{2}\cos 2\varphi + \frac{b}{4}\left(\cos 4\varphi + 3\right) = c \tag{B.3}$$

is obtained, where the integration constant is conveniently chosen as $c - 3b/4$. The analysis is limited to solutions where $c > \frac{a}{2} + b > 0$, and the auxiliary variable $t \equiv \tan\varphi$ is introduced. Eq. (B.3) may now be re-arranged as

$$\frac{dt}{\sqrt{(t^2+\alpha^2)(t^2+\beta^2)}} = \pm r\sqrt{2c + a - 2b}\ d\chi \ , \tag{B.4}$$

which integrates into

$$\mathrm{F}\left(\tan^{-1}\frac{t}{\beta}\Big|m\right) = \pm\alpha r\sqrt{2c + a - 2b}\,(\chi - \chi_0) \ , \tag{B.5}$$

where $\mathrm{F}(u|m)$ is the elliptic integral of the first kind with modulus m[42], given by $m = (\alpha^2 - \beta^2)/\alpha^2$, χ_0 is an integration constant, and the roots of the 2nd degree polynomial in t^2

$$(c + a/2 - b)\,t^4 + 2ct^2 + c - a/2 - b = 0 \ , \tag{B.6}$$

are denoted by $-\alpha^2$ and $-\beta^2$, respectively. They may be expressed as

$$\alpha = \sqrt{\frac{4c}{2c + a - 2b}\ \frac{1}{2 - m}} \tag{B.7}$$

and

$$\beta = \sqrt{\frac{4c}{2c + a - 2b}\ \frac{1 - m}{2 - m}} \ . \tag{B.8}$$

Solving Eq. (B.5) for φ yields

$$\tan\varphi = \pm\beta\ \mathrm{sc}\left(\alpha r\sqrt{2c + a - 2b}\,(\chi - \chi_0)\,\Big|m\right) \ . \tag{B.9}$$

Rewriting the boundary condition, Eq. (5.74), as $\tan\varphi(\chi + n\pi) = \tan\varphi(\chi)$ and using the periodicity of the Jacobi amplitude function [106], $\mathrm{am}(s + 2nK(m)|m) = \mathrm{am}(s|m) + n\pi$, the relation

$$\alpha r\sqrt{2c + a - 2b} = \frac{2}{\pi}K(m) \ , \tag{B.10}$$

is found. From the above equation, m may be determined from

$$c = b\frac{2-m}{m}\left(\frac{2-m}{m} \pm \sqrt{\left(\frac{2-m}{m}\right)^2 - 1 + \frac{a^2}{4b^2}}\right) \ , \tag{B.11}$$

which was obtained by insertion of Eqs. (B.7) and (B.8) into $m = (\alpha^2 - \beta^2)/\alpha^2$.

In the limit $m \to 1$ Eqs. (B.7), (B.8) and (B.11) yield

$$\lim_{m\to 1} \alpha = \frac{a+2b}{a} \ , \tag{B.12}$$

$$\lim_{m\to 1} \beta = 0 \ , \tag{B.13}$$

$$\lim_{m\to 1} c = \begin{cases} a/2 + b \\ a/2 + b/2 \end{cases} \ . \tag{B.14}$$

Since $\lim_{m\to 1} K(m) = \infty$, Eq. (B.10) states that $m \to 1$ must correspond to $r \to \infty$. Thus, in order to satisfy $c > \frac{a}{2} + b$ for all r, + sign in Eq. (B.11) must be chosen.

For $a = 4\eta$, $b = 1/2$ and $\chi_0 = 0$, Eqs. (B.7)-(B.11) yield the solution given by Eqs. (5.75)-(5.78). Note, that χ_0 only corresponds to a rotation of the frame of reference so, without loss of generality, $\chi_0 = 0$ can be chosen.

For $a = 0$ and $b = 1/2$ Eq. (B.1) reduces to

$$\nabla^2\phi + \frac{1}{2}\sin 4\phi = 0 \ , \tag{B.15}$$

which has the solution[107]

$$\phi = \pm\frac{1}{2}\mathrm{am}\left(\frac{4K(m)}{\pi}\chi\Big|\mu\right) \ , \tag{B.16}$$

where $\mathrm{am}(s|\mu)$ is the Jacobi elliptic amplitude function with modulus μ, where μ must be determined from[1]

$$\sqrt{\frac{2}{\mu}}\, r\pi = 4K(\mu) \ . \tag{B.17}$$

The general solution in Eqs. (B.7)-(B.11) reduces to Eqs. (B.16) and (B.17) when $a = 0$, $b = 1/2$, $\chi_0 = -\pi/4$, and

$$m = \frac{4\sqrt{\mu}}{(1+\sqrt{\mu})^2} \ . \tag{B.18}$$

B.1 Equivalence between Eqs. (5.75) and (B.16) when $\eta = 0$

It might seem like a trivial task to put $\eta = 0$ in Eq. (5.75) and get Eq. (B.16), but as usual with elliptic functions this is not the case.

If the two solutions are to be equivalent, then c in Eq. (B.3) for the two solutions must be equal. Calculating c by inserting the solutions and equating the two c's, gives a relation between the two moduli, m and μ, which can be written as

$$m = \frac{4\sqrt{\mu}}{(1+\sqrt{\mu})^2} \ , \tag{B.19}$$

where it was used that $0 < m < 1$ and $0 < \mu < 1$. Using this in the expression for β in Eq. (B.8) it simplifies to

$$\beta = \sqrt{\frac{1-\sqrt{\mu}}{1+\sqrt{\mu}}} \ . \tag{B.20}$$

[1] Please note, in Ref. [107] there is a misprint in this expression.

Transforming the sc function in Eq. (B.9) according to[108]

$$\mathrm{sn}\left(s\Big|\frac{4\sqrt{\mu}}{(1+\sqrt{\mu})^2}\right) = \frac{(1+\sqrt{\mu})\mathrm{sn}(s/(1+\sqrt{\mu})|\mu)}{1+\sqrt{\mu}\ \mathrm{sn}^2(s/(1+\sqrt{\mu})|\mu)}\ , \tag{B.21}$$

and

$$\mathrm{cn}\left(s\Big|\frac{4\sqrt{\mu}}{(1+\sqrt{\mu})^2}\right) = \frac{\mathrm{cn}(s/(1+\sqrt{\mu})|\mu)\mathrm{dn}(s/(1+\sqrt{\mu})|\mu)}{1+\sqrt{\mu}\ \mathrm{sn}^2(s/(1+\sqrt{\mu})|\mu)}\ , \tag{B.22}$$

and re-writing $K(m)$ to $K(\mu)$ by[108]

$$K\left(\frac{4\sqrt{\mu}}{(1+\sqrt{\mu})^2}\right) = (1+\sqrt{\mu})K(\mu)\ , \tag{B.23}$$

yields the expression

$$\tan\left(\phi - \frac{\pi}{4}\right) = \frac{\left(1-\sqrt{\mu}\right)\mathrm{sn}(u|\mu)}{\mathrm{cn}(u|\mu)\mathrm{dn}(u|\mu)}\ , \tag{B.24}$$

where $u \equiv \pm\frac{2}{\pi}K(\mu)\,(\chi-\chi_0)$. It turns out to be easier to compare $\sin\phi$ and $\cos\phi$ instead of ϕ directly, so after a little algebra, the equations

$$\sin\phi = \pm\sqrt{\frac{1}{2} + \frac{\sqrt{1-\mu}\ \mathrm{cn}(u|\mu)\mathrm{dn}(u|\mu)\mathrm{sn}(u|\mu)}{\mathrm{dn}^2(u|\mu) - \mu\mathrm{cn}^2(u|\mu)\mathrm{sn}^2(u|\mu)}} \tag{B.25}$$

and

$$\cos\phi = \pm\sqrt{\frac{1}{2} - \frac{\sqrt{1-\mu}\ \mathrm{cn}(u|\mu)\mathrm{dn}(u|\mu)\mathrm{sn}(u|\mu)}{\mathrm{dn}^2(u|\mu) - \mu\mathrm{cn}^2(u|\mu)\mathrm{sn}^2(u|\mu)}} \tag{B.26}$$

are derived.

Since Eq. (5.72) is invariant under the transformation $\chi \to \chi - \chi_1$ where χ_1 is a constant, Eq. (B.16) may be written more generally as

$$\phi_{\eta=0} = \frac{1}{2}\mathrm{am}\left(\pm\frac{4K(\mu)}{\pi}(\chi-\chi_1)\Big|\mu\right)\ . \tag{B.27}$$

Choosing $\chi_1 = \chi_0 - \pi/4$ and calculating $\sin\phi_{\eta=0}$ and $\cos\phi_{\eta=0}$ gives

$$\sin\phi_{\eta=0} = \pm\sqrt{\frac{1-\mathrm{cn}\left(\frac{4K(\mu)}{\pi}\,(\chi-\chi_0)\,|\mu\right)}{2}} \tag{B.28}$$

and

$$\cos\phi_{\eta=0} = \pm\sqrt{\frac{1+\mathrm{cn}\left(\frac{4K(\mu)}{\pi}\,(\chi-\chi_0)\,|\mu\right)}{2}}\ . \tag{B.29}$$

Using[108]

$$\mathrm{cn}\,(s+K(m)|m) = -\sqrt{1-m}\ \mathrm{sd}(s|m) \tag{B.30}$$

and

$$\mathrm{sd}(2s|m) = \frac{2\mathrm{sn}(s|m)\mathrm{cn}(s|m)\mathrm{dn}(s|m)}{\mathrm{dn}^2(s|m) - m\mathrm{sn}^2(s|m)\mathrm{cn}^2(s|m)} \tag{B.31}$$

gives

$$\sin\phi_{\eta=0} = \pm\sqrt{\frac{1}{2} + \frac{\sqrt{1-\mu}\ \mathrm{cn}(u|\mu)\mathrm{dn}(u|\mu)\mathrm{sn}(u|\mu)}{\mathrm{dn}^2(u|\mu) - \mu\mathrm{cn}^2(u|\mu)\mathrm{sn}^2(u|\mu)}} \tag{B.32}$$

and

$$\cos\phi_{\eta=0} = \pm\sqrt{\frac{1}{2} - \frac{\sqrt{1-\mu}\ \mathrm{cn}(u|\mu)\mathrm{dn}(u|\mu)\mathrm{sn}(u|\mu)}{\mathrm{dn}^2(u|\mu) - \mu\mathrm{cn}^2(u|\mu)\mathrm{sn}^2(u|\mu)}}\ , \tag{B.33}$$

which are the same as Eqs. (B.25) and (B.26), and this shows the equivalence between the two solutions when $\eta = 0$.

Bibliography

[1] H. Kamerlingh-Onnes, Proc. Roy. Acad. Amsterdam **11**, 168 (1908).

[2] H. Kamerlingh-Onnes, Commun. Phys. Lab. **12**, 120 (1911).

[3] H. Kamerlingh-Onnes, Nobel Prize Lecture:
http://nobelprize.org/physics/laureates/1913/onnes-lecture.html .

[4] http://nobelprize.org/physics/laureates/1913/index.html .

[5] F. London and H. London, Proc. Roy. Soc A **149**, 71 (1935).

[6] http://nobelprize.org/physics/laureates/2003/index.html .

[7] http://nobelprize.org/physics/laureates/1972/index.html .

[8] L. P. Gor'kov, J. Exptl. Theoret. Phys. (U.S.S.R.) **9**, 1364 (1960).

[9] http://nobelprize.org/physics/laureates/1973/index.html .

[10] Image used with permission from http://radium0.stanford.edu/Projects/Sample/BSCCO .

[11] http://nobelprize.org/physics/laureates/1987/index.html .

[12] J. Nagamatsu, N. Nakagawa, T. Muranaka, Y. Zenitani, and J. Akimitsu, Nature **410**, 63 (2001).

[13] H. Suhl, B. T. Matthias, and L. R. Walker, Phys. Rev. Lett. **3**, 552 (1959).

[14] V. L. Ginzburg and L. D. Landau, J. Exptl. Theoret. Phys. (U.S.S.R.) **20**, 1064 (1950).

[15] J. Bardeen, L. N. Cooper, and J. R. Schrieffer, Phys. Rev. **108**, 1175 (1957).

[16] T. Schneider and J. M. Singer, "Phase Transition Approach to High Temperature Superconductivity - Universal Properties of Cuprate Superconductors", Imperial Collage Press (2000).

[17] E. M. Lifshitz and L. D. Landau, "The Classical Theory of Fields: Volume 2", English Edition 3rd rev., Pergamon Pr. (1976).

[18] W. Buckel and R. Kleiner, "Superconductivity - Fundamentals and Applications", 2nd Edition, Wiley-VCH (2004).

[19] R. Kato, Y. Enomoto, and S. Maekawa, Phys. Rev. B **47**, 8016 (1993).

[20] W. D. Gropp, H. G. Kaper, G. K. Leaf, D. M. Levine, M. Palumbo, and V. M. Vinokur, Jour. Comp. Phys. **123**, 254 (1996).

[21] W. H. Press (Editor), S. A. Teukolsky (Editor), W. T. Vetterling, and B. P. Flannery, "Numerical Recipes in C++", 2nd edition, Cambridge University Press (2002).

[22] R. Kato, Y. Enomoto, and S. Maekawa, Phys. Rev. B **44**, 6916 (1991).

[23] M. Christensen, Y. Verbin, and A. L. Larsen, Phys. Rev. D **60**, 125012 (1999).

[24] A. Vilenkin and E. P. S. Shellard, "Cosmic Strings and Other Topological Defects", Cambridge University Press Cambridge England (1994).

[25] See, e.g., Y. Verbin, S. Madsen, A. L. Larsen, and M. Christensen, Phys. Rev. D **65**, 063503 (2002); Y. Verbin, S. Madsen, and A. L. Larsen, Phys. Rev. D **67**, 085019 (2003) and references therein.

[26] D. O. Guntherm H. G. Kaper, and G. K. Lead, SIAM J. Sci. Comput **23**, No. 6, 1943 (2002).

[27] E. Merzbacher, "Quantum Mechanics", 3rd Edition, Wiley (1998).

[28] A. A. Abrikosov, J. Exptl. Theoret. Phys. (U.S.S.R.) **5**, 1174 (1957).

[29] A. Scott, "Nonlinear Science - Emergence & Dynamics of Coherent Structures", Oxford University Press (1999).

[30] T. P. Orlando and K. A. Delin, "Foundations of Applied Superconductivity", Addison-Wesley (1991).

[31] H. B. Nielsen and P. Olesen, Nuclear Physics B **61**, 45 (1973).

[32] See, e.g., B. J. Baelus, F. M. Peeters, and V. A. Schweigert, Phys. Rev. B **63**, 144517 (2001) and references therein.

[33] B. D. Josephson, Phys. Lett. **1**, 251 (1962).

[34] T. L. Boyadjiev and Z. D. Genchev, Journal of Physical Studies **5** no. 3/4 316 (2001).

[35] A. Barone and G. Paterno, Physics and Applications of the Josephson Effect, Wiley (1982).

[36] D. W. McLaughlin and A. C. Scott, Phys. Rev. A **18**, 1652 (1978).

[37] M. Cirillo, N. Grønbech-Jensen, M. R. Samuelsen, M. Salerno, and G. V. Rinati, Phys. Rev. B **58** 12377 (1998).

[38] M. Salerno and M. R. Samuelsen, Phys. Rev. B **59**, 14653 (1999).

[39] M. D. Fiske, Rev. Mod. Phys. 36, 221 (1964).

[40] A. V. Ustinov and N. F. Pedersen, Phys. Rev. B **72**, 052502 (2005).

[41] G. Costabile, S. Pagano, and R. D. Parmentier, Phys. Rev. B **36**, 5225 (1987).

[42] M. Abramowitz and I. A. Stegun, Handbook of Mathematical Functions with Formulas, Graphs, and Mathematical Tables, Dover, New York (1970).

[43] S. Pagano, M. P. Sørensen, R. D. Parmentier, P. L. Christiansen, O. Skovgaard, J. Mygind, N. F. Pedersen, and M. R. Samuelsen, Phys. Rev. B **33**, 174 (1986).

[44] N. F. Pedersen and K. Saermark, Physica **69**, 572 (1973).

[45] O. Tønnesen, "Power Applications for Superconductivity", Publication No. 9801, Department of Electrical Power Engineering, Technical University of Denmark Dk-2800 Kgs. Lyngby.

[46] American Superconductor website:
http://www.amsuper.com/products/htsWire/images/2g_hts_detail_lg.jpg .

[47] S. Sakai, P. Bodin, and N. F. Pedersen, J. Appl. Phys. **73**, 2411 (1993).

[48] R. Kleiner and P. Müller, Phys. Rev. B **49**, 1327 (1994).

[49] A. V. Ustinov, H. Kohlsted, M. Cirillo, N. F. Pedersen, G. Hallmanns, and C. Heiden, Phys. Rev. B **48**, 10614 (1993).

[50] S. M. Kim, H. B. Wang, T. Hatano, S. Urayama, S. Kawakami, M. Nagano, Y. Takano, T. Yamashita, and K. Lee, Phys. Rev. B **72**, 140504(R) (2005).

[51] L. X. you, P. H. Wu, Z. M. Ji, S. X. Fan, W. W. Xu, L. Kang, C. T. Lin, and B. Liang, Supercond. Sci. Technol. **16**, 1361 (2003).

[52] R. Kleiner, Phys. Rev B **50**, 6919 (1994).

[53] N. F. Pedersen and S. Sakai, Phys. Rev. B **58**, 2820 (1998).

[54] R. Kleiner, T. Gaber and G. Hechtfischer, Phys. Rev. B **62**, 4086 (2000).

[55] S. Sakai and N. F. Pedersen, Phys. Rev. B **60**, 9810 (1999).

[56] A. Petraglia, A. V. Ustinov, N. F. Pedersen and S. Sakai J. Appl. Phys. **77**, 3 (1995).

[57] N. Grønbech-Jensen, M. R. Samuelsen, P. S. Lomdahl, and J. A. Blackburn, Phys. Rev. B **42**, 3976 (1990).

[58] C. Gorria, P. L. Christiansen, Yu. B. Gaididei, V. Muto, N. F. Pedersen, and M. P. Sørensen, Phys. Rev. B 66, 172503 (2002).

[59] C. Gorria, P. L. Christiansen, Yu. B. Gaididei, V. Muto, N. F. Pedersen, and M. P. Sørensen, Phys. Rev. B 68, 035415 (2003).

[60] E. Goldobin, A. Wallraff, N. Thyssen, and A. V. Ustinov Phys. Rev. B **57**, 130 (1998).

[61] E. Goldobin, A. Wallraff, and A. V. Ustinov Jour. Low Temp. Phys. **119**, 589 (1999).

[62] N. Grønbech-Jensen, D. Cai, A. R. Bishop, A. W. C. Lau, and P. S. Lomdahl, Phys. Rev. B **50**, 6352 (1994).

[63] E. Goldobin, B. A. Malomed, and A. V. Ustinov, Phys. Rev. B **62**, 1414 (2000).

[64] E. Goldobin, B. A. Malomed, and A. V. Ustinov, Phys. Lett. A **266**, 67 (2000).

[65] N. Grønbech-Jensen, J. A. Blackburn, and M. R. Samuelsen, Phys. Rev. B **53**, 12364 (1996).

[66] A. V. Ustinov and H. Kohlsted, Phys. Rev. B **54**, 6111 (1996).

[67] G. Carapella, G. Costabile, A. Petraglia, N. F. Pedersen, and J. Mygind Appl. Phys. Lett. **69**, 9 (1996).

[68] A. Ustinov, Physica D **123**, 315-329 (1998).

[69] N. F. Pedersen and G. Filatrella, Physica C **369**, 171-176 (2002).

[70] N. F. pedersen, M. R. Samuelsen, and D. Welner, Phys. Rev. B **30**, 4057 (1984).

[71] See, e.g., Ref. [49] and [65]; G. Carapella, G. Costabile, J. Mygind, and N. F. Pedersen, IEEE Trans. Appli. Supercond. **9**, 4558 (1999); P. Barbara, Ph.D. thesis, The Technical University of Denmark (1995).

[72] M. Salerno, M. R. Samuelsen, G. Filatrella, S. Pagano, and R. D. Parmentier, Phys. Lett. A **137**, 75 (1989); Phys. Rev. B **41**, 6641 (1990); N. F. Pedersen and A. Davidson, Phys. Rev. B **41**, 178 (1990).

[73] N. Grønbech-Jensen, Phys. Rev. B **47**, 5504 (1993); Phys. Lett. A **169**, 31 (1992).

[74] N. Grønbech-Jensen, Ph.D. Thesis, The Technical University of Denmark (1991).

[75] M. Tachiki, M. Iizuka, K. Minami, S. Tejima, and H. Nakamura, Phys. Rev. B **71**, 134515 (2005).

[76] See the top 500 list from November 2005 at: http://www.top500.org/lists/2005/11/basic .

[77] See, e.g., G. Filatrella, G. Rotoli, N. Grønbech-Jensen, R. D. Parmentier, and N. F. Pedersen, J. Appl. Phys. **72**, 3179 (1992); G. Filatrella and N. F. Pedersen, Physica C **372**, 11 (2002); N. Grønbech-Jensen, R. D. Parmentier, and N. F. Pedersen, Phys. Lett. A **142**, 427 (1989).

[78] See, e.g., G. Filatrella, N. F. Pedersen, and K. Wiesenfeld, Phys. Rev. B **61**, 2513 (2000); E. Almaas and D. Stroud, Phys. Rev. B **67**, 064511 (2003).

[79] S. Ooi, T. Mochiku, and K. Hirata, Phys. Rev. Lett. **89**, 247002 (2002).

[80] I. Kakeya, M. Iwase, T. Yamamoto, and K. Kadowaki, cond-mat/0503498 (2005).

[81] T. Hatano, H. Wang, S. Kim, S. Urayama, S. Kawakami, S. J. Kim, M. Nagao, K. Inomata, Y. Takano, T. Yamashita, and M. Tachiki, IEEE Trans. Appl. Supercond. **15** no. 2, 912 (2005).

[82] A. V. Ustinov and N. F. Pedersen, Phys. Rev. B **72**, 052502 (2005).

[83] N. F. Pedersen and S. Madsen, IEEE Trans. Appl. Supercond. **15**, 948 (2005); N. F. Pedersen and S. Madsen, Proceedings of the Plasma 2004 conference, Tsukuba, Japan, II-48 (2004).

[84] I. O. Kulik, Pis'ma Zh. Eksp. Teor. Fiz. 2, **134** (1965)[Sov. Phys. JETP Lett. 2, **84** (1965)].

[85] N. Grønbech-Jensen, M. R. Samuelsen, P. S. Lomdahl, and J. A. Blackburn, Phys. Rev. B **42**, 3976 (1990).

[86] N. Grønbech-Jensen, D. Cai, and M. R. Samuelsen, Phys. Rev. B **48**, R16160 (1993).

[87] F. Bonquet, R. A. Fisher, N. E. Phillips, D. G. Hinks and J. D. Jorgensen, Phys. Rev. Lett. **87**, 047001 (2001); S. Tsuda, T. Yokaya, Y. Takano, H. Kito, M. Matsushita, E. Yin, J. Itoh, H. Marima and S. Shin, Phys. Rev. Lett. **91**, 127001 (2003).

[88] C. Buzea and T. Yamashita, Supercond. Sci. Technol. **14**, R115 (2001); M. Iavarone, G. Karapetrov, A. E. Koshelev, W. K. Kwok, G. W. Crabtree, D. G. Hinks, W. N. Kang, E. Chao, H. Kim and S. I. Lee, Phys. Rev. Lett. **89**, 187002 (2002) and references therein.

[89] M. E. Zhitomirsky and V. H. Dao, Phys. Rev B **69**, 054508 (2004).

[90] A. E. Koshelev and A. A. Golubov, Phys. Rev. Lett. **92**, 107008 (2004).

[91] A. A. Golubov and A. E. Koshelev, Phys. Rev. B **68**, 104503 (2003).

[92] E. Babaev, Nucl. Phys. B **686**, 397 (2004).

[93] M. S. Soskin and M. V. Vasnetsov, Progress in Optics **42**, 219 (2001).

[94] C. O. Weiss, M. Vaupel, K. Staliunas, G. Slekys and V. B. Taranenko, Appl. Phys. B **68**, 151 (1999).

[95] P. Coullet, L. Gil and F. Rocca, Optics Communications **73**, 403 (1989).

[96] E. Babaev, Phys. Rev. Lett. **89**, 067001 (2002).

[97] M. R. Eskildsen, M. Kugler, S. Tanaka, J. Jun, S. M. Kazakov, J. Karpinski, and Ø. Fischer, Phys. Rev. Lett. **89**, 187003 (2002).

[98] J. M. Speright, Phys. Rev. D **55**, 3830 (1997).

[99] R. MacKenzie, M. A. Vachon and U. F. Wichoski, Phys. Rev. D **67**, 105024 (2003).

[100] E. Babaev, cond-mat/0302218 (2004).

[101] S. M. M. Virtanen and M. M. Salomaa, J. Phys. Condens. Matter **12**, L147 (2000).

[102] See, e.g., E. Goldobin, A. Sterck, T. Gaber, D. Koelle, and R. Kleiner, Phys. Rev. Lett. **92**, 057005 (2004) and references therein.

[103] H. Büttner, Yu. B. Gaididei, A. Saxena, T. Lookman and A. R. Bishop, J. Phys. A. Math. General **37**, 8595 (2004).

[104] A. E. Koshelev and I. Aranson, Phys. Rev. B. **64**, 174508 (2001).

[105] T. W. B. Kibble, Physica C **369**, 87 (2002).

[106] P. F. Byrd and M. D. Friedman, "Handbook of Elliptic Integrals for Engineers and Scientists", Springer-Verlag (1971).

[107] S. Madsen, Yu. B. Gaididei, P. L. Christiansen and N. F. Pedersen, Proceedings for the Plasma 2004 conference in Tsukuba, Japan (2004).

[108] I. S. Gradshteyn, I. M. Ryzhik and A. Jeffrey (Editor), "Table of Integrals, Series, and Products", 5th Edition, Academic Press (1994)